Seismic Retrofit of Bridges Supported on Hollow Core Prestressed Concrete Pile-Columns

Samuel Turner

A thesis

submitted in partial fulfillment of the

requirements for the degree of

Master of Science in Civil Engineering

University of Washington

2020

Committee:

John F. Stanton

Paolo M. Calvi

Dawn E. Lehman

Program Authorized to Offer Degree:

Civil and Environmental Engineering

University of Washington

Abstract

Seismic Retrofit of Bridges Supported on Hollow Core Prestressed Concrete Pile-Columns

Samuel Earl Turner

Co-Chairs of the Supervisory Committee:
John F. Stanton
Civil and Environmental Engineering
Paolo M. Calvi
Civil and Environmental Engineering

The Washington State Department of Transportation (WSDOT) began a bridge seismic retrofit program in 1991 in order to address the earthquake risks associated with state-owned bridges. The majority of these bridges were constructed in the 1960s, prior to the development of modern seismic design standards during the 1970s and 1980s, and one class of bridges built during that era represents a particular cause for concern. In that class of bridges, circular, hollow-core precast, prestressed concrete piles were driven into the ground, with sufficient length left projecting above ground level to form the columns. Hence, they are referred to in this thesis as "pile-columns." Cap beams were then cast in place on the pile-columns and were connected to them by means of concrete plugs with longitudinal reinforcement cast into the tops of the columns. Many of these hollow pile-column bridges form part of the state's "Lifeline Routes" for seismic events and are consequently slated for retrofit in the near future.

Previous, but limited, experimental research have shown that hollow, prestressed concrete specimens show minimal ductility under cyclic lateral loading and fail suddenly, because the wall of the column spalls both inwards and outwards. However, cyclic lateral loading performed during an earlier phase of this research program on an as-built scaled model specimen of the column-to-

cap-beam connection showed better ductility than expected. In this portion of the research program, reported in this thesis, experiments were conducted to better understand the behavior of the hollow core pile-columns under pure bending (relevant in the pile region below-grade) as well as combined bending and shear (relevant in the column region above-grade). Finally, a column-to-cap-beam connection retrofitted with a carbon fiber jacket was tested under cyclic lateral loading.

Under elastic conditions, the peak moment demand in the pile-column occurs at column-to-cap-beam connection; the moments below-grade are approximately half as large. As a result, the retrofit concept for these bridges is concentrated on that connection. The tested retrofit option involved jacketing the as-built plug region in a carbon fiber wrap on the basis that that procedure is simple and reliable, it slightly lowers the peak moments below-grade, and, if a fiber jacket could be used over only the upper part of the column, it would avoid invoking environmental restrictions for bridges over waterways. Concerns with this, and any other retrofit option, include vulnerability to combined bending and shear failure of the hollow cross section just beyond the end of the plug, as well as susceptibility to pure bending failure of the hollow pile below-grade.

Three experimental programs were conducting during this investigation. The first and second were conducted to determine the pure bending, and combined shear and bending, strengths of a hollow pile-column section. The results of these tests aided in calibrating the transverse load capacity of hollow prestressed concrete specimens under two separate load configurations. The third experiment was conducted on a scaled cantilever column-to-cap beam connection, retrofitted with a fiber jacket around the plug region, under reversed cyclic displacement. The results of the third experiment showed that the retrofitted pile-column performed slightly better than the as-built specimen, and that the critical mode of failure was not internal spalling, as suggested by previous researchers, but rather by column cracking, followed by strand debonding. Review of the test results from the as-built specimen concluded that that specimen, too, had failed by strand debonding. Debonding failure proved to be non-ductile, because the strands buckled during the half-cycle following debonding, then fractured as they re-straightened. It was further concluded that the fiber jacket had provided little benefit because strand debonding, and not concrete confinement, was the primary failure mechanism.

A third retrofit option was then developed, but limitations on resources prevented it from being tested. Strand debonding can occur only after the column wall cracks, which requires high net

tension stress, due primarily to bending. A thick steel jacket, made composite with the concrete components, would increase the flexural stiffness of the region and reduce the bending stress in the concrete column wall, thereby preventing cracking. A methodology for selecting the jacket thickness was developed, and it is recommended that this retrofit option be tested and, if the test is successful, it should be adopted.

TABLE OF CONTENTS

iii

iv

LIST OF FIGURES

ix

x

xiii

LIST OF TABLES

NOTATION LIST

A_{col} = area of above-grade hollow column

ADRS = acceleration displacement response spectrum

A_{plug} = area of plug

ARS = acceleration response spectrum

A_{str} = cross-sectional area per prestressing strand

A_v = area of interface shear reinforcement

A_{wall} = area of column/pile wall

b = coefficient used for Menegotto-Pinto calibration

B = distance between vertical string potentiometers on cantilever column tests

BC = bare column

b_{deck} = deck width

c = neutral axis depth

CB = cap beam

C_c = creep coefficient

CDP = cotton duck padding

CFRP = carbon fiber reinforced polymer

d = diameter of spiral reinforcement

$D/D_{col}/D_{pile}$ = outer diameter of hollow column or pile

D_{ave} = average diameter of steel jacket

DCR = demand to capacity ratio

D_{plug} = diameter of plug

d_{str} = diameter of prestressing strand

E_i = modulus of elasticity of material, i

epu = strain in prestressing strand at peak stress

f'_c = specified 28-day concrete compressive strength

f'_{cc} = confined concrete compressive strength

f_{0e} = effective initial concrete stress due to prestressing, accounting for losses

f_{ax} = concrete stress due to external axial load

f_b = concrete stress due to bending

f_{cr} = concrete cracking stress

F_{eff} = effective lateral force

F_{EQ} = earthquake amplification factor

f_{p0} = initial prestressing stress

$f_{pe} =$	effective prestressing stress, accounting for losses
$f_{pj} =$	jacking stress
$f_{pj+} =$	prestressing stress just before release
$f_{ps} =$	stress of most extreme prestressing strand at member failure
$f_{pu} =$	minimum ultimate stress of prestressing strands
$f_{py} =$	minimum yield stress of prestressing strands
$f_y =$	yield stress of steel reinforcement
$f_{tot} =$	total concrete stress
$f_u =$	ultimate stress
FWC $=$	fiber wrapped column
$g_a =$	function describing distribution of axial load between plug and column
$h =$	depth of cross section
$I_i =$	moment of inertia of cross section, i
$k =$	factor relating neutral axis depth, c, to cross section depth, h
$L =$	distance from cap beam to point of horizontal load application on test specimens
$L_{col} =$	length of above-grade column
$L_d =$	development length of reinforcement (either steel or prestressing strand)
$L_{deck} =$	length of bridge deck
$L_{end} =$	distance from point load to end of column or plug
L_{PI}	distance from cap beam to point of inflection
$L_{pile} =$	length of below-grade pile
$L_{plug} =$	length of plug
$L_{slip} =$	length of disturbed region in filled section
$L_t =$	transfer length for prestressing strands
$M_b =$	effective base moment accounting for P-Delta effects
$M_{col} =$	moment taken by hollow column in filled section
$M_{cycle} =$	moment demand reached on testing cycle
$M_{max} =$	maximum moment demand
$M_{n,filled} =$	nominal moment capacity of pile-column in plug region
$M_{n,hollow} =$	nominal moment capacity of hollow column
$M_{n,plug} =$	nominal moment capacity of plug only
$M_{n,predicted} =$	Nominal predicted moment capacity of cross section of interest
$n =$	exponent used in composite analysis or ratio of Young's moduli for 2 materials
NLTHA $=$	nonlinear time history analysis
$P =$	total axial load
$pga =$	peak ground acceleration
PTFE $=$	Polytetrafluoroethylene
$P_{wall} =$	Axial load carried by column wall

$R =$	coefficient used for Menegotto-Pinto calibration
$s =$	spacing of spiral reinforcement
$S_a =$	spectral acceleration
$S_d =$	spectral displacement
$S_{d1} =$	design response spectral acceleration corresponding to a 1-second period
$SDOF =$	single degree of freedom
$S_{ds} =$	design response spectral acceleration corresponding to short periods
$S_{eff} =$	effective composite section modulus
$T =$	period of structural system
$T_0 =$	reference initial short period of structural system
$t_{jacket} =$	jacket thickness
$T_{long} =$	reference long period of structural system
$t_{wall} =$	thickness of wall
$v =$	deck deflected shape equation
$V =$	effective horizontal actuator load
$V_{actuator} =$	actual horizontal actuator load
$V_c =$	concrete shear capacity
$V_{col} =$	shear demand in column
$V_{cycle} =$	shear demand reached on testing cycle
$V_{flex} =$	shear capacity corresponding to pure bending failure
$V_n =$	nominal shear capacity of cross section of interest
$V_{n,predicted} =$	nominal predicted shear capacity of cross section of interest
$V_s =$	steel shear capacity
$V_u =$	ultimate shear demand
$w/c =$	water to cement ratio
$y_i =$	outer radius of element, i
$z =$	distance on column from cap beam interface
$z_{cr} =$	critical distance from cap beam where stress is largest
$\alpha =$	angle around circumference of cross section, starting at bottom
$\beta =$	Young's modulus factor
$\beta_{soil} =$	soil stiffness in kcf
$\Delta =$	horizontal displacement at point of load application
$\Delta f_{p(t)} =$	function describing the change in total prestressing
$\Delta f_{p,es} =$	function describing the change in prestressing due to elastic shortening
$\Delta_{rot} =$	displacement due to inelastic rotation in the plug

$\Delta_{v,north/south} =$ vertical displacement on north or south side of specimen in plug region

$\varepsilon_{c,bot} =$ concrete strain at most tensile face

$\varepsilon_{c,inner\ wall} =$ concrete strain at inner face of pile wall on compression side

$\varepsilon_{c,top} =$ concrete strain at most compressive face

$\varepsilon_{r1} =$ prestressing losses from source 1 (relaxation)

$\varepsilon_{r2} =$ prestressing losses from source 2 (elastic shortening)

$\varepsilon_{sh} =$ strain at which strain hardening begins

$\varepsilon_{shr} =$ concrete strain due to shrinkage

$\varepsilon_T =$ strain in most extreme tensile reinforcement

$\varepsilon_u =$ ultimate strain

$\varepsilon_y =$ yield strain of material of interest

$\theta =$ limiting drift ratio

$\theta_{base} =$ rotation measured at the base of the test specimen

$\kappa =$ bond capacity factor accounting for cross section depth

$\mu =$ coefficient of friction

μ_Δ displacement ductility ratio

ρ or $\rho_g =$ volumetric reinforcement ratio

$\sigma_1 =$ principal stress

$\tau =$ shear stress in column wall

$\phi_{cr} =$ cracking stress reduction factor

$\omega =$ system frequency

$\mu\varepsilon =$ microstrain

ACKNOWLEDGMENTS

I would first like to thank my advisors, Professor John Stanton and Professor Paolo Calvi for their continuous guidance and support throughout this research project. I am extremely thankful for the time I spent in their company, and through it all I learned to not get lost in individual "rabbit-hole problems" and to rather always keep the big picture in mind. I would also like to thank Professor Dawn Lehman for serving on my committee.

A special thanks also to all those who helped with the construction and testing of all specimens in the UW Structural Research Lab. Without the following people this project would not have been possible: Vince Chaijaroen (UW's very own Dumbledore!) for his unmatched practical wisdom and wizardry; Tasha Tardieu for being everything from my first TA, to project supervisor, to friend and confidant; Stephan Ahn, Austin Anderson, Kai Gallagher, Kiran Kaur, Dalton Lundberg, Chris Pyke, Ben Terry, and Alec Yeutter for their help on test or cast days, or whenever a big task required many hands. I am forever grateful to all of you.

Monetary support and project guidance from the Washington State Department of Transportation is greatly appreciated.   In addition, thank you to Concrete Technology Corporation for manufacturing the test specimens, and to Combined Construction for the donation of carbon fiber wrap material and labor.

Finally, and most importantly, thank you to my family, friends, and mentors who got me through graduate school.

DEDICATION

To my parents, Diane and Scott Henshaw and Clayton and Kara Turner, and all of my siblings:

Ben, Rachel, Connor, Lauren, Jacob, and Katherine. To Emily… always. I could not have done

it without all of you.

Chapter 1. INTRODUCTION

1.1   BACKGROUND

The state of Washington is ranked nationally as one of the most susceptible to economic loss caused by earthquakes, second only to California, according to a 2008 Federal Emergency Management Agency (FEMA) study. These losses would be amplified if critical transportation infrastructure were damaged since the movement of key personnel and emergency responders would be limited. Seattle is especially dependent on the bridges that form hundreds of miles of its critical highway networks, such as Interstate 5 and Interstate 405. Multiple studies exploring the impact of megathrust or Seattle fault earthquakes have found that the city's transportation system would be severely impacted by these types of earthquakes (Seattle Office of Emergency Management).

The Washington State Department of Transportation (WSDOT) undertook a large-scale bridge retrofit program beginning in 1991 to address the seismic risk associated with the nearly 3,000 state-owned bridges that WSDOT maintains. The majority of these bridges were constructed prior to the implementation of modern seismic design standards in the 1970s and 1980s. In particular, hollow prestressed concrete pile-columns were used as the foundation of 22 bridges in Washington State built in the 1960's and 1970's. These pile-columns were typically driven into the ground with the upper end projecting above ground to form the columns of the bridge piers. Cap beams were then cast-in-place over the columns with a longitudinally reinforced solid concrete plug section that extended a short distance into the top of the hollow section to form the moment connection at the top of the above-grade column. A typical cross-section of these bridges is illustrated in Figure 1-1.

1
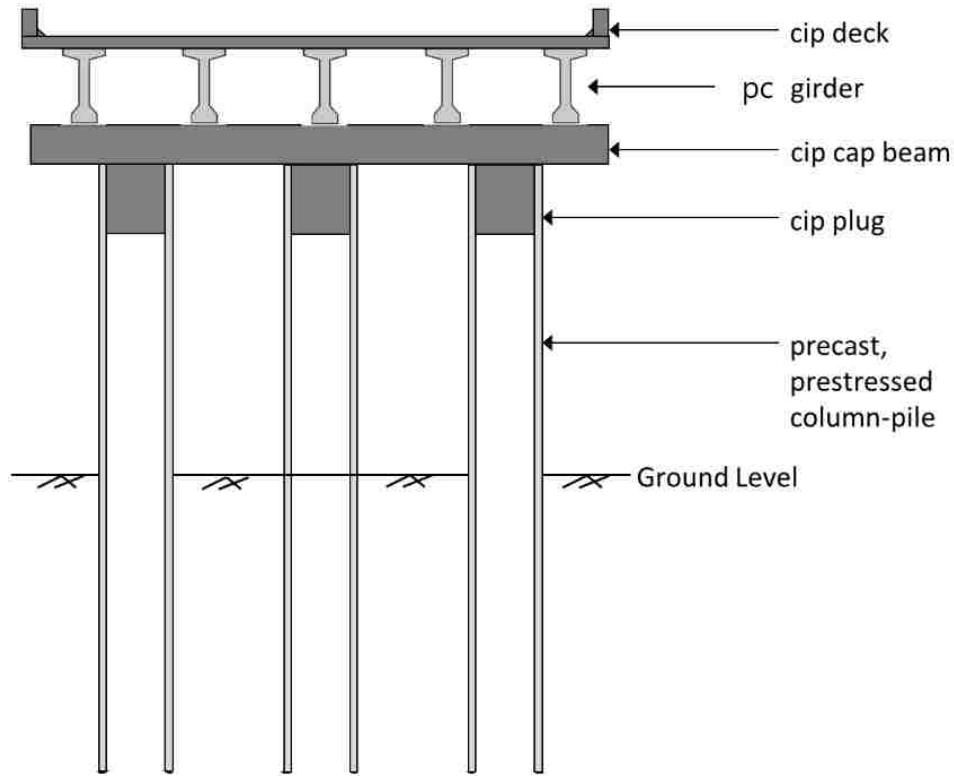
Figure 1-1. Typical section of bridge founded on hollow prestressed concrete pile-columns

The hollow core prestressed concrete pile-columns are a part of the state's retrofit program after previous research experiments showed that these hollow prestressed elements fail suddenly and show very little ductility (Pizzano, 1984; Budek et al. 1997). With this knowledge, WSDOT intends to retrofit the affected bridges in coming years. Because hollow prestressed pile-columns have not been widely used in seismic regions, relatively little research has been conducted on them. The studies that have been completed, discussed in Chapter 2, have largely focused on vulnerabilities, rather than retrofit schemes. Development of an effective retrofit concept is the overarching objective of this research program.

1.1.1 *Reference Bridges*

WSDOT asked the research team to focus on a bridges that form parts of the Interstate 5 highway system that runs north to south through the state, as well as parts of the Interstate 405 highway that runs parallel to Interstate 5 on the east side of Lake Washington. Interstate 5 is Washington's

2

busiest roadway and sees over 250,000 vehicles daily (Gutman, 2018). In a large seismic event, damage to this highway would hinder travel through the city and state, and cause significant traffic delays and/or high economic losses. Interstate 405 is also part of the state's "lifeline route" (in addition to Interstate 5), which is intended to facilitate transportation needs in the event of a disaster and serves the tech-concentrated regions of Bellevue and Kirkland. The bridges that were used as reference structures in this study are described below and further details are provided in Appendix A.

1.1.1.1 Ravenna Boulevard Overcrossing

The Ravenna Boulevard Overcrossing is located in the Ravenna neighborhood of Seattle near NE 63rd Street and 8th Avenue NE. The bridge is 1,310 feet long and has 19 spans, supporting four lanes of traffic on each of three sections. It was constructed between 1960 and 1962 and is made up of precast, prestressed concrete girders and columns. The columns are hollow with a 48-inch outer diameter and a 5-inch thick wall, and extend into the ground to act as pile shafts. The above ground height of the columns varies from 15 to 27 feet and they are spaced at 18 feet centers for every bent (Greenwood, 2008). At the top of the columns, there is a four-foot long (one column diameter) inner plug of reinforced concrete with longitudinal bars that extend into the cap beam. The cap beam is 54 inches wide by 36 inches deep and is typically supported by four to seven columns.

The columns on Ravenna Bridge were all post-tensioned except for two test piles, which were pre-tensioned. According to historical documents obtained from WSDOT, the post-tensioned piles were line-cast with metal ducts in the walls; the spaces between the ends of the piles were blocked and the whole line was post-tensioned. The ducts were grouted, after which the anchors (which were present only on the end piles of the line) were cut, leaving the prestressing forces to be transferred by bond alone. By contrast, two of the piles were pre-tensioned by a separate company after construction workers reported seeing large longitudinal splitting cracks form while driving the post-tensioned piles. The pre-tensioned piles were manufactured and driven to compare the development of cracks, which the contractor noted was minor for the two pre-tensioned test piles in the soil conditions present on site. The researchers inspected the columns at the Ravenna Bridge, and saw long cracks along the height of the column, especially to the north end of the bridge where

المنارة للاستشارات

www.manaraa.com

the first piles were driven (See Figure 1-2). These cracks also aligned well with the three-strand tendons of the column, which were detected using a reinforcement locator, but the precise cause of the cracks is unknown.

Figure 1-2. Longitudinal cracks on columns of Ravenna Bridge

Lastly, while most piles had to be cut off to the correct height, some piles had to be extended. From the contractor's explanation of the pile extensions it is unclear whether they were solid or hollow and, reinforced or not further adding to the uncertainty of the as-built conditions of the columns.

1.1.1.2 East Galer St. to Lakeview Boulevard Viaduct

The East Galer St. to Lakeview Boulevard Viaduct (will be referred to as the Galer-Lakeview Bridge) is located at the intersection of three major neighborhoods in Seattle – Eastlake, South Lake Union, and Capitol Hill. The viaduct consists of three bridges approximately 1691 feet long with 19 spans, supporting multiple lanes of traffic. This bridge began construction shortly after the Ravenna Bridge and was completed one year after it. The Galer-Lakeview Bridge is of a similar design to the Ravenna Bridge, but with one major difference: while the Ravenna Bridge was made up of hollow core columns that extended below ground to act as pile shafts, the contractor of the Galer-Lakeview Bridge stated that they chose an alternative method for the

4

foundation of the piles. From the drawings, this alternative method was to cast a 54-inch outer diameter solid, reinforced concrete pile with a bell footing below ground and have the hollow core column sit aboveground only, on top of the solid pile (See Figure 1-3). The two were attached by a cip concrete plug, similar to the one used at the cap beam level. The effect that this method of construction would have on the response of the pile-columns to seismic forces as compared to the Ravenna Bridge was unknown to the researchers.
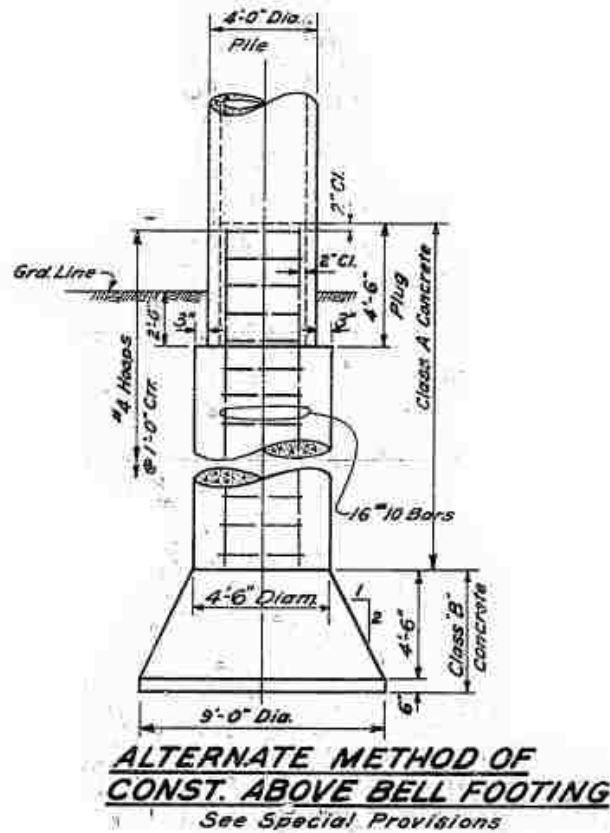
Figure 1-3. Alternative method of pile-column construction for East Galer St. Bridge

Another potential difference between the two bridges upon initial investigation of existing drawings and reports was that, although the Galer-Lakeview Bridge called for almost identical post-tensioned piles to the Ravenna Bridge, the contractor on the project was the same contractor who supplied the two pre-tensioned test piles to the Ravenna Bridge project. This suggests that the piles on the Galer-Lakeview Bridge were actually pre-tensioned. The researcher visited the

site with reinforcement-detection equipment, and found reinforcement at 2-inch centers, which suggests pre-tensioning.

1.1.1.3 L^E Line Bridge over Slide (South 184th Street to South 144th Street)

The L^E Line Bridge over Slide is located to the south of Seattle in the Tukwila neighborhood (will be referred to as Slide the remainder of the paper). The bridge is 515 feet long and consists of five spans. Construction of the original bridge took place between 1965 and 1966, and the bridge was widened in 1994. The two exterior piers consist of hollow core columns that were filled with weak, fill concrete while the interior piers each consist of four hollow core prestressed columns. These columns have a 54-inch outer diameter, that is, six inches wider than the previous two bridges and were pre-tensioned rather than post-tensioned. The bridge is built over a steep gradient in the transverse direction so that the columns on each pier have a height gradient between 15% and 25%. Lastly, the cross beam on the Slide Bridge is quite shallow (three feet deep and five and a half feet wide), which is much different than the previous bridges described. These design components suggest the potential for other, different failure modes in addition to those associated with the hollow columns.

1.1.1.4   Green River Bridge

The Green River Bridge is located along the Interstate 405 system between Tukwila and South Renton, south of Seattle. This bridge is the only one of the four investigated that crosses over water and is very short compared to the others, with three spans covering 245 feet altogether. The two interior piers consist of ten and eleven hollow core pre-tensioned columns, respectively, and are topped by a cip box girder. The Green River Bridge was originally constructed in 1964 and widened in 1988 to accommodate HOV lanes. The lengths of the concrete plugs at the tops of these columns are typically longer than those seen in the other bridges, usually between five and seven feet; however, they were reinforced with fewer bars. The pile design details also varied between Green River and Slide as the Green River Bridge used fewer prestressing strands. A typical pretensioned pile detail is provided in Figure 1-4 (note that the amount of strand reinforcement will vary between the bridges); additionally, these pile-columns contained spiral transverse reinforcement evenly spaced through the length of the plug around the longitudinal reinforcement. The drawings show details for pile splices, achieved with a plug that extends into

the pieces of the pile being spliced. The field records do not show whether splices were used. Because the flexural strength of the splice plug is similar to that of the hollow column itself, the presence of a splice would significantly affect the response only if it were placed at a region of peak flexural demand.
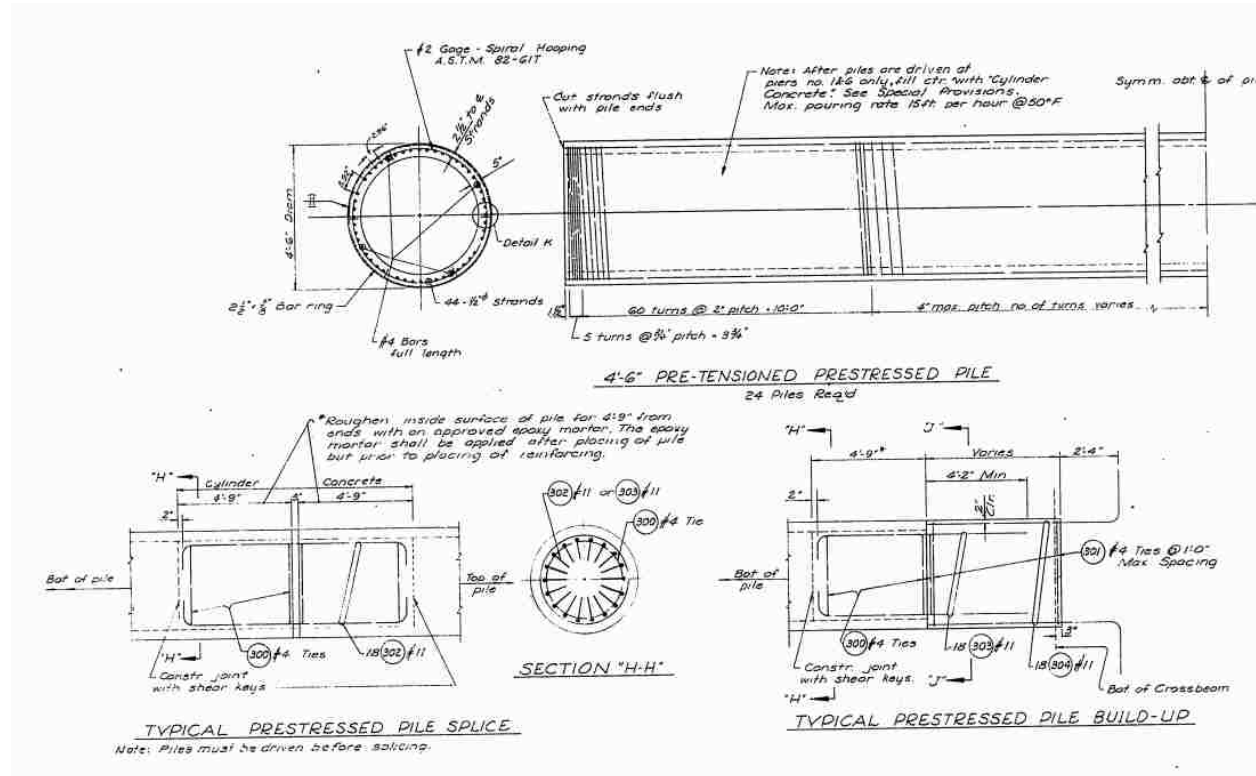
Figure 1-4. Typical details for pretensioned pile-column

1.2   RESEARCH MOTIVATION

Previous studies show that the seismic performance of the as-built bridge system, consisting of a hollow prestressed column connected by a plug to a cast-in-place beam, is suboptimal (Tardieu 2018). While the initial concern of the research team was that hollow sections have been shown to have little flexural ductility because they fail prematurely by internal spalling (implosion) when bent into the inelastic range, the as-built specimen was able to reach a surprisingly high rotation at the cap beam connection (Tardieu 2018). However, after discussions with WSDOT, this rotational capacity was deemed unacceptable, and retrofit methods that were efficient from both a structural and constructability point of view were explored. It should be noted that the as-built specimen

7

failed by splitting near the end of the plug region (but still within the plug region), and not by implosion of the hollow section. This suggested that some other mechanism might be at play at the end of the pile-column (where it connects to the cap beam), and that it might not have been seen by previous researchers (e.g. Budek et al., 1997) because in their test specimens the peak moment was in the central region rather than at the end.

Two locations in the pile-column are particularly susceptible to large moments and were deemed critical by the research team. These are at the cap-beam-column connection and below-grade (See Figure 1-5, grade line is at the x-axis, positive downwards into soil). For elastic response, the above-grade column moments are shown by the red line in Figure 1-5, while the below-grade pile moments are shown in blue and are based on a beam-on-elastic-foundation formulation (Hetényi, 1946). The peak column moment occurs at the cap beam connection and is higher than the peak pile moment, which occurs one to two column diameters below-grade, depending on the soil conditions. The presence of the solid concrete plug at the cap beam connection prevents the inward implosion of the hollow section there under large moments but depending on the length of the plug and the moment gradient along the length of the column, there exists the risk of a hollow section flexural failure just beyond the end of the plug at the sudden change in the column's flexural capacity. The below-grade moment also poses problems as moments high enough to cause potentially non-ductile failure there could be reached after the cap beam connection has yielded. Tests conducted on the as-built specimen and subsequent analysis showed that the more critical component is the cap beam connection. In addition, this location is more practical and convenient for retrofit, and efforts were focused on improving the ductility there by commercially available means.
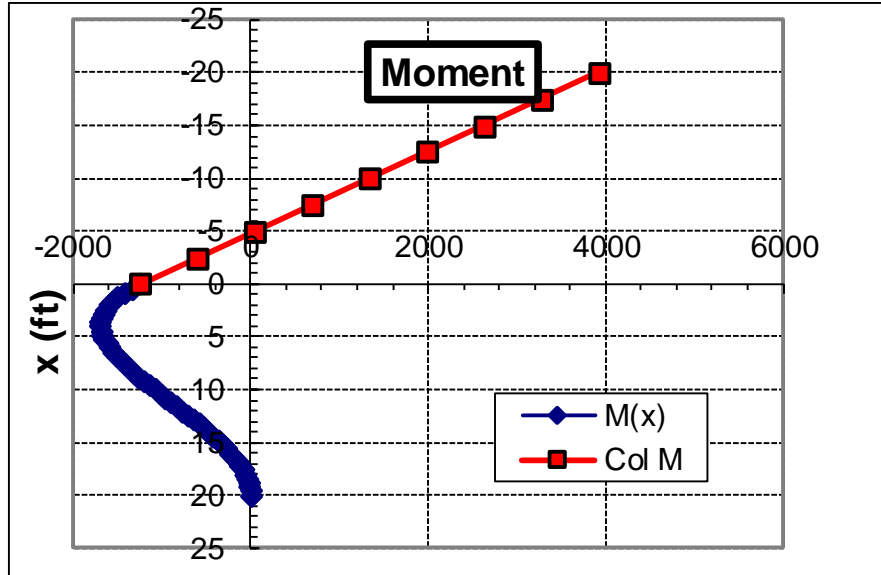
Figure 1-5. Moment demand for as-built conditions

Following the as-built test conducted by Tardieu in 2018, some questions regarding the nominal flexural and combined shear and flexural capacities remained about the hollow core specimens. Prior to that test, the intended retrofit approach had been to use capacity protection to ensure the integrity of the hollow column. By cutting back the column wall for a short distance below the cap beam the flexural strength would be reduced to that of the plug alone. That strength would limit the moments that could be induced in the adjacent hollow regions, so the plug would act as a fuse, rendered ductile by suitable jacketing. While the solution was seen as structurally efficient, two arguments prevailed against it. First, the gravity load of the superstructure would have to be transmitted to the pile-column by shear friction between the plug and the column wall, and tests (Tardieu, 2018) had shown that mechanism could not be relied upon with certainty. Second, cutting back the column wall was seen as difficult in practice, and potentially expensive.

The decrease in capacity protection of the new retrofit idea garnered cause for concern regarding the behavior of the hollow column under different load configurations, namely pure bending and combined bending and shear. The combined shear and bending behavior is relevant to the hollow section just beyond the end of the plug, while the pure bending behavior is applicable to the hollow pile below-grade. An experimental program was therefore developed to gain a better understanding of the hollow column's behavior when undergoing pure bending as well as

9

combined bending and shear. Following this, a commercially available retrofit option (carbon fiber reinforced polymer wrapping around the plug region) was tested under cyclic loading to gage its seismic performance, with the intent of using the jacketed filled (plug + column wall) region as a fuse to protect the hollow column to the extent possible. That fuse would be stronger, and therefore less effective than the plug alone, but because the moments reduce with distance down from the cap beam, it would still provide a measure of capacity protection.

1.3   RESEARCH OBJECTIVES

The objective of this research project were:
- To investigate the seismic response of a typical bridge bent constructed using hollow prestressed concrete pile-columns and a cast-in-place cap beam,
- To develop numerical models that describe that behavior, and
- To develop a retrofit concept to overcome the structural shortcomings of the system.

These objectives were addressed using both analytical and experimental methods, as outlined below:
- An experimental program to determine the specimen behavior under a pure bending load configuration.
- An experimental program to determine the specimen behavior under a combined shear and bending load configuration.
- An experimental program to evaluate the seismic response of the retrofitted column through reversed cyclic cantilever bending (retrofit with a carbon fiber wrap around the solid plug section).
- An analysis to evaluate whether the proposed retrofit will perform as a ductile fuse, and to determine how much safety margin exists with respect to the standard AASHTO 1000-year return period response spectrum for Washington State, before the bridge fails.

10

1.4 ORGANIZATION OF THESIS

To achieve the objectives outlined in Section 1.3, this thesis involves the following chapters:

- **Chapter 2**: **Literature Review**, provides an overview on the existing research that relates to the seismic performance of hollow-core prestressed concrete pile-columns.

- **Chapters 3-5**: **Design, Results and Analysis of Experimental Program** to evaluate the specimen behavior under pure bending (relevant below-grade) and combined bending and shear (relevant above-grade).

- **Chapters 6-8**: **Design, Results and Analysis of Experimental Program** to evaluate the seismic behavior of a retrofitted column specimen.

- **Chapter 9**: **Global Analysis**, extrapolates data from the experimental programs and applies it to the reference field bridges.

- **Chapter 10**: **Summary, Conclusions, and Recommendations**, contains the main findings of the research and provides recommendations for future work before field implementation.

- **Appendices**: Details of the reference bridges are given in Appendix A. Virtual work calculations conducted to determine the effective coefficient of friction during the retrofit cantilever test are provided in Appendix B. Theoretical linear elastic stiffness calculations for the pure bending and combined shear and bending tests are given in Appendix C. Appendix D contains the closed form beam-on-elastic-foundation formulation as well as a derivation of the 3D span/depth ratio used for the global analysis in Chapter 9.

11

Chapter 2. LITERATURE REVIEW

This chapter provides a brief overview of previous research involving the key concepts explored throughout this research program. First, it includes results from previous studies that investigated the flexural and shear behavior of both hollow and solid prestressed concrete piles and/or columns, as well as bond of prestressing strands. Next, a summary of the results of an analytical model of the Ravenna Overcrossing, as well as results from previous experimental and analytical work on this project are presented. Lastly, the effects of external jacketing to improve the seismic performance of concrete columns are outlined.

2.1 PRESTRESSED CONCRETE PILES AND COLUMNS

The majority of previous research has been done on the flexural behavior of solid prestressed concrete piles, especially in the below-grade hinge region. Since below-grade flexural failure is one of the potential modes of failure of the bridge columns, a review of the literature regarding this behavior is included.

2.1.1 *Flexural Behavior*

Ikeda et al. (1982) tested circular, hollow prestressed piles under monotonic and cyclic lateral loading by varying four main parameters: transverse reinforcement ratio, non-prestressed longitudinal reinforcement ratio, prestressing steel reinforcement ratio, and prestressing force. The prestressed piles showed brittle failure at displacement ductility ranging from 4.0-8.0, shortly after yield due to fracture of the prestressing tendons. However, the researchers found that the failure mode could be made more ductile by using closely spaced transverse reinforcement to confine the core and prevent shear failure or by including non-prestressed longitudinal reinforcement in order to increase ductility after rupture of the prestressing tendons.

Pizzano (1984) conducted a series of tests on prestressed octagonal concrete piles to examine their behavior under combined axial and lateral cyclic deformations. This study was done to establish the requirements for designing and detailing prestressed concrete piles to resist severe earthquakes in terms of the curvature capacity of the piles in two critical locations – at the grade level pile to

12

pile cap connection and at the location along the pile body of maximum curvature induced by relative motion at the interface of soils with different stiffnesses. The tests found that hollow piles were less ductile than solid piles and that hollow piles may fail in the body by internal implosion of the wall rather than by bursting the spiral outward, especially in the case of heavy spiral reinforcement. The ductility of solid prestressed concrete piles, however, can be improved by increasing the amount of spiral reinforcement and the ductility achieved at the pile cap is greater than the ductility achieved below-grade in the pile body, for solid piles. Furthermore, no improvement in the curvature capacity was obtained from the addition of non-prestressed reinforcement.

Muguruma, Watanabe, and Nishiyama (1987) tested thirteen high-strength prestressed concrete spun hollow piles in order to find practical ways of improving the flexural ductility of these members. The experimental program varied the net volumetric transverse reinforcement ratio from zero to 3% based on the net concrete area using high-strength wire, and the ductility of the steel using prestressing bars with a maximum elongation from 2% to 5.13%. The unconfined specimens failed by concrete crushing in the compression zone at peak load with no plastic behavior exhibited. For the confined specimens, the prestressing bars showed large post-peak deformation before fracture and obtained much higher tensile strains than the unconfined bars, but there was no significant difference in the measured flexural strength. The study concluded that the flexural capacity of high-strength prestressed concrete spun hollow piles can improve significantly by using high-uniform-elongation prestressing steel. However, the transverse reinforcement should be carefully designed since its contribution to increased ductility can also cause the attainment of high tensile strains in the prestressing bars that can lead to undesirable bar fracture.

Budek, Benzoni and Priestley (1997) experimentally investigated the ductility of in-ground hinges in both solid and hollow prestressed concrete piles since analytical studies showed that these subgrade plastic hinges had to form in order to develop the full inelastic potential at the pile to pile cap connection. The experiments looked at six solid and four hollow prestressed piles by varying the transverse reinforcement levels and the provision of external confinement through the load fixture configuration. For the hollow piles, the addition of non-prestressed longitudinal

13

reinforcement in the pile wall was considered. The piles were loaded cyclically with a test fixture that simulated a soil subgrade moment pattern for an in situ pile.

For the solid piles, the results showed that in the absence of external confinement, a higher transverse reinforcement ratio led to a higher displacement ductility capacity but only up to a volumetric ratio of 2%. On the other hand, the hollow piles' flexural behavior was hardly affected by the variation in transverse reinforcement or external confinement. Failure was due to implosion when the strain at the core's inner surface reached a value of 0.005 (See Figure 2-1) and this occurred at a higher displacement ductility for those piles with non-prestressed longitudinal reinforcement. The authors suggest that the use of hollow prestressed concrete piles should be limited in seismic applications and that they should be designed to remain elastic since they have little ability to dissipate energy by hysteresis.

Figure 2-1. Internal spalling at core face of hollow specimen (Fig. 6.1.2., Budek, Benzoni and Priestley, 1997)

Budek and Benzoni (2009) conducted a parametric study of the inelastic seismic response of a precast, prestressed concrete pile with a grade level cap beam using a project-specific nonlinear, inelastic finite element program. The purpose of the study was to evaluate whether piles with low amounts of transverse reinforcement could act as ductile structural elements since large code-

14

specified minimum amounts of spiral steel have made prestressed concrete piles an uncompetitive design due to congested reinforcement. The program used nonlinear, inelastic constitutive models for both the pile and soil structure in order to account for the change in flexural stiffness of the pile as inelastic action took place at each load step.

The analysis found that increasing soil stiffness increased the maximum magnitude of the subgrade moment since the stiffening soil reduced the shear span between the two maximums and required a greater flexural resistance of the pile-shaft below-grade. Both elastic and inelastic analyses showed similar ultimate moments at the pile head but the below-grade pile shaft maximum moment was much larger for the inelastic conditions. Additionally, the redistribution of moment down the pile shaft after formation of the hinge at the pile cap connection created much higher levels of shear in the pile shaft which was not the case in the purely elastic analysis. The depth of the maximum subgrade moment or hinge was strongly influenced by the whole system stiffness but it approached a limiting value as system stiffness increased, with the largest depth seen in softer soils. Lastly, the ductility capacity decreased with both axial load and soil stiffness, while also being significantly affected by the presence of mild steel reinforcement in the pile wall.

2.1.2 *Shear Strength*

Ranzo and Priestley (2001) investigated the shear strength of thin-walled circular hollow columns, made of reinforced concrete with one layer of transverse reinforcement. The specimens were subject to a constant compressive axial load and a cyclic lateral load sequence. The specimens had a column outer diameter to wall thickness ratio between 10 and 11. The experimental results showed good agreement with existing shear models (UCSD model, ATC-32 model and Caltrans Memo 20-4 model) and the study concluded that the enhancement of shear strength of hollow columns by axial load was less in hollow columns than in solid columns.

Turmo et al (2009) presented an analytical model for evaluating the contribution of transverse reinforcement in solid and hollow circular concrete members (non-prestressed). In particular, a formula for calculating the shear strength in hollow core circular columns with both vertical and spiral reinforcement was deduced theoretically and confirmed experimentally. The deduction of the formula to calculate the contribution of spiral reinforcement to shear strength was based on the

15

development of shear cracking in the form of a helix of constant pitch and this was confirmed through shear strength tests of four hollow circular specimens. The researchers found that the steel contribution to shear strength is more effective in hollow cross-sections as compared to solid cross sections, especially if the transverse reinforcement is spiral. This is because the geometry of the reinforcement follows the orientation of the shear stresses. As a result, the well-known formula for calculating the shear strength of transverse reinforcement can be used with an efficiency factor of 1.0 for hollow circular sections.

2.1.3 *Bond*

Mitchell (2008) investigated the effects of strand diameter and effective prestressing on the transfer length through a finite element analysis of a simplified model. The main conclusion drawn from this study was that for a given coefficient of friction (quality of bond of a strand), the transfer length is independent of the effective stress. This is thought to be due to the increase in the Hoyer effect that occurs with increased applied stress (i.e. the normal force between the strand and the concrete interface increases, increasing the friction along the interface, increasing the bond stress). A secondary conclusion from this study is that transfer length is related to strand size by a power function, rather than linearly; however, this only needs to be applied to strands with a diameter of 0.6 inches or larger.

Marti-Vargas (2013) conducted an experimental program addressing the bond behavior of strands in pretensioned concrete members after anchorage failure has occurred. The prestressing strand force and strand end slip at the specimens' free end was measured for different embedment lengths using twelve concrete mixes. The study found that the when the embedment length is shorter than or equal to the transfer length, the maximum strand force achieved at first slip is nearly equal to the effective prestressing force. For specimens with an embedment length greater than the transfer length, the maximum strand force is greater than the effective prestressing force.

16

2.2　PREVIOUS STUDIES FOR WASHINGTON STATE BRIDGES

Greenwood (2008) performed a series of inelastic nonlinear analyses on an individual hollow pile-column model to understand the failure mechanisms associated with hollow core prestressed concrete piles and the reinforced concrete column to crossbeam connections used in constructing the Interstate 5 Ravenna Overcrossing Bridge near Seattle, Washington. A simplified model using a beam with plastic hinge behavior in SAP2000 was compared alongside a detailed three-dimensional finite element model using ABAQUS/Standard. The models showed good agreement with past experiments that failure occurs once concrete in the compression zone spalls, allowing the exposed reinforcing steel and prestressing tendons to buckle. Additionally, the transverse reinforcement ratio had little effect on load capacity or displacement ductility. The response of the in situ pile is governed by the tensile capacity of the concrete so that tensile cracks forming led to a nearly linear response until compressive failure began at the opposite pile surface. The model also found that confinement of the exterior surface may improve ductility slightly, but eventually the compressive zone would extend and the wall would spall internally and fail. The study suggested that a viable retrofit method may be to pump non-shrink grout into the hollow void while jacketing the exterior with steel or fiber reinforced materials.

El Gawady et al (2009) assessed the inelastic seismic behavior of the Interstate 5 Ravenna Overcrossing Bridge through nonlinear static and dynamic analyses. A three-dimensional finite element analysis of the whole bridge including modelling of the bridge bearings, expansion joints, and nonlinear soil-structure interaction of three different soil types was performed in SAP2000 (2007) using three response spectra to represent ground motions with different return periods. The study found that dense sand led to piles that are more vulnerable to failure so that even a low-level earthquake induced overall bridge failure. On the other hand, piles in stiff clay performed the best and could withstand higher level earthquakes. In all cases, the ductility of the piles was very low and elastic pile behavior was followed by an immediate and brittle failure that always occurred first for pile-columns toward the center of the bridge. However, when a pile-crossbeam connection model was included, the performance of the bridge improved significantly but the nonlinear dynamic analyses found that the bridge is safe only for a 475-year return period earthquake while

17

larger earthquakes would likely cause failure. Higher mode effects made a significant difference in the response of the whole bridge.

Tardieu (2018) analytically assessed the viability of a retrofit option whereby the column wall adjacent to the cap beam was cut back to the plug concrete to limit the maximum possible moment demand achievable beyond the end of the plug and capacity protect the hollow section. The plug region would have also been wrapped in a jacket to improve the ductility capacity of the connection. Following this, an experimental program was developed to test a scaled model column-to-cap-beam connection under reverse cyclic lateral loading to simulate dynamic loading from earthquake. The main conclusions from that investigation are as follows:

- The retrofit option of cutting back the column wall adjacent the cap beam would reduce the moment demand above-grade, however higher moments would be developed below-grade after the plug region yields.
- Additionally, the new connection introduces the need to transfer vertical gravity loads from the plug to column wall by shear friction rather than the as-built mode of direct bearing.
- For these reasons, combined with the required careful construction in the field, this retrofit method was discarded.
- The as-built column-to-cap-beam connection specimen exhibited higher ductility than was expected by the researchers, but it was achieved almost exclusively through inelastic deformation of the plug, and not the prestressed column wall. Subsequent analysis showed that if comparable ductility were available in the field structures, system failure would be controlled by yielding of the below-grade hollow pile after inelastic displacement to a ductility of approximately 2.0. This would occur only at 100% of the design ground motion specified by AASHTO for the Seattle region, which is more favorable than was expected.

2.3   EXTERNAL JACKETING OF CONCRETE COLUMNS

Concrete columns are known to be deficient in flexural ductility, shear strength, and flexural strength when affected by lap splices in critical regions or by premature termination of longitudinal

18

reinforcement (**Priestley et al, 1996**). Jacketing of concrete columns has been shown in many studies to be an effective retrofit to improve the seismic performance of concrete columns if they show any of the foregoing deficiencies. The jackets can be made of different materials including steel, reinforced concrete (or ultra-high performance concrete (UHPC)) and composite materials such as carbon fiber or fiberglass. **Wu et al. (2005)** published a state-of-the-art review of concrete column retrofitting using steel and fiber reinforced polymer jackets. This report summarized the following advantages of the increased confinement provided by external jacketing:

- The external confinement prevents concrete spalling and the buckling of longitudinal reinforcement which enhances the concrete strength and ultimate strain capacity, leading to enhanced flexural ductility.
- The shear strength is improved by the additional hoop confinement that adds to shear reinforcement of the member.
- The jacket confinement provides greater clamping pressure on the longitudinal reinforcing bars that increases their bond and inhibits slipping.

Steel jacketing has long been the most common retrofit technique for concrete columns in seismic regions and has been shown to be effective for all three deficiencies of flexural ductility, shear strength, and flexural strength. **Priestley et al. (1996)** provided a brief summary of the method and reason for steel jacketing: for circular columns, two half shells of steel plate are site-welded at the vertical seams to form a continuous tube with a diameter that is typically 1.0 to 2.0 inches larger than that of the original concrete column, and the gap is typically filled with cement grout. The steel jacket adds to passive confinement of the concrete column and is equivalent to continuous hoop reinforcement. The confining hoop stress from the steel jacket is induced in the concrete when the concrete attempts to expand laterally in the compression zone under high axial compression strains, or in the tension zone due to dilation of lap splices near splice failure. The level of confinement depends on the hoop strength and stiffness of the steel jacket.

Lignola et al. (2008) calibrated a unified theory for confinement of RC in both solid and hollow circular columns when jacketed with FRP by using Mander's model for lateral dilation and comparing the analytical with experimental data from various research programs. This research

19

concluded that the addition of an FRP wrap can "significantly" increase strength and ductility in terms of axial stress capacity. These findings are thought to be less applicable to this project as no bending stresses were accounted for in this research.

Riahi and Faridafshin (2008) reported on the use of carbon fiber-reinforced polymer (CFRP) composites in the seismic retrofit of concrete bridges. The authors state that CFRP composites alter the stiffness of the bridge component only in the direction of the fiber orientation, which gives it an advantage over the conventional use of isotropic steel sheets. Altogether, high strength and stiffness in one direction, low density, high corrosion resistance, minimal disruption to traffic and low maintenance cost make fiber wrapping an ideal retrofit method. However, the fabrication procedure along with the curing conditions and installation process have a big influence on the functionality of the retrofit and these should be monitored carefully. Additionally, these jackets depend on the formation of large strains in the layers during seismic events, therefore FRP jacketing will only be effective for severe earthquake events when structures undergo substantial nonlinear behavior. Lastly, when CFRP wraps are used for the retrofit of columns and piers, two things need to be checked to confirm their suitability:

- CFRP wraps on the members may induce additional shear stresses in the joints so the shear capacity of these regions should be checked for adequacy after retrofitting.
- The stiffness of the CFRP wrap and the concrete substrate should be compatible so that the hinge location does not shift and cause premature shear failure in the unwrapped potions of piers.

20

Chapter 3. BENDING AND SHEAR TEST DESIGN

3.1   INTRODUCTION

In May 2019, the research team performed two tests of a scaled model of an existing pile-column under two loading conditions to simulate failure caused by pure bending and failure caused by combined bending and shear demands, respectively. The pile-columns used for these tests were the same scaled model pile-column described in Tardieu 2018. The factors affecting the design of the test specimen, the experimental setup, and specimen construction are discussed in this chapter.

3.1.1   *Design Prototype*

Figure 3-1 shows a sketch of the prototype selected by the research team. After discussions with WSDOT and review of the construction drawings, it was decided to test a pre-tensioned hollow pile-column to accommodate the state's retrofit schedule. Tardieu (2018) tested an as-built column-to-cap-beam connection, which will be discussed in more detail in Chapter 6; however, the same hollow pile-column specimens used by Tardieu were used in this research.
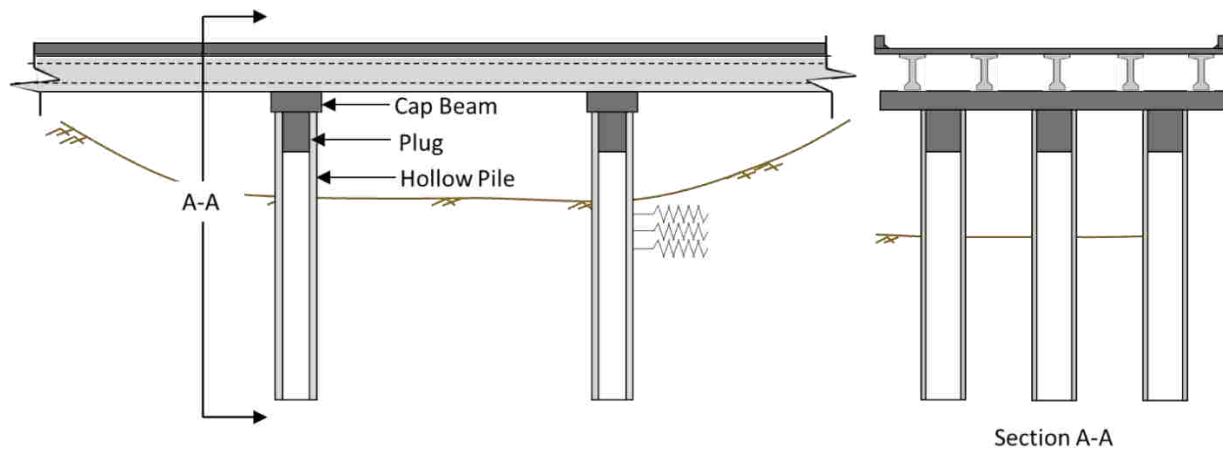
Figure 3-1. Sketch of field prototype conditions

3.2   TESTING CONSIDERATIONS

When designing a model specimen to study the behavior of larger structures, it is important that it is both an accurate representation of the overall structure and has the greatest research breadth

while using the fewest testing resources (A. Jellin, 2008). The pile-column specimens were manufactured by Concrete Technology Corporation in Tacoma, Washington who were also the manufacturers of the post-tensioned piles on the Ravenna Bridge and the pre-tensioned piles on the Slide Bridge and the Green River Bridge. They were 11 feet long with a 36-inch outer diameter and a 28.875-inch inner diameter, leaving a wall thickness of 3.4375 inches. The outer diameter was constrained by the sizes of sonotube formwork that was commercially available; this diameter gives a 3/4 scale ratio to the 48-inch post-tensioned piles in the Ravenna Bridge and a 2/3 scale ratio to the 54-inch pre-tensioned piles used elsewhere (Tardieu 2018). The specimen had a specified concrete strength of 9000 psi, and the prestressing was achieved using thirty-two ⅜-inch diameter, 270 ksi, low-relaxation strands pre-tensioned to 16 kips each. The spiral reinforcement was #7 gage cold-drawn wire, spaced at a 3.5-inch center to center pitch everywhere except at the very top (in the field orientation) where there were 5 turns of wire at a 1.25-inch pitch. The elevation and cross-section views are shown in Figure 3-2 and Figure 3-3.
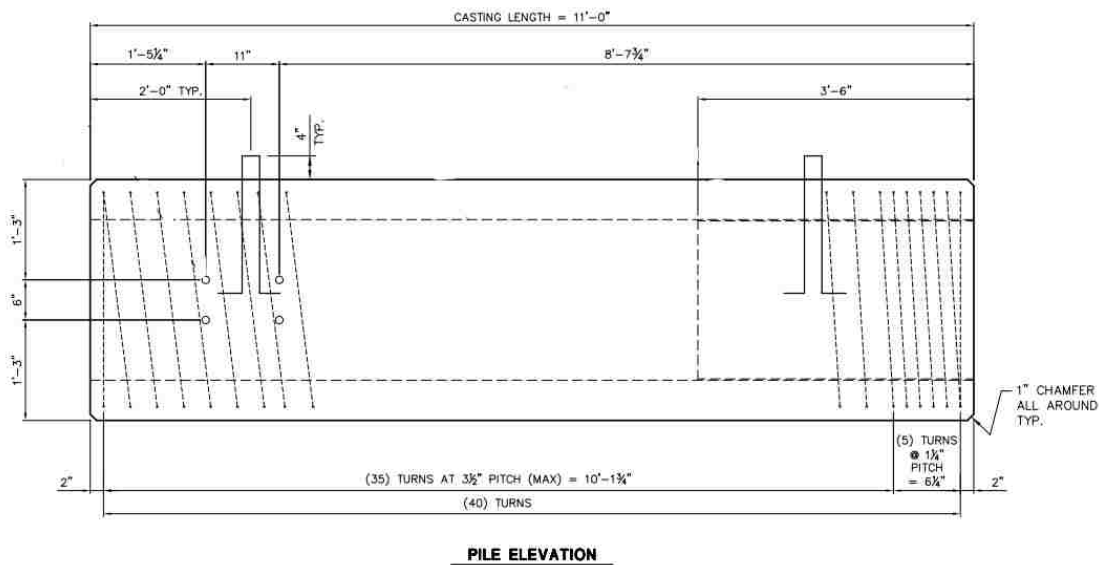
Figure 3-2. Elevation of pile-column, showing dimensions (courtesy of Concrete Technology Corporation)
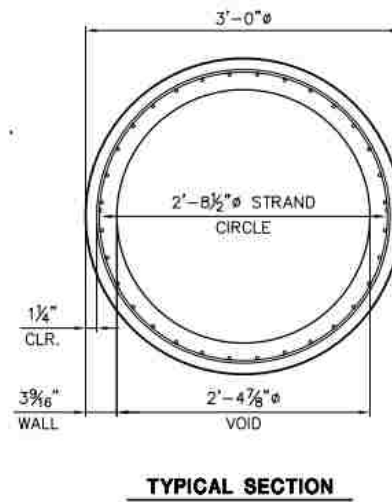
Figure 3-3. Cross-section view of test pile-column, showing dimensions (courtesy of Concrete Technology Corporation)

The two tests to be described in this chapter were chosen by the research team to further understand the behavior, and establish a basis for strength, of the hollow piles in pure bending, as well as combined bending and shear. In order to achieve the desired failure modes while minimizing construction time and resources required, the pile-columns were tested as beams (see Figure 3-4 and Figure 3-5). The support and load cradles were custom made, 4-inch thick steel cradles (see Figure 3-6).
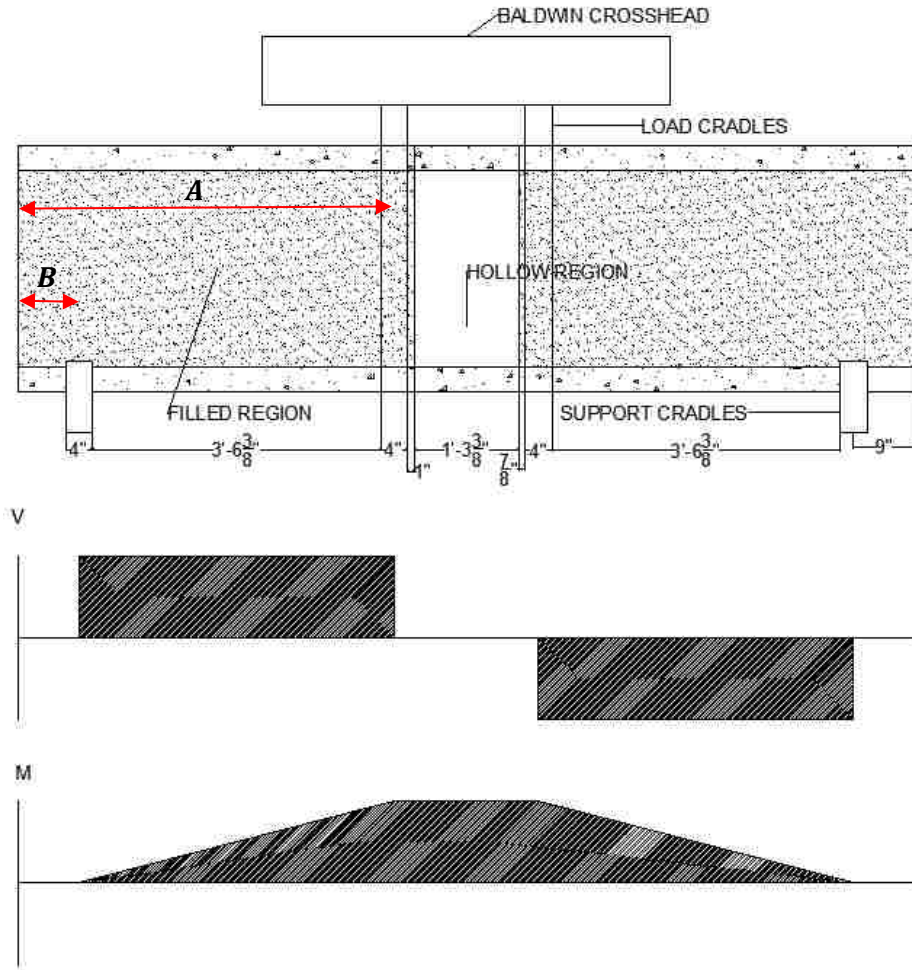
Figure 3-4. Four-point bending (pure bending) test, corresponding shear and moment diagrams

The shear demand and moment demand in the region of failure for this test were calculated as follows:

$$V_{hollow} = 0 \tag{1}$$

$$M_{hollow} = P * (A - B) \tag{2}$$

P = load applied by one load cradle (i.e. half of the total Baldwin load)
A = distance between end of specimen and center of nearest load cradle
B = distance between end of specimen and center of nearest support cradle
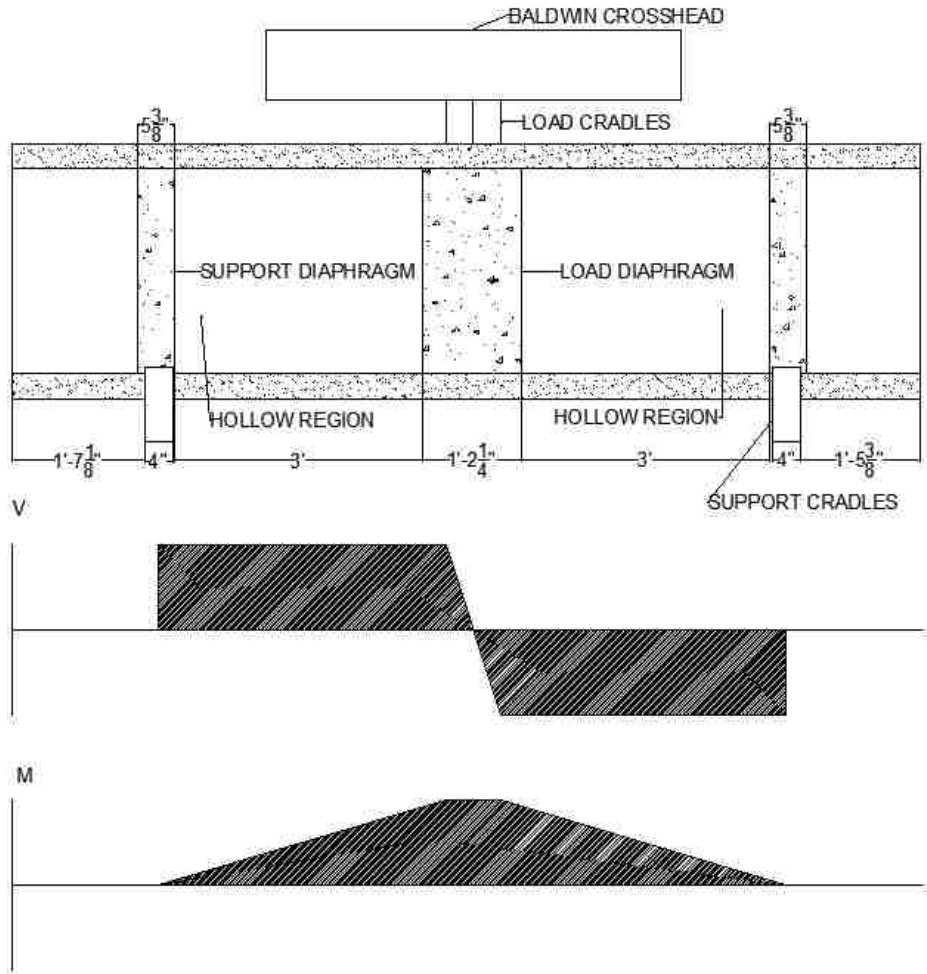
Figure 3-5. Three-point bending (combined shear and bending) test, corresponding shear and moment diagrams

The shear demand and moment demand in the region of failure for this test were calculated as follows:

$$V_{hollow} = \text{P} \qquad (3)$$

$$\text{M}_{peak} = \text{P} * \frac{\text{L}}{4} \qquad (4)$$

P = load applied by one load cradle (i.e. half of the total Baldwin load)
L = distance between support cradles

25
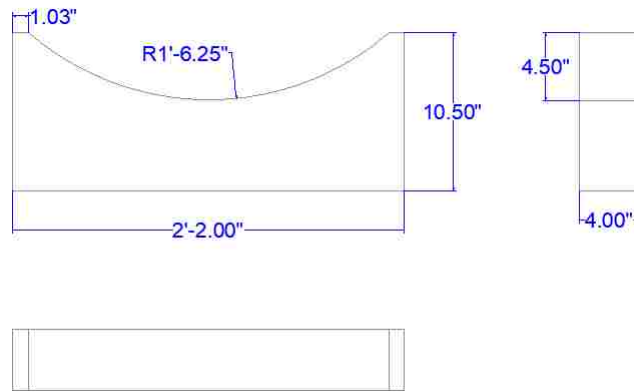
Figure 3-6. Load and support cradles

Figure 3-4 and Figure 3-5 show the two loading patterns that were chosen by the research team, and their resulting shear and moment diagrams. The pure bending ("Four-point bending") test had two symmetrically applied point loads about the center of the specimen and two symmetrically placed supports. The maximum moment from this load pattern occurs in between the two load points, where there is also no shear, resulting in a pure bending failure. To ensure that no local failures occurred in the hollow pile-column (e.g. concrete crushing or excessive deformations under the points of load application), the exterior portions of the pile-column were filled (see Figure 3-4). This resulted in a completely solid test specimen, except for the region in between the load cradles; this ensured that this region of the test specimen had both the highest demand and lowest capacity.

The combined shear and bending ("Three-point bending") test had a single point load applied at the center of the specimen and two symmetrically placed supports. This load pattern results in constant maximum shear across the entire specimen, and variable bending, with a maximum moment demand at the middle of the specimen. To ensure that the failure mode was governed by shear behavior, the specimen was constructed to have concrete "diaphragms" (i.e. solid concrete discs) at both supports as well as underneath the point of load application (i.e. where the max moment occurs), leaving the hollow regions with maximum shear demand (see Figure 3-5). The diaphragms serve a purpose similar to that of a bearing stiffener in a steel girder.

3.3   SPECIMEN DESIGN

The overall dimensions of the test specimens used in this study are shown in Figure 3-7. The dimensions show that the specimens are not perfectly symmetric. (The diaphragms had to be poured with the columns vertical). This is a result of imperfections during specimen construction; the research team did not believe the lack of perfect symmetry would impact the test results.

27
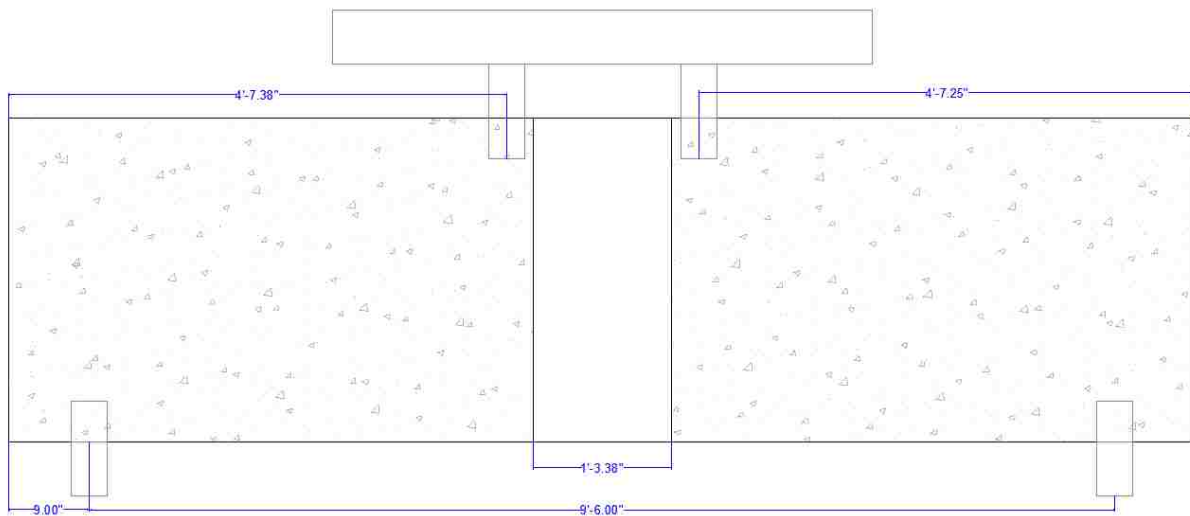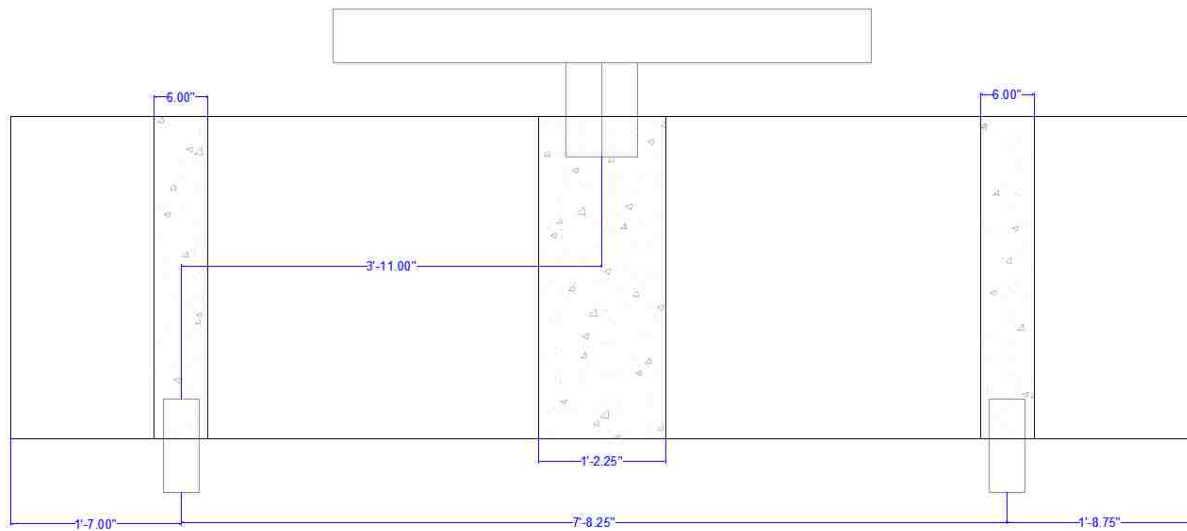
Figure 3-7. Dimensions of testing equipment for Four-point bending (top) and Three-point bending (bottom) tests

3.3.1 *Materials*

The pile-columns on the existing bridges were typically specified to be constructed using concrete with a 28-day strength of 6000 psi which suggests that the columns would have an approximate present-day strength of 8000 psi using a 1.3 factor for increase in strength over time (Caltrans Seismic Design Criteria). Self-consolidating concrete with a 28-day nominal strength of 9,000 psi was used for the pile-columns in order to ensure good consolidation in the narrow walls. It should be noted that the original piles were built using a moving steel mandrel to form the inner void. This allowed the use of internal vibrators and conventional concrete. The larger scale, implying thicker walls, also helped to achieve full consolidation.

The fill concrete was cast-in-place in the Structural Research Laboratory at the University of Washington in three casts: one cast provided by a commercial ready mix company, and two separate casts using concrete made in the Construction Materials Laboratory at the University of Washington. The fill concrete during the first pour provided all the concrete for the Four-point bending specimen as well as the thicker (middle) diaphragm on the Three-point bending specimen and needed to be pumped through a truck. The concrete had a specified nominal slump of 6-inches; the strength of the concrete was not of concern as the desired regions of

28

failure had much lower capacities in both shear and bending than any type of filled section. The strength was approximately 5000 psi. The fill concrete for the remaining diaphragms of the Three-point bending specimen was cast in the Construction Materials Laboratory and used the following mix:

- 58 lb. cement
- 117.5 lb. sand
- 152 lb. recycled coarse aggregate
- 31.5 lb. water (w/c ratio of 0.54)
- The strength was not recorded

3.4   SPECIMEN CONSTRUCTION

The precast, prestressed hollow core pile-columns were constructed at Concrete Technology Corporation's facility in Tacoma, Washington. At the plant, the pile-column was cast using a 36-inch diameter steel tube for the outer form and a 28.875-inch outside diameter Sonovoid® Round concrete void form (sonotube) capped with plywood to create the hollow core (see Figure 3-8 and Figure 3-9). The sonotube was used because a steel inner form was unavailable. The specimens were line cast so that three were fabricated at the same time (see Figure 3-10).

Figure 3-8. Pile-column reinforcement being prepared for casting at Concrete Technology Corporation

Figure 3-9. Sonovoid® round concrete void forms

30

Figure 3-10. Pile-column formwork ready to be line-cast at Concrete Technology Corporation

In order to prevent the sonotube from floating up during the concrete casting, a hold-sown system was necessary. This was accomplished with curved steel plates attached by lag screws at discrete locations along the top length of the form (see Figure 3-11). The plates were 8-inches wide oriented along the length of the pile-column by 14-inches circumferentially and were placed at 15-inch centers. Some additional spiral was also used around the sonotube at discrete locations for construction purposes. These additions are important to note but are not believed to affect the failure conditions observed later.
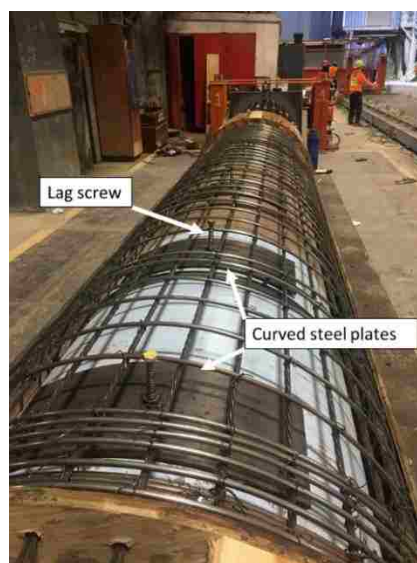
Figure 3-11. Hold-down plates used for sonotube during casting

The formwork was constructed using sheets of 0.75-inch thick CDX plywood sheathing and SPF 2x4 Premium #2 & Better Grad Kiln dried studs. The formwork for each specimen was constructed in a way to expedite the construction process as much as possible and maximize the amount of concrete that could be ordered in one cast.

3.4.1 *Four-Point Bending Specimen*

The load pattern for this test results in a maximum moment demand and zero shear demand in between the points of load application (see Figure 3-4). The formwork was constructed in house to accommodate a single pour to leave a single hollow region in between the load points and a solid section everywhere else (see Figure 3-4). The formwork was installed into the test specimens while they were horizontal on the lab floor, but the concrete was poured after the specimens had been flipped 90 degrees and stood vertical (see Figure 3-12).

Figure 3-12. Specimen orientation prior to casting fill concrete

To construct the formwork the plywood was first cut into four discs that were slightly smaller in diameter than the inner diameter of the test specimens. One of the discs remained solid while the remaining three were cut into annular shapes, with an inner diameter of approximately 18-inches to accommodate the hose of the concrete pumper truck (see Figure 3-13). Two of the rings were screwed together and were then connected to the solid disc via. 56-inch long 2x4 studs (see Figure 3-14).

Figure 3-13. Concrete pump truck used for fill concrete

Figure 3-14. Solid disc connected to two plywood rings by 2x4 studs inside Four-point bending specimen

33

Next, a 15-inch thick foam ring was cut and was attached to the two-plywood ring-stud-solid plywood disc assembly with super glue. The last plywood ring was glued on top of this foam ring (see Figure 3-15); all seals around the plywood discs were created with white plumbers' caulking and foam.

Figure 3-15. Foam spacer followed by last plywood ring

The intent of the foam ring was to provide a hollow region that a pump could pass a hose through to fill the bottom half of the column with concrete, followed by a plug, then the top half of the specimen would also be filled with concrete. The construction sequence is illustrated in Figure 3-16.
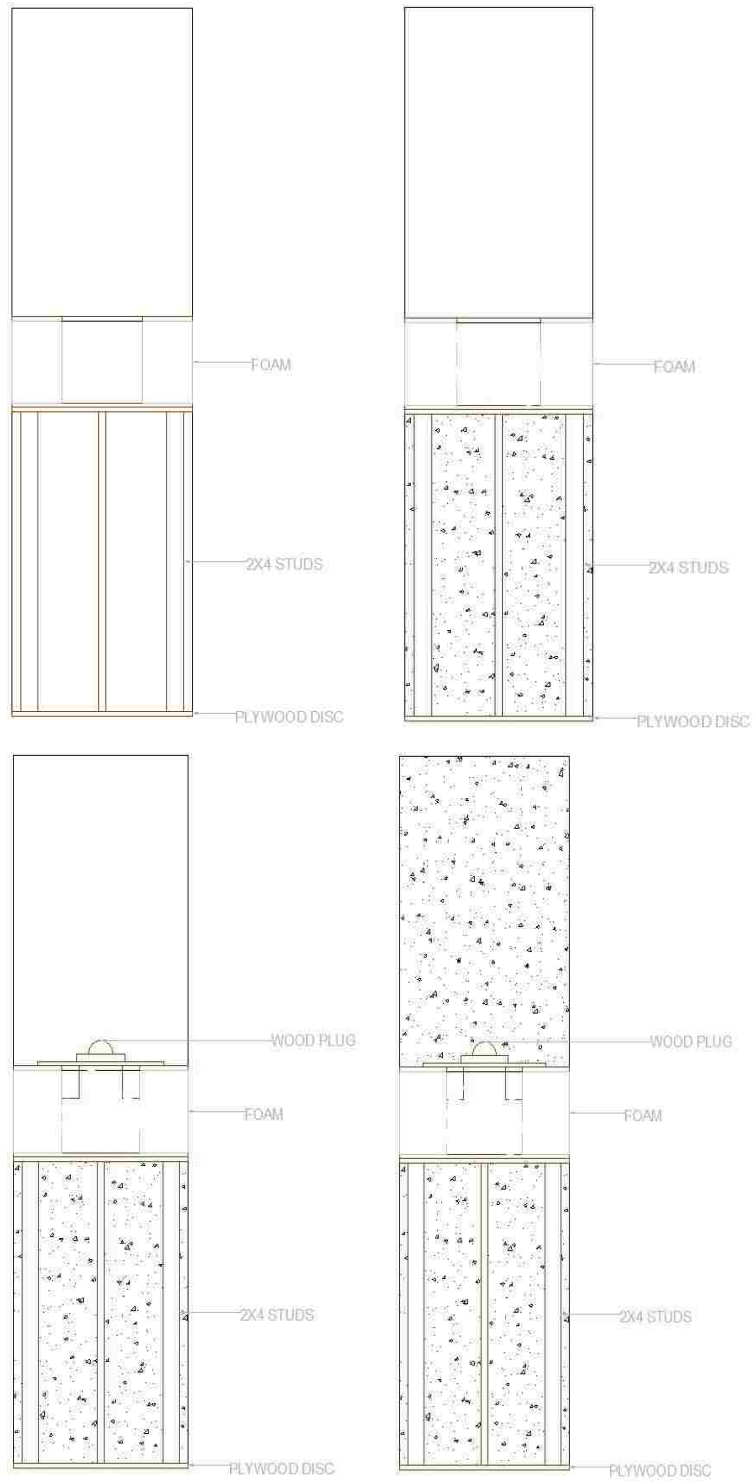
Figure 3-16. **Top left**: Vertical specimen with formwork; **Top right**: Bottom half of Four-point bending specimen fill concrete; **Bottom left**: Plug over hose hole; **Bottom right**: Top half of fill concrete
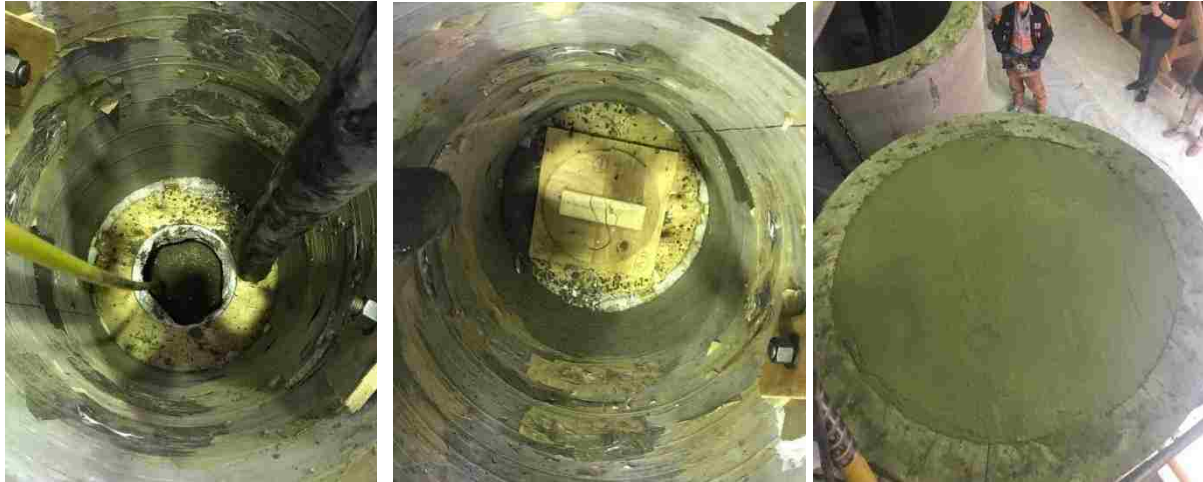
Figure 3-17. **Left**: Bottom half of fill concrete; **Middle**: Wood plug inserted; **Right**: Top half of fill concrete

3.4.2 *Three-Point Bending Specimen*

The load pattern for this test resulted in a constant shear demand and variable moment (see Figure 3-5). The formwork was constructed so that a 14.25-inch thick concrete diaphragm could be cast in the middle of the test specimen during the same cast as the Four-point bending specimen. This was accomplished by creating two "spacers" and one "support table" (see Figure 3-18).
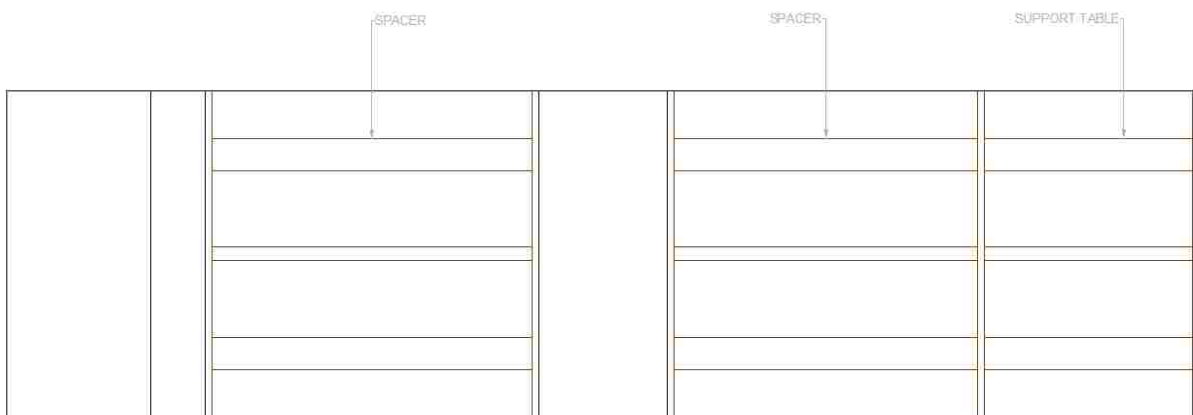
Figure 3-18. Formwork used for Three-point bending specimen

The spacers consisted of two solid plywood discs like the disc used for the other specimen connected to each other with three 33.75-inch 2x4 studs. The support table consisted of one solid plywood disc and three 23-inch 2x4 studs. The "support table" was inserted into the specimen first, followed by one spacer that was placed so it was in contact with the support table. The specimen was then flipped 90 degrees (i.e. so that it was vertical) and the thick diaphragm was cast onto the spacer with the concrete pump (see Figure 3-19). The inner column wall was roughened at all diaphragm locations before casting the diaphragms.

Figure 3-19. Middle diaphragm cast into Three-point bending specimen

After one week of curing the second spacer was placed on top of the thick diaphragm, and the second diaphragm was poured on top of this spacer. After the second diaphragm cured for one week the specimen was rotated 180 degrees so that the support table was facing up and it could be removed, exposing the first spacer; the final diaphragm was poured on top of the first spacer. The construction sequence is illustrated in Figure 3-20.
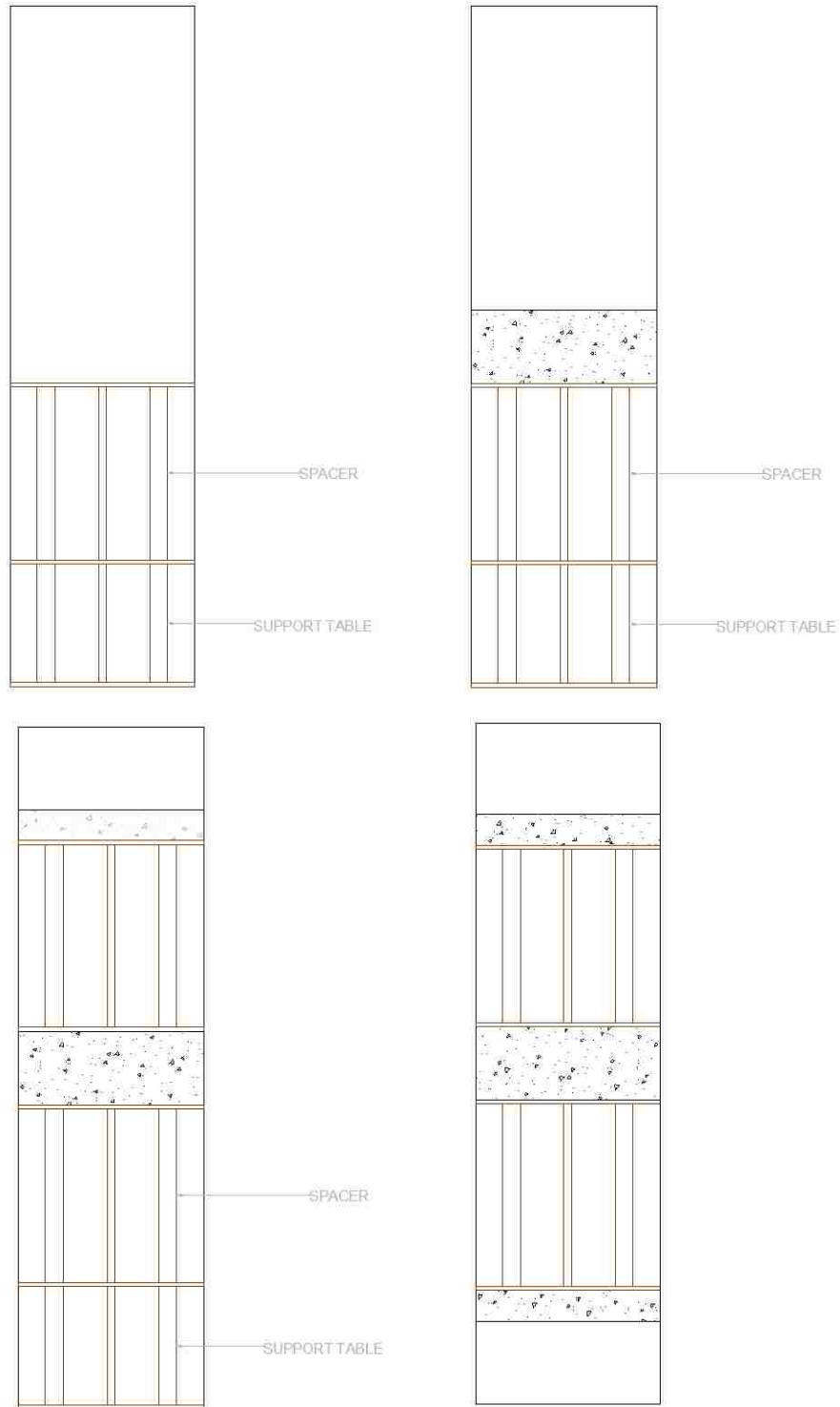
Figure 3-20. **Top left**: Vertical specimen with formwork; **Top right**: Middle diaphragm poured;
Bottom left: Second spacer inserted, second diaphragm poured; **Bottom right**: Support table
removed, third diaphragm poured

3.5   TEST SETUP

A monotonic test was performed on both test specimens described in this chapter using the Baldwin Universal Testing Machine to apply the loads. To set up the experiment, after the full specimens were constructed as described in the previous section, the specimens were individually moved and installed under the Baldwin machine on the lab floor.

3.5.1   *Test Equipment*

The support cradles were held down to the lab floor with 1-inch rods and lock nuts placed in the rails of the floor; the rods were tightened down through slotted angles that were welded to the support cradles (see Figure 3-21). This ensured that the specimens were rigidly attached to the lab floor and no sliding or uplift of the support cradles occurred during testing.

Figure 3-21. Support cradle arrangement

Cotton duck padding strips were placed in between the support and load cradles and the test specimens. This was done to evenly distribute the load out if the cradles were not perfectly aligned with the outer wall of the specimens (see Figure 3-21), and to allow for end rotation of the specimen as it bent.   The spacing of the support cradles was limited by the slots in the lab floor that were used for the angle hold downs; the support cradles were center-to-center spaced 9-feet and 6-inches apart for the Four-point bending specimen and 7-feet and 8.25-inches apart for the Three-point bending specimen. The load cradles were spaced center-to-center 1-foot and 6-inches apart on top of the Four-point bending specimen and they were touching on the Three-point bending specimen. The load was applied directly with the head of the Baldwin machine (see Figure 3-4).

3.5.2   *Test Protocol/Procedure*

The predicted moment capacity of the hollow section was determined using a moment-curvature analysis program developed by Dr. John Stanton at the University of Washington, this is discussed further in Section 4.4. The predicted transverse load capacity of the hollow section was calculated using a custom-written program used to determine the principal stresses around the cross section of the specimen, accounting for the stresses induced by shear, bending, and prestressing; this is discussed further in Section 5.4. The predicted loads to cause failure were 512 and 454 kips, respectively.

3.5.2.1   Four-point bending test

The Baldwin machine applied the load directly to the load cradles, as described in the previous section. To maximize the results that were obtained from the test, four loading cycles were used. First, a load-controlled cycle was performed up to the approximate "decompression load," that is, when the concrete first overcame the compressive stress induced by the prestressing. The goal of this cycle was to check all instruments while also checking the settlement of the cotton duck padding at all of the cradles. Second, a load-controlled cycle was performed up to 120% of the approximate cracking load (determined from a moment-curvature analysis), the load was then decreased to zero. The goal of this cycle was to detect cracking and any losses in system stiffness due to cracking. The second cycle was repeated in an attempt to detect decompression (i.e. where the load-deflection curve starts to become nonlinear because the cracks start to re-

40

open) and thereby to determine how much prestressing was left in the strands. Lastly, a displacement-controlled cycle was performed until incipient failure; the test protocol is summarized below in Table 3-1. Cracks on the test specimen were inspected and marked following each cycle; each complete cycle took approximately 15 minutes.

Table 3-1. Four-point bending test protocol

Cycle	Purpose	Total Load (kips)	M_{cycle} (ft-kips)	$\dfrac{M_{cycle}}{M_{n,predicted}}$
1	Instrument check, CDP settlement	125	241.54	0.26
2	Decompression	300	579.69	0.63
3	Cracks opening	300	579.69	0.63
4	Failure	515 (est.)	995.14	1.00

3.5.2.2 Three-point bending test

Three loading cycles were used for the three-point bending test. First, a load-controlled cycle was performed up to 200 kips to do an instrumentation check as this load was well below the predicted cracking load. Second, a load-controlled cycle was performed up to 325 kips and back down to zero to check cracking. Third, a displacement-controlled cycle was performed until incipient failure, which was predicted to be approximately 500 kips. Cracks on the test specimen were inspected and marked following each cycle; each complete cycle took approximately 10 minutes.

Table 3-2. Three-point bending test protocol

Cycle	Purpose	Total Load (kips)	V_{cycle} (kips)	$\dfrac{V_{cycle}}{V_{n,predicted}}$
1	Instrument check, CDP settlement	200	100.00	0.42
2	Cracking	325	162.50	0.68
3	Failure	480	240.00	1.00

41

3.6   INSTRUMENTATION

Instrumentation for the tests consisted of strain gages (10mm and 90mm, only on the four-point bending test), linear potentiometers, inclinometers, and an Optotrak motion capture system (See Figure 3-22 - Figure 3-23).   All instruments were recorded using computer-controlled data acquisition systems and loads were measured using the internal load cells of the Baldwin machine. The instruments are summarized in Table 3-3.

Table 3-3. Shear and moment capacities, Baldwin loads required to reach capacities

Instrument	Location	Label
Duncan Pot	North Support Cradle	NSC
Duncan Pot	South Support Cradle	SSC
Duncan Pot	North side, bottom of specimen	NBS
Duncan Pot	Center, bottom of specimen	CBS
Duncan Pot	South side, bottom of specimen	SBS
Duncan Pot	South side, midline of specimen	SMS
Duncan Pot	Center, midline of specimen	CMS
Duncan Pot	North side, midline of specimen	NMS
Inclinometer	South side, midline of specimen	SINC
Inclinometer	North side, midline of specimen	NINC
Duncan Pot	South cradle, near CDP	CDP
Duncan Pot	North strand, slip detection	NStr
Duncan Pot	South strand, slip detection	SStr
Strain Gage	Interior wall, top center	SGI3
Strain Gage	Interior wall, top right	SGI4
Strain Gage	Interior wall, far right	SGI5
Strain gage	Exterior wall, far left	SGE1
Strain gage	Exterior wall, top left	SGE2
Strain gage	Exterior wall, top center	SGE3
Strain gage	Exterior wall, top right	SGE4
Strain gage	Exterior wall, far right	SGE5
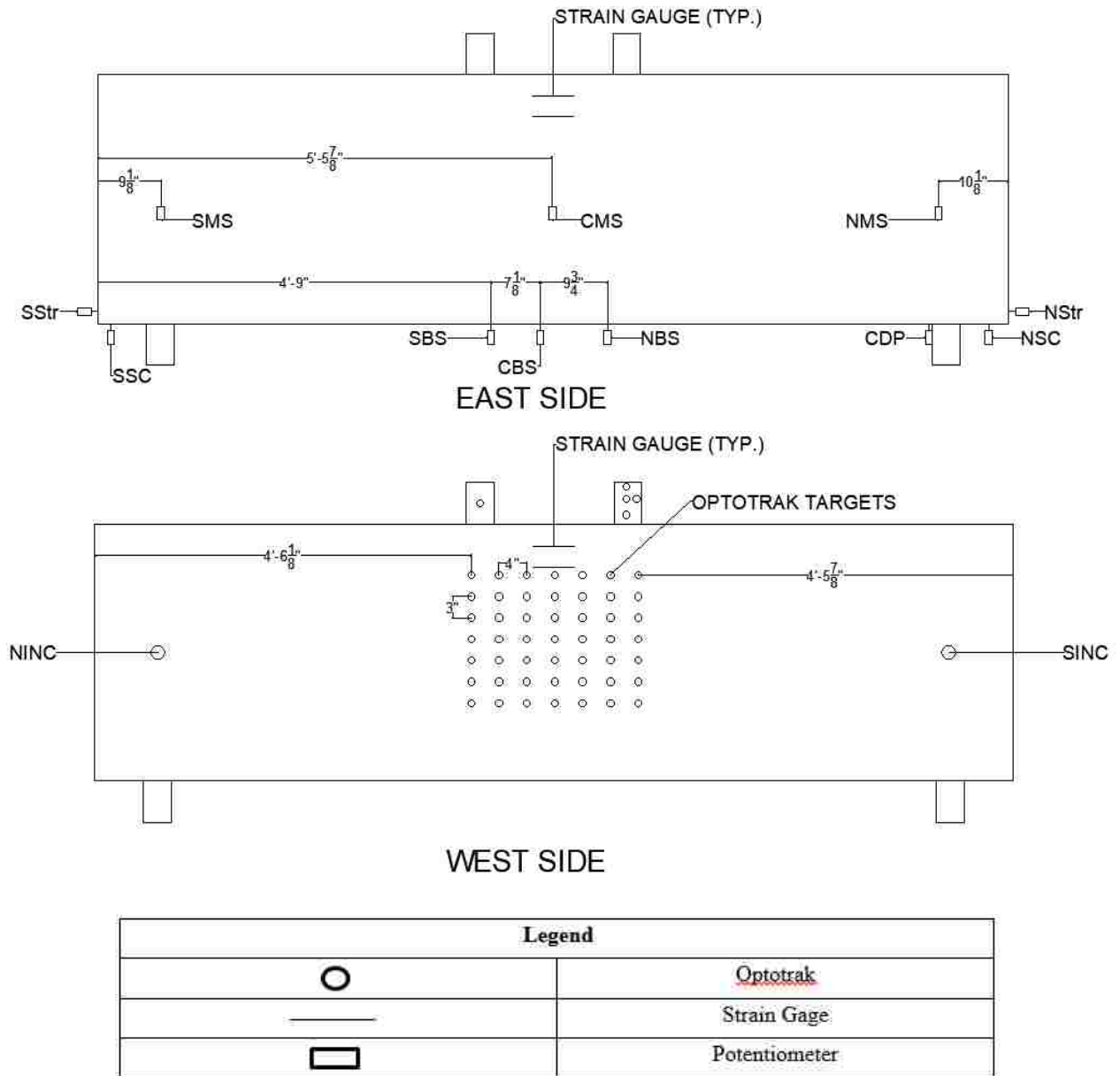
Figure 3-22. Four-point bending test instrumentation
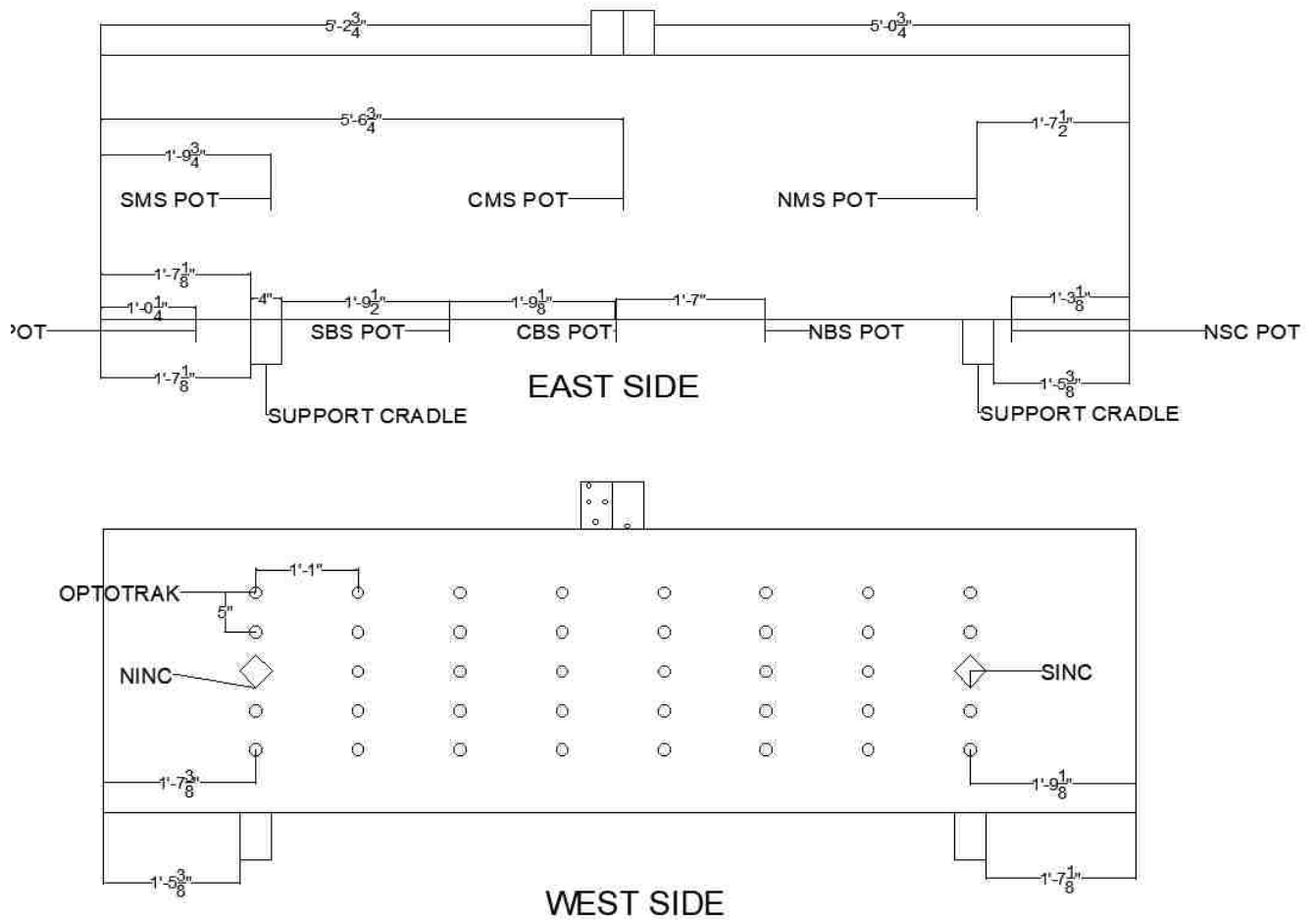
Figure 3-23. Three-point bending test instrumentation

Strain gages were used to measure the strains of the outer and inner faces of the walls in the hollow section. The 90mm gages on the outer surface were placed symmetrically about the top of the pile and spaced at 6.75-inches (see Figure 3-24). The 10 mm gages on the inner surface were first stuck to pieces of wood to increase their effective gage length and glued to the inner pile wall (see Figure 3-25), they were spaced at 5.5-inches. Two different gage sizes were used to accommodate the casting times. The 90 mm gages had not yet arrived in the lab when the formwork and foam ring needed to be installed into the Four-point bending specimen, so 10 mm gages had to suffice.

Figure 3-24. Exterior 90 mm strain gages on outer wall of Four-point bending test specimen

Figure 3-25. Interior 10 mm strain gage on Four-point bending test specimen

Displacements were measured using linear Duncan potentiometers and were placed along the bottom of both specimens as well as along the east side of the specimens. The potentiometers along the bottom of the specimens were hot glued to aluminum angles, which were hot glued to the lab floor (see Figure 3-26). The potentiometers along the side of the specimens were hot glued to threaded rods that were attached to magnets that were magnetized to the metal lab floor

(Figure 3-27). The displacements measured using the Duncan potentiometers allow for the development of a displacement profile of the specimens under the different loading conditions and determine the rotations along the specimen. The same Duncan potentiometer arrangement was used on both test specimens.

Figure 3-26. Bottom Duncan potentiometers

Figure 3-27. East side Duncan potentiometers attached to threaded rods that are magnetized to the lab floor

The rotations were also measured directly using inclinometers attached to the sides of the specimens over the support cradles (see Figure 3-28 - Figure 3-29). Lastly, an Optotrak Certus motion capture system was used to measure the deformations in the hollow region on the west side of the specimen (see Figure 3-28 - Figure 3-29). The Optotrak system consists of a 3-dimensional optical sensor (camera) and a series of LED markers arranged in a pre-determined grid system. The system records the 3-dimensional position of each marker with respect to the camera's own coordinate system. From these position measurements, deformations of the column wall can be calculated.
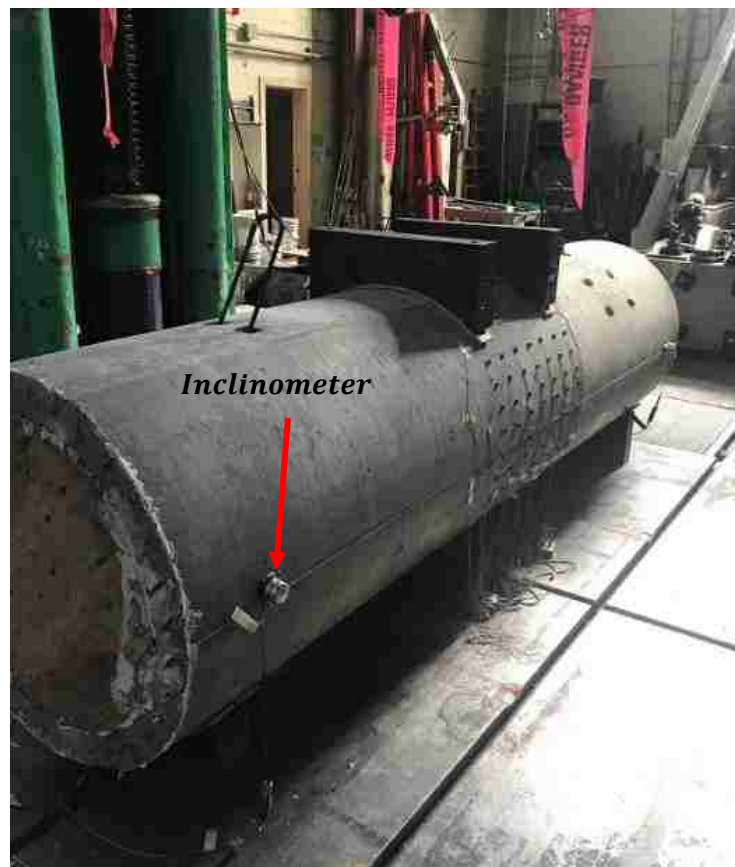
Figure 3-28. Four-point bending test inclinometers Optotrak targets

Figure 3-29. Three-point bending test optotrak and instrumentation

Chapter 4. BENDING TEST RESULTS AND ANALYSIS

4.1 INTRODUCTION

In this chapter the results of the pure bending test are presented and analyzed. In that test, the specimen experienced maximum bending moments in a region with zero shear demand. The results are important because they allow verification of the computational model used to predict pure bending capacity, as well as quantification of the vulnerability of the below-grade pile. The observed test behavior is first presented in Section 4.2, followed by the measured response in Section 4.3. Then, in Section 4.4, the prediction approach is outlined, and the predictions for the test specimen's behavior are compared with the measured data.

4.2 OBSERVED RESPONSE

In this section, the observed behavior is discussed. The test protocol described in Table 3-1 was implemented, starting with a cycle to check instruments and check the settlement of the CDP. On the next cycle, a moment demand of approximately 7000 in-kips was achieved, with the intention of cracking the specimen and detecting decompression. Vertical and diagonal cracks grew progressively on the sides of the specimen (see Figure 4-1), and grew at an incline slightly smaller than 45°. The smaller crack inclination can be explained by the presence of extra compression from the longitudinal prestressing, making it difficult for the cracks to grow vertically. The red cracks appeared first at a mid-span deflection of approximately 0.1 inches, followed by the vertical (blue) cracks as the specimen was loaded further.
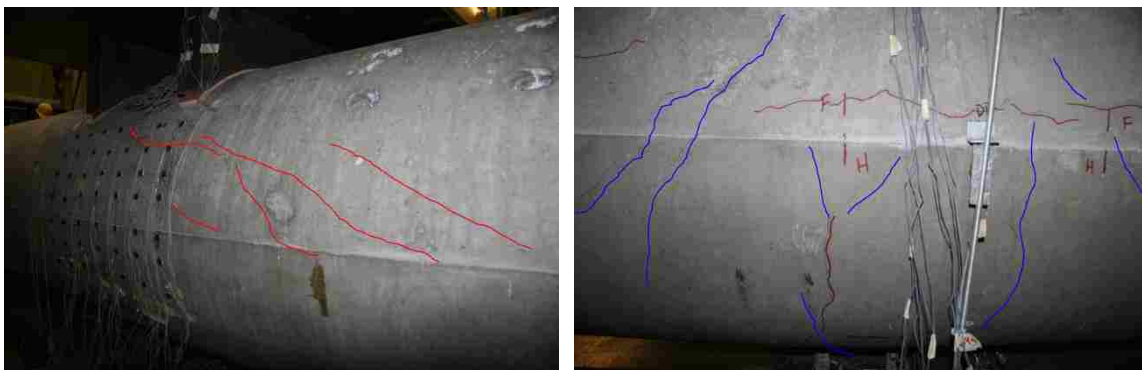
Figure 4-1. Progression of cracks on the west (left) and east (right) faces of specimen

49

Similar behavior was observed on the third cycle, when the specimen was loaded to the same moment demand of the previous cycle (the intention being to give another chance to accurately predict the decompression load, and thus, how much prestressing remained). On the final cycle, a moment demand of 12,761 in-kips was achieved at ultimate failure. During the test there was no visible evidence of premature internal spalling (the primary concern at the start of the research project); however, the internal diaphragms prevented placement of any cameras or sensors inside the specimen to confirm these observations. Ultimate failure occurred due to concrete crushing on the outer face of the wall and subsequent buckling of strands (see Figure 4-2); the specimen position at failure is shown in Figure 4-3.

Figure 4-2. Concrete crushing and buckled strands

50

Figure 4-3. Specimen position at failure

4.3 MEASURED RESPONSE

The measured response is discussed here. On a global level, the force-displacement and moment-rotation behavior are examined; on a local level, the strains at different points along the cross section and the corresponding curvature achieved are examined.

4.3.1 *Force-Displacement relationship*

The maximum achieved force was 550 kips. Figure 4-4 shows the force-displacement curve, as measured by the potentiometers along the bottom of the specimen. The potentiometers are color coded on the sketch of the specimen to match the corresponding force-displacement curve.

51
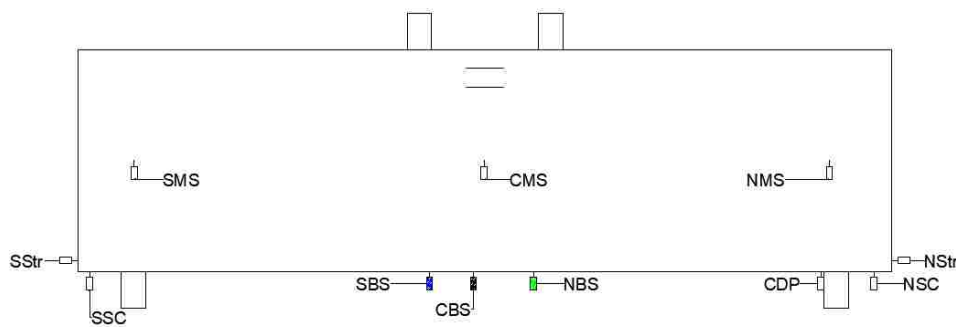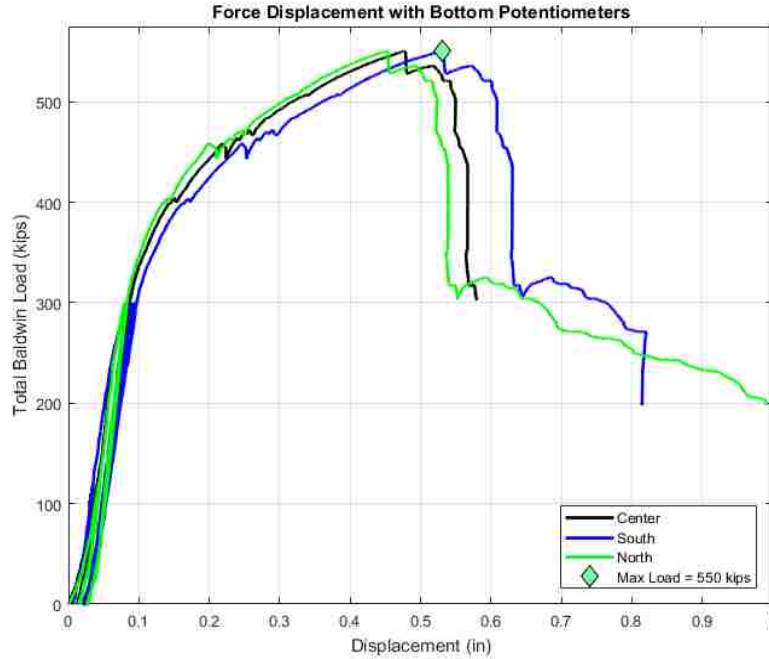
Figure 4-4. Force-displacement curve for all bottom potentiometers

The plot in Figure 4-4 shows that there was agreement amongst the bottom potentiometers, and that the deflection at the south end of the hollow region was slightly higher than the center or north end. This suggests that the specimen was either not filled in a perfectly symmetric fashion and/or the load cradles were not perfectly level relative to one another. In addition, the strength degradation after the ultimate load was reached was rapid.

To determine the associated displacement ductility, a linear-elastic stiffness tangent to the measured data was projected to the maximum force (see Figure 4-5). Where the linear-elastic stiffness intersects the maximum force is denoted as the "elastic displacement." The ductility capacity was taken as the ratio of the measured displacement at peak load to the elastic displacement. In a reinforced concrete specimen, the linear elastic line represents the cracked elastic stiffness, and the majority of the additional displacement arises from inelastic elongation of the bars. By implication, high ductility implies extensive inelastic strain in the bars, and the potential for high energy dissipation. Those two connotation of the word ductility are synonymous.

52

However, in prestressed concrete members such as these pile-columns, the linear elastic line corresponds to the uncracked deflection, and a significant portion of the additional, nonlinear, displacement arises from elastic elongation of the strands. The load-deflection response of the specimen is nonlinear because the strands are gradually debonding on either side of the crack, and the only "material" that is inelastic is the bond. Upon load reversal, the cracks close completely, and very little energy is dissipated. Thus the word ductility, if applied here, does not have its usual meaning. The nonlinear displacements are present, but the significant energy dissipation is not. It would perhaps be better to call the behavior observed here the "elastic ductility ratio."

The linear elastic (uncracked) stiffness line was drawn tangent to the measured data, which resulted in an elastic displacement of 0.15 in. The load at peak displacement was 0.48 in, leading to an elastic ductility ratio of 3.2. The slope of this elastic stiffness is lower than the theoretical value (see Appendix C). If the latter were to be used, the elastic ductility ratio would be higher.
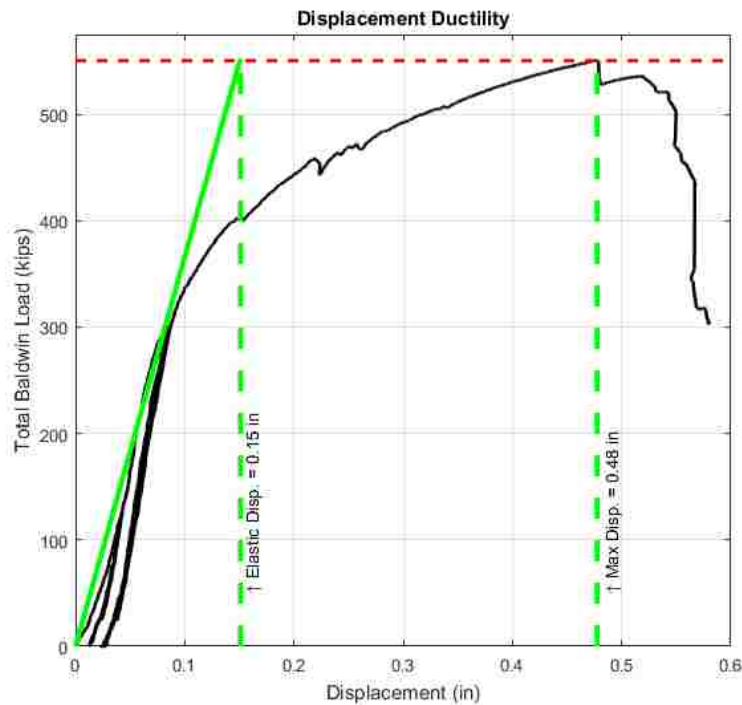
Figure 4-5. Displacement ductility in pure bending

www.manaraa.com

4.3.2   *Moment-Rotation relationship*

The maximum achieved mid-span moment was 12,761 in-kips. Figure 4-6 shows the moment-rotation curve, where moments are taken at mid-span and the rotations are measured by the inclinometers over each support cradle. The absolute rotations are shown, in order to more easily compare the two curves. The inclinometers are color coded on the sketch of the specimen to match the corresponding moment-rotation curve. Rotations, rather than curvatures, were used in these plots to allow for easy comparison between the inclinometers and potentiometers. In addition, translating rotation measurements is easier to apply to the global system.
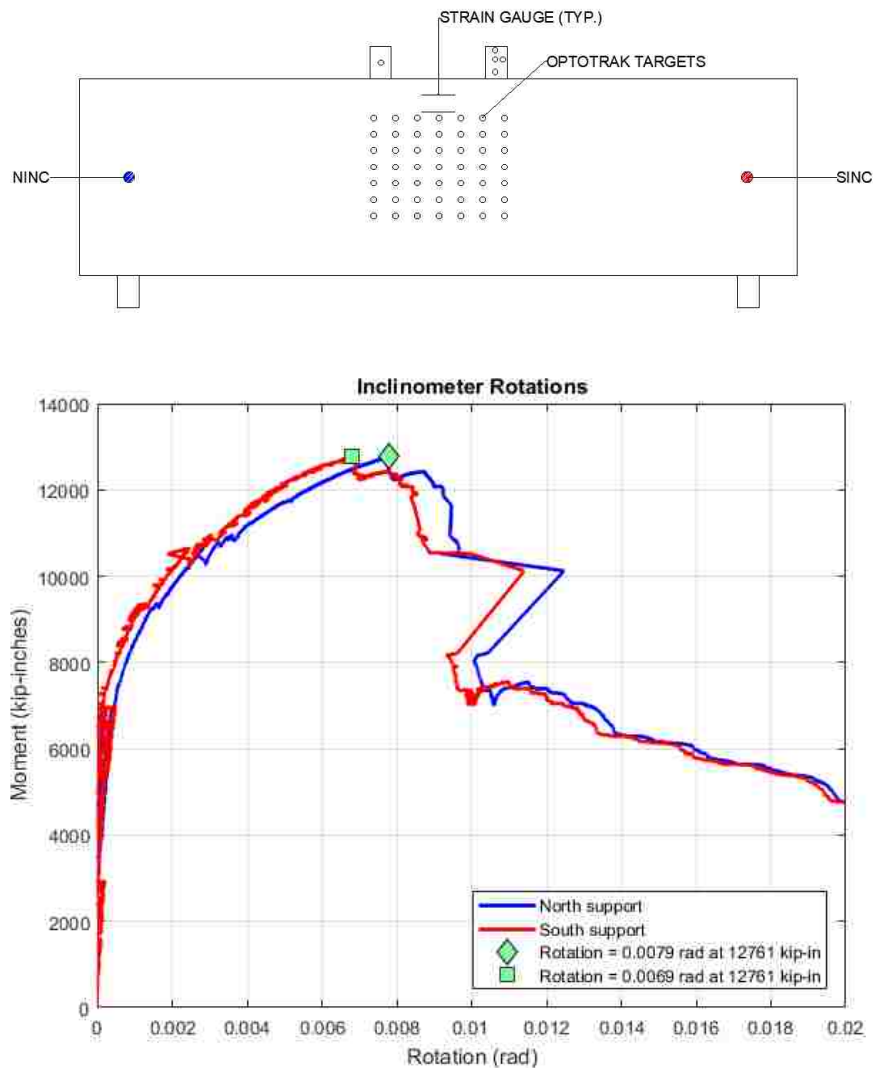
Figure 4-6. Moment-rotation curve for inclinometers that were over support cradles

The average rotation measured by the inclinometers was calculated, and was compared to the rotations measured by the potentiometers on both the bottom and side of the specimen (see Figure 4-7). Again, the sketch of the specimen depicts which instruments correspond to which curve. These rotations were either obtained directly (inclinometers) or by dividing the difference between readings of a pair of potentiometers by the distance between them. There was general agreement amongst the various instruments, and the rotation at the edges of the hollow region (green curve) was higher than the rotation at the center of the specimen (red and blue curves). This is typical of the deflected shape of a specimen undergoing pure bending.
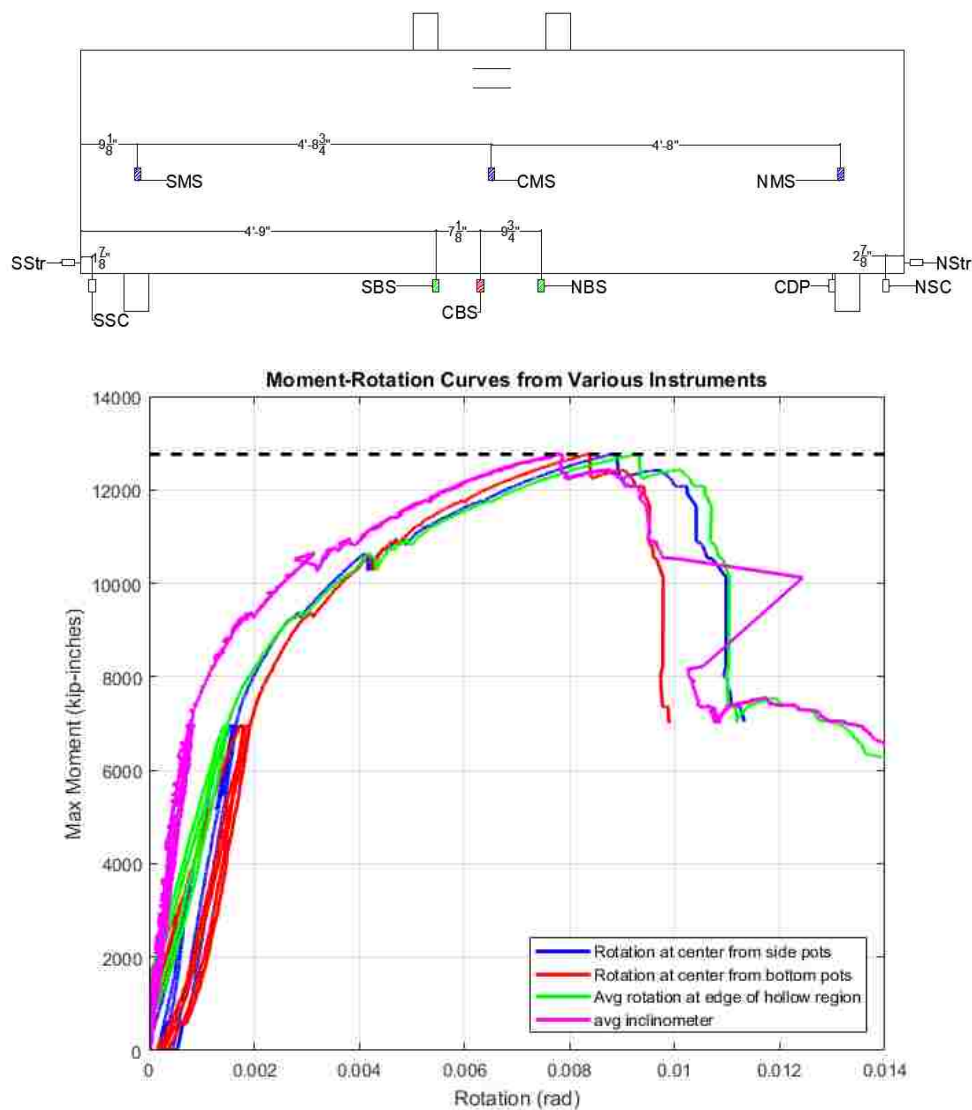
Figure 4-7. Moment-rotation curves all potentiometers and inclinometers

In Figure 4-8 the moment-rotation curves from the center potentiometers are isolated to calculate the associated rotation ductility factor. Again, a linear elastic stiffness tangent to the measured data is projected to the maximum moment achieved. The corresponding "elastic rotation" is 0.0028 radians, while the total achieved rotation was ~0.009 radians, giving an elastic ductility ratio of 3.20 (same as the displacement ductility). The drop in strength after the peak moment was rapid (see Figure 4-7), suggesting that failure was initiated by external spalling, followed almost immediately by internal spalling.
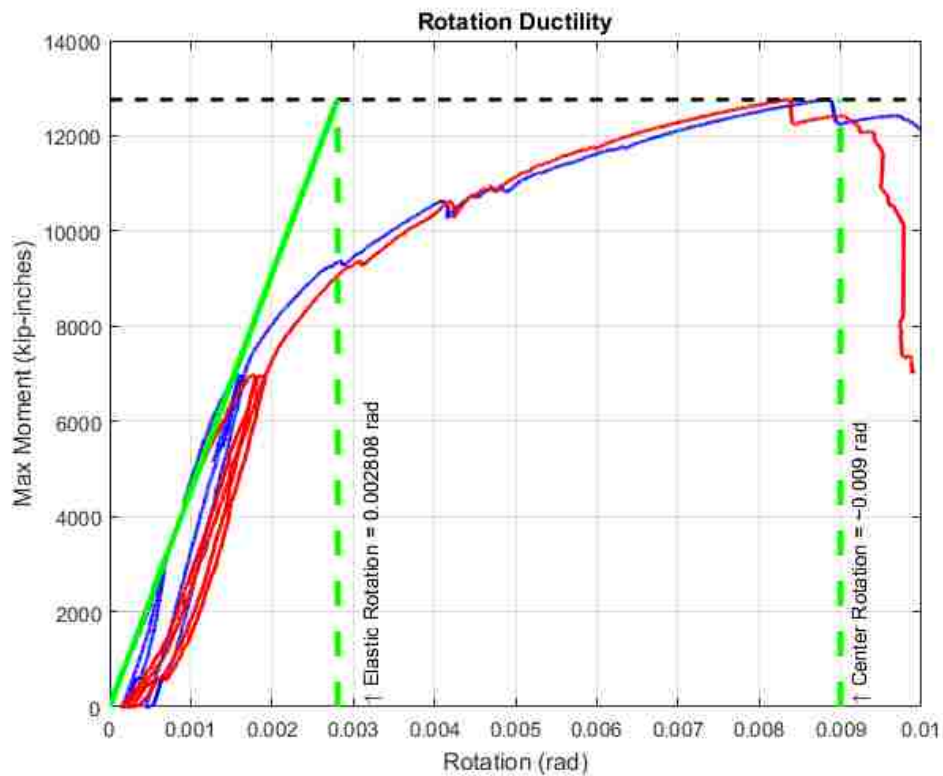
Figure 4-8. Center moment-rotation curves with associated ductility measurements

To further investigate this elastic ductility ratio, more moment-curvature analyses were conducted on the test specimen geometry to determine the curvature at which the most extreme tensile strand reached the yield stress. This corresponding "yield curvature" was compared with the curvature at maximum moment to calculate a ductility factor; the result was a ductility factor (calculated in the same way as before) of 2.8, which was similar to what was observed during the pure bending test. If the material properties and geometry for the field bridges are used, the

56

corresponding ductility may decrease with weaker concrete or higher axial loads. Analysis of each individual bridge lay outside the scope of this project, however this issue needs to be addressed when assessing the field bridges.

4.3.3 *Strain Gages*

Longitudinal strain gages (90mm gage length) were placed circumferentially around the compressive face of the specimen. Strain gage #1 was placed at the approximate neutral axis location and the gages increased in number as one travels clockwise along the circumference (i.e. gage #5 was at the neutral axis on the opposite side of the specimen, gage #3 was at the top of the specimen, and gages #2 and #4 were in between). The measured strains are shown in Figure 4-9. The highest strain recorded was about -0.0019 in/in, which is lower in absolute magnitude than the -0.003 in/in conventionally accepted at failure.
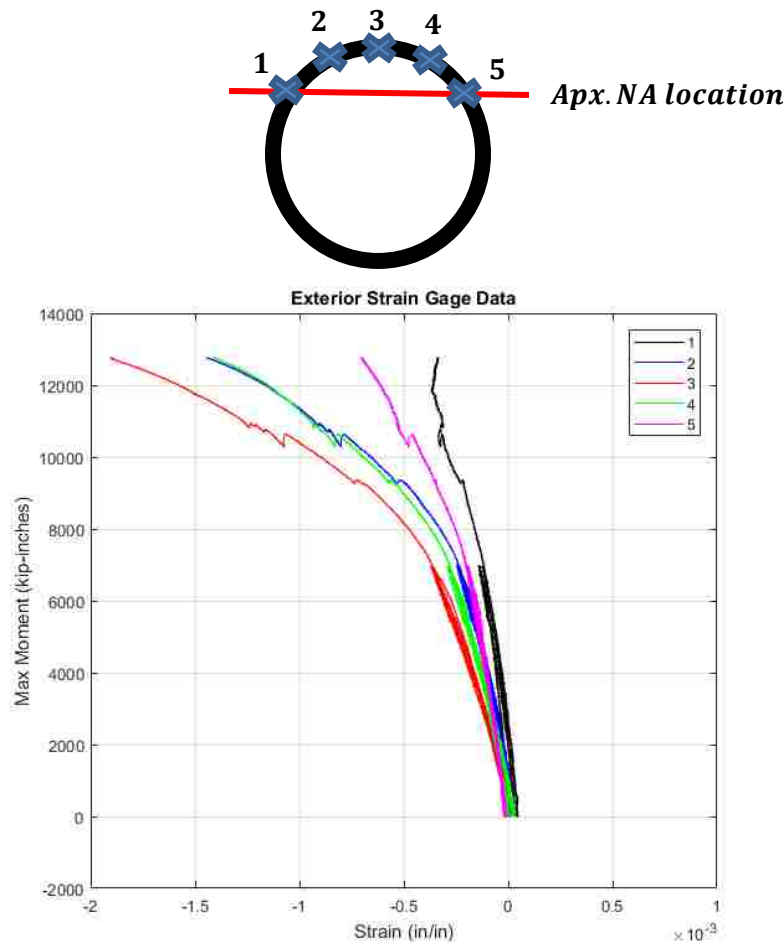
Figure 4-9. Raw data from exterior strain gages (gage labels shown above)

57

4.4 ANALYSIS

4.4.1 *Moment Capacity*

To determine the expected loads, a moment-curvature analysis was conducted before testing using a custom-written program that permits prestressing. For constitutive laws, it uses the Popovicz curve (1973) for concrete, the Raynor (2002) law for reinforcement steel and the Menegotto-Pinto curve (1973) for strand. The concrete law did not include any effects of confinement and the moments were calculated without the application of an axial load. The assumed conditions were:

- *Hollow pile-column only*: The geometry was that of the hollow pile-column alone, the concrete strength was that of the pile-column, and the reinforcement consisted of the strand, assumed to be fully bonded.

The predicted moment capacity of the test specimen within the central region and the corresponding test loads are summarized in Table 4-1; the moment-curvature plot is shown in Figure 4-10. The predictions were checked using the program Response2000 (Bentz, 2000a), which is based on Modified Compression Field Theory (Vecchio and Collins, 1986). Response2000, developed at the University of Toronto, is a sectional analysis program that can capture full member response. It provides engineers with the ability to assess the response of reinforced concrete and prestressed concrete elements subject to shear, bending, and axial loads (Bentz, 2000b). It has been successfully used in past projects for assessing the bending and shear strength of bridge structures. The peak moment predicted by Response2000 was 1.7% lower than with the custom written moment-curvature program. Both predictions were made using measured material properties.

Table 4-1. Predicted moment capacity, total load required to reach flexural capacity

Moment Capacity (in-kips)	11882.00
Moment Capacity (ft-kips)	990.20
Load to reach moment capacity (kips)	511.88

58
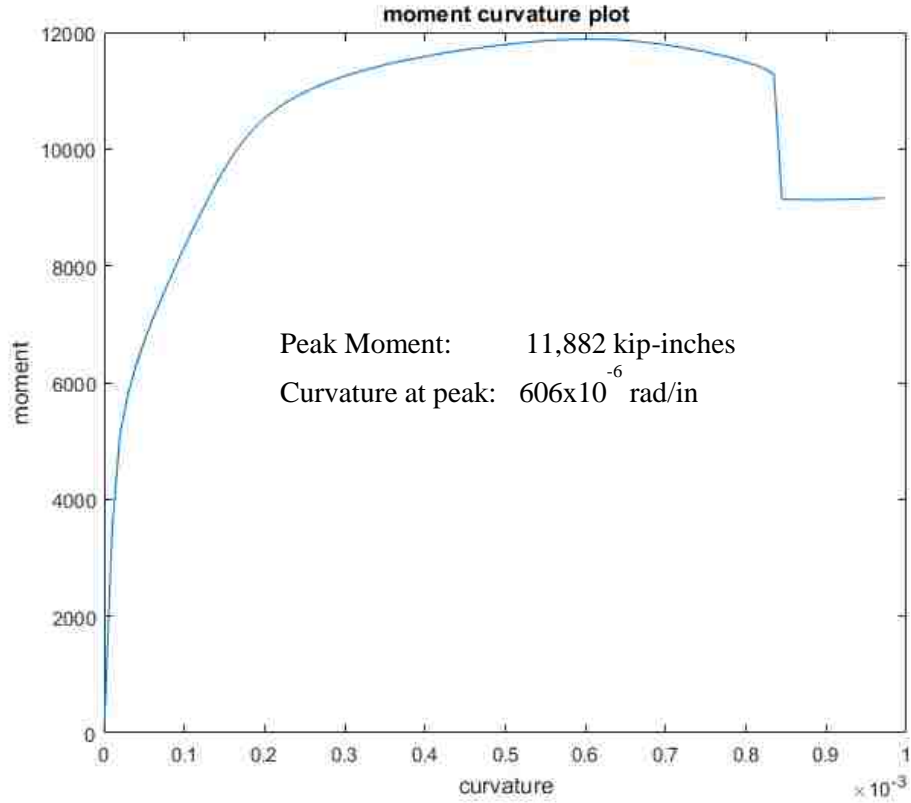
Figure 4-10. Moment-curvature prediction

Table 4-2 summarizes the measured capacities during the test and compares them with the predictions. The curvature was calculated using the rotation measurements from the string potentiometers along the bottom of the specimen. The inclinometers gave very similar information.

Table 4-2. Bending test moment-curvature results

Item	Measured	Predicted	Meas./Pred.
Moment (in-kips)	12800	11900	1.08
Curvature (rad/in)	589×10^{-6}	606×10^{-6}	0.97

59

The moment capacity of the four-point bending specimen was higher than predicted. This can be explained by the following:

- The moment-curvature program does not take into account the effects of confinement. This is expected to have only a very small effect, because, only half of the pile wall thickness was within the spiral.
- The strand stress that was inputted into the moment-curvature program could have been incorrect (difficult to quantify all of the prestressing losses that may have occurred). After inspecting this further however, the strands would have needed to be stressed to 300 ksi to reach the calculated capacity, which exceeds the ultimate stress of the strand and is thus not possible. (Note that the strength predicted by Response2000 was within 2% of that predicted by the moment-curvature program).
- The support cradles may have provided extra capacity by restraining the outward horizontal movement of the specimen as it continued to increase its curvature. This explanation is the most plausible.

4.4.2 *Strain Diagrams*

A strain diagram can also be developed using the prediction calculations at the peak moment, shown in Figure 4-11. The predictions are used because the predicted and measured curvature values were nearly identical. Because the neutral axis is close to the inner face of the wall, the strains at the inner face are much smaller than those at the outer face, suggesting that internal spalling is not the event that initiates failure. However, once the outer wall has spalled, its strength is lost, the demand in the inner wall exceeds its capacity and so it spalls inwards. If the measured strain on the top face of the concrete was used, the corresponding strain on the inner wall would be +0.0002 in/in, given the geometry and measured curvature.

$\varepsilon_{c,top} = -0.0028$ in/in

$\varepsilon_{c,inner\,wall} = -0.0006$ in/in

$\varepsilon_{c,bot} = +0.019$ in/in
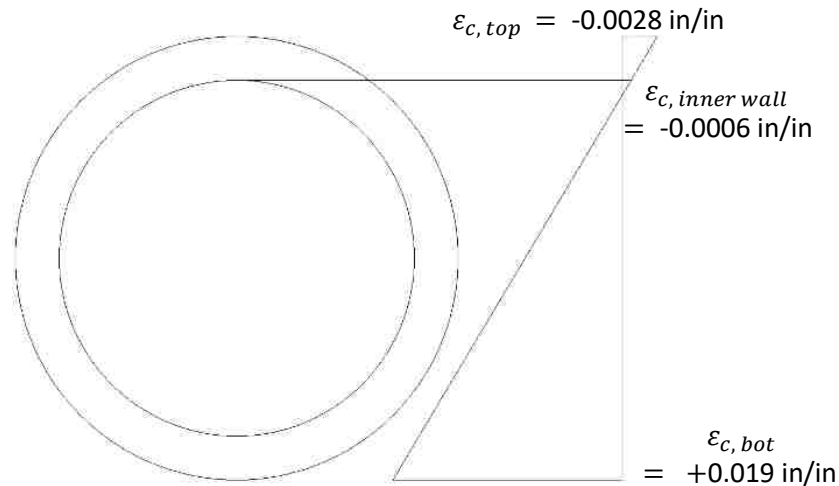
Figure 4-11. Strain diagram at maximum moment

The previous research had suggested that flexural failure in this region was non-ductile and initiated by premature implosive internal spalling. That behavior was therefore of primary concern. The test results from the pure bending test show that this failure mode is unlikely because failure is in fact initiated by external spalling, as in a conventional solid column. It is worth noting however that the concrete strength in the test specimen is much higher than what would be seen in the field bridges, and for that reason the strains at the inner face of the pile walls in the field may be higher than what was observed in the pure bending test. Because internal spalling follows external spalling rapidly, the hollow pile-column fails sooner after its peak load than does a solid column, but the test specimen was nonetheless able to reach at least the predicted nominal flexural strength and a ductility factor of 3.20. In the bending test, the specimen was prestressed to approximately 1200 psi (effective) but carried no axial load. The prestressing in the field pile-columns varies among sites, but averages about 900 psi; they also carry an axial load causing stress in the range 460 to 770 psi. In the field pile-columns, the total stress in the concrete thus lies in the range of 1360-1670 psi; on that basis, they should be expected to be somewhat less ductile than the bending test pile-column as the additional axial load will increase the overall strength.

Chapter 5. SHEAR TEST RESULTS AND ANALYSIS

5.1 INTRODUCTION

In this chapter the results of the combined shear and bending test are presented and analyzed. In that test, the specimen experienced both shear and bending moments simultaneously. The results are important because they allow verification of two computational models for combined shear and bending, which can then be used to evaluate the transverse load capacity of a hollow pile-column in the field. The transverse load capacity is likely to depend on combined shear and bending behaviors if the soil is stiff or the above-grade column length is short. The observed test behavior is first presented in Section 5.2, followed by the measured response in Section 5.3. Then, in Section 5.4, the two computational approaches are outlined, and their predictions for the test specimen's behavior are compared with the measured data.

5.2 OBSERVED RESPONSE

In this section, the observed behavior is discussed. The test protocol described in Table 3-2 was implemented, starting with a cycle to check instruments and check the settlement of the Cotton Duck Padding (CDP). A shear demand of 100 kips was achieved on the first cycle, corresponding to a mid-span deflection of approximately 0.05-inches, and it caused the specimen to crack. This load was smaller than the predicted cracking load. This was attributed to the additional stresses due to bending and prestressing that were not originally accounted for in the cracking load prediction. On the next cycle, a shear demand of approximately 165 kips was achieved, followed by a cycle to failure that achieved a total load of 478 kips (or a shear demand of 239 kips). Figure 5-1 shows the specimen after failure. During the test, progressive cracking occurred in both of the hollow regions. The cracks grew at an incline flatter than 45° (see Figure 5-1). This is consistent with the existence of longitudinal compression from the prestressing.

Figure 5-1. Specimen position after failure, note the angle of the cracks

5.3   MEASURED RESPONSE

The behavior of the specimen on a global level is discussed in this section. For each plot shown, a sketch of the test specimen is included to depict which instruments correspond to which curves.

5.3.1   *Force-Displacement relationship*

The maximum achieved force was 478 kips, corresponding to 239 kips of shear demand. Figure 5-2 shows the force-displacement curve, as measured by the potentiometers along the bottom of the specimen.
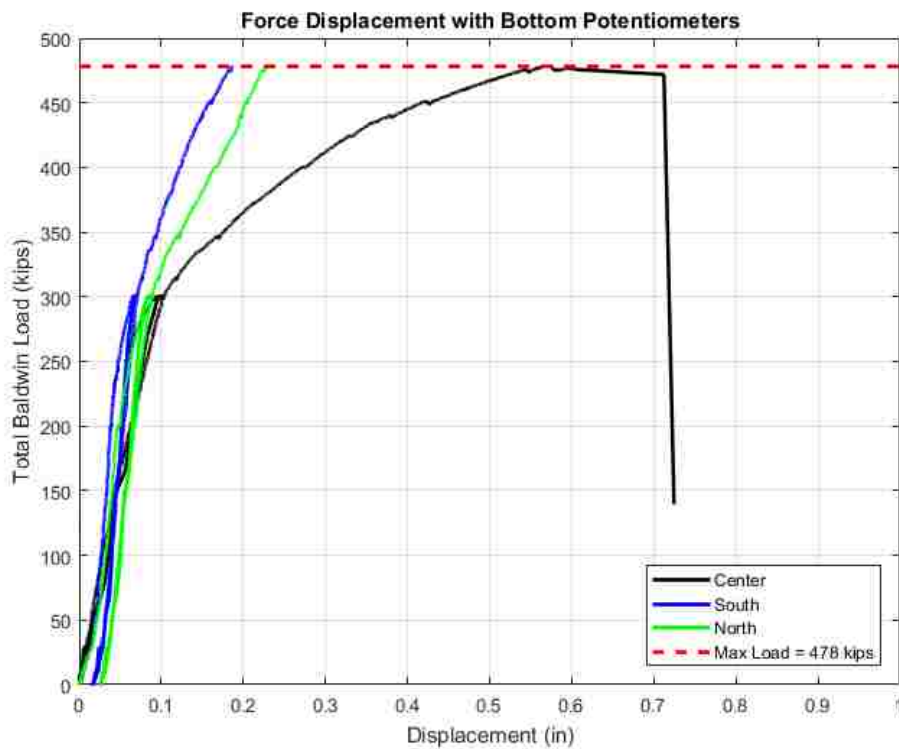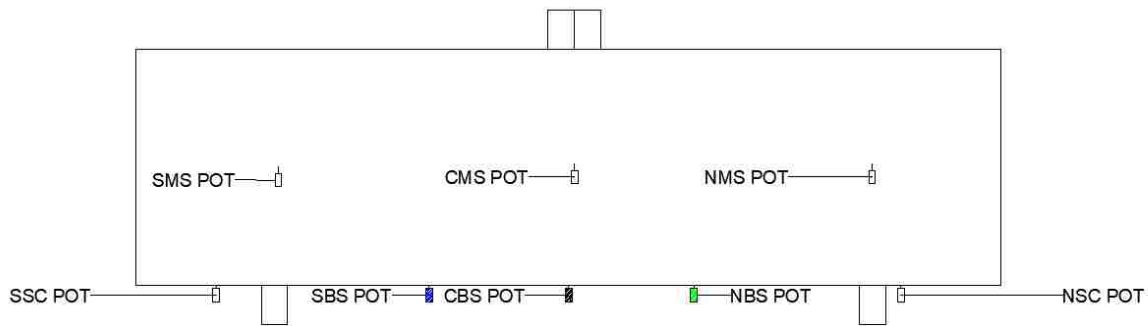
Figure 5-2. Force-displacement curve for all bottom potentiometers

The force-displacement curve shows a slight decrease in stiffness at approximately 200 kips. This loss in stiffness was followed by gradual softening until the maximum load of 478 kips was reached, at which point a sudden strength loss occurs at failure.

Figure 5-3 focuses on the force-displacement curve corresponding to the potentiometer at the center of the specimen, and projects a linear elastic tangent stiffness to the measured data to the maximum force. The corresponding "elastic displacement" is ~0.16 inches. The total achieved displacement was ~0.58 inches, giving a ductility factor of 3.63. It is worth noting that the

theoretical linear elastic stiffness is higher than what was measured; the consequence of this is that the theoretical ductility is higher because the theoretical "elastic displacement" would be smaller (see Appendix C).
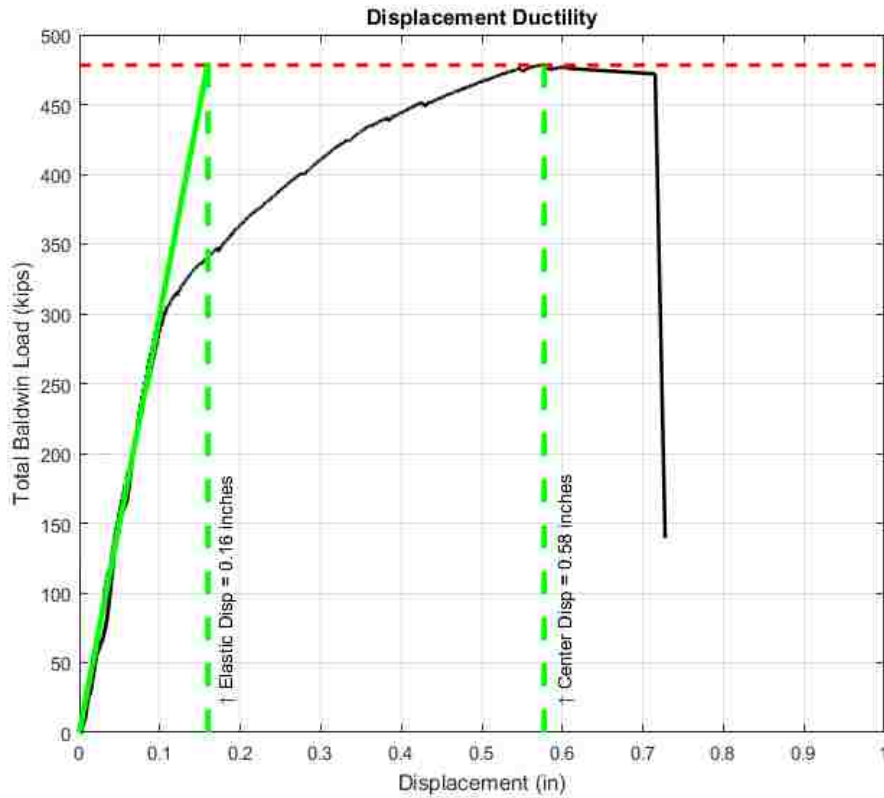
Figure 5-3. Center force-displacement curve with associated ductility measurements

5.3.2   *Rotations*

Figure 5-4 shows the force-rotation curve as measured by the inclinometers over each support cradle, while Figure 5-5 shows the same curve as measured by the various potentiometers. The rotations plotted in Figure 5-5 were obtained in the same manner as the bending test, and show that the rotation at the center of the specimen (shown in the red or blue curve) is still smaller than the rotation at a point further north or south along the specimen (shown in the green curve). The difference between these rotations however is smaller than in the pure bending test due to the larger role played by the shear deformations in the combined shear and bending test. To determine the extent of the shear deformations, the average rotation at the supports (0.004 radians, see Figure 5-4) is multiplied by the shear span (3 feet) to get the displacements due to

65

bending (0.14 inches). Since the total displacement achieved at mid-span was 0.6 inches, it is clear that the displacement was dominated by shear behavior.
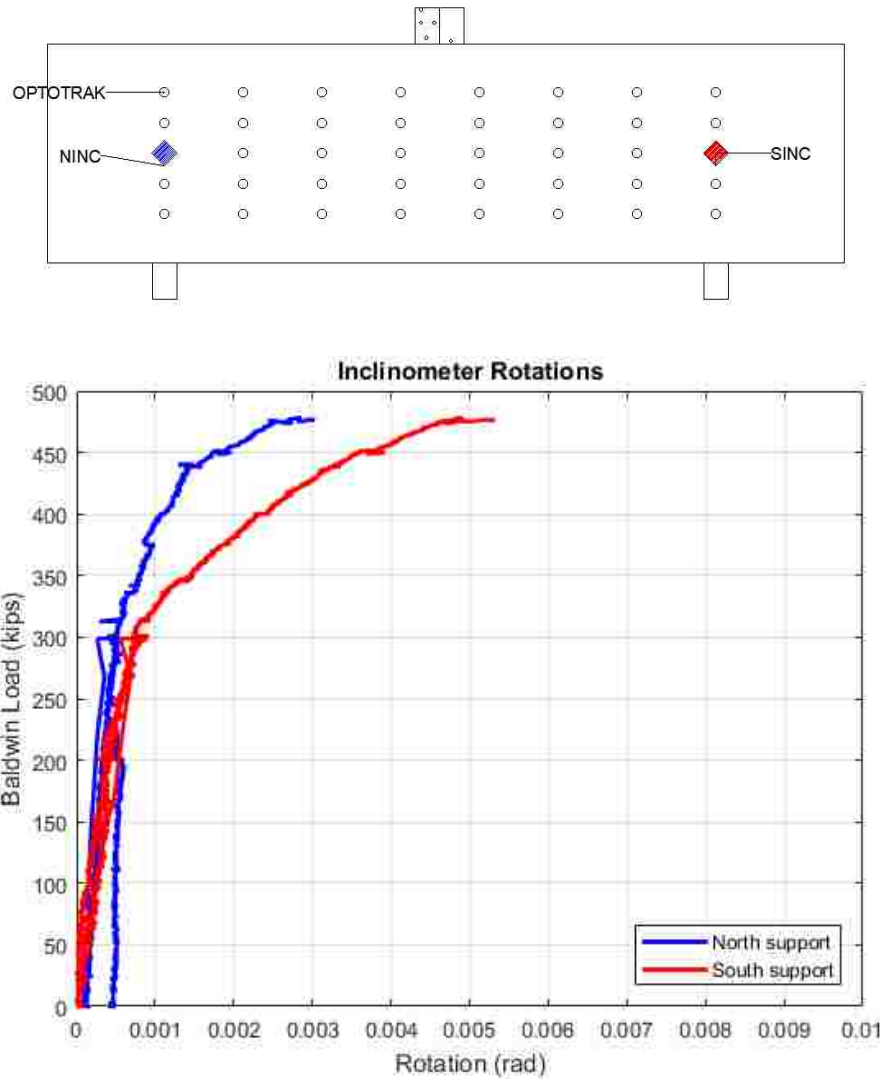
Figure 5-4. Force-rotation curve for inclinometers that were over support cradles
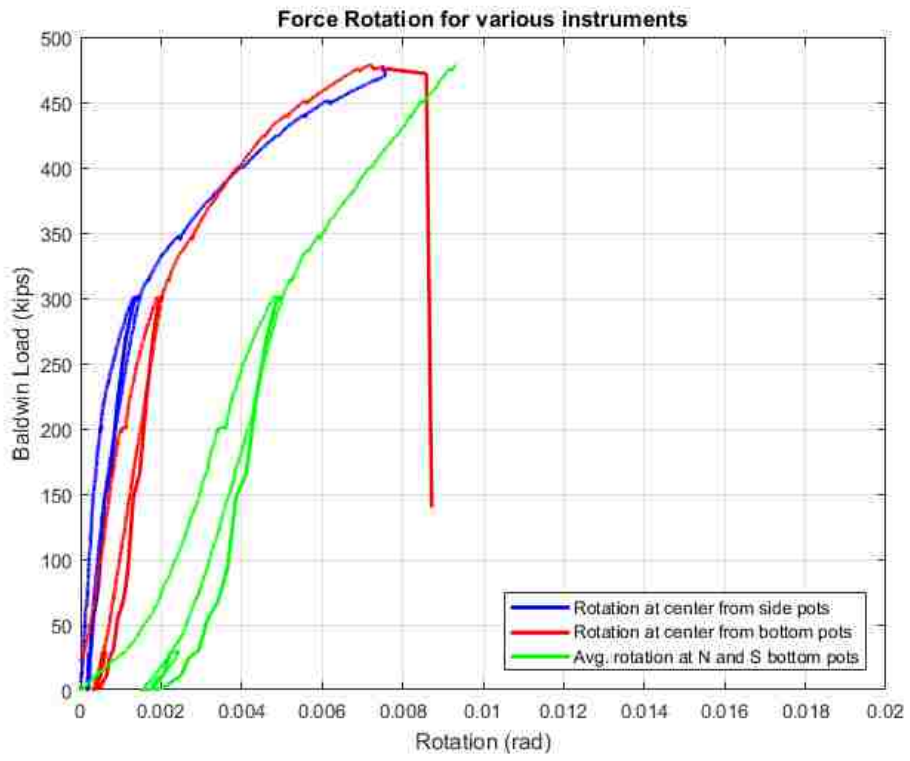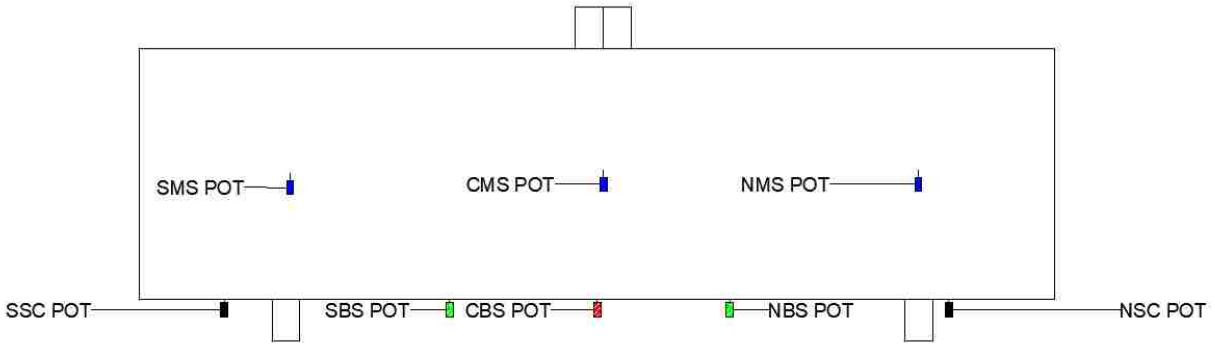
Figure 5-5. Force-rotation curves for all potentiometers

5.4 ANALYSIS

In this section, two approaches for computing the transverse load capacity, in the presence of combined shear and bending, are presented. They are used to generate a plot of capacity vs. shear span ratio, and their predictions are compared with the test result.

67

5.4.1 *Transverse load capacity*

To determine the transverse load capacity of the test specimen and the corresponding expected loads during testing, two programs were used. First, a custom-written program was made for this research that was based on a Mohr's circle analysis. The program computes the maximum principal stress in the wall of the hollow section, assuming uncracked behavior and given the applied stresses due to prestressing, axial force, and a shear span ratio. It computes the maximum principal stress at many points around the circular cross-section, and finds the largest value. It then varies the shear force to find the value that causes the largest maximum principal stress to reach $4\sqrt{f_c'}$ (psi). That is the criterion used by ACI 318-19 Section 22.5.6.3.3 used to define shear failure.

Figure 5-5 shows the Mohr's circle used for the referenced analysis and identifies the key points.
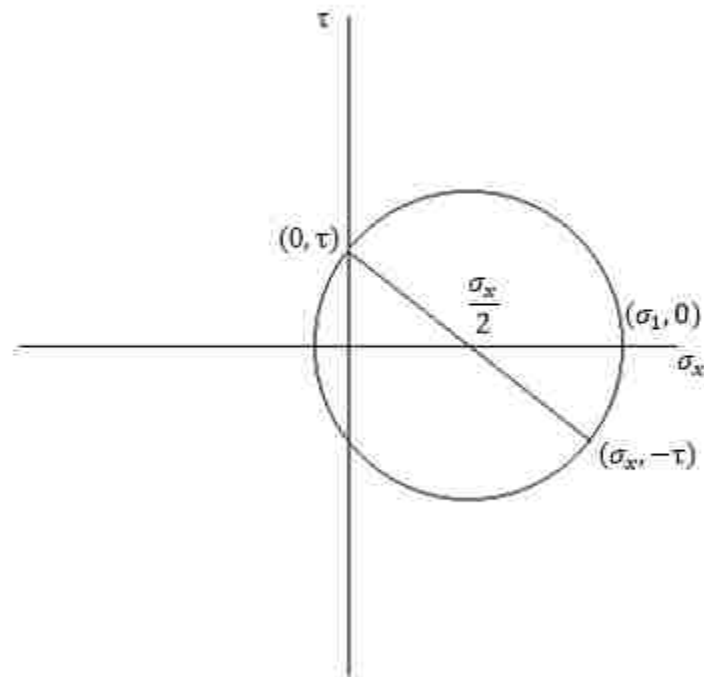
Figure 5-6. Mohr's circle used for transverse load capacity analysis

First the local shear stress in the wall, caused by a transverse load, V, is computed using elastic theory for a thin-walled cylinder. The result is:

68

$$\tau = \frac{V*sin(\alpha)}{A_{sh}} \qquad (5)$$

Where: V = shear demand

$A_{sh} = \frac{1}{2}A_c$ for a hollow cylindrical section (derived for thin-walled cylinders).

α = the angle around the cross section starting at the extreme tensile face (see Figure 5-7)
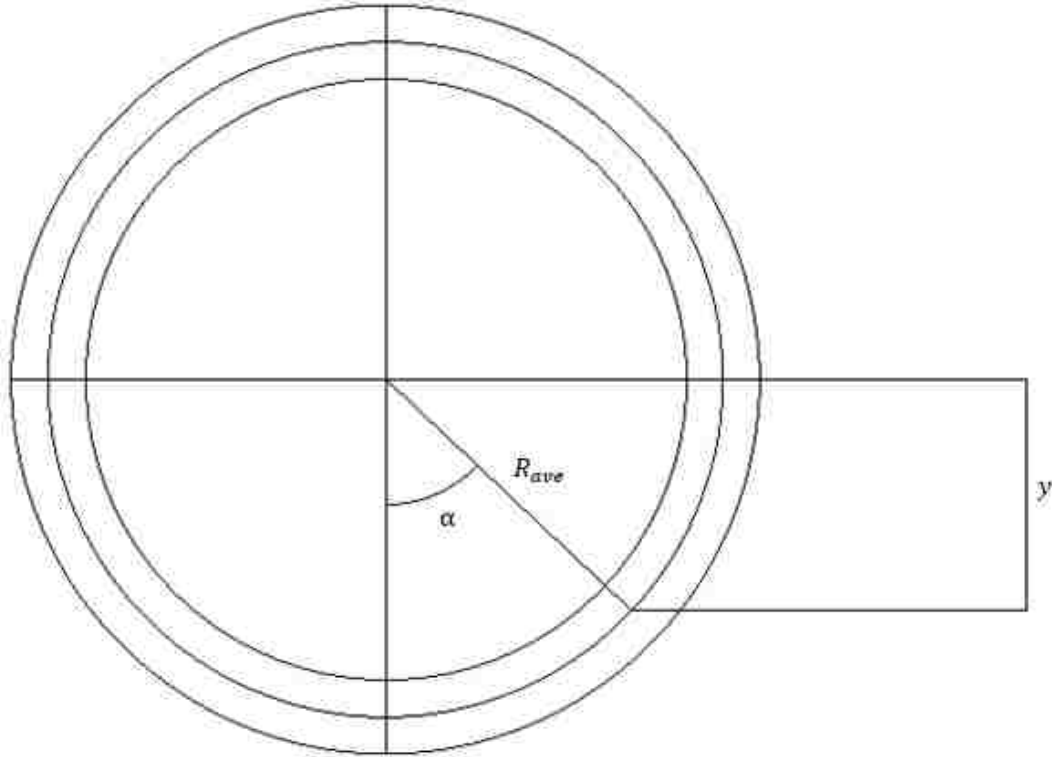
Figure 5-7. Cross-section of test specimen used for transverse load capacity calculations

Then, the maximum principal tension stress is computed using Equations 6 and 7:

$$\sigma_1 = \frac{\sigma_x}{2} + R \qquad (6)$$

$$R = \sqrt{\left(\frac{\sigma_x}{2}\right)^2 + (\tau)^2} \qquad (7)$$

69

Equation 8 defines the stress due to bending. Equation 9 defines the normal stress for combined loading (moment plus the axial stress induced by prestressing). The bending moment in Equation 8 is positive.

$$\sigma_b = \frac{M*y}{I} = \frac{M*R_{ave}*\cos(\alpha)}{I} \qquad (8)$$

$$\sigma_x = \sigma_b - \frac{F_p}{A_c} \qquad (9)$$

Where: M = moment demand

R_{ave} = average radius of cross section

I = moment of inertia

F_p = total prestressing force (positive)

Using the test specimen properties, the corresponding predicted transverse load capacity was 227 kips; the measured shear demand was 239 kips.

The second program that was used was Response2000, which is based on modified compression field theory and already accounts for the interaction of the various stress components. The transverse load capacity predicted by Response2000 was 213 kips, which is within 6.12% of that predicted by the ACI-based analysis.

Table 5-1 summarizes the measured capacities during the test and compares them with the predictions. The maximum shear demand achieved during the test was 239 kips, which is slightly greater than the capacity predicted using both Response2000 and the ACI-based procedure.

Table 5-1. Shear test capacity results

Item	Measured	ACI Predicted	Meas./ACI Pred.	Response2000 Predicted	Meas./R2K Pred.
Shear Force (kips)	239	227	1.05	213	1.12

Figure 5-8 was prepared using the geometry and material properties for the test specimen and compares the ACI and Response2000 approaches for calculating transverse load capacity. This plot shows the transverse load capacity, *V*, versus the ratio of *L/D*, where *L* is the shear span (equal to *M/V*) of the specimen and *D* is the specimen outer diameter.
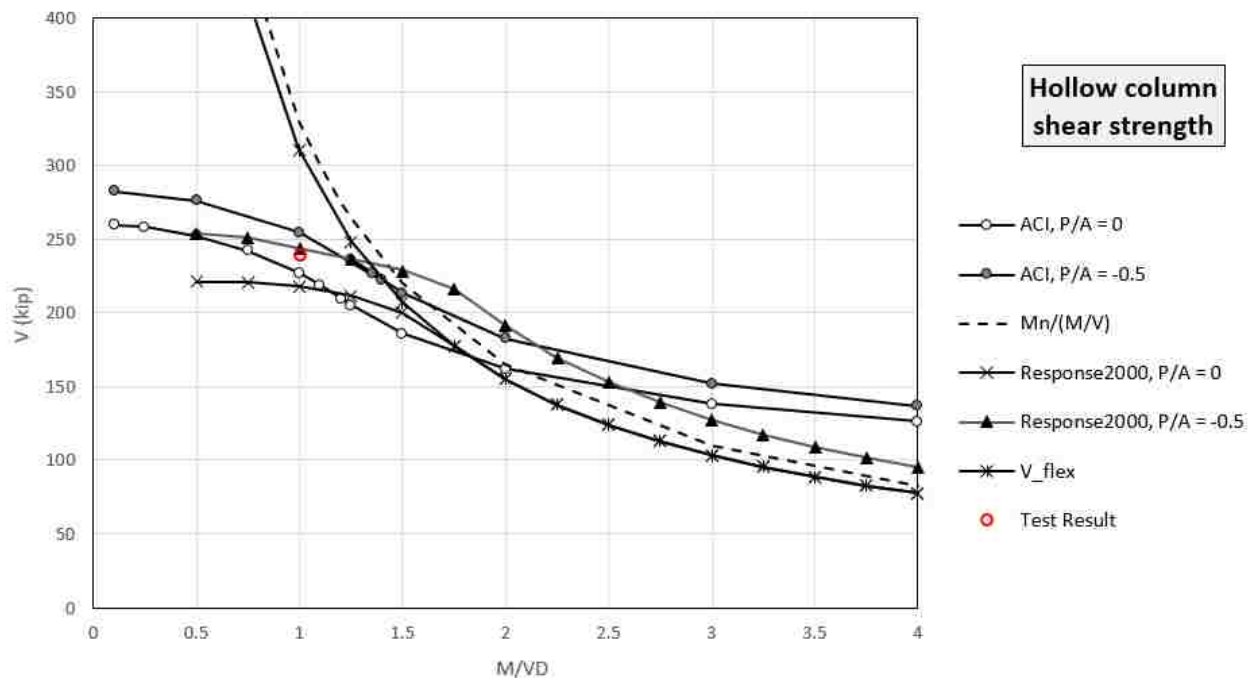
Figure 5-8. Shear strength of 36-inch outer diameter hollow pile-column as function of normalized shear span ratio, M/VD

The figure shows curves of two different types. The two marked "Vflex" and "Mn/(M/V)" use the pure flexural strength divided by the shear span ratio, to define the transverse load capacity.

71

This approach corresponds to the formation of two plastic hinges, separated by a distance equal to twice the shear span ratio, M/V. Shear stresses are assumed not to detract from the flexural strength. The model is appropriate for pile-columns in which the shear span ratio is large. The curve "Vflex" was generated using Respons2000, while the curve "Mn/(M/V)" was generated based on the flexural strengths computed using the moment-curvature program described in Chapter 4. The two curves agree closely.

The other curves, marked "ACI" and "Response2000" account for the interaction of shear and bending, as outlined above. Two curves are shown for each; one with no axial load, and another with 500 psi of axial compression. The latter is approximately the axial load used in the cantilever column test described in the chapters that follow, and is representative of loads in the field. All of those curves flatten out at low shear span ratios, where shear governs the specimen strength.

The ACI approach and Response2000 are based on quite different concepts, but they give results that are remarkably similar over much of the range. As can be seen in Figure 5-8, compressive axial load increases the shear strength slightly. For the test specimen, the shear span ratio *L/D* was 1.0, the axial load was zero, and the measured shear force was 239 kips. For the same conditions, the ACI criterion and Response2000 respectively predicted failure at a shear demand of 227 and 218 kips, respectively.

The combined shear and bending test provides a good basis for determining the specimen strength when the failure mode is dominated by shear behavior. The test also provides calibration data for both Response2000 and the ACI approach for predicting failure in members subjected to prestressing, bending, and shear. The results from the shear and bending test combined with the results of the pure bending test allowed the research team to determine the conditions under which shear would be critical in the field. The results show that shear failure in a hollow section in the field is likely in only very short columns with a very short distance between the points of inflection and maximum moment. Very stiff soil conditions would make

72

the above-ground column behave nearly as fixed-fixed, but if the soil is flexible, particularly in the upper layers, it will increase the distance between those two points. This issue is discussed in greater detail in Section 8.4.

Chapter 6. COLUMN CANTILEVER BENDING TEST DESIGN

6.1 INTRODUCTION

This chapter describes the design and preparations for the cantilever bending test, conducted on a hollow pile-column specimen attached to a simulated cap beam by means of a plug connection. The goal was to investigate the behavior of the connection and the adjacent hollow region of the specimen, under cyclic lateral load. The strength and rotation capacity were of primary concern. A similar specimen had been tested previously by Tardieu (2018); the only difference was that the specimen described here was equipped with a CFRP jacket, which Tardieu's specimen lacked. Hereinafter, the previous specimen is referred to as "as-built," while the jacketed specimen is referred to as "retrofitted." Upon inspection of the reference bridges it was found that no two bridges were completely alike, making a true scale model of an existing column not possible. Therefore, to evaluate the behavior of the hollow core concrete pile-columns themselves, the research team modified the design of the specimen to mitigate other potential failure modes. The factors affecting the design of the specimen and the experimental setup will be discussed in this chapter. The intention of the researchers was to ensure a flexural failure in the pile-column at the cap beam connection.

6.1.1 *Design Prototype*

Prior to the as-built test (Tardieu 2018), the researchers consulted with WSDOT regarding how to proceed with testing a model column. Figure 6-1 shows a sketch of the prototype selected by the research team, and the region that was being investigated. Following the as-built test (Tardieu 2018), the retrofit concept finally agreed on was to use a CFRP wrap around the exterior of the pile-column in the plug region (see Figure 6-2). For easier constructability, a length of 5 feet was selected for the fiber wrapped region (the CFRP wrap comes in 2-foot layers and can be easily cut in half).

74
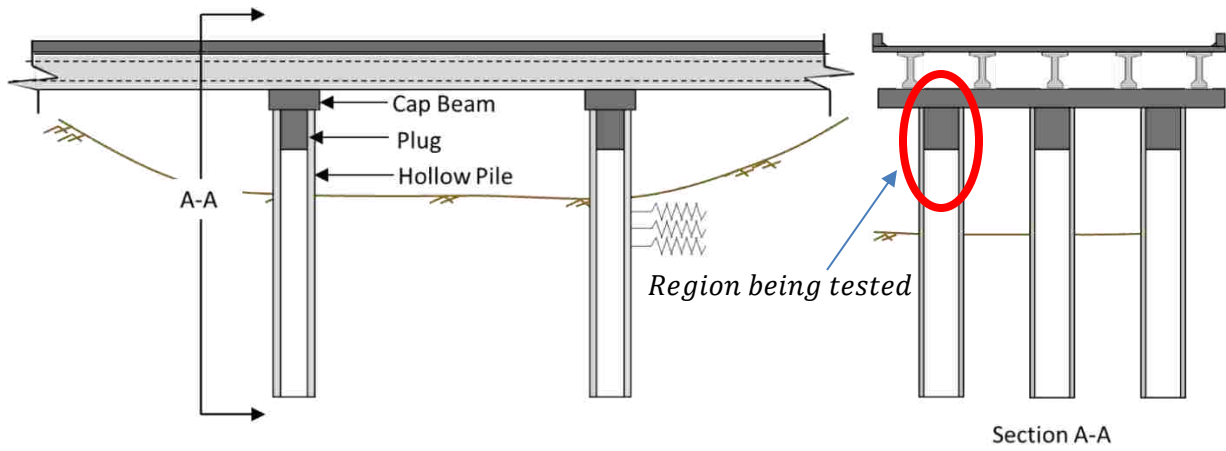
Figure 6-1. Sketch of field prototype conditions
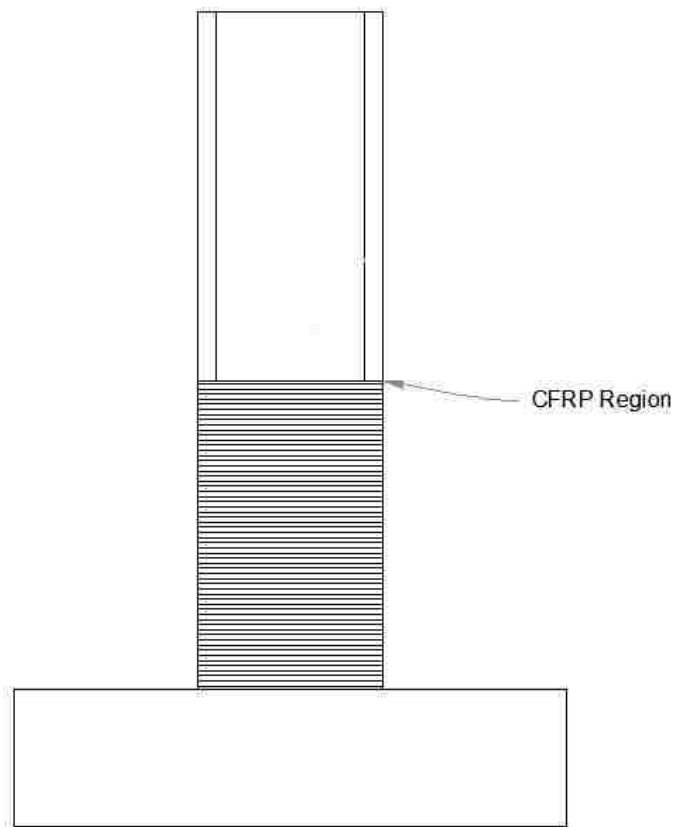
Figure 6-2. Proposed CFRP region on test specimen

75

6.2   TESTING CONSIDERATIONS

To understand the behavior of the pile-column above ground, particularly at the retrofit location (column-to-cap-beam connection) under seismic loading, the structure can be modelled by placing a lateral load at the predicted point of inflection. However, it should be noted that since the lengths of pile-columns varied greatly among the bents of all bridges, the length from the cap beam-column interface to the point of inflection, L_{inf}, also varies. For this reason, L_{inf} was chosen based on the scale factor of the model and the limitations of the test rig.

The test specimens for the pure bending test, combined shear and bending test, and the cantilever bending test were all manufactured by Concrete Technology Corporation, and were all nominally identical. They are described in Sections 3.2-3.4 of this thesis.

Some minor adjustments had to be made to the aforementioned scale to account for the equipment being used. Firstly, due to the capacity of the lifting crane in the lab, the length of the cap beam had to be restricted to 8 feet between supports which is only a 0.44 scale of the prototype between columns. As a result of this, the shear reinforcement in the cap beam was also increased by using a tighter spacing to deal with the higher shear force caused by the shorter shear span. Secondly, the length to the inflection point, L_{inf}, was determined by the maximum height of the horizontal actuator on the test rig and was taken as approximately 109 inches, or 3.0 column diameters, above the cap beam.

6.3   SPECIMEN DESIGN

The overall dimensions of the test specimens used in this study are shown in Figure 6-3.

76
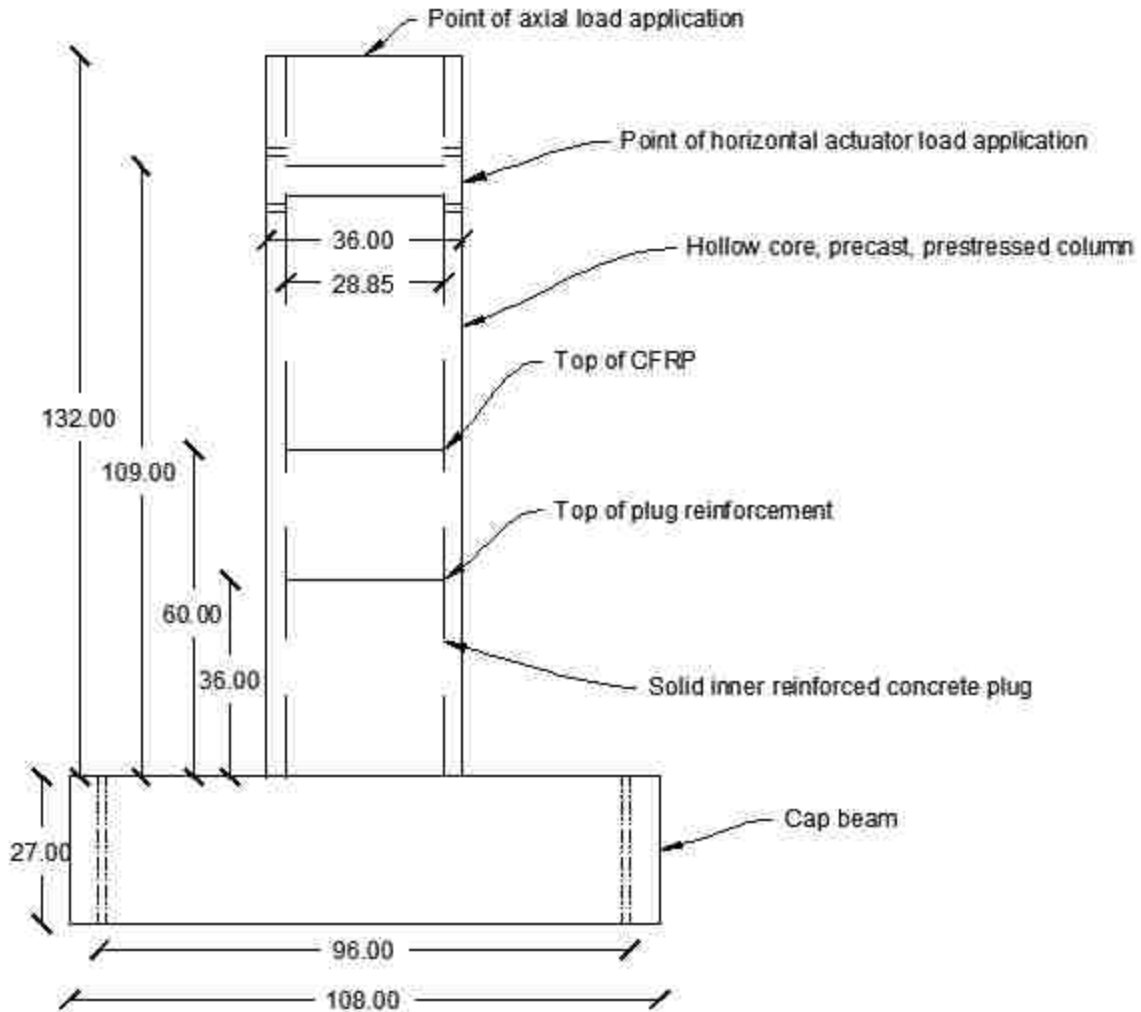
Figure 6-3. Overall specimen dimensions (all dimensions given in inches)

On the existing bridges, there is a solid concrete plug that extends between four and five feet into the core of each pile-column from the cap beam-column interface, and it is reinforced with longitudinal bars that extend into the full depth of the cap beam. For the test, the plug was designed in order to maintain a length/diameter (L/D) ratio similar to what exists on the bridges in the field (see Table 6-1). The average L/D ratio of the plug on the existing bridges was approximately 1.34, ignoring that of Le Line Slide which was much lower than the others (Tardieu 2018). A plug length of 39 inches was chosen for the specimen design (by rounding to the nearest inch), given that the diameter of the plug was nominally 28.875 inches. The length of the plug compared with the cantilever column length affects the moment experienced by the hollow region of the pile-column beyond the end of the plug.

77

Table 6-1. Length to diameter ratios of pile-column plug

Reference Bridge	Pile Outer Diameter (in)	Length of plug (typ.) (in)	Diameter of Plug (in)	L/D
Ravenna Overcrossing	48 inches	50 inches	38 inches	1.32
Galer-Lakeview	48 inches	51 inches	38 inches	1.34
Le Line Slide	54 inches	52 inches	44 inches	1.18
Green River	54 inches	60 inches	44 inches	1.36
	Average L/D ratio = 1.34			
Test Specimen	36 inches	38.66 inches	28.875 inches	1.34

The longitudinal reinforcement for the plug was designed so that the ratio, $\frac{M_{n,filled}}{M_{n\_hollow}}$, was similar to that of the field conditions. $M_{n,filled}$ represents the nominal moment capacity of the reinforced plug with the pile-column concrete contributing to the moment capacity, whereas $M_{n,hollow}$ represents the nominal moment capacity of the hollow pile-column alone. The bars were fully developed (see Table 6-2).

Table 6-2. Moment capacities of reference bridge pile-columns

Reference Bridge	$M_{n,plug}$	$M_{n,filled}$	$M_{n,hollow}$	$\dfrac{M_{n,filled}}{M_{n\_hollow}}$
	(in-kip)	(in-kip)	(in-kip)	(-)
Ravenna Overcrossing	16525	22910	25450	0.900
Galer-Lakeview	15700	21040	25815	0.815
Le Line Slide	30900	43410	41910	1.036
Green River	24000	33650	35650	0.944
Average (field)				**0.924**
Test Specimen	9960	14700	14600	01.01

The moment capacities in Table 6-2 were calculated using the material properties summarized in Table 6-3, Table 6-4, and Table 6-5 and using the following cross-sections:

- M_{n_plug} – The moment capacity of the inner plug, ignoring the outer pile-column concrete and prestressing strands.

- M_{n_hollow} – The moment capacity of the hollow pile-column only, considering the prestressed strands as the reinforcement.

- M_{n_filled} – The moment capacity of the combined pile-column and plug ("filled") section, using the nominal strength of the hollow pile-column concrete and plug concrete, considering the plug reinforcement only (ignoring the prestressed strands, which are discontinuous at the cap beam).

The material properties were nominal values, and were taken from the drawings where possible. The values for the prestressing strand reflect the use of stress-relieved vs. low-relaxation strand in the different field bridges. The values for the strand used in the test specimens were obtained from the mill certificates provided by the supplier.

Table 6-3. Reinforcement material properties

Reference Bridge	E	f_y	f_u	ε_{sh}	ε_u	n
	(ksi)	(ksi)	(ksi)	(in/in)	(in/in)	(-)
Ravenna Overcrossing	29000	60	90	0.01	0.1	6
Galer-Lakeview	29000	60	90	0.01	0.1	6
Le Line Slide	29000	60	90	0.01	0.1	6
Green River	29000	60	90	0.01	0.1	6
Test Specimen	29000	60	90	0.01	0.1	6

Note: the variables ε_{sh} and n are used in the Raynor model for reinforcing bar stress-strain.

Table 6-4. Prestressing strand material properties

Reference Bridge	E	f_y	f_u	ε_u	b	R	f_{pe}
	(ksi)	(ksi)	(ksi)	(in/in)	(-)	(-)	(ksi)
Ravenna Overcrossing	28000	221	250	0.049	0.025	5.3	163.06
Galer-Lakeview	28000	221	250	0.049	0.025	5.3	124.36
Le Line Slide	28500	239	270	0.052	0.025	6.6	118.72
Green River	28500	239	270	0.052	0.025	6.6	127.73
Test Specimen	29000	280	292	0.052	0.01	20	135.94

Note: the variables b and R are used in the Menegotto-Pinto model for strand stress-strain.

Table 6-5. Concrete material properties

Reference Bridge	Column f'_c	Plug f'_c
	(ksi)	(ksi)
Ravenna Overcrossing	7.8	5.2
Galer-Lakeview	7.8	5.2
Le Line Slide	9.1	5.2
Green River	8.45	5.2
Test Specimen	15.5	6.5

Since there was high variability in the M_{n_plug}/M_{n_hollow} ratio, the plug reinforcement of the specimen was designed to match the M_{n_plug}/M_{n_filled} ratio as closely as possible. As such, sixteen #8 bars were used with a 180 degree hook on the both ends of the reinforcement (see Figure 6-4 and Figure 6-5). Hoop ties made of #3 reinforcement were spaced at 6.5-inch centers around the plug reinforcement.
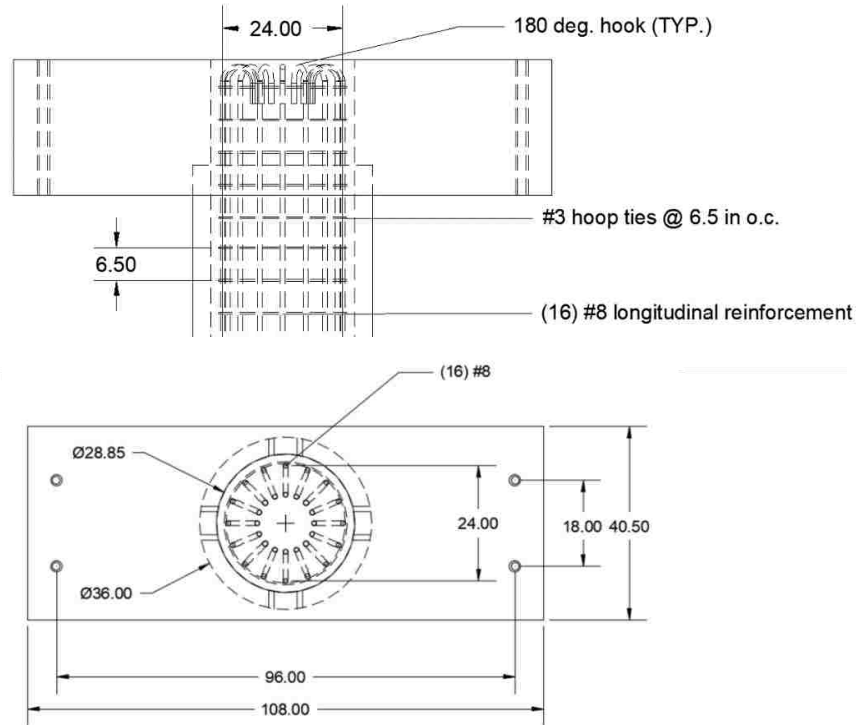
Figure 6-4. Plug dimensions and reinforcement
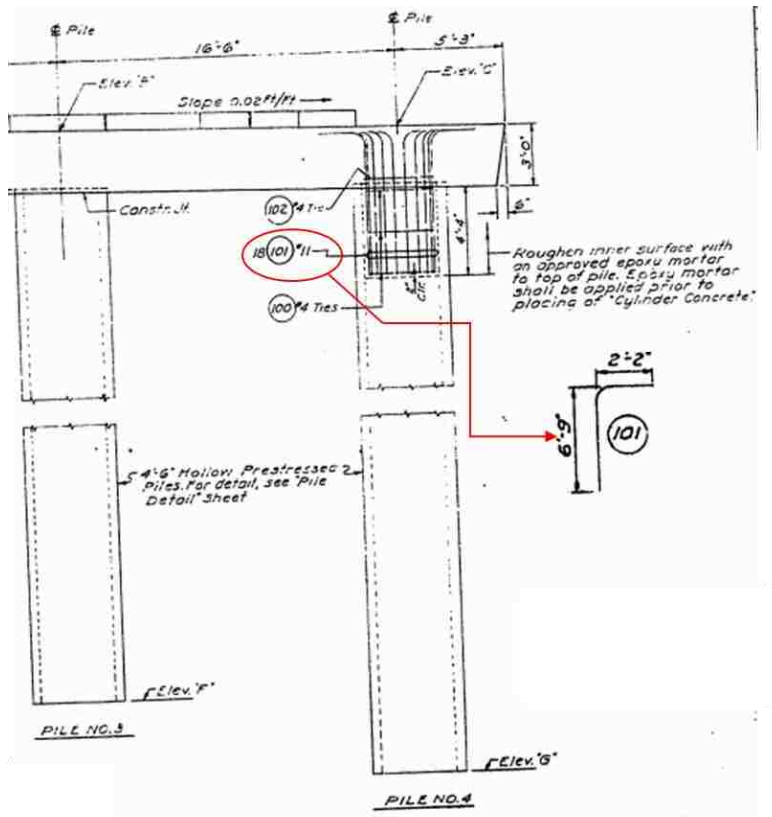
Figure 6-5. Plug reinforcement details for Le Line Slide Bridge

81

The last main component of the specimen design is the cap beam (see Figure 6-6). While all effort was made to design the cap beam to a 2/3 scale like the pile-column and plug, restrictions existed due to the size of the testing equipment. The cross-section area and reinforcement were designed to the same scale, but the length of the beam and the amount of shear reinforcement included was changed to accommodate testing conditions. The length of the cap beam was shortened to 8 feet between supports, that is, between points of zero bending moment. The tension reinforcement was designed so that the moment capacity was 25% greater than the expected demand at the face of the pile-column, given the predicted ultimate moment capacity of the pile-column and connection. This was done to avoid premature failure in the cap beam. The compression reinforcement was designed to be 2/3 of the area of tension reinforcement which was similar to what was used in the cap beams of the prototype bridges. As such, the cap beam reinforcement consisted of ten #8 bars (in tension) at the bottom and eight #8 bars (in compression) at the top. The shear reinforcement was a six-legged stirrup made of #5 bars and implemented via one large outer and two smaller inner rectangles (see Figure 6-6). The reinforcement layout modeled the current field conditions except for some top and bottom bars which were displaced slightly to avoid congestion and to accommodate hold-down anchor rods for the test. It should be noted that although there is no joint shear reinforcement in any of the existing bridges, this was included in the specimen design in order to capacity-protect the cap beam and ensure a failure in the pile-column. The joint shear reinforcement consisted of two layers of #6 reinforcement, 30 inches long with 6-inch long 90-degree hooks on either end, placed approximately 7 inches apart along the cross-section of the cap beam within the region defined by the plug reinforcement (see Figure 6-6) (Tardieu 2018).

In the bridges in the field, the shear reinforcement varied along the span, indicating that it was designed for gravity loads. In the test specimen, the goal was to test the connection under seismic loading, so the shear reinforcement was designed to prevent shear failure in the cap beam. The required shear strength was derived from the flexural strength of the cap beam and its length as built in the laboratory.
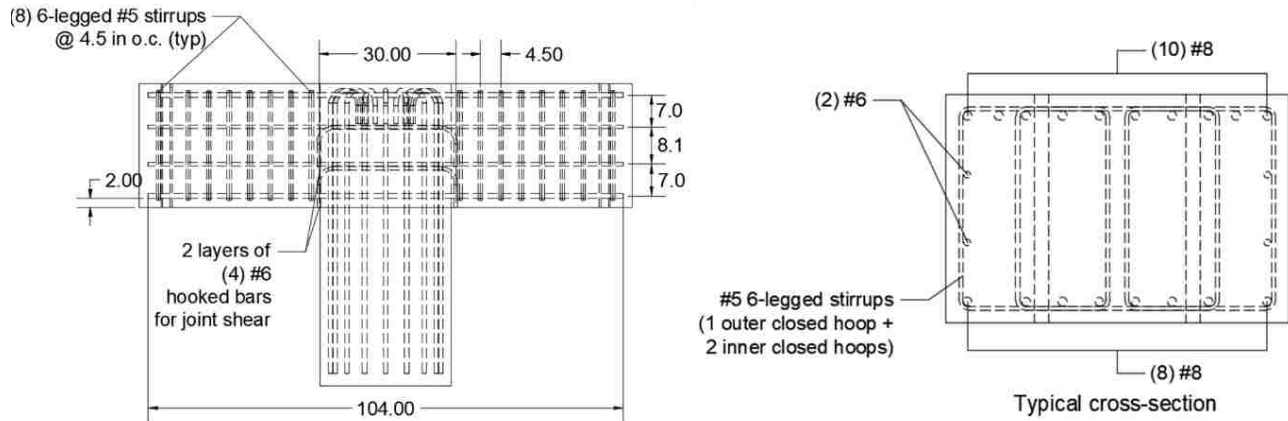
Figure 6-6. Cap beam dimensions and reinforcement

6.3.1 *Materials*

The pile-column concrete and strand reinforcement was described in Section 3.3.1. The cap beam and plug of the reference bridges were both cast-in-place on site with lower strength concrete than that of the pile-columns. The concrete used was Class A concrete with a specified strength of 4000 psi. For the test specimen, concrete with a specified strength of 5000 psi was used for these components to simulate the expected present-day strength of the concrete on the bridges. The reinforcement for the cap beam and plug were ordered from ASTM A615 Grade 60 stock.

The material properties of the specimen are provided in Table 6-6 and Table 6-7, as well as Figure 6-7 and Figure 6-8. The average concrete compressive strength of the cap beam, plug and hollow pile were obtained in accordance with ASTM 39. The tensile stress-strain relationship for the reinforcement steel used as longitudinal plug reinforcement was obtained in conformance with ASTM A370-15 and ASTM A615-16

Table 6-6. Concrete compressive strength at different ages for specimen components (psi)

	7 days	14 days	28 days (f'_c)	Test day (age in days indicated in parentheses)
Hollow pile-column	8800	-	13155	15569 (322)
Plug	5316	6197	7057	7798 (266)
Cap Beam	4782	5695	6216	6850 (280)

83
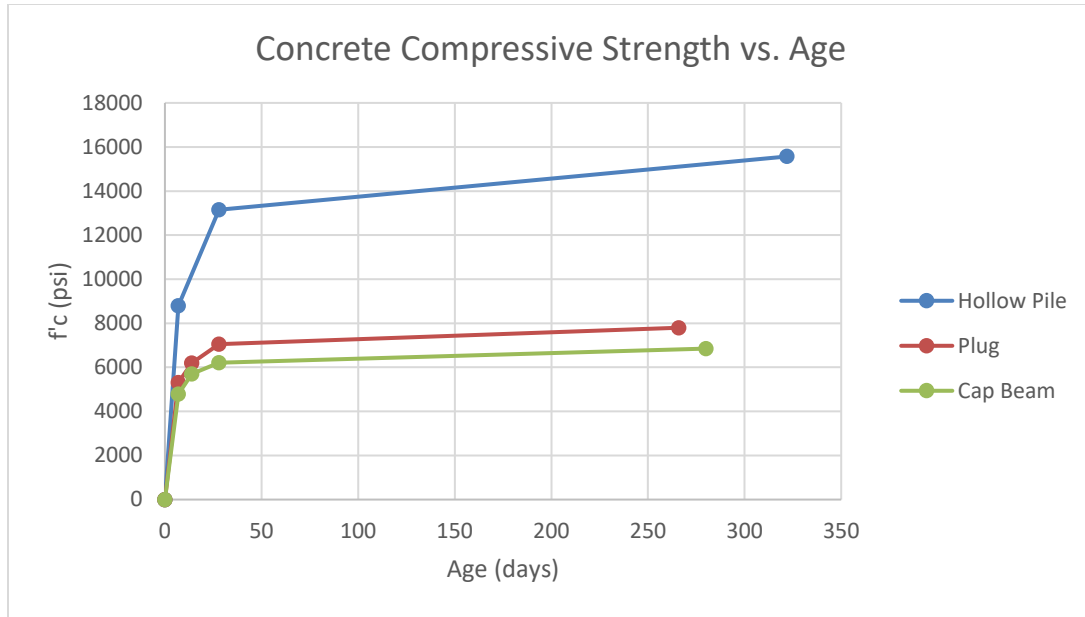
Figure 6-7. Concrete compressive strength for pile-column

The concrete strength was likely higher than that used in the structures built using this method in the 1960s. However, the pile-column concrete used for this test was constrained by the fact that the column specimens were cast horizontally using a fixed sonotube form to create the void, and an SCC mix was required to permit consolidation of the concrete without a mechanical vibrator. The pile-columns made in the 1960s were made with a movable steel mandrel, allowing the use of conventional concrete rather than SCC, which was not available at the time.

Table 6-7. Plug reinforcement yield and ultimate stresses (ksi)

f_y	f_u
66.5 ksi	94.0 ksi

84
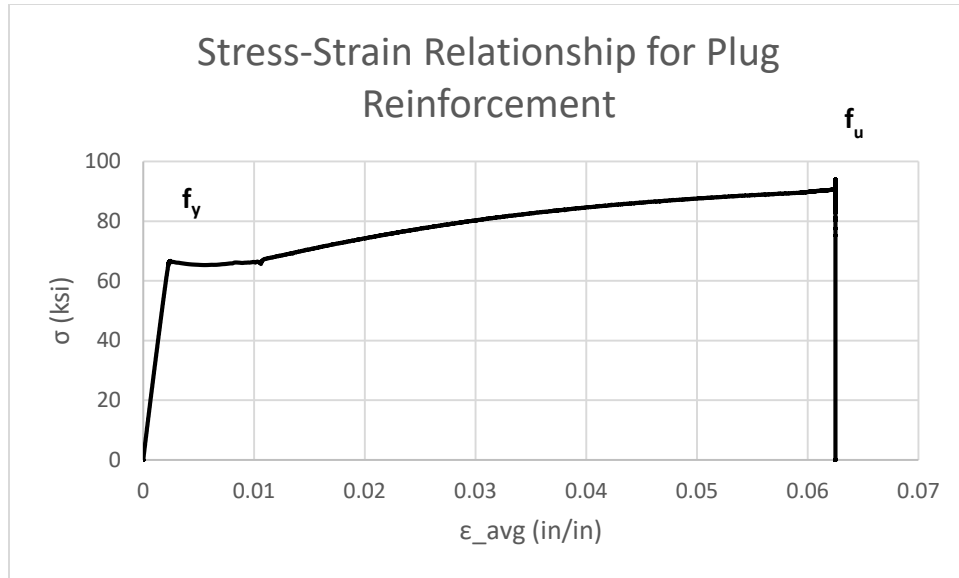
Figure 6-8. Stress-strain relationship for plug reinforcement

The sudden drop after the reinforcement reached its ultimate stress is caused by the bar fracturing. No material testing was conducted on the prestressing strand as it remained elastic throughout the test. Yield and ultimate stress values for the prestressing strand used for analysis were provided by Concrete Technology Corporation.

6.4 SPECIMEN CONSTRUCTION

The precast, prestressed hollow core pile-columns were constructed at Concrete Technology Corporation's facility in Tacoma, Washington. Construction of the specimens was described in Section 3.4. In order to create an inner surface roughness similar to what may have been caused by mandrel-casting used in the past, especially in the region where the plug would be cast, a retarder (Euro-Tard 05) was applied to the surface of the sonotube before casting. When the sonotube was later removed, this gave the inner surface a sandblasted roughness (see Figure 6-9). After the columns were cast in a line, the strands were cut flush when the concrete had obtained a compressive strength of at least 5,000 psi although cylinder tests indicate strengths greater than 6,500 psi in all cases.

85

Figure 6-9. Comparison of surface roughness after removal of sonotube, with and without retardant

The remainder of each specimen was constructed in the Structural Research Laboratory at the University of Washington. To remove the need for the construction of temporary shoring in the lab, the specimens were constructed and tested upside down so that the columns were connected to the cap beams while the cap beams rested on the floor. In this regard, the construction sequence did not follow what was done in the field where the cap beam forms were supported on the upright piles and poured after the piles had been placed and driven.

Firstly, the cap beam formwork was constructed using sheets of 0.75-inch thick CDX plywood sheathing and SPF 2x4 Premium #2 & Better Grade Kiln dried studs (see Figure 6-10).
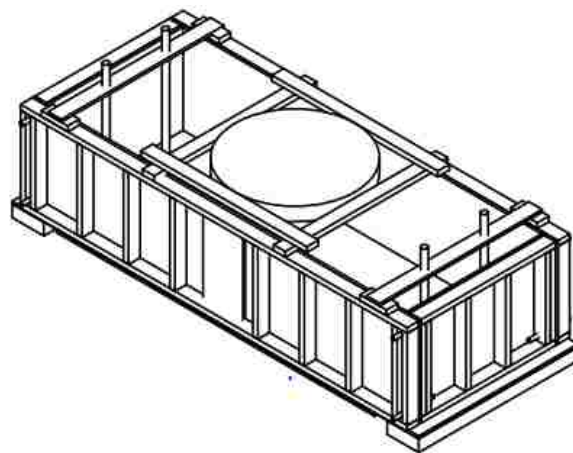
Figure 6-10. Isometric view of cap beam formwork

86

The cap beam reinforcement cage, including the plug reinforcement, was fabricated outside of the formwork and then positioned into the beam form (see Figure 6-11).

Figure 6-11. Reinforcement cage for cap beam being lifted into formwork for casting

PVC pipes were then placed to create the necessary voids for 1.25-inch diameter threaded anchor rods that would anchor the specimen to the reaction block of the test frame. The cap beam was cast-in-place, leaving a small 1-inch deep circular recess at the top in order to grout the pile-column into place and model the field conditions where the pile-columns were embedded approximately 2 inches into the cap beam. This void was achieved using a 5-inch wide plywood ring around the plug reinforcement (see Figure 6-12).

Figure 6-12. Cap beam and plug reinforcement in formwork before casting

Prior to the as-built test in December 2018, the cap beam reinforcement was inadvertently flipped upside down (i.e. top bars on bottom and vice versa). To fix this, the cap beam was externally prestressed before testing using two 1.75-inch diameter Williams Form Engineering All-Thread high strength steel bars loaded to 90 kips each (see Figure 6-13). Even with the prestressing however, joint shear cracks were still seen during the test (Tardieu 2018). For this reason, the same prestressing arrangement was used during the retrofit test, even though the primary reinforcement was in this case correctly placed.
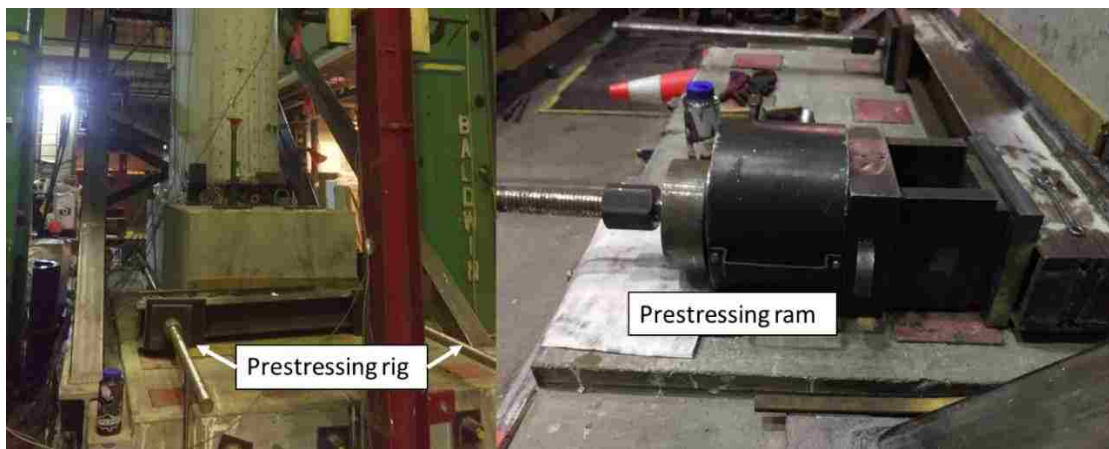
Figure 6-13. External prestressing to increase moment capacity of cap beam

Before erecting the pile-column onto the cap beam, an epoxy mortar paste was applied to the roughened region to once again imitate conditions of the field pile-columns as indicated by the drawings (see Figure 6-14).

Figure 6-14. Inner surface of pile-column roughened with epoxy mortar

To set the column in place, the precast, prestressed hollow pile-column was lifted using the laboratory crane, lowered over the plug bars, and centered on the cap beam. The pile-column was placed on timber shims to allow grout to flow underneath the bottom face and was grouted around its base so that it would be seated correctly on the cap beam. A timber bracing system was built to hold the column in place so that the plug could be cast (see Figure 6-15). A concrete truck was brought in to pour the inner plug through the top of the column. Since the plug was cast using a bucket and funnel over the top of the column (see Figure 6-16), it was difficult to ensure that the exact length of plug was poured and as such, the plug ended up being 48 inches long which was longer than specified.

Figure 6-15. Pile-column braced on top of cap beam

Figure 6-16. Casting plug inside of pile-column

The CFRP jackets were made of Tyfo® SCH-41-2X Composite using Tyfo® S Epoxy and were applied to the specimens following standard wet layup procedures developed by FYFE® Co. LLC (http://www.aegion.com/about/our-brands/fyfe). The CFRP jackets were applied by Combined Construction out of Seattle, Washington; the specimen was jacketed by applying the jackets

www.manaraa.com

directly to the pipe wall (see Figure 6-17) in two layers. The final CFRP wrapped region was five feet long, with two 2-foot wide double layers followed by one 1-foot wide double layer.

Figure 6-17. CFRP application: sanding concrete (top left), base epoxy (top right), first layer of CFRP (bottom left), finished epoxy (bottom right)

6.5 TEST SETUP

A cyclic test was performed on the as-built and retrofit model specimens using a self-reacting test frame with a 220-kip horizontal actuator. The setup was identical for both the as-built and retrofit test. The frame worked in conjunction with a Baldwin Universal Testing Machine to apply both lateral and axial loads to the column. The Baldwin machine applied a 200-kip gravity load while the 220-kip capacity actuator applied cyclic lateral load, using displacement control, to simulate earthquake effects (see Figure 6-18).

To set up the experiment, after the full specimen was constructed as described in the previous section, it was moved and installed under the Baldwin machine on top of the self-reacting base block. It was leveled and grouted into place using a very thin layer of hydrostone under the base so that the column was vertical under the head of the test machine.
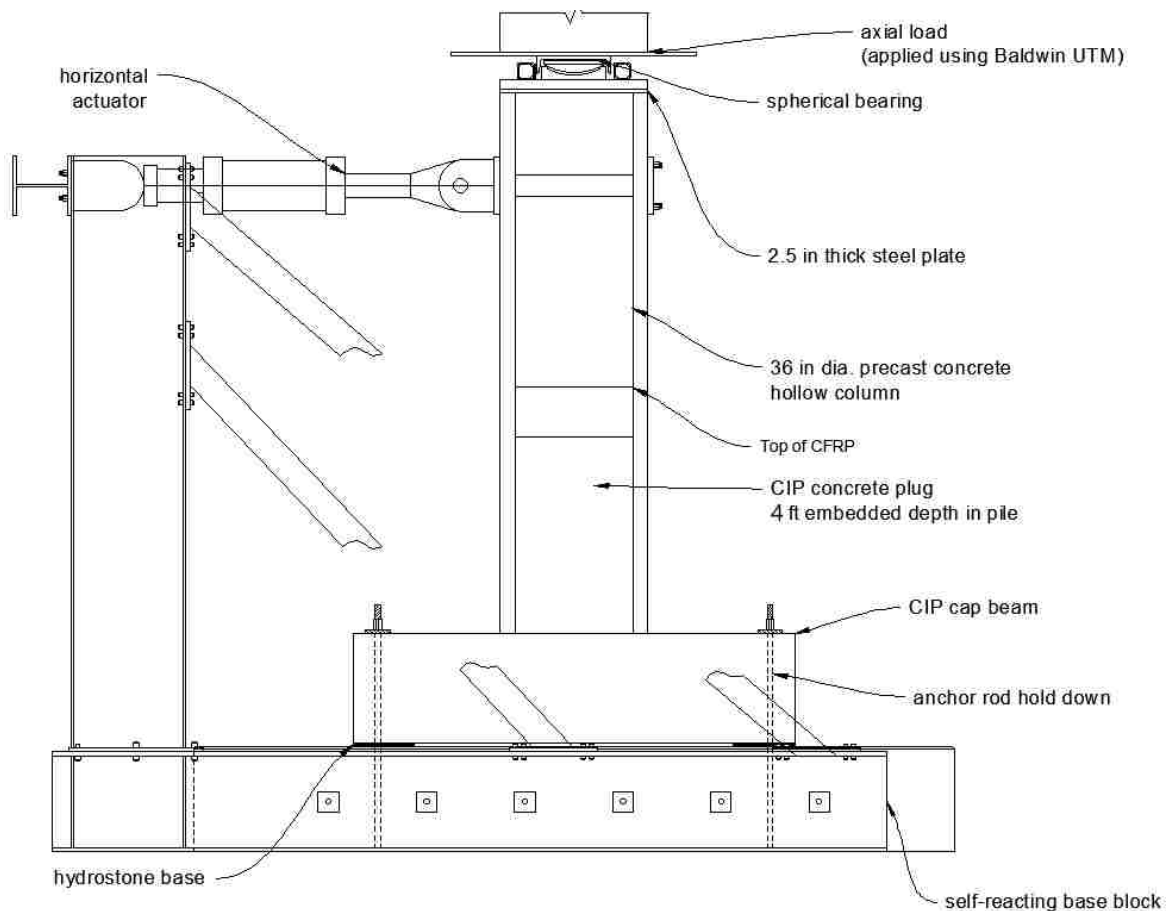
Figure 6-18. Test setup with specimen

91

6.5.1 *Test Equipment*

The specimen was anchored to the self-reacting base block using 1.25-inch Williams Form Engineering All-Thread high strength steel bars post-tensioned to 85 kips each and placed 96 inches apart in the longitudinal direction and 18 inches apart in the transverse direction. This ensured that the specimen was rigidly attached to the concrete anchor block and no sliding or uplift of the cap beam occurred during testing.

The actuator was connected to the specimen using four 1-inch diameter high-strength steel threaded rods and two steel plates (1 inch thick) with timber and steel shims and thin rubber pads to protect the concrete wall (see Figure 8-4). The timber shims were machined to conform to the outside circumference of the column. On the interior of the specimen, a precast concrete diaphragm was grouted in place between the rods to eliminate the possibility of punching shear through the thin pile-column walls by the applied lateral load (see Figure 6-19).

Figure 6-19. Concrete diaphragm to prevent punching shear (temporary wood formwork)

The pile-column axial load was applied using the Baldwin load head and simulated a pin connection through the use of a spherical bearing, a Teflon surface and a channel track (see Figure 6-20). The spherical bearing allowed for rotation of the specimen under the lateral load while keeping the axial load constant. The top surface of the spherical bearing had a recessed Maurer Sliding Material (MSM) pad that bore against the inner web of the channel that was lined with silicon greased stainless steel to create a low friction sliding surface. The outer surface of the channel flanges was also lined with silicone greased stainless steel that bore against rectangular HSS tubes, lined with Teflon strips, to create a low friction sliding track. These HSS pieces were welded to a 2-inch thick steel plate that was placed on top of the column to evenly distribute the load to the pile-column wall. The channel was fixed to the bottom of the Baldwin head using four high strength threaded rods to prevent out-of-plane movement. It is worth noting that the spherical bearing arrangement was exactly as described above during the as-built test (Tardieu 2018), but some slight alterations were made before the retrofit test, the implications of which are discussed in Section 7.3.1. The HSS pieces were cut to allow the larger anticipated rotation, the welds on the HSS were redone, and the PTFE and stainless steel pieces were replaced.
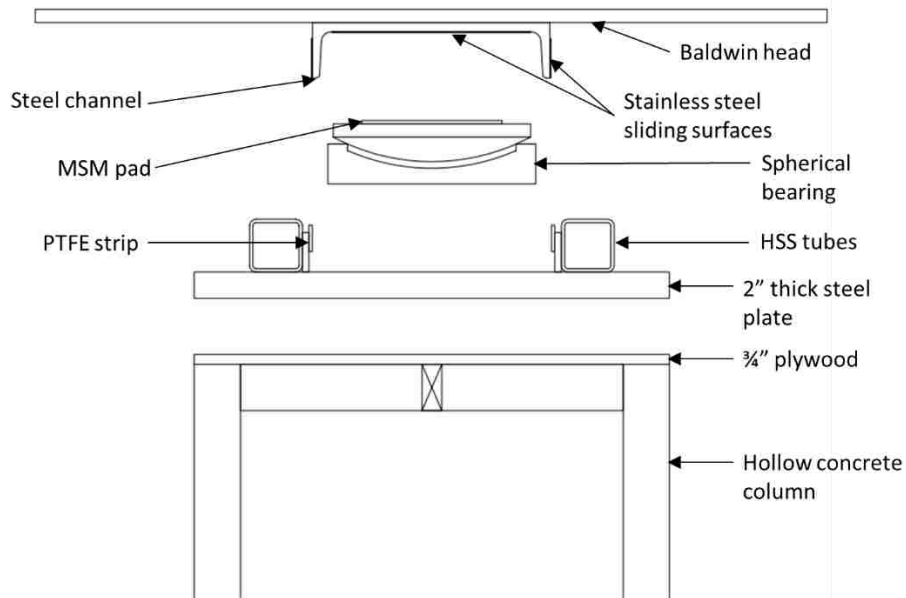
Figure 6-20. Spherical bearing with low friction sliding surface

6.5.2 *Testing Protocol*

A 200-kip axial load was applied to the specimen using the 2400-kip Baldwin Universal Testing Machine. This load was chosen to represent approximately the average axial stress in the four field bridges considered (see Table 6-8). The gravity loads were calculated from the weight of the superstructure including girders, traffic barriers, cap beam and diaphragms acting over the tributary width of each pile-column. The concrete stress due to prestressing is also given. It is higher in the test specimens than the average of the field bridges because the pile-columns were ordered before a detailed evaluation of the prestress losses had been completed. However, the total compressive stress on the concrete is representative of field conditions.

Table 6-8. Gravity load stress for reference bridges

Bridge	Column load	Column dia.	Column area	Axial stress	Prestress (effective)
	(kip)	(in)	(in^2)	(ksi)	(ksi)
Ravenna	428	48	675	-0.637	-0.769
Galer/Lakeview	299	478	675	-0.448	-0.856
LeLine (Slide)	407	54	770	-0.832	-0.757
Green RIver	633	54	770	-0.533	-1.117
Field avg.				**-0.609**	**-0.875**
Test	200	36	363	-0.551	-1.210

A displacement-controlled lateral cyclic history was employed, whereby a benchmark first yield deformation was predicted using a moment-curvature analysis of the pile-column strength (see Table 6-9). The displacement history was designed according to the nominal displacement of the actuator and the target drifts are calculated using a height of 109 inches. A series of three cycles at an elastic displacement level were chosen, followed by three cycles at the predicted yield displacement. Following this, cycles at post-yield displacements that increased by multiples between 1.25 and 1.5 were chosen until the rotation capacity allowed by the test setup was achieved which is in accordance with ACI ITG/T1.1-99's suggested test method. The exception to this was that the 3 series were done at an increase of 20% or less in order to try to capture the failure drift more accurately at the higher inelastic drifts. The displacement sequence is illustrated in Figure 6-21.

Table 6-9. Displacement history

Series	Purpose	MTS disp (in)	N cycles	Target drift (%)	Ratio Increase
0	Instrument	0.25	1	0.20	-
1	Elastic	0.5	3	0.46	2
2	predicted yield	1.0	3	0.93	2
3	post-yield	1.5	3	1.38	1.5
4		2.0	3	1.83	1.333
5		3.0	3	2.75	1.5
6		4.0	3	3.70	1.333
7		5.0	3	4.59	1.25
8		6.0	3	5.50	1.2
9		7.0	3	6.42	1.167
10		8.0	3	7.34	1.143
11	rig limit	9.0	1	8.26	1.125
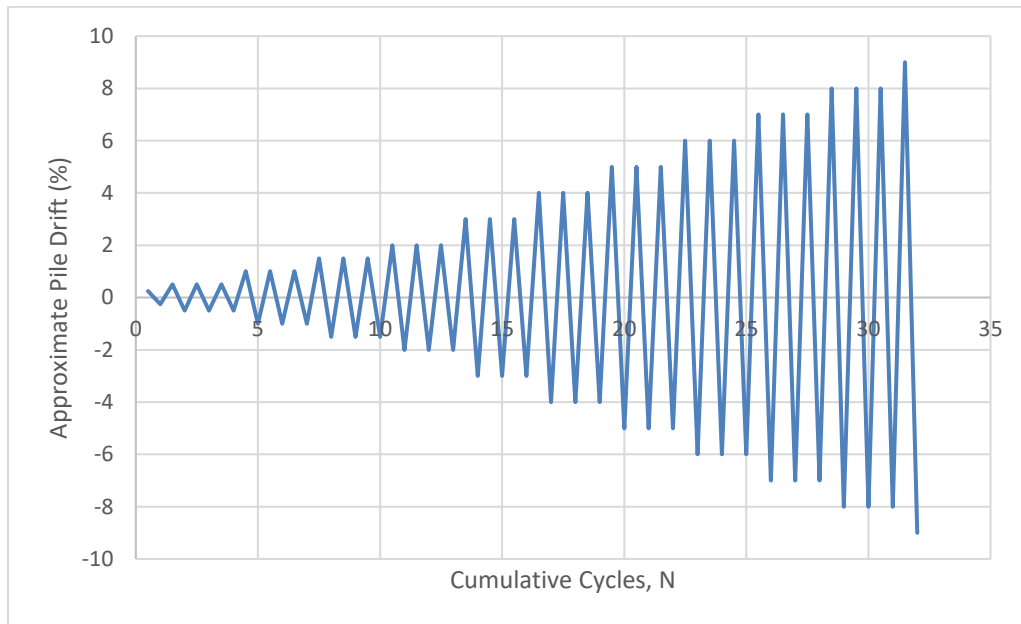
Figure 6-21. Displacement history

6.5.3 *Testing Procedure*

During testing the axial load was first applied with the specimen in the neutral position and then this load was held "constant" throughout the remainder of the experiment. Because the top of the specimen rises and falls during the lateral motion, the vertical load had to be adjusted continuously by the control software of the Baldwin Testing Machine. The load was thus maintained constant

95

within ±8 kips. Following this, the displacement history as shown in Figure 6-21 was implemented.

The lateral load sequence consisted of 11 series, with each series consisting of 3 cycles each at a nominal displacement. The nominal displacement for each series was defined as the maximum absolute displacement of the horizontal actuator during each cycle. This displacement was always greater than that of the specimen because of deformations in the testing rig as well as compression of the connections between the actuator and the specimen. This issue is discussed in more detail in Section 8.28-2. A single cycle was defined as moving from zero displacement, travelling to the nominal displacement in both the positive and negative directions (south then north) and then returning to zero displacement.

The first two cycles of each series were typically performed without stopping in order to collect instrument data without interruption. During the third cycle, the specimen was pulled to the south (positive direction) to the desired nominal displacement and was held there so the research team could inspect for cracks, mark them in a red color on the specimen, and take photographs. The specimen was then pushed to the north (negative direction), testing was paused, and the crack inspection and documentation repeated, this time in a black color. The specimen was then returned to zero displacement and the next series started.

6.6 INSTRUMENTATION

Instrumentation for the test comprised of strain gages (10mm and 90mm), linear potentiometers, string potentiometers, inclinometers and an Optotrak motion capture system (see Figure 6-22 - Figure 6-25). All instruments were recorded using computer-controlled data acquisition systems.

Loads were measured using the internal load cells of the Baldwin machine and the MTS horizontal actuator. Additionally, the displacement stroke of the horizontal actuator was measured by its own LVDT and this was used to track the nominal displacement for each series.

Strain gages (10mm gage length) were used to measure the strains of the plug reinforcement, while 90mm gages were used to monitor the strain in the CFRP (see Figure 6-22). The plug

96

reinforcement strain gages were placed on the east and west sides of four separate bars (one each in the north, south, east, and west faces of the specimen) in order to only measure axial bar strains. Gages were placed at 3 inches and 9 inches above the cap beam on all four bars, and at 15 inches above the cap beam on the north and south bars. This meant that the strain gages were placed in the region that would allow understanding of the behavior within the expected plastic hinge. The strain gages on the CFRP jacket were placed at heights of 6 inches, 18 inches, and 48 inches above the cap beam on all four sides of the specimen. More gages were placed closer to the cap beam connection as more hoop strain was expected in this region.
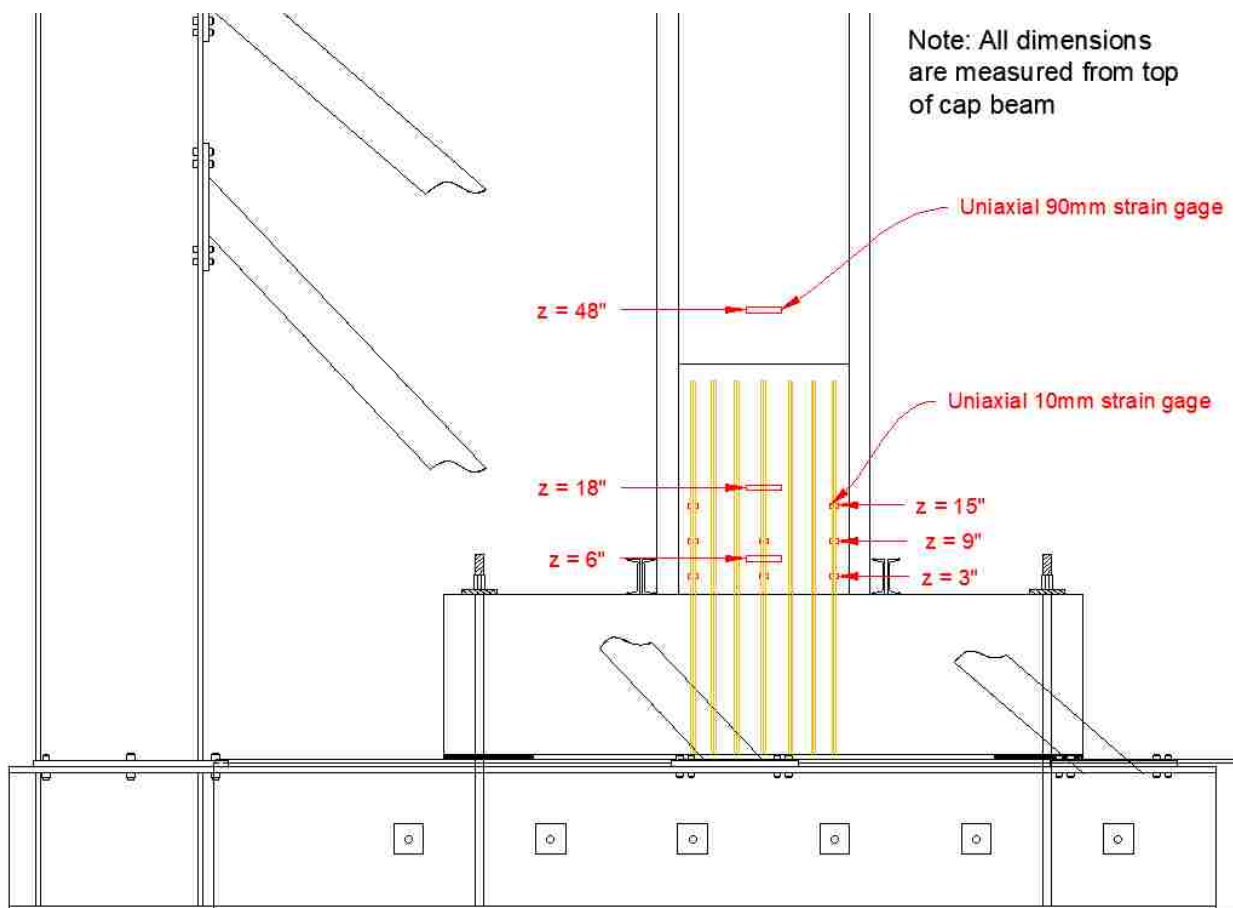
Figure 6-22. Strain gage locations on specimen

Displacements were measured using two types of potentiometers (see Figure 6-23). Short-stroke linear Duncan potentiometers were used to monitor any uplift or slip of the cap beam. String potentiometers are capable of measuring a large range of displacements (typically 10 – 20 inches maximum) and these were used to measure the lateral displacement of the pile-column at five

97

discrete locations along its height, including at the height of the actuator where the load was directly applied (see Figure 6-23). The string potentiometers were attached using thin steel wire to a fixed reference tower at the north of the test rig in order to ensure independent, global measurements were recorded. The displacements measured using the string potentiometers allow for the development of a displaced profile of the pile-column and to determine the rigid body rotation of the pile-column.
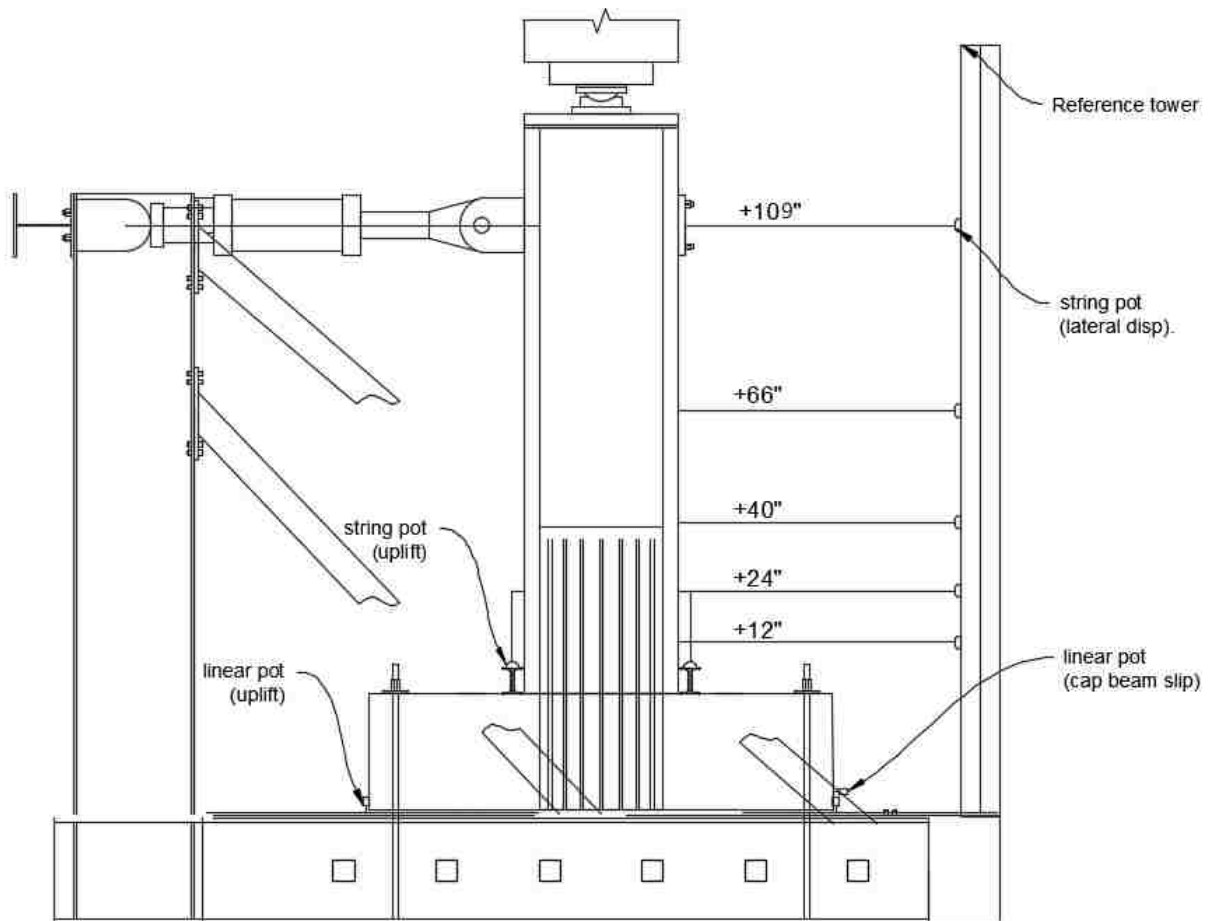
Figure 6-23. String pot and linear pot locations used for testing (numbers signify how far from cap beam interface the instrument was placed)

These rotations were also measured by inclinometers along the height of the pile-column on its east and west sides as shown in Figure 6-24. String pots were also used to measure the vertical displacement of the pile-column in the case of any crushing or uplift at the base and these were placed on the north and south side of the pile-column using heavy steel pieces to set them on the

98

base (see Figure 6-23, string pot (uplift)). Linear Duncan potentiometers were used to measure both slip and uplift of the cap beam relative to the surface of the reaction frame; however, after testing it was found that it would have been more beneficial to measure the uplift of the reaction frame relative to the lab floor (discussed in Section 8.2).
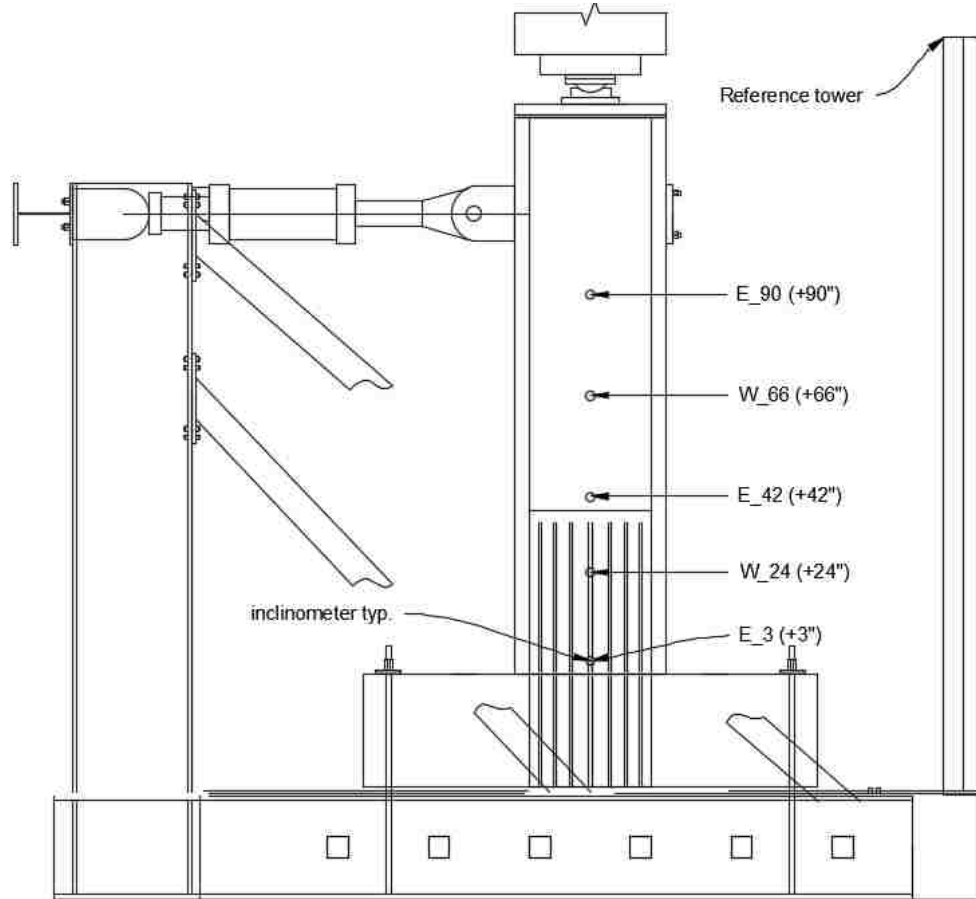
Figure 6-24. Location of inclinometers to measure rotation (E-East face, W-West face)

Lastly, an Optotrak Certus motion capture system was used to measure the deformations in the north-west quadrant of the specimen in the region of the inner plug (see Figure 6-25). The Optotrak system consists of a 3-dimensional optical sensor (camera) and a series of LED markers arranged in a pre-determined grid system. The system records the 3-dimensional position of each marker with respect to the camera's own coordinate system. From these position measurements, deformations of the pile-column wall can be calculated, in particular, shear and vertical deformations.

99

Figure 6-25. Optotrak marker grid on northwest face of specimen. Markers are all placed on CFRP within the plug region

Chapter 7. COLUMN CANTILEVER BENDING TEST RESULTS

This section will discuss the results observed during the test that was conducted on July 12th, 2019 at the University of Washington Structural Research Laboratory. It contains descriptions of the visual damage that was observed and a summary of the local and global behavior that was recorded from the instrumentation. Analysis of the data is provided in Chapter 8.

7.1 GENERAL

Table 7-1 compares the target drift values for each series and the actual drift levels that were achieved during testing; the results will be reported in terms of the actual values. The drift ratio is calculated as the ratio between the horizontal displacement at the point of load application and the distance to the point of load application from the cap beams surface, which was 109 inches. The actual drift levels were lower than the target drift levels in all cases due to the deformations of the testing rig and compression of packing in the connections on the actuator; this issue is discussed in detail in Section 8-2. The reference coordinate system is defined in Figure 7-1.

Table 7-1. Target drift levels and actual drift levels achieved

S	Target Actuator Displacement (in)	Nominal Target Drift	South Cycles		North Cycles	
			Actual Drift	Peak Load (kips)	Actual Drift	Peak Load (kips)
1	0.5	0.0046	0.0032	92.49	-0.0045	-97.31
2	1.0	0.0092	0.0049	113.54	-0.0079	-123.80
3	1.5	0.0138	0.0078	131.93	-0.0120	-135.12
4	2.0	0.0183	0.0113	144.80	-0.0179	-144.91
5	3.0	0.0275	0.0182	156.52	-0.0269	-147.57
6	4.0	0.0370	0.0275	159.79	-0.0362	-148.15
7	5.0	0.0459	0.0371	161.50	-0.0454	-146.50
8	6.0	0.0550	0.0470	160.21	-0.0549	-145.44
9	7.0	0.0642	0.0564	158.36	-0.0639	-160.12
10	8.0	0.0734	0.0659	154.20	-0.0725	-139.51
11	9.0	0.0826	0.0809	115.97	-0.0400	-42.75
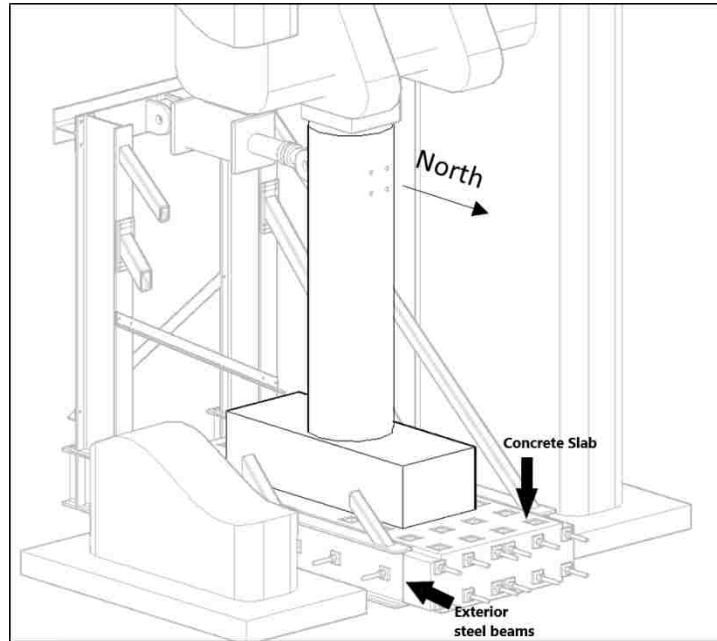
Figure 7-1. Coordinate system for results

Figure 7-2. Initial position of specimen

7.2 VISUAL OBSERVATIONS

In this section, the observed behavior is discussed. The major events and damage states are summarized in Table 7-2 and a sketch of the specimen, with dimensions, was provided in Figure 6-18.
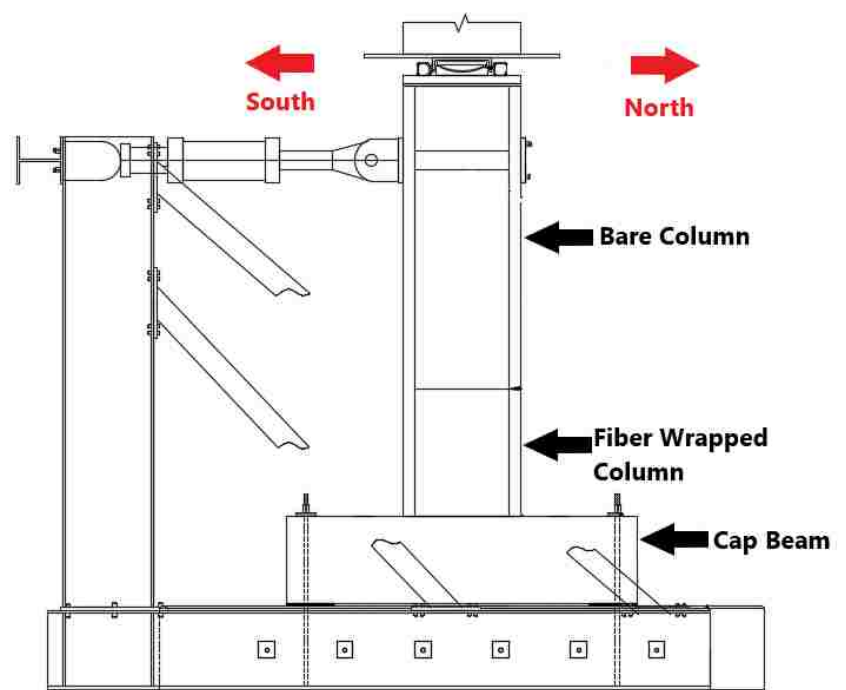
Figure 7-3. Test setup with labeled specimen components

Table 7-2. Summary of damage states and locations

CB	Cap Beam
FWC	Fiber Wrapped Column
BC	Bare Column

	Drift									
Damage State	0.45%	1.20%	1.79%	2.69%	3.62%	4.54%	5.49%	6.39%	7.25%	8.09%
First cracking	CB					BC				
First base uplift		FWC								
Fiber 'creaking'			FWC	FWC	FWC	FWC	FWC			
Extensive cracks							CB / BC			
Noticeable uplift							FWC	FWC	FWC	
Fiber split									FWC	
Fiber rupture										FWC

103

From the beginning of the test until Series 4 (+1.13%, -1.79% drift) there was relatively little action apart from progressive cap beam cracking due to joint shear (see Figure 7-5) and some creaking noises from the fiber wrap being strained. On Series 3 (+0.78%, -1.20% drift) however, the first uplift was detected at the base of the column (see Figure 7-4).

Figure 7-4. Uplift on Cycle 3 of Series 3 (+0.78%, -1.20% drift)
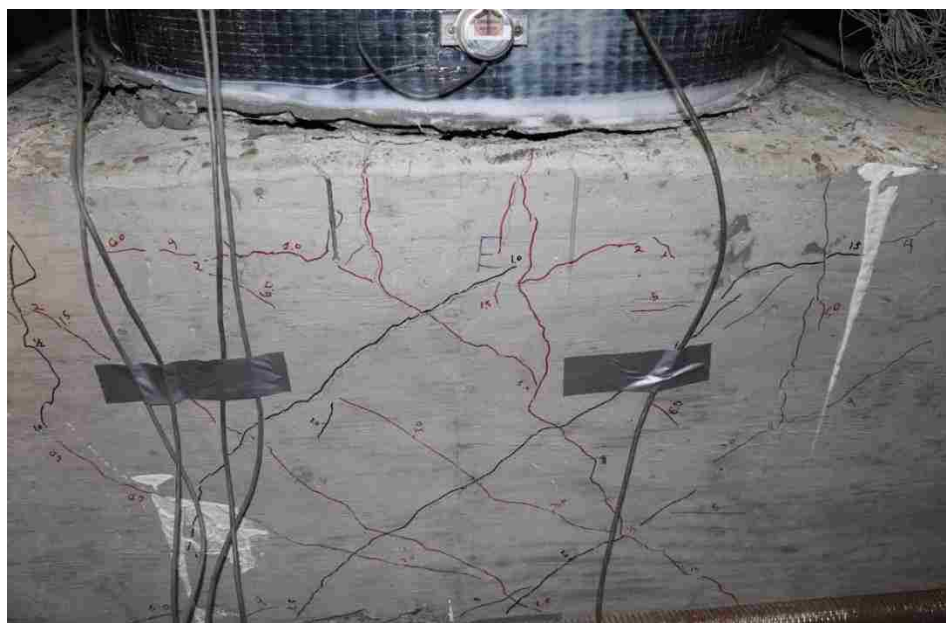
Figure 7-5. Progressive joint shear cracking on base beam on Series 8 (+4.70%, -5.49% drift)

104

At the start of Series 5 (+1.82%, -2.69% drift) a loud popping noise was heard, and the test was paused. After investigation it was concluded that the steel hold-down devices for the testing rig had jarred loose suddenly due to the uplift of the south end of the rig. The test was resumed, and the rig uplift was more closely monitored.

Vertical cracks were first observed above the fiber, on the east and west faces of the bare portion of the pile-column, during Cycle 3 of Series 7 (+3.71%, -4.54% drift, see Figure 7-6). In addition to cracking above the fiber, noticeable uplift was seen at the base, at the cap beam interface (see Figure 7-7). Further prodding with a steel rod gave reason to believe that the plug was staying put and the pile-column was "rocking" about the plug. In addition, the plug could not have experienced the uplift seen by the pile-column wall without fracturing the plug reinforcement. Progressive vertical cracks on the east and west faces were seen on Series 8 (+4.70%, -5.49% drift, see Figure 7-8).
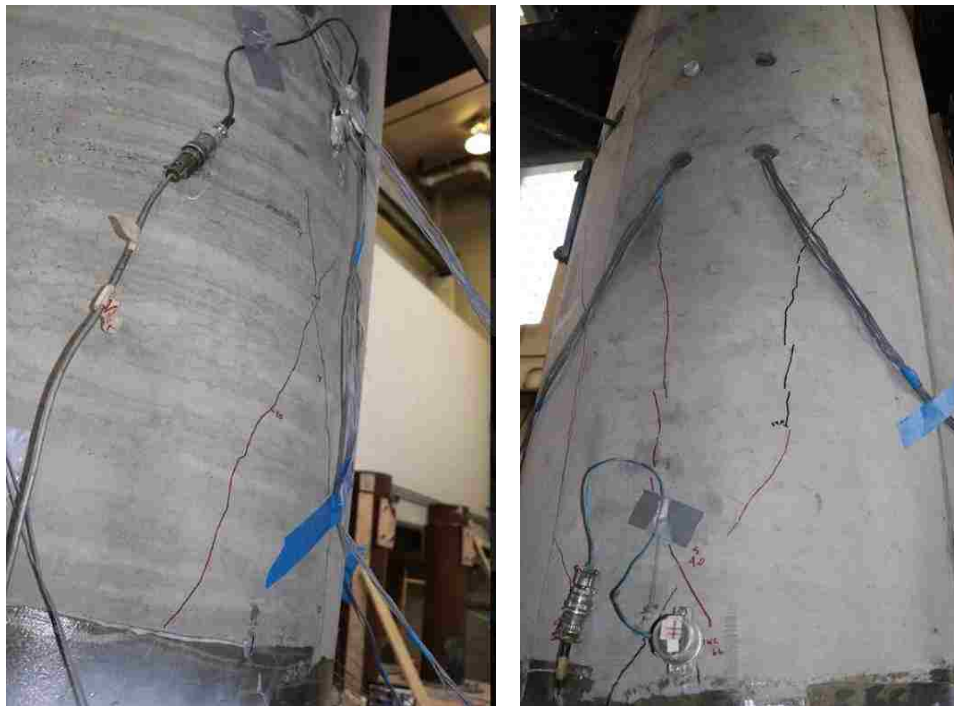
Figure 7-6. First cracks above fiber on east (left) and west (right) faces

Figure 7-7. Uplift on Cycle 3 of Series 7 (+3.71%, -4.54% drift)

Figure 7-8. Progressive cracking above fiber on Series 8 (+4.71%, -5.49%)

During Series 10 (+6.59%/-7.25% drift), when the specimen was pulled to the south, the fiber split horizontally on the north face (tension side) at a height of 35 inches above the cap beam. Splitting was also observed along a seam between two layers of fiber at a height of 24 inches above the cap beam (see Figure 7-10, Figure 7-11, and Figure 7-12). When the cycle was reversed and the specimen was pushed to the north, more splits in the fiber were observed on the south face, however they were less prominent (see Figure 7-13). It is worth noting that the plug reinforcement ends at a height of approximately 36 inches above the cap beam surface, so the main split formed at approximately the end of the plug bars. Figure 7-9 shows a sketch of the test specimen to identify where each fiber split occurred, where $z = 0$ (i.e. the reference datum) is the surface of the cap beam.
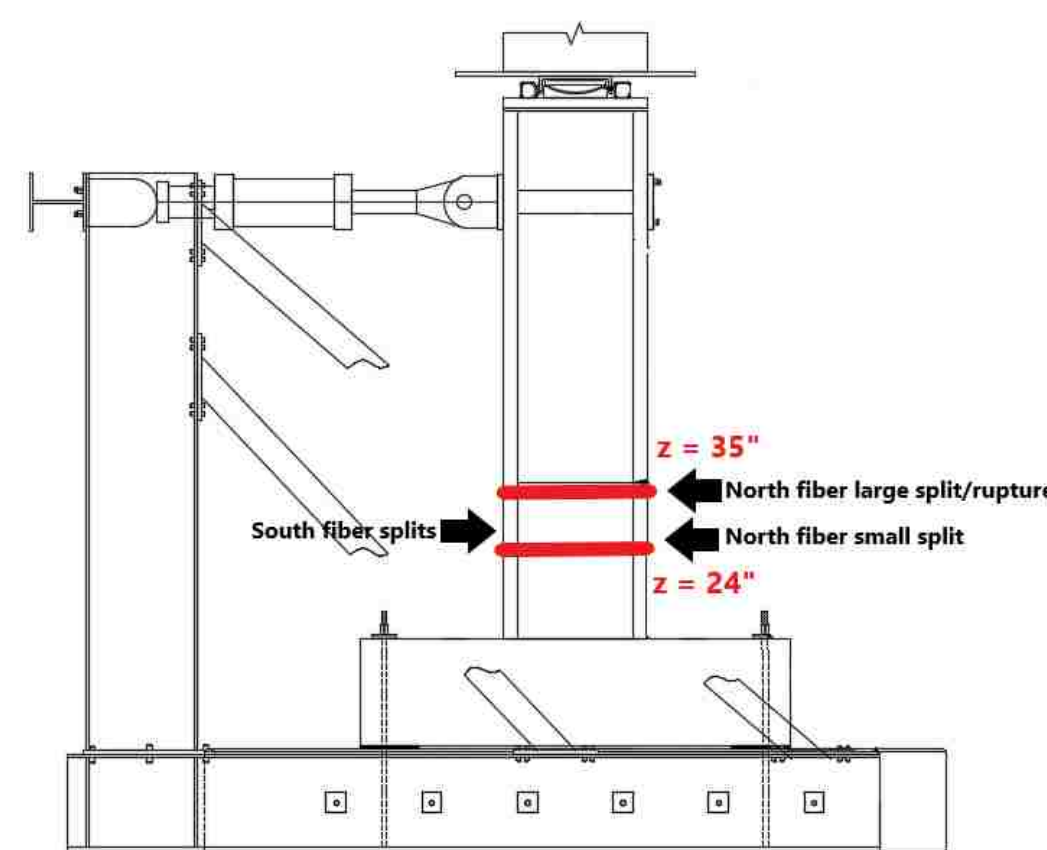
Figure 7-9. Fiber split locations
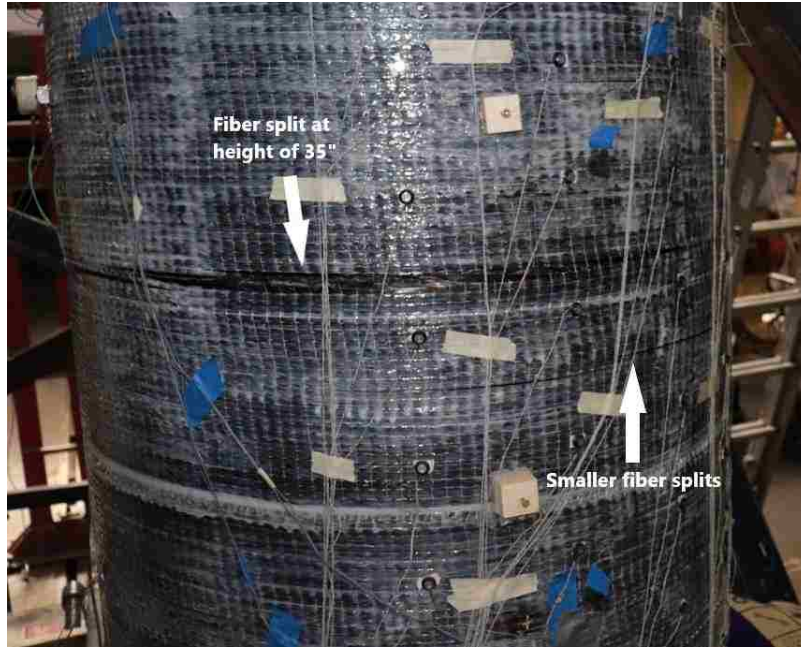
Figure 7-10. Fiber splitting on north face during Series 10

Figure 7-11. Close up view of split at 35-inches above cap beam

Figure 7-12. Close up view of split at 24-inches above cap beam

Figure 7-13. Fiber splitting on south face during Series 10

109

During the final series (Series 11) a drift ratio of +8.09% was reached when the specimen was pulled to the south; the north segment of the cycle could not be completed due to safety concerns. As the specimen moved south, the split in the fiber at a height of 35 inches widened into a rupture, exposing many buckled and fractured strands (see Figure 7-16). At no time during the test were signs of shear (i.e. diagonal tension) failure seen.

Figure 7-14. Fiber rupture on north face during Series 11

Figure 7-15. Widened fiber split on north face during Series 11

Figure 7-16. Buckled strand (left) and fractured strand (right)

Figure 7-17. Specimen position at +8.09% drift

This mode of failure was unexpected and needed to be evaluated in order to plan subsequent actions. For example, it was unclear whether the strand had slipped or yielded in tension to allow the split in the pile-column wall to open. After some deliberation, it was decided that the most probable sequence of events prior to failure was as follows:

- The pile-column wall cracked horizontally and the tension stress in the strand rose above its initial value, causing higher bond stresses and eventually slip, during specimen displacement to the south.
- On the next movement to the north, the split started to close and the strand experienced compression. It buckled before a compression force occurred that was high enough to force it to slip back to its original position.

- On the next half cycle to the south, the buckled strand re-straightened and again experienced tension stress. The re-straightening caused many wires to fracture, particularly those on the north face, however a few had not (see Figure 7-16)

It was thus important to determine whether the strand really had slipped. The goal was to get a look at the bottom face of the pile-column (i.e. the face at the cap beam interface) to confirm whether or not the strands had slipped. In order to do this, the top segment of pile-column above the fiber split needed to be removed (see Figure 7-18 and Figure 7-19). As Figure 7-18 shows, the crack that propagated from the fiber split was right at the top of the plug reinforcement and followed the path of the hooked reinforcement. In addition, there appears to be slip between the pile-column and the plug. The slip between the plug and the pile-column wall may provide some additional rotational capacity to that of the plug rotation if acting alone.

Figure 7-18. Looking down at plug reinforcement after top segment of specimen (portion above the plug in test orientation) had been removed

Figure 7-19. Top segment of specimen after detachment from plug connection to cap beam

After the pile-column was detached, two locations were selected whereby the fiber was cut along a vertical line, the pile-column concrete was jack hammered along that same line, and the spiral reinforcement was cut away. The pile-column wall was then pried away from the plug so that the bottom of the specimen (where it intersected with the cap beam) could be examined (see sequence in Figure 7-20).
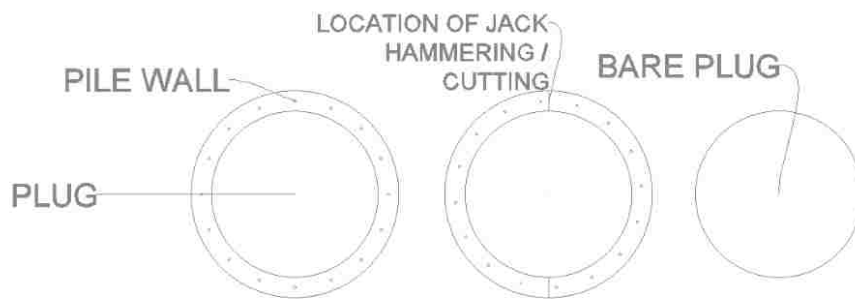
Figure 7-20. Sequence of wall detachment

The strands appeared to have slipped at least ¾-inch to 1 inch and, although some of the concrete was damaged when the pile-column wall was removed, it can be clearly seen that the strands slipped in multiple locations (see Figure 7-21 and Figure 7-22). Some cracks were also seen on the north and south faces of the plug (see Figure 7-24) and more evidence that the pile-column wall slipped at the epoxy between the pile and the plug arose (see Figure 7-25).

Figure 7-21. Strand slip at the base of the pile-column wall
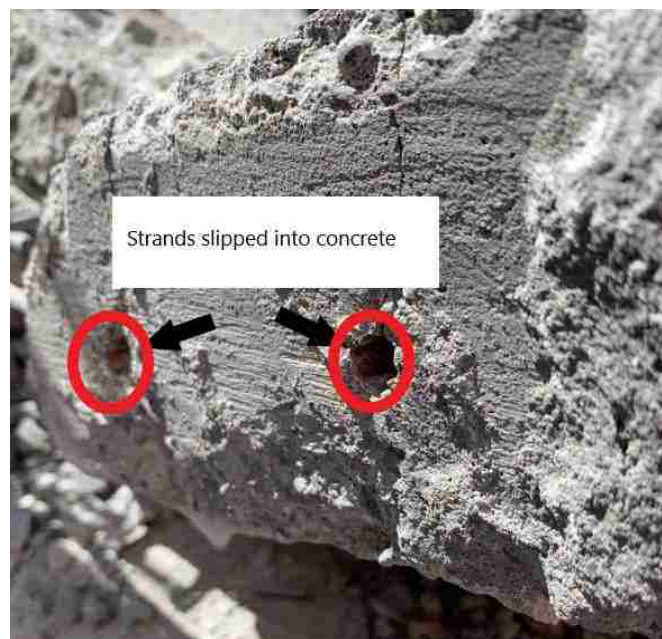
Figure 7-22. Slipped strands at base of pile-column wall

115

Figure 7-23. Measuring of the strand slip
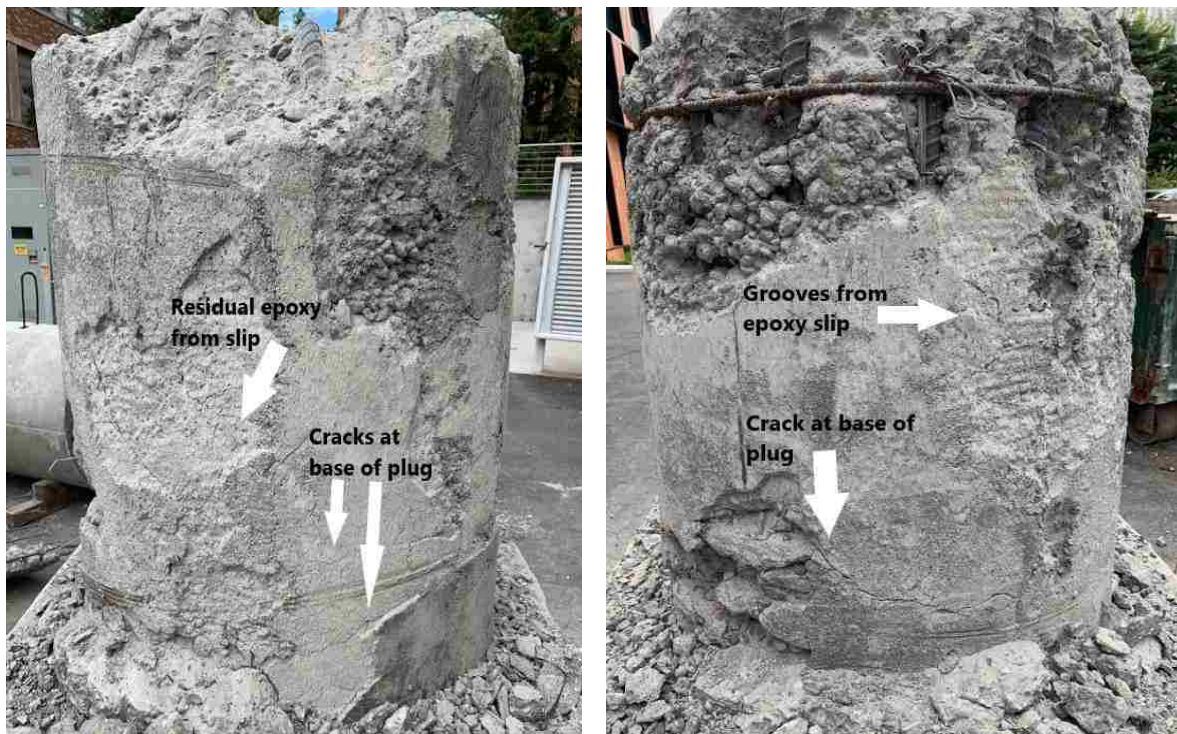
Figure 7-24. North (left) face and south (right) face of plug after pile-column wall detachment

116

Figure 7-25. Grooves from epoxy mortar where pile-column wall slipped

7.3 MEASURED RESULTS

The behavior of the specimen can be evaluated on a local and a global level. On a global scale, the hysteretic base moment vs. drift behavior and the hysteretic effective force vs. drift behavior is examined. On a local scale, the strains, deformations and rotations of various components are computed and analyzed. For all plots shown, positive behavior is defined as the specimen moving south and negative behavior is defined as the column moving north.

The effective force and base moment calculations are shown in Equations 11 and 12, with reference to Figure 7-26. The reference displacements were measured at the point of load application.
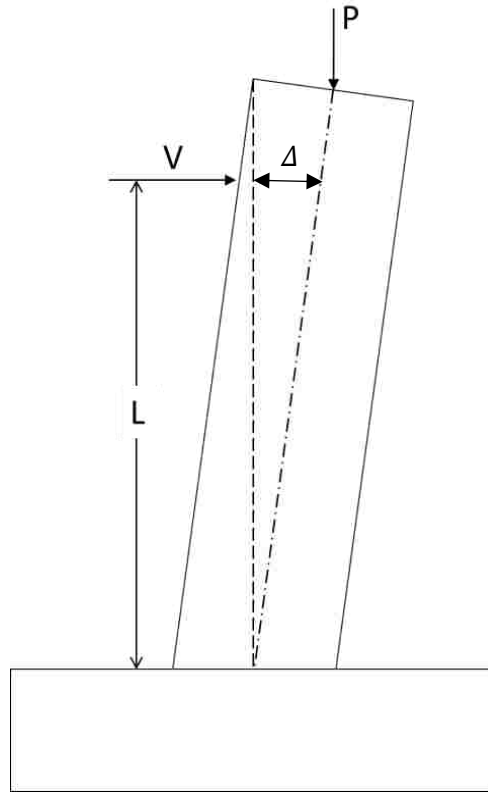
Figure 7-26. Effective force and base moment calculation details

$$V = V_{actuator} - P * (\mu_{eff}) \qquad (10)$$

$$M_b = V * L + P * \Delta \qquad (11)$$

$$F_{eff} = \frac{M_b}{L} \qquad (12)$$

V = Effective Horizontal Load applied by the Actuator

$V_{actuator}$ = Horizontal Load applied by the Actuator

P = Axial load applied by the Baldwin machine (Nominal Load = 200 kips)

μ_{eff} = Effective coefficient of friction (discussed in Appendix B)

M_b = Base moment (at column-cap beam interface)

L = Height from cap beam interface to horizontal load application point (109 inches)

Δ = Horizontal displacement of column, taken as the average of two string potentiometers at the horizontal load application point

F_{eff} = Effective Lateral Force

7.3.1 *Global Behavior*

The base moment vs. drift ratio hysteretic response is shown in

Figure 7-27, along with two backbone curves. For these purposes, the drift is defined as the displacement measured from the point of load application divided by the height above the cap beam (109 inches). That displacement is taken from the string potentiometers secured to the fixed reference columns on the north side, and implicitly assumes that the cap beam did not rock at all. This assumption was confirmed by the short stroke Duncan potentiometers on the cap beam. The first backbone curve is from the as-built test conducted in December 2018 (Tardieu 2018), while the second backbone curve is from the CFRP retrofit test, described here. The maximum base moment of 17,604 in-kip was achieved at a drift ratio of +3.71%, during the first Cycle of Series 6. The plot shows a jump in the negative moment region of consistent slope from a drift ratio of approximately -5% to just over -6%. The sudden strength increase was not expected by the research team; it is thought that the changes made to the spherical bearing assembly described in Section 6.5, combined with potential misalignments of the testing rig, likely caused this spike. If any two pieces of the assembly became lodged against one another at the end of the test, it would cause a spike in the MTS load. In addition, the drastic increase in stiffness at such a large drift is not typical of a prestressed concrete system such as this.
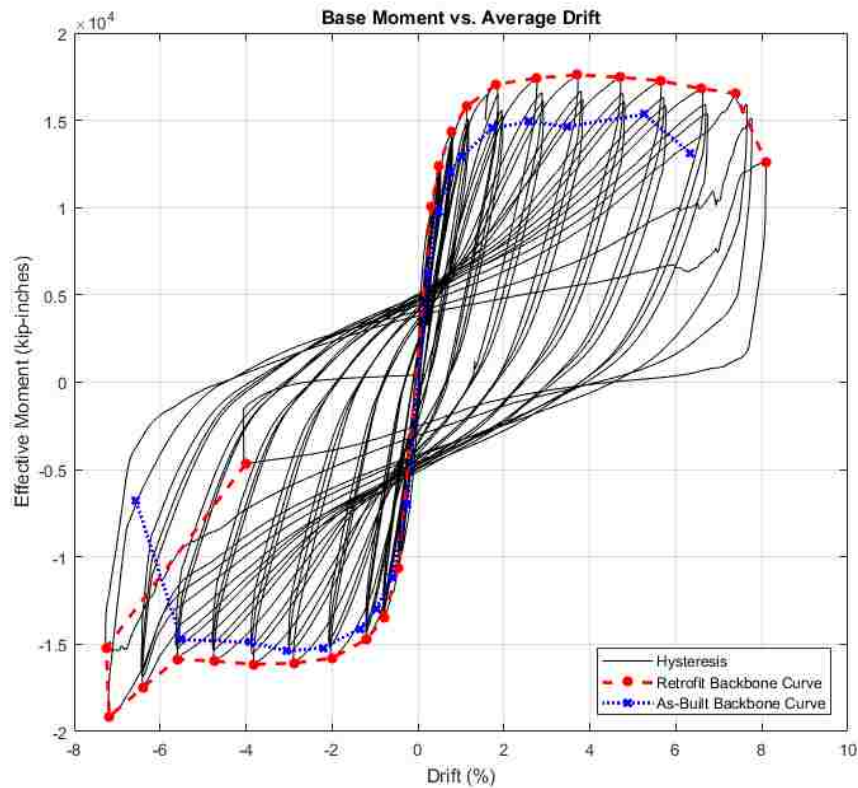
Figure 7-27. Base moment vs. average drift

The plot shows that in the negative direction (i.e. specimen moving north), the resistance was essentially identical between the as-built and the retrofit specimen, while in the positive direction the retrofit specimen was ~5-10% stronger. It is worth pointing out that the as-built test data did not initially take any friction at the spherical bearing into account, but was added in later. The friction was calculated to be approximately 5.4% of the total axial load (or 10.83 kips); the calculations are described in Appendix B. A further plausible explanation for the asymmetric response of the retrofitted specimen is that the plug bars may not have been exactly center in the pile-column during casting.
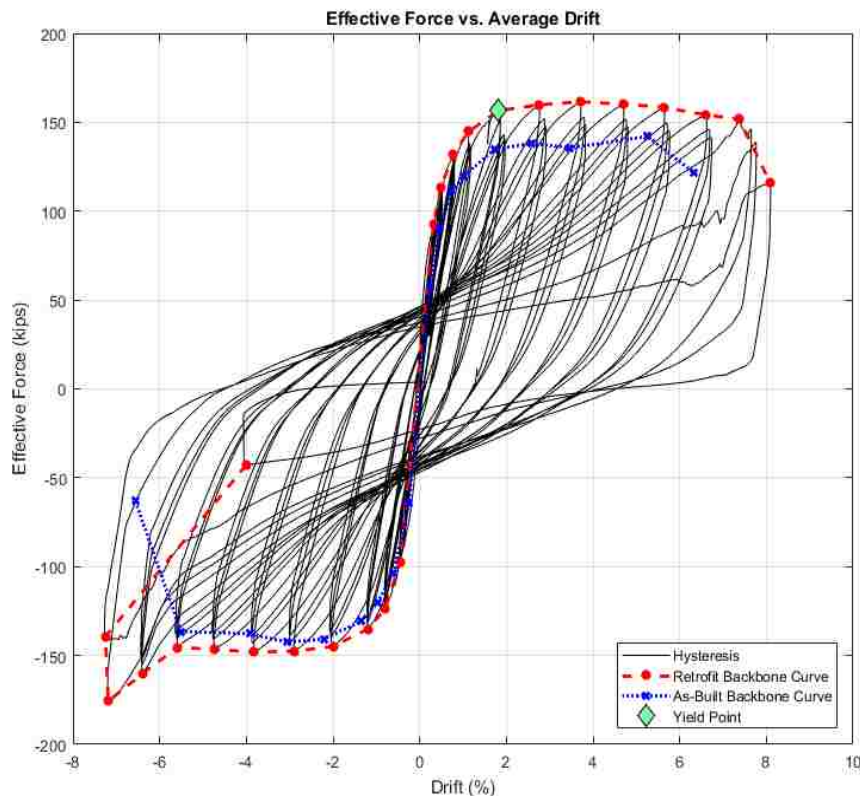
Figure 7-28. Effective force vs. average drift

Figure 7-28 shows the effective horizontal force vs. drift ratio, along with the backbone curve identifying the peak forces associated with each loading series for both the as-built and retrofit specimens. From the backbone curve, it can be seen that past a drift ratio of about 2%, the force in the retrofitted specimen remained roughly constant throughout the test at about 160 kips,

120

indicating very little strength degradation until failure. It is clear that the retrofit only had a negligible influence on strength.

7.3.2   *Local Behavior*

Horizontal string potentiometers were placed at various heights on the specimen to characterize the motion under cyclic loading, while strain gages were used to monitor the status of the longitudinal plug reinforcement as well as measure the circumferential strain in the fiber wrap. To see the locations of these instruments, please refer to Figure 6-23 and Figure 6-22, respectively. The specimen appeared to experience largely rigid body motion, with all of the rotation being concentrated to the plug region, throughout the experiment until the fiber split open and the pile-column began rotating about the location of the split. The local behavior of the column will be separated into three components: pile-column bending deformations, plug behavior, and pile-column hoop strains.

7.3.2.1   *Pile-Column bending deformations*

Figure 7-29 shows the total displacement measured at the point of load application by the horizontal string pots and the proportional displacement from rigid body rotation, as measured by the vertical string pots, which were attached at 24 inches above the cap beam (Equations 13 and 14).

$$\theta_{base} = \frac{\Delta v_{north} - \Delta v_{south}}{B} \qquad (13)$$

$$\Delta_{rot} = \theta_{base} * L \qquad (14)$$

θ_{base} = rotation at base
Δ_{vnorth} = vertical displacement on north side of column
Δ_{vsouth} = vertical displacement on south side of column
B = distance between point of measurements of vertical string pots
Δ_{rot} = displacement from rigid body rotation
L = Height from cap beam interface to horizontal load application point (108 inches)

121
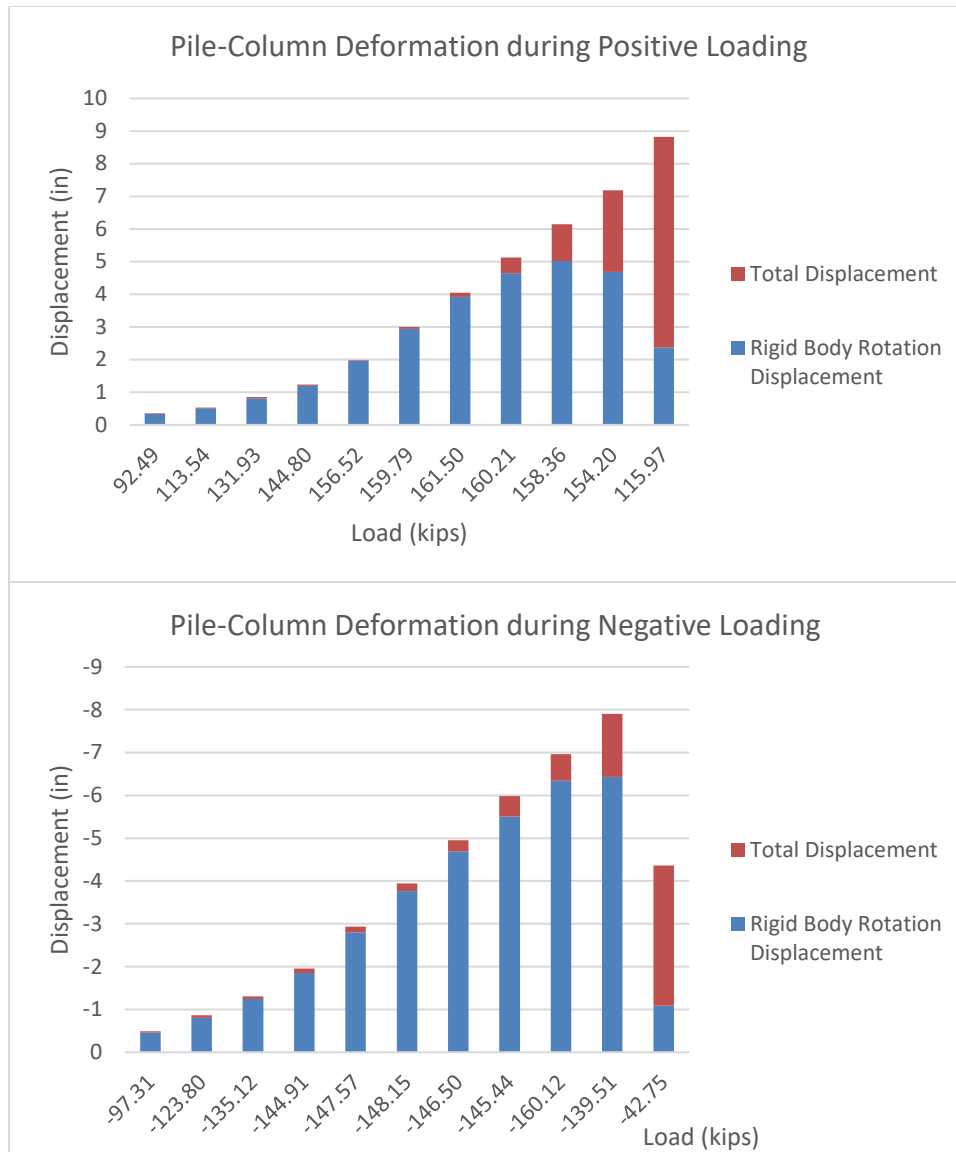
Figure 7-29. Difference between total displacement and rigid body displacement

The displacement from base rotation is a measure of the rigid body motion of the pile-column while the difference indicates any local pile-column bending deformations. From Figure 7-29, it can be seen that the majority of the pile-column displacement is due to rigid body motion throughout the experiment until Series 10. This is consistent with the observation that the specimen appeared to be "rocking" about the plug connection until Series 10, when the fiber split open at a height of 35 inches. Prior to the fiber splitting, rigid body motion accounted for between 90% and 96% of the total displacement, as can be seen in Figure 7-29. Once the fiber split the pile-column began hinging about that point, progressively widening the split.

An additional component of the local behavior of the pile-column to assess is whether the pile-column experienced any shear deformations. This can be determined by comparing the rotations measured due to horizontal displacement to those due to vertical displacements. If the pile-column underwent any shear deformations there would be no difference between the vertical displacements measured on either side of the specimen, and therefore zero rotation, since the horizontal displacement would be due to pure sliding (See Figure 7-30). By contrast, if there are no shear deformations the horizontal displacement would be a result of rotation at the base and both rotations measured from horizontal and vertical displacements would be equal (See Figure 7-30).
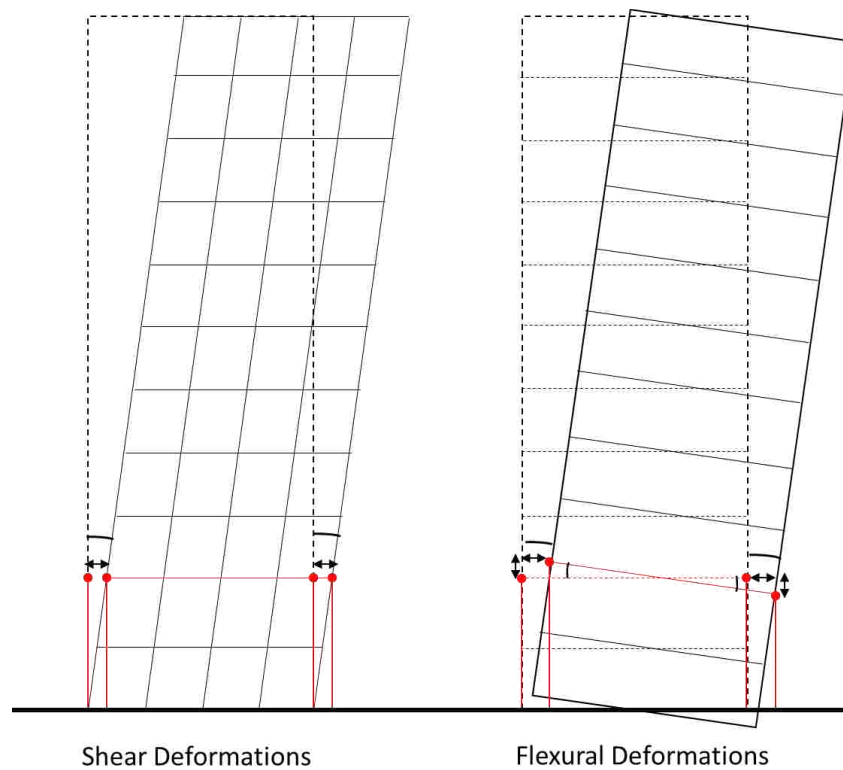
Figure 7-30. Shear vs. flexural deformations due to pile-column displacement

Figure 7-31 shows the rotations measured from 3 different instruments at the same height along the pile-column (24 inches). As can be seen, the rotations measured and calculated from each instrument are very similar at the peak loads of all series indicating that the pile-column did not deform in shear and confirming a flexural failure. This evidence is supported by the visual observation that no inclined shear cracks were seen. The elastic, uncracked shear strain at peak

123

load was calculated and corresponds to an approximate displacement of 0.05 in, or 0.00044 drift. This is too small to be distinguished from the other sources of displacement.
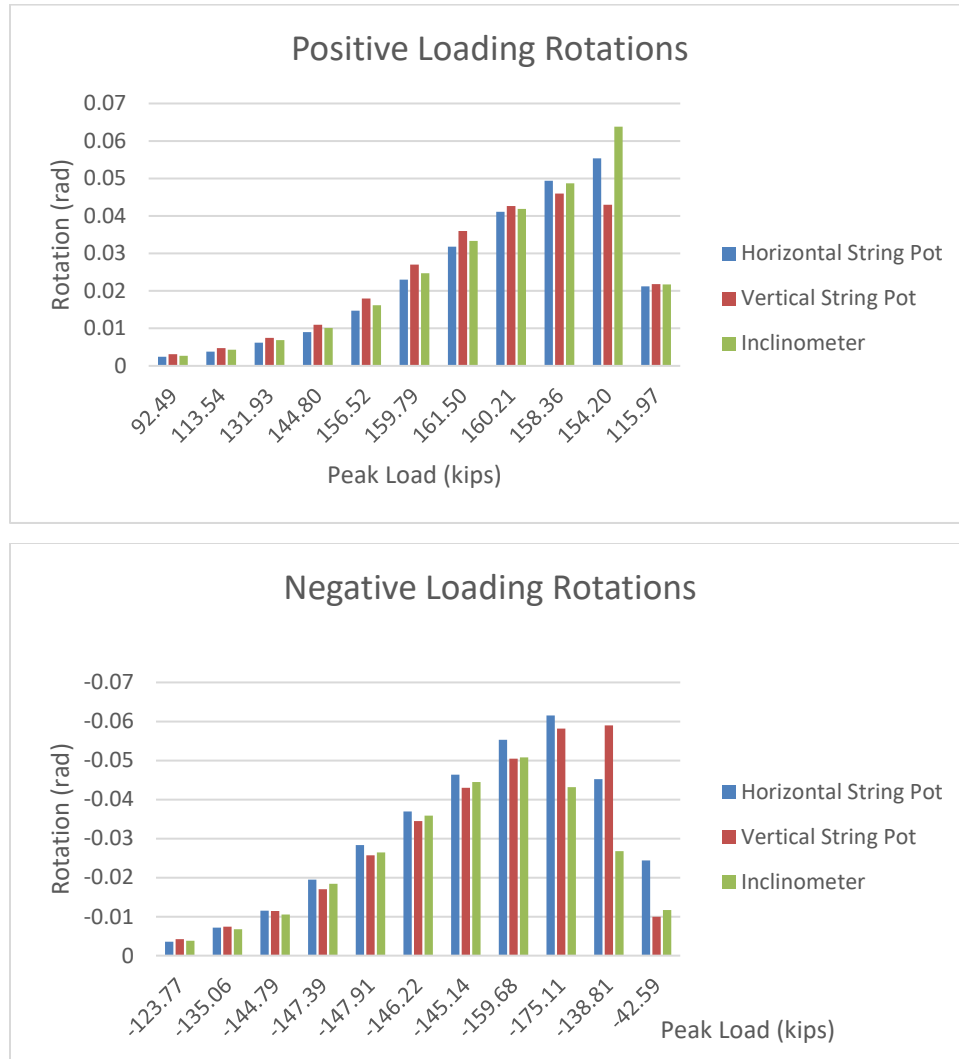
Figure 7-31. Rotations due to vertical and horizontal displacement of pile-column

7.3.2.2   *Plug behavior*

Figure 7-32 shows the longitudinal reinforcement strains recorded at the peak displacement during the first cycle of each loading series, for the four bars that were monitored. The gages were placed on both the east and west faces of the reinforcement at each height specified in the previous

124

chapter; the strains shown are the average of the measurements acquired from the pair of gages at the various locations along each bar.
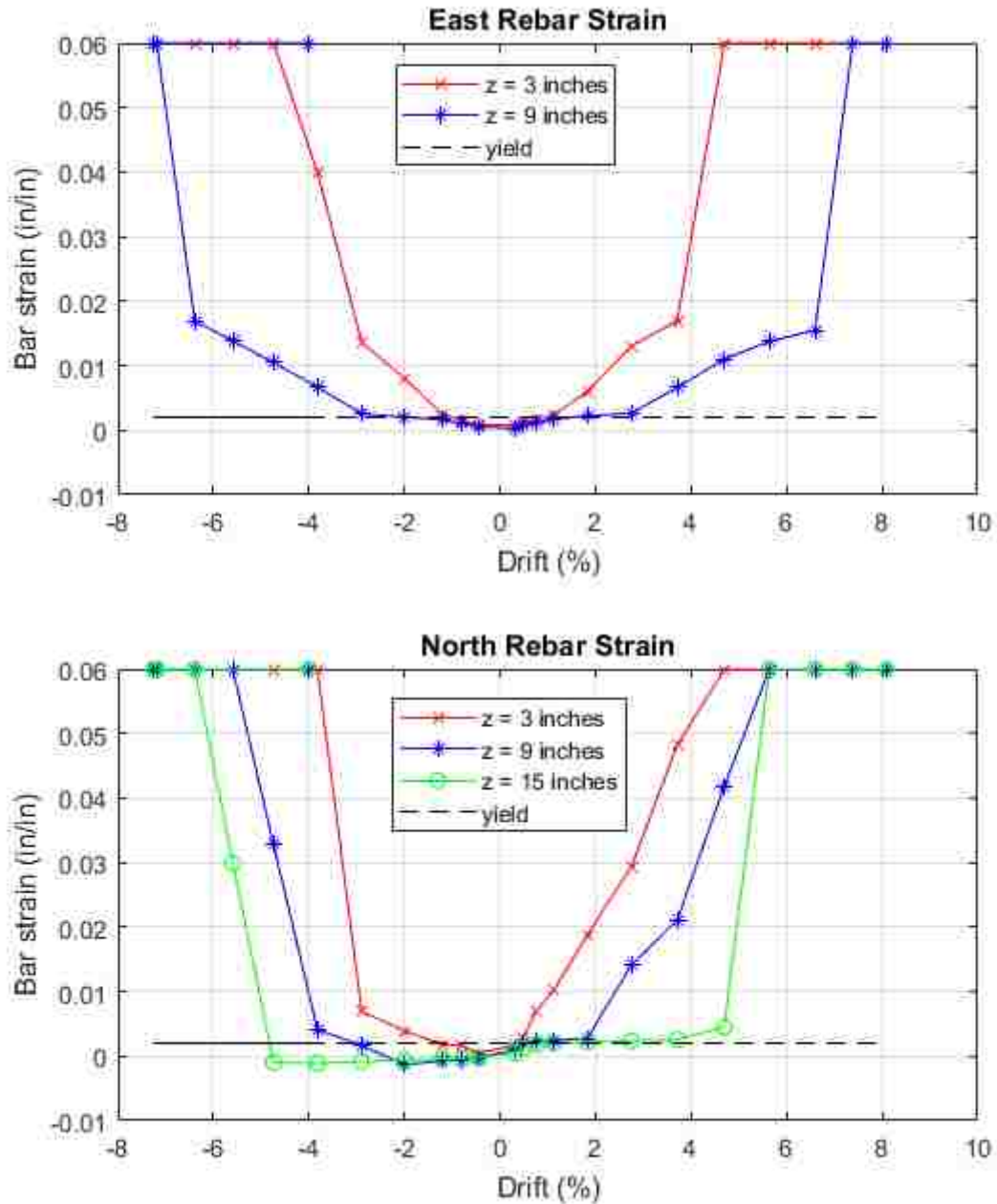
Figure 7-32. Plug reinforcement strains at peak drifts on Cycle 1 for all Series.

Some initial conclusions can be drawn from the plots. First, the north and south plug bars yielded earlier than the east and west bars (+/- 0.5% drift compared to +/- 1% drift), which is consistent with significant decrease in slope (i.e. a loss in stiffness) with reference to the force-displacement backbone curve (See Figure 7-28). Second, higher gages (i.e. at z = 9" or z = 15") on the north and south bars show compressive strain where one would expect to see it. For example, when the specimen is being pulled south (i.e. positive drift), the higher gages on the south plug reinforcement show compressive strain. Lastly, up until approximately 6% drift all of the plots show a strain gradient (i.e. a change in strain), indicating that the concrete remained confined and maintained its bond to the strands. The extent to which this was achieved by the spiral or the fiber jacket is unknown.

7.3.2.3   *Pile-Column hoop strains*

Figure 7-33 shows the hoop strain in the CFRP wrap vs. drift, measured on all four sides of the column at three different heights corresponding to the peak drifts pertaining to the first cycle of each loading series. Focusing on the north and south hoop strain plots, it can be seen that the strains increase more rapidly on the north fiber at positive drifts (i.e. when the specimen is being pulled south) and vice versa. This graph indicates that the measured hoop strains at the base of the column did not exceed a strain of $1000\mu\varepsilon$ until approximately + or – 2% drift. It is also worth noting that the strains on the east and west faces were consistently smaller than those on the north and south faces, and that the strains measured at a height of 48-inches were smaller on all faces. This is consistent with the observations above that the specimen largely exhibited rigid body rotation; if the specimen is rotating as a rigid body, then the hoop strains at lower heights will be larger than the hoop strains at higher heights. If the Young's modulus of the fiber is taken to be 36,000 ksi (Tyfo), the stresses in the fiber at this drift level are around 36 ksi (or a lateral confining stress in the concrete of 400 psi). This level of confinement indicates an increase in axial strength of 4.1*400 = 1640 psi (ACI 318), which is only about 10% of f'_c, and thus of low significance.

126
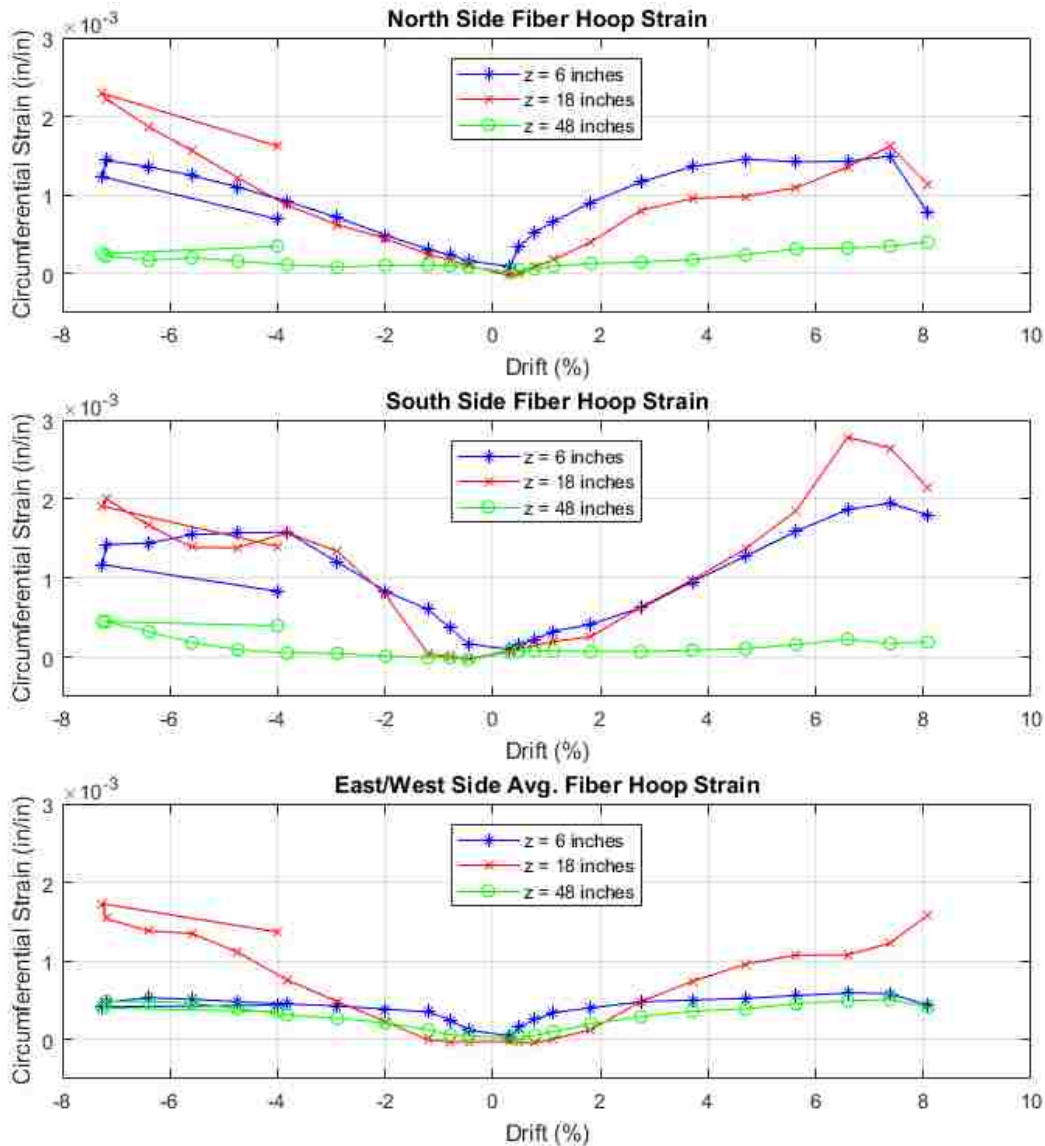
Figure 7-33. Hoop strains on all four pile-column faces at different heights

In addition, the fiber strains on all four specimen faces at $z = 6$ inches and $z = 18$ inches were plotted against each other at four drift levels to see how the strains varied around the circumference of the pile-column (See Figure 7-34). The plot shows that the south face of the fiber exhibited higher strains at negative drifts (i.e. the specimen being pushed north) and vice versa, as expected. In addition, it shows that the east face of the fiber wrap consistently had the lowest strain regardless of the drift level. The west face of the fiber appeared to take some of the demand from the north and south faces when the drifts got higher, possibly indicating some local slip around the column.

127
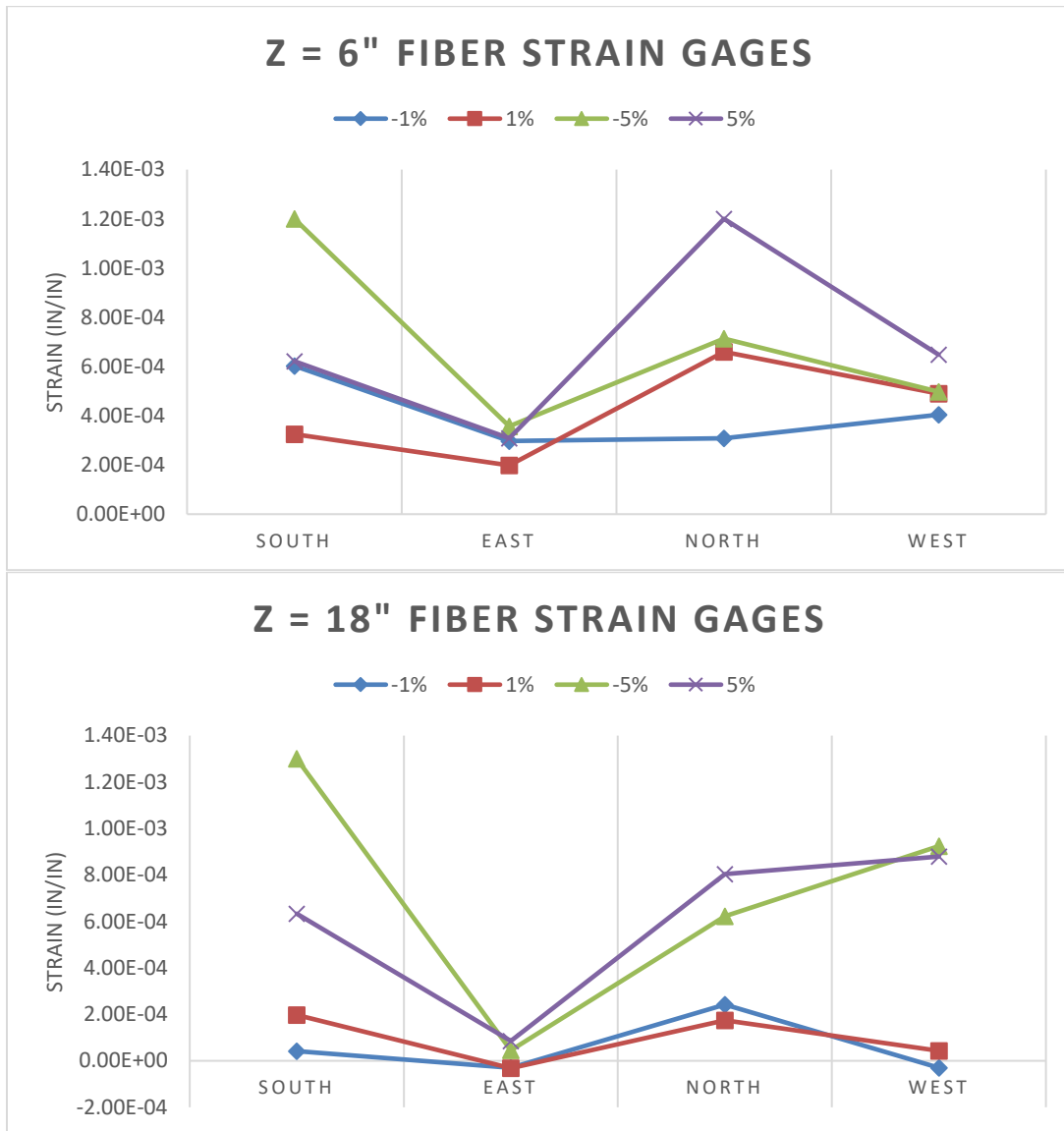
Figure 7-34. Hoop strains along pile-column circumference at z = 6 inches and z = 18 inches

Chapter 8. COLUMN CANTILEVER BENDING TEST ANALYSIS

8.1   GENERAL

The cantilever bending test described in Chapters 6 and 7 was done to understand the response of the retrofitted specimen to seismic loads. The results of that test are analyzed in this chapter. First, the deformations of the testing rig, and their effect on the measured results are evaluated. Then the observed and measured behaviors are analyzed with the goal of identifying the underlying mechanics, so that the lessons learned can be applied to field pile-columns.

8.2   RIG DEFORMATIONS

During the cantilever bending test the self-reacting testing rig experienced larger base moments than had been applied in any previous test. The specimen was tall enough that the actuator needed to be placed at the maximum height that the rig could accommodate. This, combined with the high transverse actuator load that was achieved, placed large bending moments on the testing rig and caused individual elements on the rig to deform. In order to truly understand the specimen behavior, the testing rig deformations first need to be examined. The testing rig deformations were measured by a horizontal string potentiometer spanning from the actuator's support beam to a reference column that was bolted to the floor.

The nature of the deformations was unclear at the time of testing, but when rig deformations were visible to the naked eye, an additional displacement sensor (a mechanical dial gage) was added to measure the uplift from the floor. The following discussions is based on the available measurements and analysis of the loading rig.

In all, four separate forms of rig deformations were identified. The list is not exhaustive, but serves both to shed additional light on these tests and to inform future research using the same rig. The modes are:
* Slip between the steel base beams and the concrete base slab.
* Deformation in the north-south plane of the base beams, columns, and diagonal braces, caused by strains in the elements.

129

- Deformation of the east-west spanning crossbeam that supports the actuator. These deformations include both bending of the beam and deformation of the connections.
- Deformations of the connection between the actuator swivel and the test specimen.

These deformations are described and analyzed in turn.

8.2.1 *Slip between the base beams and the concrete base slab*

The rig base consists of a concrete slab, approximately 13 feet long x 6.67 feet wide x 21 inches thick, which is connected to two steel beams (W24x94) as shown in Figure 7-1. The connection is made by six high strength bars that pass transversely through the slab and webs of the beams. They are stressed together, creating a clamping force between the concrete and the steel, thereby allowing friction to resist any slip between the two elements. The rods are 1.25-inch diameter Williams bars, with f_u = 150 ksi. The exact level of stress in the rods is unknown, but is believed to lie in the range of 100 to 150 kips (max of 75 ksi).

When the horizontal actuator is in tension (i.e. pulling the specimen to the south), the force causes the concrete base to slip to the south and to rotate (clockwise as seen from the west side). If the bars were stressed to too low of a level, those two motions would be readily visible; however, the bar stress was, in fact, high enough to suppress that movement. Furthermore, any such motion is limited by shear in the bars when they come into contact with the edge of the duct in which they are installed, and, for the rotation, by the concrete coming into contact with the flange of the steel base beams. That contact and reversal was observed during the test.

The foregoing displacements represent rigid body motions. They would have no effect on the forces in the system, but they would cause the sensors measuring displacement to record the real deformation of the pile-column plus those of the rig. So the measured pile-column drifts would be larger than the true drifts. It is believed that no horizontal slip occurred, and that any rigid body rotation was also very small compared with the drift angle of the specimen, if for no other reason that the fact that the clearance between the concrete slab and steel beam flanges was on the order of ¾-inch. That, coupled with the slab length of 156-inches, limits the rotation angle to 0.005 radians. However, it is believed that some slip occurred in the end rods (and particularly the one at the south end), and that that slip interacted with the deformations of the steel. The

130

result would be overestimation of the pile-column drift. That interaction is discussed in the next section.

8.2.2 *In-plane deformation of the steel rig*

Each of the two rig frames experiences loading at two locations: the horizontal north-south reactions from the crossbeam supporting the actuator, and a moment and horizontal shear transferred from the concrete base slab by friction. These are illustrated in Figure 8-1.
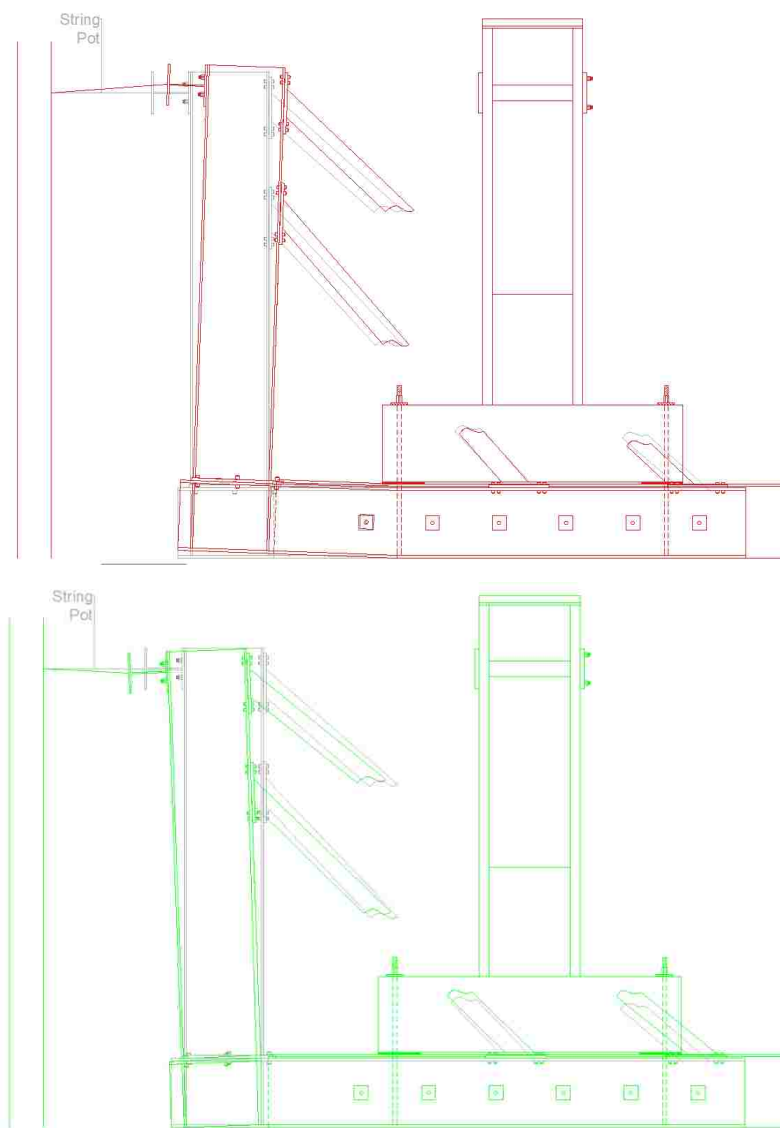
Figure 8-1. **Top**: rig uplift at south end caused by vertical force in rig columns; **Bottom:** elongation of rig diagonal braces

131

When the specimen is pulled to the south, an upward vertical reaction force is experienced by the columns of the testing rig (W24x94) when the diagonal braces try to shorten. The section of the base beams that "overhang" (i.e. is not held to the slab by friction from the Williams rods) then act essentially as a cantilever beam loaded vertically. When the columns have an upward reaction (i.e. tensile), the base beams lift off of the lab floor. By contrast, when a downward reaction is seen in the columns and the braces try to elongate, the base beam will be pushed into the lab floor (here, the elongation of the braces is the dominant rig deformation).

8.2.3 *Actuator crossbeam deformations*

The actuator crossbeam is a W14x94 wide flange section, approximately 7 feet between support centers. The actuator load causes a concentrated load at mid-span of the beam, and subsequent bending deformations (see Figure 8-2). The peak actuator load was approximately 160 kips. The corresponding calculated bending and shear deflections are 0.063-inches and 0.18-inches, and the calculated bolt stretch is 0.026-inches. The values amount to approximately 0.2% drift of the column, and so are considered to be minor errors in the light of a total peak drift of approximately 7%.
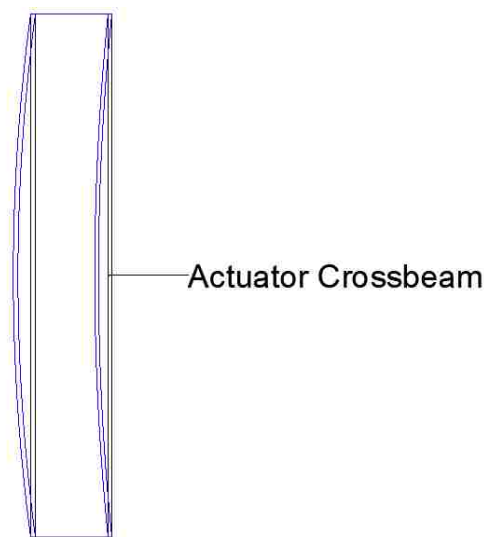
Figure 8-2. Flexing of actuator crossbeam

Figure 8-3. Bracket used for connection between actuator beam and reaction frame

8.2.4   *Deformation of connection between swivel and pile-column*

The actuator swivel was bolted to the specimen using a flat steel plate with timber packing

behind it to accommodate the curved pile-column surface. This was done because no curved

steel plate of the required radius (18-inches) was available, and neither the time nor the resources

needed were available for having new ones machined. The deformations of the timber packing

were not measured, but they can be estimated. The dimensions of the timber were 10-inches x

21-inches, so the peak load of 160 kips caused an average stress of ~750 psi. The thickness of

the timber at the thinnest point was approximately ¼-inch. The material was cedar, chosen

because it is relatively soft, especially when stressed perpendicular to the grain, thereby

providing a material that would deform to accommodate the inevitable lack of perfect contact

without excessive local bearing stresses. The four, 1-inch diameter threaded rods connecting the

swivels to the pile-column were tightened to approximately 90 kips each, which pre-compressed

133

the timber. The total corresponding stress in the timber was thus ~2500 psi, and a subsequent deformation of 0.022-inches.

Figure 8-4. Packing underneath actuator connected to specimen

In theory, the potentiometer should pick up any of the modes of deformation as long as the rig deformation is limited to the exterior steel beams, and the concrete slab stays put (see Figure 7-1).   In addition, the potentiometer captures any compression of the connections between the actuator cross beam and the testing rig (comprised of a steel bracket assembly constructed in the structural research laboratory, see Figure 8-3) or the connections between the actuator and the test specimen (see Figure 8-4). Figure 8-5 shows the displacement of the testing rig at peak loads, positive displacement signifying the rig moving south and negative north.

Equation 15 shows how the deformation of the testing rig was calculated.

$$\Delta_{rig} = \Delta_{actuator} - \Delta_{column} \qquad (15)$$

134
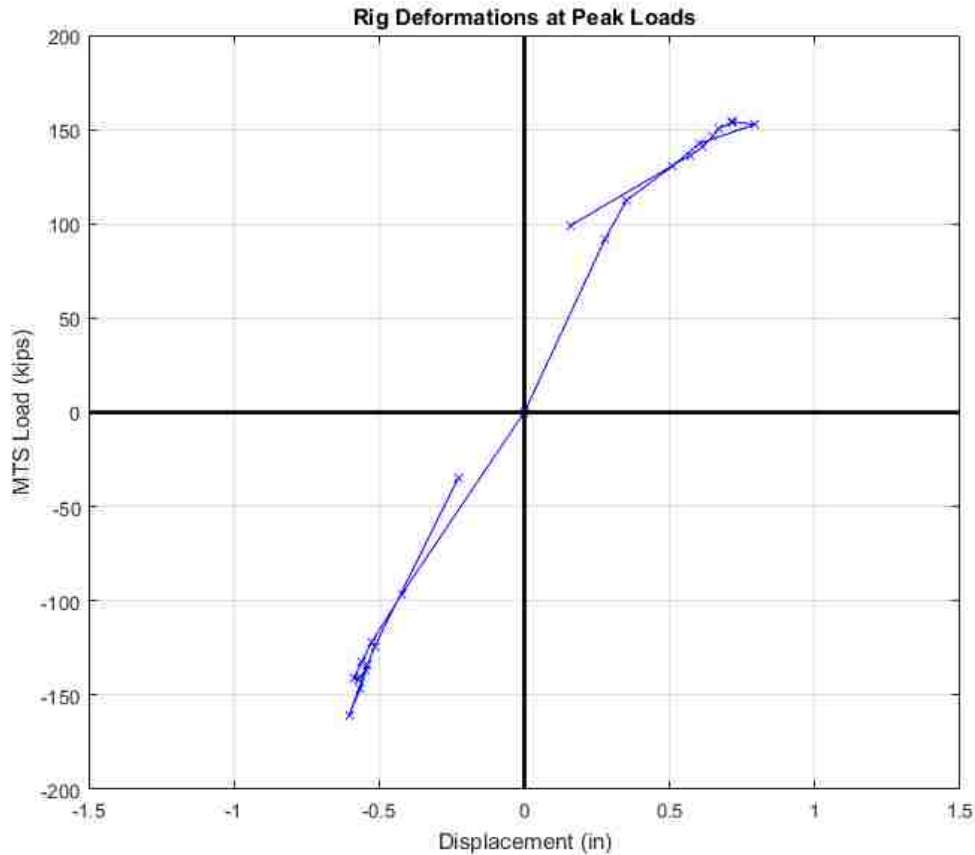
Figure 8-5. Load-displacement curve of testing rig at peak loads

The plot shows that the stiffness of the actuator connections is slightly larger when the specimen is pulled to the south (i.e. positive displacement). This is consistent with the results in Table 7-1, which showed that the specimen drift was higher when pushed to the north. The sudden decrease in deformations at the end of the test is due to the strength loss of the specimen and thus less demands on the connections and less deformations of the rig.

The uplift that was observed during the test was experienced only by the steel columns and beams, and not the concrete slab, meaning that the specimen drifts recorded were not affected. To confirm this a SAP2000 model was made of the testing rig, the details are outlined below:

- The concrete slab element was connected to "ghost nodes" that represent the lab floor via a link spring. The link spring had a very high stiffness in compression and a very low stiffness in tension; the intention was to allow uplift of the slab but make it stiff enough that it couldn't be pushed through the lab floor.

135

- The "ghost nodes" were pin supported.
- The concrete slab element was connected to the steel beam elements via different link springs. These link springs were multi-linear, elasto-plastic springs, intended to mimic the friction caused by the post-tensioning rods.
- A "specimen" element was added to account for the moment transfer between the test specimen and the testing rig.

The results of the SAP model are outlined below and shown in Figure 8-6.

- When the specimen was being pulled south (worst case, see Figure 8-6), the max uplift of the steel beams was 0.45-inches, resulting in a horizontal displacement at the point of load application of -0.60 inches.
- When the specimen was being pushed north, the steel did not move (it couldn't be pushed through the floor) and the horizontal displacement at the point of load application was 0.11 inches.
- All of the motion was restricted to the steel components of the testing rig, the concrete did not move.
- Since the concrete slab stayed in place the rig deformations did not affect the drift readings from our string potentiometers.
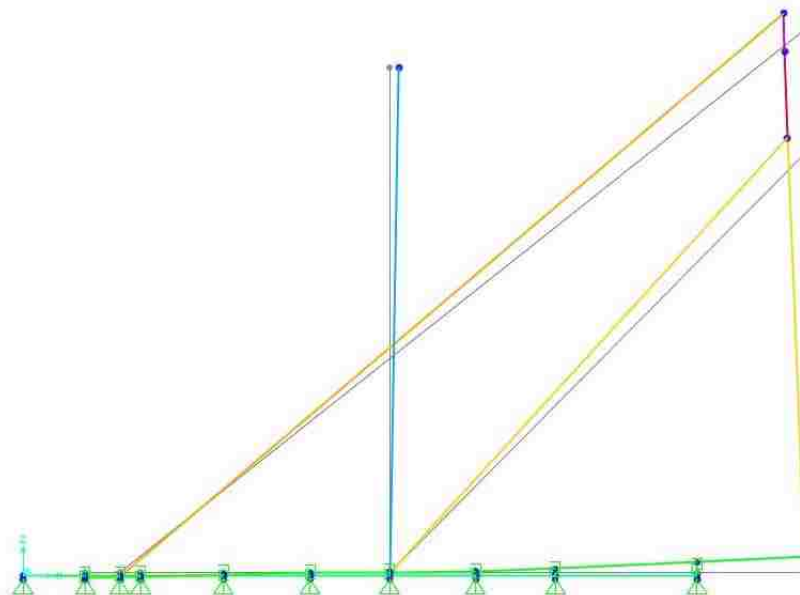
Figure 8-6. SAP2000 model of rig deformations

136

Following the SAP model it was confirmed that the uplift of the steel beams observed during testing did not affect the results of the cantilever bending test. The string potentiometer between the actuator crossbeam and the reference column picked up the total displacement caused by the uplift. The actuator is told by the MTS (Materials Testing System) computer what displacement to achieve, and measures this by the change in length between the shackles of the actuator. When the steel beams of the testing rig lift up, the actuator thinks it is displacing as if the steel beams were still on the lab floor because their uplift has no impact on the elongation or shortening of the actuator between its shackles. When the moment and force hysteresis plots were made (see

Figure 7-27 and Figure 7-28), readings from the top string potentiometer on the north side of the test specimen were used. The readings of this potentiometer were influenced by the uplift in that the displacements were higher when the specimen was pushed to the north because when the specimen was pulled south, the uplift of the steel beams took away some of the displacement that the actuator thought it was experiencing when trying to achieve the target drift. This is further confirmed by Table 8-1, in which all estimates of error are added; the total estimated from the different sources of error is 0.12% of the maximum total drift.

Table 8-1. Rig deformations

Source	Deformation (inches)
Slip and base rotation	0.60
Actuator crossbeam	0.27
Timber packing	0.02
Total	0.89

8.3 MOMENT CAPACITY

The maximum moment at the base of the pile-column (directly adjacent to the cap beam) during the test was measured as 17,604 in-kip at a drift ratio of +3.71%, during the first cycle of Series 6. The expected moment capacities of the hollow pile-column, as well as the combined pile-column, plug, and jacket (defined in Figure 8-7) were calculated using the same custom-written moment-curvature program described in Section 4.4.1. Because moment-curvature analysis applicable to

137

a section, it is based on the assumption of perfect bond, and failure by material overstress. The moments were found using the material properties from Section 6.3.1, while also applying an axial load of 200 kips. The maximum moments are presented in Table 8-2 for each case. The assumed conditions, illustrated in Figure 8-7, were:

- *Hollow pile-column only*: The geometry was that of the hollow pile-column alone, the concrete strength was that of the pile-column (15.5 ksi), and the reinforcement consisted of the strand (32, 3/8-inch diameter, fpe = 163 ksi), assumed to be fully bonded.
- *Combined pile-column, plug, and jacket*: The geometry was taken as a circular section with diameter equal to that of the pile-column, because the pile-column concrete could resist compression by direct bearing. The concrete strength was taken as that of the pile-column (15.5 ksi), because the moment-curvature program has provision for only one strength. The great majority of the compression force occurs in the pile-column wall, and not in the plug. The reinforcement consisted of the plug bars alone (16 #8 bars); the strand was not included because, at the column-cap beam interface, the strands terminate and carry no stress.

Table 8-2. Moment capacities for pile-column components

	Hollow Pile	**Combined Pile-Column, Plug, and Jacket**
Moment Capacity (in-kip)	14600	14700

Hollow Pile   Combined Pile and Plug
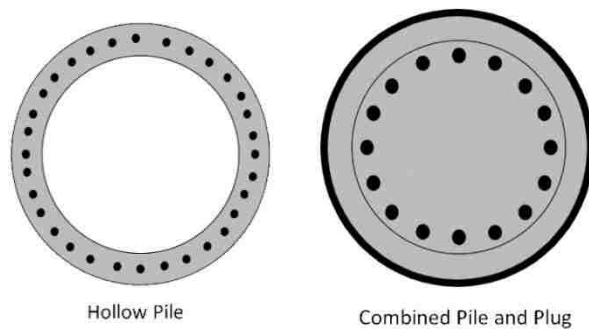
Figure 8-7. Cross-sections used to calculate moment capacities

138

Figure 8-8 shows the measured moment diagram, as well as two lines, which lie almost on top of one another, signifying the predicted capacities of the hollow section alone and the combined hollow pile-column, plug, and CFRP. The diagram shows that the measured moment at the base was larger than predicted capacity of the combined pile-column, plug, and CFRP.
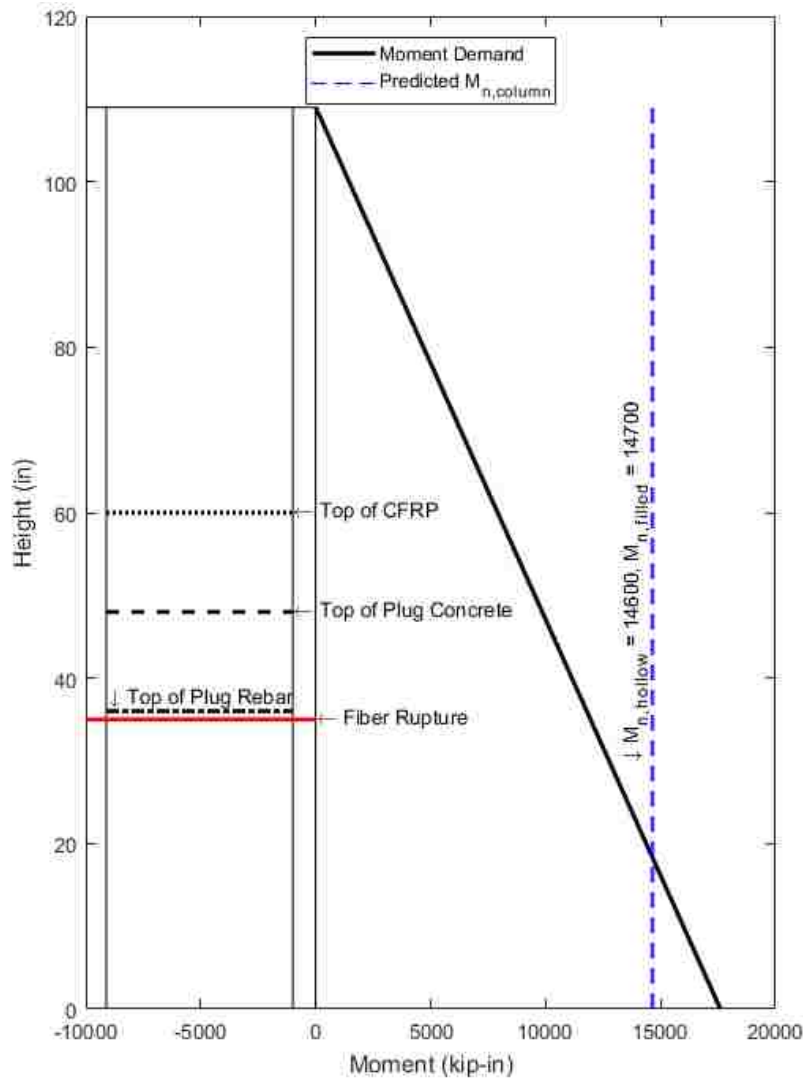
Figure 8-8. Conditions at maximum moment

The measured moment at the cap beam, where the plug bars yielded and the pile-column wall crushed, was 17,604 in-kip, which is 16.5% larger than the predicted 14,700 in-kip for the combined cross-section. This difference between the measured and predicted moment strength could be because the moment-curvature program does not account for the added confinement of

139

the concrete provided by the spiral reinforcement in the pile-column wall; however, only half of the pile-column wall thickness lies inside the spiral. Furthermore, the program showed that the flexural strength is controlled by the tension capacity of the bars and not the compression capacity of the concrete. To further investigate the higher measured strength, a series of moment-curvature analyses were conducted using elasto-plastic stress-strain curves for the plug reinforcement to determine the actual stress in the reinforcement at failure during the test. Elasto-plastic curves were chosen in order to limit the number of variables to one. The true value of the steel stress is important, because it plays a crucial role in the capacity protection of the hollow pile-columns in the field. It was found that the yield stress in the model had to be 82 ksi in order to match the measured test moment (see Figure 8-9), the corresponding moment-curvature plot is shown in Figure 8-10.
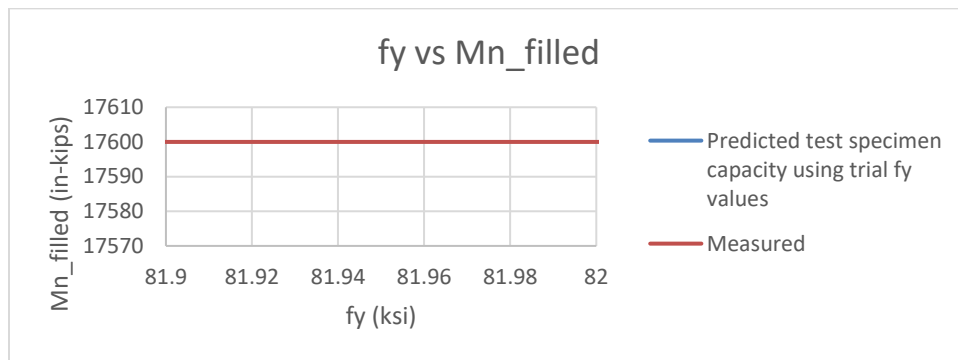
Figure 8-9. Flexural strength of the test specimen filled section as a function of yield stress
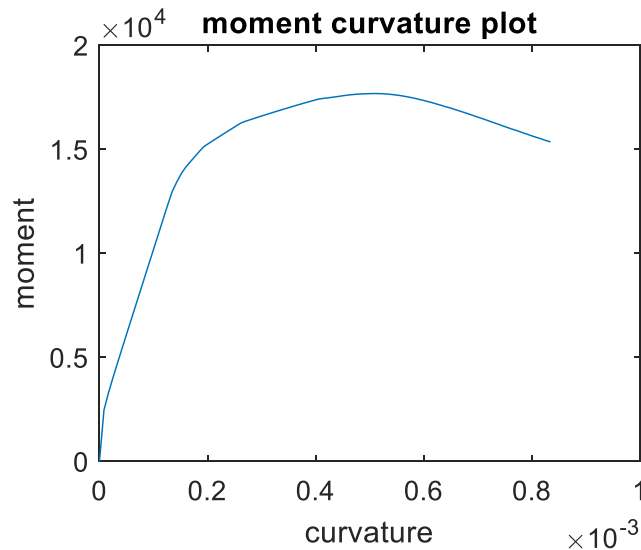
Figure 8-10. Moment-curvature plot for filled section

140

The true yield strength of the bars used in the field was not available, but 82 ksi is significantly higher than any probable yield strength. For example, Mander and Matamoros (2019) provide statistics for strengths across a variety of metrics, and, for A615 bars, they report an average yield strength of 72 ksi. The actual stress in the lab test was probably slightly higher than 82 ksi, because the moment-curvature analysis was conducted using only one concrete strength (that of the column wall, f'_c = 15.5 ksi), due to a limitation of the program. The neutral axis distance was approximately 6 inches from the compressive face, whereas the wall was approximately 3.5 inches thick, showing that some of the compression force must have been resisted by the plug concrete (f'_c = 6.5 ksi). Therefore the true stress block would have been deeper, and so the lever arm would have been slightly shorter and the steel stress slightly higher, than the values output by the program. It is concluded that cyclic strain hardening must have occurred, which is not picked up by the monotonic moment-curvature analysis. To calibrate a strain hardening curve to be used to extrapolate the strength of the field bridges, material parameters were varied in the moment-curvature analysis to match the test results; the Raynor model was used for strain hardening. The corresponding material parameters are summarized in Table 8-3, and the implications of the increases in predicted strengths in the field is discussed in Section 9.2.

Table 8-3. Material parameters for calibrated strain hardening curve

E (ksi)	29000
f_y (ksi)	79
f_u (ksi)	118.5
ε_{sh} (in/in)	0.009
ε_u (in/in)	0.1
n	6

While there was damage at the base of the pile-column, the main region of failure was at a height of 35 inches above the cap beam, where the CFRP split (see Figure 7-11 and Figure 8-8). This location was well within the plug region, so the pile-column wall could not spall inwards, in which case the section might be expected to behave like a solid one. However, the moment demand at the location of the fiber split was approximately 11,951 in-kips, which is less than

141

either the predicted hollow capacity of 14,600 in-kips (assuming the strands can reach full strength), or the filled capacity of 14,700 in-kips (based on the plug bars providing the tension capacity). As was discussed in Section 7.2 the primary mode of failure was due to slip and subsequent debonding of the prestressing strands; this issue is discussed more in Section 8.4.

The highest moment demand in the hollow region (at the end of the plug) was 9,518 in-kips. This is 65.2% of the predicted capacity of the hollow section, and largely explains why the pile-column did not fail in the hollow region just beyond the end of the plug. The illuminating outcome is that the filled section, with the plug bars alone providing the tension capacity, appears to capacity protect the hollow region. The extent of the capacity protection is defined by the demand/capacity ratio (DCR) of the hollow column, with values less than 1.0 indicating effective protection. In the case of a hollow column, the DCR is given by:

$$DCR = \frac{M_{n,filled}}{M_{n,hollow}} \left(\frac{L_{PI} - L_{plug}}{L_{PI}} \right) \qquad (16)$$

Where L_{PI} = the vertical distance from the underside of the cap beam down to the point of inflection (can be estimated as approximately $0.7 * L_{col}$), and L_{plug} (typically $1.0 D_{col}$). In the test, $M_{n,filled}$ was 17,604 in-kips (the peak moment measured in the cantilever test), while M_{n_hollow} was approximately 12,800 in-kips, as measured in the pure bending test. (The true M_{n_hollow} would be slightly higher with the addition of axial load). The ratio of $\frac{M_{n,filled}}{M_{n\_hollow}}$ was thus 1.38. The length ratio was (108-36)/108 = 0.67, so the DCR was approximately 1.38*0.67 = 0.92 and the capacity protection was (just) effective. The test result confirmed this.

In the field, both elements of the DCR vary among bridges, and even among pile-columns, so the extent of capacity protection varies. In the four example bridges, using nominal steel strengths, $\frac{M_{n,filled}}{M_{n\_hollow}}$ was < 1.0 in three cases, and was 1.03 in the L^E Line ("Slide") bridge. The DCR is thus most heavily dependent on the length ratio and, because all of the plugs were about the same length, long columns (with high $\frac{L_{PI}}{L_{plug}}$) will experience the least capacity protection. But, they

142

might also *need* the least capacity protection. If the above-grade column lengths vary, as at Galer, the short above-grade columns will control the displacements of, and thus the moments induced in, the long above-grade columns. If all the above-grade columns are long (as on the SR 520 ramp from I-5), the period will be longer and the seismic forces lower than for shorter above-grade columns. These principles can be used to evaluate each bridge individually.

8.3.1 *Bond*

The flexural strength of the pile-column in the plug region appeared to be controlled by bond slip of the pretensioned strand. The corresponding analysis of bond failure is conceptually more complicated than for other modes of failure. The development length of the 3/8" diameter strands, if taken as $150d_b$, is approximately 56 inches according to ACI318, assuming that it is fully stressed initially. That assumption is likely not valid, because the location is close to the free end of the pile-column. Consequently, the development length was probably longer than 56 inches, in which case the strands were not fully developed at the location of the fiber split. The split formed when the north face of the specimen was in tension, and its width suggests some debonding of the strand occurred. Upon further investigation it was found that the strand slipped (see Figure 7-21), allowing the split to widen. On the next half cycle (when the north face went into compressions) the remaining bond stress was high enough to prevent the strand slipping back before it buckled. The buckling strand pushed radially outwards on the spiral, then fractured at the kinks on the next tension cycle (see Figure 7-16). The calculations needed to evaluate the bond capacity of the strands are given in the following sections.

8.3.1.1 Modeling of behavior

Failure by bond slip occurs when the stress in the strand rises to a value just equal to its anchorage strength under the influence of the internal prestressing, plus external axial load and moment. The anchorage strength depends on the effective prestressing, and that depends on both the distance from the end of the member and the prestressing losses. Over the length of the plug region, the axial load and bending moment in the wall of the pile-column also depend on the distance from the member end, because the total axial load and moment are transferred from the hollow pile-column to the isolated plug. The exact manner in which that transfer occurs, and therefore the stress in the pile-column wall at any point, is not clear. However, a model is

143

needed if the cracking and bond slip are to be predicted. The question is discussed in the following paragraphs.

At any point along the column, the total internal action (axial force, moment, or shear) can be determined. Because the cantilever test is statically determinant, those quantities can be computed by equilibrium alone; in the field, a system model is needed, and if the bent has multiple pile-columns, it is by definition indeterminate. The results of the system analysis then depend to some extent on the element stiffnesses.

The more difficult question is how to determine the load path by which the moment is transferred from the pile-column to the plug, and hence the stresses in the various components of the connection (plug, pile-column wall, and jacket, if one exists). Stresses in the pile-column wall are needed in order to predict when the wall will crack, because cracking must preceded debonding. Difficulties arise because load is transferred from one element to another in ways that are not in accordance with conventional Euler-Bernoulli beam theory. In particular, just outside the plug region, all the moment is resisted by the pile-column wall, because no other elements exist there. Adjacent to the cap beam, almost all of the moment is resisted by the plug, or, more precisely, by the filled section, because the plug and wall act together to display some composite inelastic behavior.

If the plug were long (say, 8 column diameters) a plausible model of behavior would consist of a central region in which the plug and pile-column wall acted compositely and the distribution of actions between them could be obtained by elastic analysis of the composite section. The forces would be transferred from the pile-column wall to the plug by vertical shear stresses at the interface, and they would be low enough for no slip to take place. These are illustrated in Figure 8-11.

www.manaraa.com
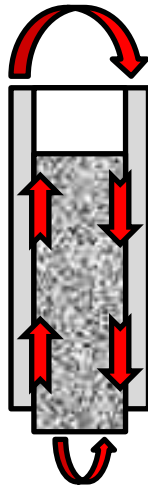
Figure 8-11. Transfer of bending moment from pile-column to plug

Near the ends of the plug, "end effects" would dominate and cause a transition between the
elastic composite behavior in the central region and response of a single element (plug or pile-
column wall) just outside it. The end effects could be considered "disturbed regions", for which
St. Venant's Principle suggests a length of about $1.0D_{col}$. In the disturbed regions, the behavior
would be much more complicated, especially at the open end of the pile-column adjacent to the
cap beam. The moments would be expected to be transferred primarily by horizontal bearing
forces at the interface, which would cause hoop tension and local bending in the pile-column
wall, and distortion of the cross-section. At the opposite end of the plug diameter, the pile-
column wall might even separate from the plug. These forces are also illustrated in Figure 8-11.
The exact behavior will depend on the local geometry, including the stiffness of the plug in
overall bending relative to the pile-column wall in local bending. Furthermore, the behavior
probably changes during cyclic loading as the stiffnesses change due to accumulation of damage
caused by slip at the plug-wall interface.
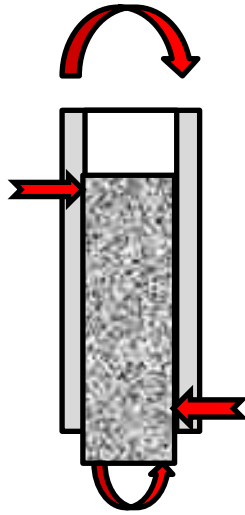
Figure 8-12. End effects in moment transfer from pile-column to plug

In the field pile-columns, the plug is typically about $1.0D_{col}$ long, so the two end (i.e. disturbed) regions might be expected to meet in the middle, leaving little or no central region. Therefore, the entire transfer region is disturbed. In the interest of simplicity, a linear variation over the plug length for the transfer of axial load and moment was used due to the fact that only two suitable tests were available for calibrating the model described above (see Figure 8-13). The linear variation is equivalent to transferring moments by means of two horizontal point loads, one near each end of the plug, as shown in Figure 8-14.
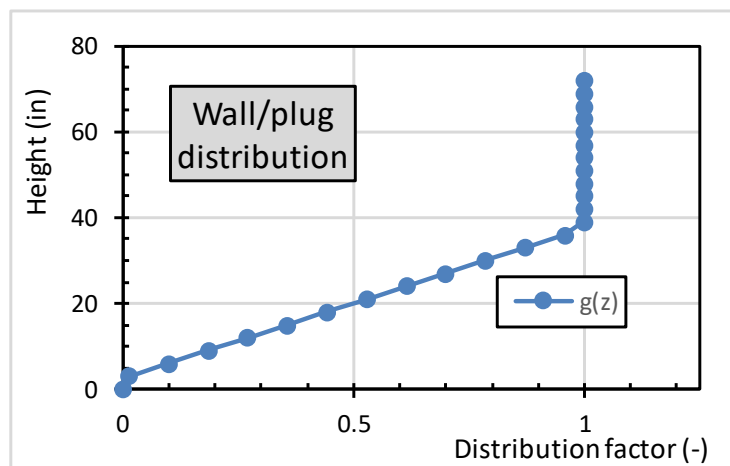
Figure 8-13. Proportion of moment and axial force carried by pile-column wall
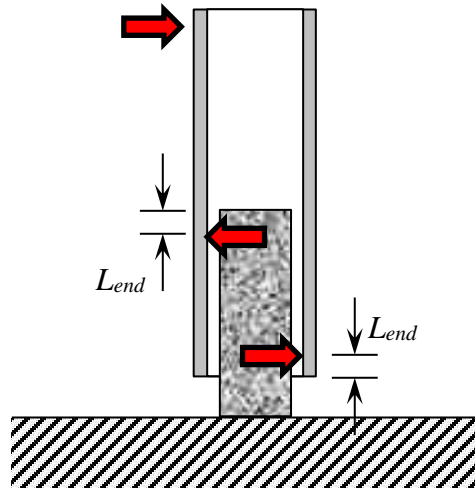
Figure 8-14. Model adopted for distribution of moment between plug and pile-column wall.
(Forces shown act on the pile-column)

8.3.1.2   Evaluate prestressing losses

The development length of the strand depends on the effective prestress, which in turn depends
on the prestress losses. Those losses are estimated in this section.

Jacking Stress

The jacking stress is typically provided on the plans; for the test specimen it was 190 ksi.

Relaxation

Relaxation occurs between jacking and release, and after release. Relaxation is significantly
higher in stress-relieved strand than in low-relaxation strand. The strand in the field bridges is
expected to be stress-relieved, because of their date of construction. The loss due to relaxation is
calculated using Equation 17 (Magura et al, 1964).

$$\frac{\Delta f_p(t)}{f_{pj}} = \frac{log(t)}{CR}\left(\frac{f_{pj}}{f_{py}} - 0.55\right) \qquad (17)$$

Where CR = 40 for low-relaxation strand and 10 for stress-relieved strand. The details on the
available plans suggest jacking to $0.70f_{pu}$, or $0.7/0.85 = 0.82f_{py}$. For the stress-relieved strand in
the field pile-columns, the total loss over approximately 55 years is therefore 15%. For the test

147

specimen, which used low-relaxation strand, assuming a release at 15 hours, the loss is rounded to 3%.

Elastic Shortening

For a concentrically prestressed member, the elastic shortening loss is calculated using Equation 18.

$$\Delta f_{p,es} = \frac{n\rho}{1+n\rho} f_{pj+} \qquad (18)$$

Where f_{pj+} is the stress after jacking and directly before release. The loss may be calculated for each pile-column in accordance with its individual characteristics, but, in most cases, it is approximately 5% of f_{pj+}.

Shrinkage

Concrete Technology Corporation report that the concretes of the time used little, if any superplasticizer, and likely had a w/c ratio of about 0.40 to achieve the required release strength of 5,000 to 6,000 psi. That suggests a total shrinkage of about 400 $\mu\varepsilon$ (Collins and Mitchell, 1991, Figure 3-17). That value is used here, and leads to a prestressing loss of 11 ksi. The concrete in the test specimen had a low w/c ratio, used superplasticizer, and was self-consolidating. The exact shrinkage for that concrete is not known, so the three effects were assumed to compensate for one another, and the same shrinkage loss was used.

Creep

The creep loss in the field bridges is taken as the ultimate value, because all of the creep has most likely occurred. The creep coefficient is assumed to be 1.5. Meader et al. (2013) found that most Washington State concretes, using local aggregates, have a creep coefficient of approximately 2.0, almost regardless of strength, paste content, etc. The slightly lower value of 1.5 used here is adopted on the basis that the pile-columns were probably heat-cured, and that the concrete strength was higher than that of most site-cast concretes of the era. Any interactions between creep and shrinkage were ignored. The creep coefficient assumed for the test specimen was 1.0, because of the high concrete strength.

148

Total Loss

These losses can be combined to give an effective prestress, f_{pe}, as seen in Equation 19.

$$f_{pe} = \left\{ \frac{f_{pj}(1+p_{r1})}{1+n\rho}(1 - n\rho C_c) + E_p \varepsilon_{sh} \right\}(1 + p_{r2}) \qquad (19)$$

Where the shrinkage strain, ε_{sh}, and the relaxation percentages, p_{r1} and p_{r2}, are negative because they represent shortening. This equation is valid for a concentrically prestressed member such as a pile-column, and can be applied to both the field and test pile-columns, provided that the appropriate constants are used.

8.3.1.3 Bond capacity

The anchorage, or bond, capacity of the strand is needed as a function of distance from the end of the member. The equation given by the AASHTO LRFD Specifications (AASHTO, 2012) is used here (see Equation 20). It gives the development length, l_d, as a function of the strand stress at member failure, f_{ps}.

$$\frac{l_d}{d_{str}} = \kappa \left(f_{ps} - \frac{2f_{pe}}{3} \right) \qquad (20)$$

The constant κ reflects the quality of the anchorage as affected by the local conditions (e.g. bond adjacent to a sheathed length of strand). Poor quality bond leads to a longer development length and thus a larger κ. The equation can be inverted to solve for f_{ps}. This value is valid only beyond the transfer length, L_t, which is implied by AASHTO to be $60d_{str}$. For both the test and field pile-columns, z_{cr}, the height at which the failure occurred, was greater than L_t, so Equation 20 is valid. Usually, the stress f_{ps} is known from a flexural analysis in which it is assumed that the member fails by yielding of the tendon and crushing of the concrete, and the development length, l_d, necessary to support that f_{ps} is calculated. Here the process is reversed, and f_{ps} is sought at a specific location, z_{cr}, from the end of the member, which is taken as l_d.

The stress, f_{ps}, that can be resisted by the strand without debonding is given by Equation 21, obtained by inverting Equation 20.

149

$$f_{ps} = min \left(\frac{z}{60d_{str}} f_{pe}, \frac{2f_{pe}}{3} + \frac{z}{\kappa d_{str}} \right) \qquad (21)$$

Where κ, which carries units of ksi^{-1}, is taken here to have the value 1.0. z is the distance from the free end of the strand at the top of the pile-column, d_{str} is the nominal strand diameter and f_{pe} is the effective stress in the strand after all losses.

In summary, the pile-column (in test configuration) is treated as transferring its moment and axial stresses to the plug linearly with distance over a length equal to $L_{plug} - 2L_{end}$. That assumption enables the axial load and bending moment in the pile-column wall to be known at any height z above the cap beam. To resist that combination of internal actions, the corresponding stress in the pile-column stand must be less than f_{ps}, the stress at which debonding will occur, defined by Equation 21.

8.3.1.4 Comparison with test results

The model described above was tried at the observed location of failure, $z = 35$ inches, for different values of κ and L_{end}, where in this case L_{end} is the distance from the point load (between the pile-column wall and the plug) to the end of the plug or pile-column, shown in Figure 8-14. The results are shown in Figure 8-15. The measured peak actuator force 157.5 kips defines the moment demand, which could be matched by several combinations of κ and L_{end}. $L_{end} = 2.5$-inches and $\kappa = 0.7$ were chosen here on the basis that $L_{end} = 0$ is implausible because it implies an infinite contact stress over the zero length, and larger L_{end} values lead to very low values of κ. In the AASHTO Specification, the constant κ is never less than 1.0. The implication of finding a good fit here using $\kappa = 0.7$ implies exceptionally good bond in the test specimen. For the field pile-columns, κ should be taken as 1.0 because the better bond displayed by the test specimens cannot be counted upon in the field. L_{end} should be related to the dimensions of the field pile-columns. It should be expected to vary with the overall scale of the column, but also with the D_{col}/t_{wall} ratio. If the wall is relatively thin, L_{end} should be expected to increase because the wall will bend near the end of the plug region. A suitable equation that matches both these criteria and the value 2.5-inches for the laboratory test pile-columns, is:

150

$$L_{end} = \frac{D_{col}^2}{150t_{wall}} \qquad\qquad (22)$$
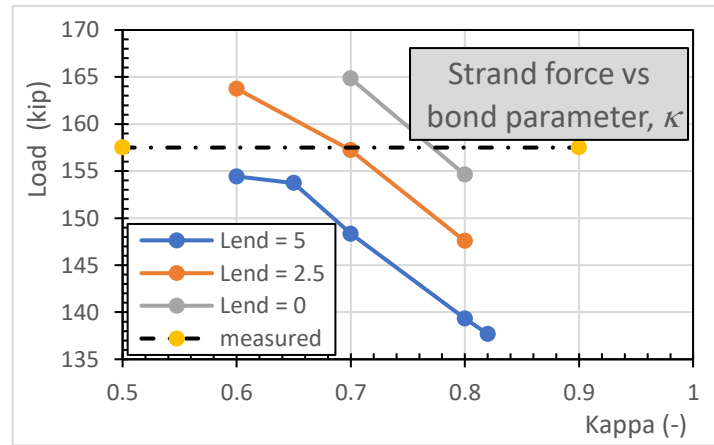
Figure 8-15. Test pile-column ($z = 35$ inches). Effect of L_{end} and κ on predicted failure load.

It is proposed that this model be used to determine whether the connection in the field pile-columns will fail by strand slip. As can be seen, it is largely a question of whether the plug length is greater than the strand development length.

8.4   TRANSVERSE LOAD CAPACITY

The transverse load capacity of the cantilever bedning test was predicted using the same methodology described in Section 5.4 (using ACI 318-19 Section 22.5.6.3.3 and Response2000). The only difference for this specimen was the addition of a 200 kip compressive axial load (approximately -550 psi). The predicted transverse load capacity of the test specimen with the addition of a -500 psi axial load was found to be 254 kips and 244 kips, using the ACI methodology and Response2000, respectively. The maximum transverse load demand experienced during the test was 157.5 kips, giving DCR values of 0.62 and 0.65 for ACI and Response2000, respectively. This finding is in agreement with the observed flexural failure due to strand debonding, and lack of evidence of shear distress.

151

Chapter 9. GLOBAL ANALYSIS

9.1   SYSTEM ANALYSES

To translate the results of the SDOF cantilever bending test to the field conditions, a representative pile-column bent was analyzed. The goals were to determine the general pattern of the internal forces, and how the magnitude and distribution of those forces are affected by varying major parameters. One key assumption in these analyses is that the cracking or bond failure observed in the test was suppressed, by the use of a steel jacket or other means. The analyses therefore focused on failure modes that may be difficult to alter by retrofitting, namely flexural failure below-grade or fracture of the plug bars. At the start of the research project, the major area of concern was the hollow section just beyond the end of the plug, and the primary goal was capacity protection at that location by cutting back the pile-column wall to reduce the maximum achievable moment demand. Following the test of an as-built specimen, that retrofit option was discarded in favor of a CFRP wrap around the plug region with no cutback of the pile-column wall. While this attracts larger moments to the cap beam region than would be the case with the cut-back column wall of the original retrofit concept (limiting the ability to capacity protect the hollow section beyond the plug), it slightly reduces the moment demand below-grade.

9.1.1   *Computational Model*

The computational model consists of an idealized, single degree of freedom elastic structure to represent the transverse response of a pile-column bent, modified to allow plastic rotation at the plug. This was done by modeling a symmetric bridge in 2-D using line finite elements, then using static condensation to condense out all of the degrees of freedom except the transverse displacement at the cap beam level. This effectively reduces the structure to a SDOF system, of which the response can be determined using the Capacity Spectrum Method (Freeman 2004); this will be described in the following subsection. The reference structure is shown in Figure 9-1: the complete model before condensing out DOFs consists of a three-span bridge with two abutments and two, four-column bents supported by hollow pile-columns. The dimensions were chosen to be representative of field conditions.

152
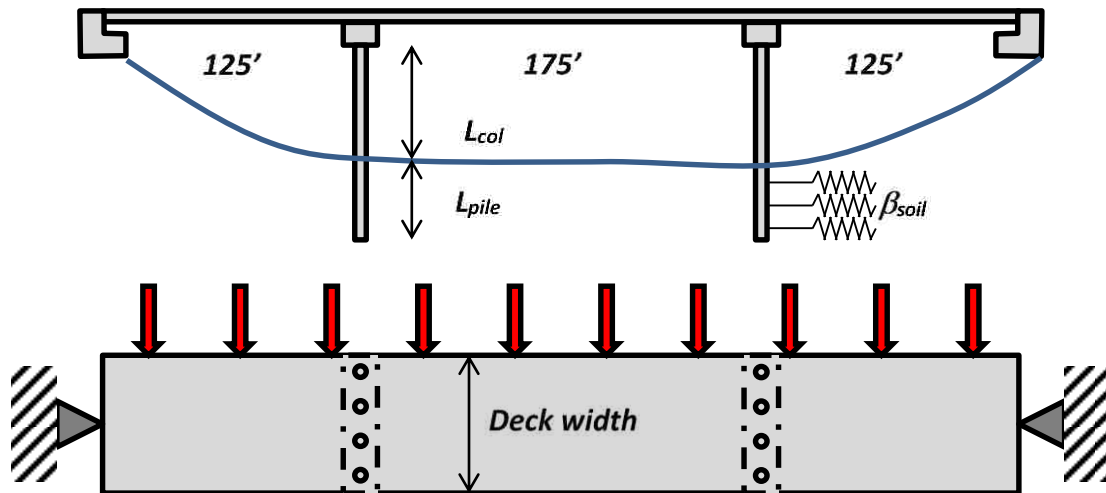
Figure 9-1. Bridge structure used for analysis

In the model, the bridge deck always contributes to the seismic mass of the system, which determines how much force it will attract; however, the contribution of the deck stiffness to the system (acting as a transverse beam with two pin supports at the abutments) was modelled as a variable because the deck may or may not be continuous at the expansion joints over the piers. The superstructure consisted of an 8-inch deck supported on WF74G girders spaced at approximately 8 ft. centers, with barriers on each side of the roadway (which contribute to the mass).

The below-grade piles were represented by beam-on-elastic foundation elements using the exact closed-form formulation (see Appendix D). The above-grade columns were represented by beam elements and were attached to the cap beam via elastic rotational springs. For analysis prior to yielding of the plug (i.e. reaching the capacity of the filled section), the rotational springs were made very stiff to simulate a fixed connection. After the plug yields the spring stiffness was set to zero, and a moment equal to $M_{n,filled}$ was applied to the head of the pile-column. For all analyses in the parameter study, the columns were taken as 54-inch outer diameter with a 5-inch wall, with $f'_c = 9.0$ ksi and $E_c = 6400$ ksi. The soil subgrade reaction modulus, β_{soil}, was an input variable, with units of kip/ft^3, and the stiffness of the soil elastic foundation was taken as $\beta_{soil}*D_{pile}$ kip/ft^2, where D_{pile} is the pile-column outer diameter.

153

Based on a user-specified number of pile-columns per cap beam bent, only the mass (and deck stiffness if used) acting on a single pile-column was considered. Furthermore, the structure and loading were both symmetric, so the response was symmetric, and it was possible to analyze only half the structure. The results of elastic analysis using the SDOF model described here were verified against an OpenSEES model using dimensions, properties and loads that were, to the extent possible, the same. The results were essentially identical and are discussed in Section 9.1.4. The reference parameters are given in Table 9-1; they were used for all parameters not being varied at the time.

Table 9-1. Reference parameters

Above-grade column length	(ft)	20
Below-grade pile length	(ft)	20
Deck span, mid	(ft)	175
Deck width	(ft)	60
Pile-Columns/bent	(-)	4
Pile-Column axial load	(kips)	564
Mn,filled	(ft-kip)	3919
Mn,hollow	(ft-kip)	3710
Girder lines	(-)	8
Soil modulus	(kcf)	1000

9.1.1.1   Capacity Spectrum Method Procedure

The Capacity Spectrum Method (CSM) estimates the peak dynamic response of a system by comparing demand and capacity. The demand is expressed by plotting an Acceleration-Displacement Response Spectrum (ADRS), in which the pseudo-spectral acceleration, S_a, is plotted against the spectral displacement, S_d (see Figure 9-2, where NRS represents the Normalized Response Spectrum). The capacity can also be represented on the plot in the form of a nonlinear "pushover" force-displacement curve, in which the force is divided by the mass of the system to give acceleration (see ACS on Figure 9-2). A damage state is chosen along the nonlinear capacity spectrum, and the reference response spectrum is scaled until the two curves intersect at the correct effective period. The point where they intersect represents the response of the system. The reference response spectrum used for the corresponding SDOF system analysis is the AASHTO LRFD 1000-yr return period design spectrum for Seattle, WA for Site Class B,

154

with 5% damping, shown in Figure 9-3. The critical points on the spectrum (PGA, S_s, S_1) were taken from the maps in Section 3.10.2.1 of the AASHTO LRFD Specifications. Those maps show contour plots, for which the characteristics for the Seattle region are $0.30g \leq PGA \leq 0.40g$, $0.75g < S_s < 1.00g$, $0.30g < S_1 \leq 0.40g$. The values adopted were PGA = 0.40g, S_s = 1.0g, S_1 = 0.35g. The PGA and S_s values represent the upper bounds for the region, and the S_1 values is also a conservative estimate. The site class was, in most cases, taken as B, for which $F_{pga} = F_a = F_v = 1.0$. Note that the AASHTO spectrum does not allow for the constant ground displacement region, at periods greater than T_{long}, that the ASCE spectra do.
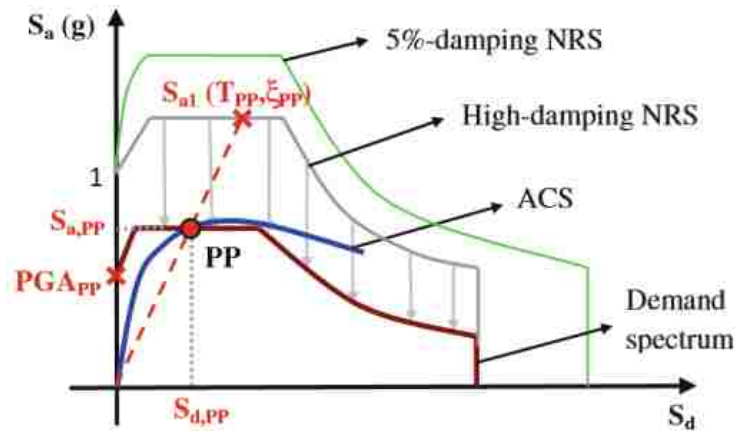
Figure 9-2. Acceleration-Displacement Response Spectrum (Cardone et. al, 2011)
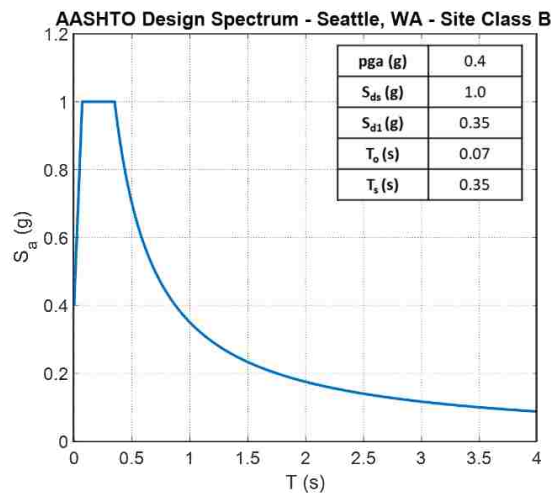
Figure 9-3. Acceleration spectrum for the AASHTO LRFD ground motion for Western Washington.

155

This approach is based on the concept that the real nonlinear system responds in the same way as an equivalent linear system with the same secant stiffness to the peak displacement and with damping based on the energy dissipation implied by the area of the real hysteresis loop. The slope of any secant line drawn from the origin to a point on the curve is the frequency square, ω^2. The approach is convenient in that it allows a spectrum to be used, rather than requiring Non-Linear Time History Analysis (NLTHA), which reduces time requirements. The general procedure for the CSM is outlined below.

- *Generate capacity curve and demand curve*
  For a SDOF system, pushover curves can be easily translated to a spectral capacity curve via Equations 23 and 24.

$$S_d = \Delta \tag{23}$$
$$S_a = \frac{V}{W} \tag{24}$$

  The demand curve is derived from the 5% damped, 1000-year return period AASHTO LRFD spectrum for site class B in Seattle, WA (see Figure 9-3).

The actual demand spectrum for each damage state should be calculated from a damping reduction factor that is a function of the effective damping associated with the energy dissipation at that displacement. The damping is defined by the equivalent viscous damping, or the idealized area under the real hysteresis. However, to remain consistent with the conservative analysis done in previous work, the hysteretic damping was taken as 5%, ignoring the potential benefits of lower response associated with higher damping after the plug yields.

The required PGA for any damage state (e.g. plug yielding) is calculated using Equations 25-27. The corresponding PGA is then compared with the reference PGA to find the equivalent earthquake factor, F_{EQ}, which is a scaling constant to the reference spectrum. For example, an F_{EQ} of 0.37 implies that the criterion will be met when the PGA is 37% of the AASHTO-specified PGA.

156

- Find the spectral acceleration corresponding to the particular damage state, Sa_{DS}

$$S_{a_{DS}} = \frac{V_{DS}}{M} \qquad (25)$$

Where: M = seismic mass.

- Find effective period of the system for the damage state, T_{eff_DS}

$$T_{eff_{DS}} = 2\pi \sqrt{\frac{M}{K_{eff_{DS}}}} = 2\pi \sqrt{\frac{M}{V_{DS}/\Delta_{DS}}} \qquad (26)$$

- Normalize the reference spectrum (AASHTO, see Figure 9-3) and, using 5% damping, find the spectral acceleration at the effective period for the damage state, Sa_{ξ}.
- Find PGA_{DS} and F_{EQ} for the damage state, then plot the demand spectrum. The PGA_{ref} is 0.4g for the reference spectrum used

$$PGA_{DS} = \frac{S_{a_{DS}}}{S_{a_{\xi}}} \qquad (27)$$

$$F_{EQ} = \frac{PGA_{DS}}{PGA_{ref}} \qquad (28)$$

The PGA values obtained from the above analysis represent an estimate of the median threshold value of the peak ground acceleration related to the selected damage state (Cardone et al, 2011) and can be used as a reasonable first estimate of the ground motion required to cause damage to a similar pile-column in the field (with as-built conditions).

9.1.2 *Elastic Response*

The results of the elastic response demonstrate the distribution of internal moments and shears and show the magnitude of earthquake that can be sustained without inelastic response, such as plug yielding. This information is useful, for example, in evaluating the response to an earthquake with moderate accelerations.

157

Figure 9-4 shows the deflected shape of the pile-columns, and the distributions of moment and shear, using the reference parameters. The vertical (z) co-ordinate is positive downwards, with the origin at grade level; the open square symbols in the negative region represent response in the above-grade column. Prior to yielding of the plug, the above-grade column is rotationally fully fixed to the cap beam, which is here treated as rigid, so the above-grade column is vertical at the connection between the two elements. The pile-column deforms elastically both over its free height, and below-grade. In the free column height, the moments are distributed linearly, and the shears are constant. The moment distribution is non-linear in the pile below-grade and was obtained directly from the beam-on-elastic-foundation elements in the computational model described in the previous section.

The peak moment in the above-grade column occurs at the cap beam, and it is larger than the peak moment in the below-grade pile, which occurs one to two pile-column diameters below-grade, depending on the soil stiffness. The magnitudes shown in Figure 9-4 represent the conditions when the moment at the cap beam has just reached the filled section's capacity there. That capacity was computed assuming both the pile-column wall and the plug contribute to the compressive capacity, and only the plug bars provide tension capacity. This pattern, in which the peak below-grade pile moment is smaller than the peak above-grade column moment, is beneficial because it means that a damaging moment cannot be reached below-grade while the rest of the system remains elastic.
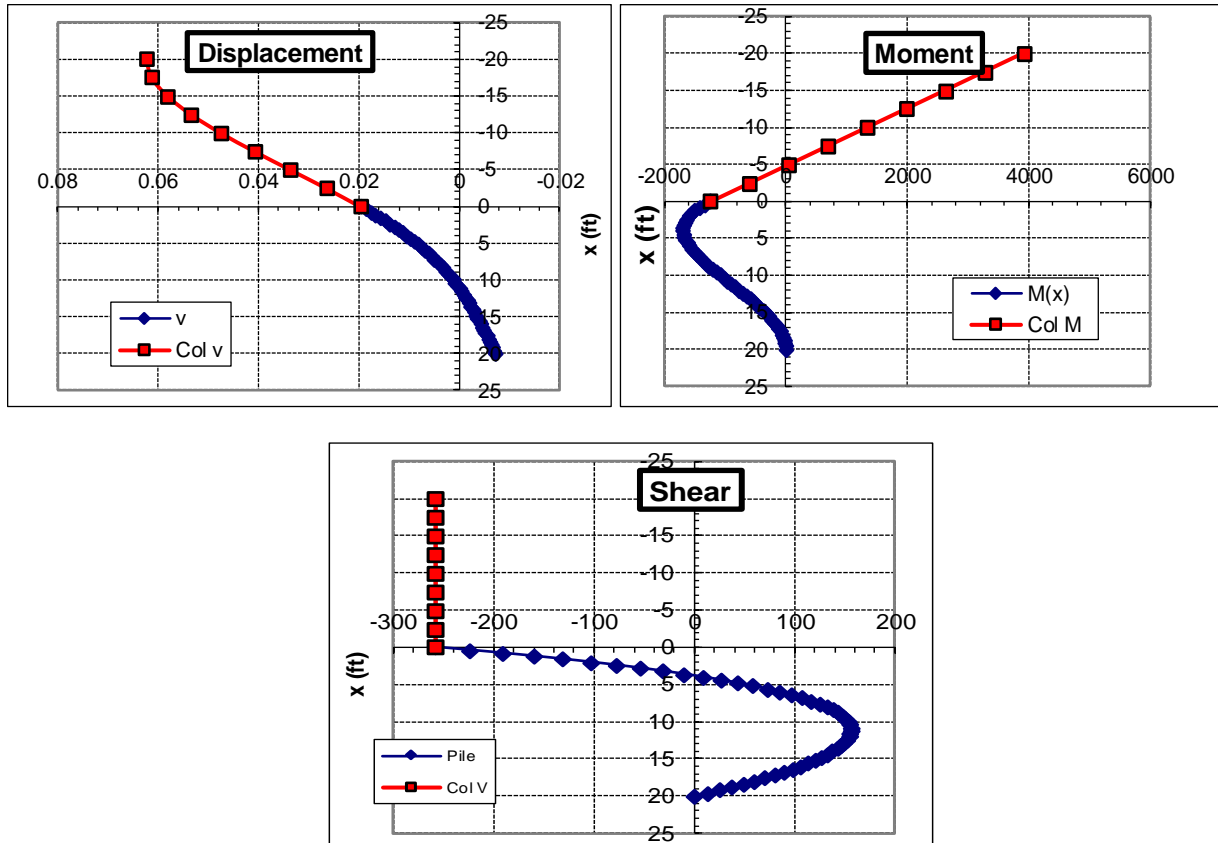
Figure 9-4. Distribution of elastic displacements, moments, and shear, using reference parameters. (ft, kip units.)

Figure 9-4 also shows that the above-grade column moment where the plug ends (4.5 ft below the cap beam) is smaller than the peak above-grade column moment (i.e. the filled section moment) by an amount equal to $V_{col}*L_{plug}$. The flexural strength of the filled section, calculated using the nominal steel strength of $f_y = 60$ ksi, is close to that of the hollow pile-column, reinforced with strand. This was found to be true in each of the four field bridges used here as examples, and it appears that the plug bars may have been chosen with that criterion in mind. It is therefore likely that the highest moment demand in the hollow above-grade column (just below the end of the plug) will be less than that section's capacity. In other words, the plug provides capacity protection for the hollow above-grade column if the stress in the plug bars does not exceed 60 ksi.

159

The moment demand on the filled section is greater than that on the hollow pile below-grade because the rotational fixity at the cap beam is higher than that provided by the soil. This can also be seen by the fact that the inflection point in the above-grade column is lower than its mid-height.

Figure 9-5 shows how the ratio of peak above-grade column/peak below-grade pile moment demand varies with soil stiffness, β_{soil}. As the soil becomes more flexible (compared with the reference value $\beta_{soil} = 1000$ kcf), the moment ratio increases. This occurs because the rotational fixity at grade decreases relative to the fixity at the cap beam, thus attracting larger moment demands to the cap beam. The peak in the curve at $\beta_{soil} = 125$ kcf occurs because, with soil stiffness values lower than that, the distribution of moments along the below-grade pile is such that the peak below-grade pile moment occurs at grade rather than below it because the point of inflection is now below-grade; however, in all cases, the moment ratio is greater than or equal to 2.0.
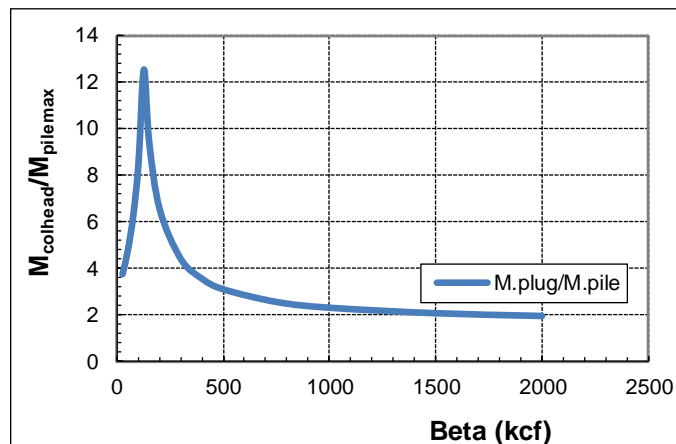
Figure 9-5. Ratio above-grade column/below-grade pile peak moment, using reference parameters (other than $\boldsymbol{\beta_{soil}}$.)

The highest moment experienced by any hollow section (either above or below-grade) usually occurs just beyond the end of the plug, and it is of interest to know the demand/capacity ratio

160

(DCR) there, because it indicates the margin of safety for the hollow sections. Note that the capacity used here is the flexural capacity based on the assumption that the strands are fully developed at the critical location. The value of the DCR changes with parameters such as soil stiffness, above-grade column height, and pile-column axial load. The presence of a deck that can resist some of the transverse load as a horizontal beam is also beneficial but is not shown here. (Those results were obtained by including the transverse bending stiffness of the deck, assuming that it had pin supports at the abutments). The DCR is plotted against soil stiffness, β_{soil}, in Figure 9-6. It rises with softer soils because then the moment at grade level is smaller, the inflection point is lower, and the moment at the end of the plug increases.
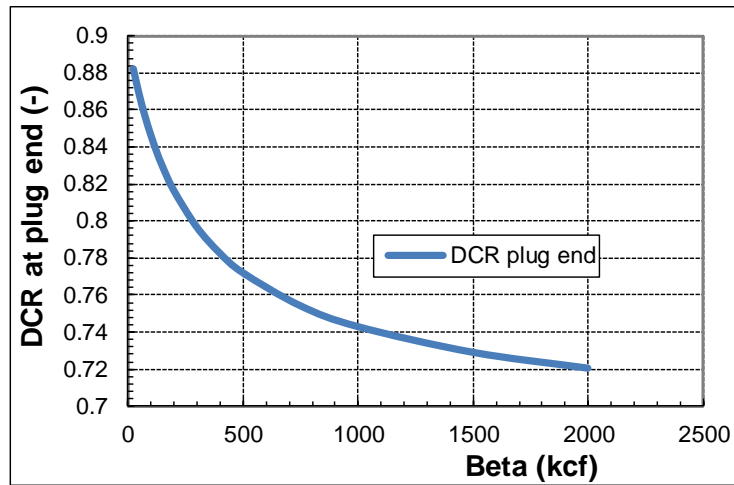
Figure 9-6. Influence of soil stiffness on DCR at bottom of plug.

The DCR at the end of the plug is also affected by above-grade column height. This is shown in Figure 9-7, which shows that the DCR increases for taller above-grade columns. This occurs because the plug length (always approximately 4.5 ft. or one pile-column diameter) is a smaller fraction of the total above-grade column height, so the moment demand at the plug end is closer to the peak moment demand, which is itself quite close to the hollow section capacity. However, it should be noted that this finding is based on the plug (within the filled section) reaching its yield moment. A bridge with very tall above-grade columns, such as the SR520 spur from I-5, will have a longer period and attract lower seismic forces. That plug may never yield.

161
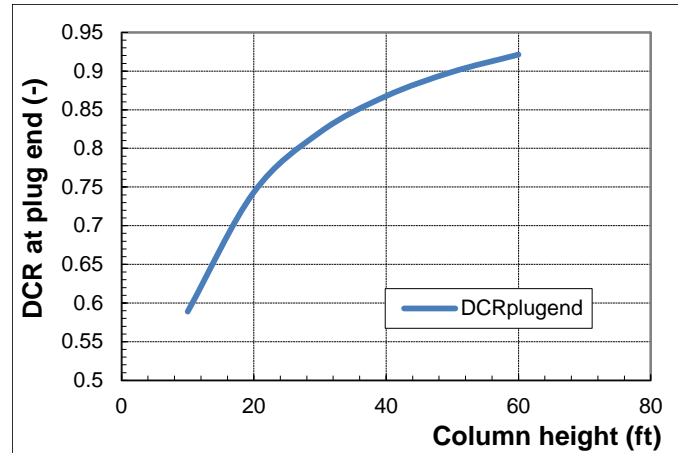
Figure 9-7. Effect of above-grade column height on DCR at the end of the plug.

The DCRs in Figure 9-6 and Figure 9-7 show that if the strands are fully developed and the nominal flexural strength can be reached, the pile-columns are capacity protected by the plug acting as a fuse within the filled section. However, the pile-column will be susceptible to at least tension cracking in that region when the plug yields. If, as seen in the cantilever bending tests, cracking of the pile-column wall leads to strand debonding and subsequent flexural failure at a moment less than M_n, the capacity protection is no longer effective. This finding emphasizes the need for preventing the strand from debonding, and the primary way to achieve that is to prevent flexural cracking by adding a stiffening element, such as a steel jacket.

The approximate magnitude of earthquake that would cause the plug to yield for different soil stiffness values is shown in Figure 9-8. This is represented by the F_{EQ} factor described in the previous section. The reference earthquake has PGA = 0.40g, and a peak spectral acceleration of 1.0g. Therefore, an F_{EQ} of 0.80 indicates that plug yielding should be expected in an earthquake of PGA = 0.80*0.40 = 0.32g. For all but exceptionally soft soils, the F_{EQ} lies in the range 0.50 – 0.60, implying that an earthquake with PGA $\geq$ 0.50*(0.4g) = 0.20g would be necessary to cause plug yielding.

162
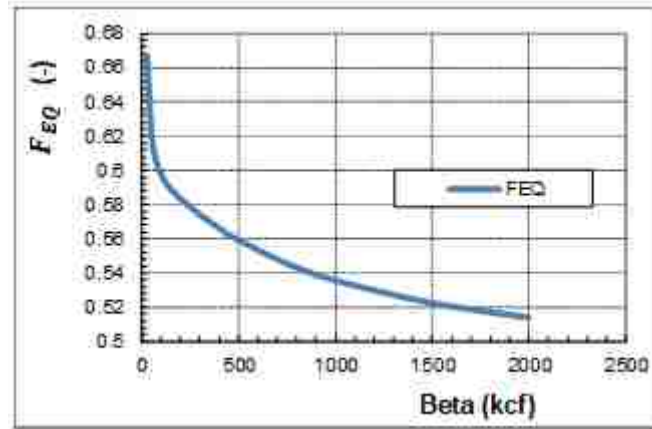
Figure 9-8. Earthquake Scale Factor for plug yielding vs soil stiffness.

9.1.3 *Inelastic Response*

After the plug yields, the moment there cannot increase if the filled section is modelled as elasto-plastic. Further increase in the applied load therefore causes higher moments in the below-grade pile, while the effective period lengthens. The plug yielding was simulated in the model by setting the stiffness of the rotational spring at the above-grade column head to zero, and adding an applied moment equal to the plug flexural strength (3919 ft-kips, in the presence of the 564-kip column axial load). The plug was assumed to have infinite rotational ductility, and to have no additional flexural strength as a result of the CFRP jacket. (The jacket hoop strains measured in the tests were too small to provide a significant increase in concrete compressive strength, and the response of the plug region was anyway controlled by the tension strength of the plug bars, and not by compression capacity. This hypothesis was confirmed in the retrofit cantilever bending test).

The next major event, after yield of the plug bars, is expected to be inelastic bending in the hollow pile below-grade. It is of interest to know the F_{EQ} necessary to cause that peak below-grade pile moment to reach the flexural strength, M_n, of the hollow section. That scale factor is shown in Figure 9-9a as a function of the soil stiffness, β_{soil}, and in Figure 9-9b as a function of above-grade column height. At low soil stiffness the system is flexible, so the corresponding period is long. The F_{EQ} thus has to be large in order to generate forces large enough to induce

163

pile yielding below-grade. For example, for β_{soil}= 200 kcf, the necessary F_{EQ} is 1.62, meaning that the PGA must be 1.62* 0.40g = 0.642g to cause yielding below-grade. At the reference value of β_{soil} (1000 kcf), the F_{EQ} is 0.96 so the PGA is 0.38g. Very stiff soil can be seen to be the most damaging condition.
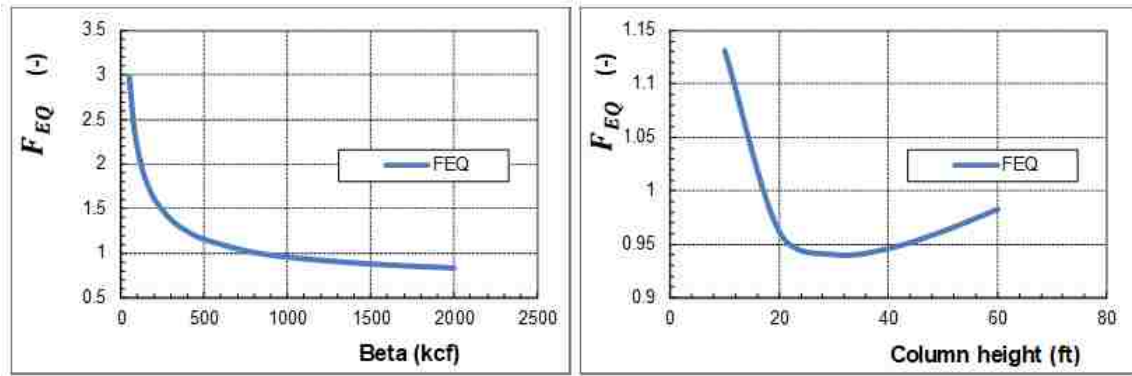
Figure 9-9. F_{EQ} needed yield the below-grade pile as a function of (a) β_{soil} and (b) L_{col}

The elongation of the effective period caused by plug yielding can be seen in Figure 9-10, which shows the effective period before and after plug yielding. In both cases, the pile below-grade remains elastic. Plug yielding causes the period to increase by 25% - 40% in the likely range of soil stiffness $500 < \beta_{soil} < 2000$ kcf.
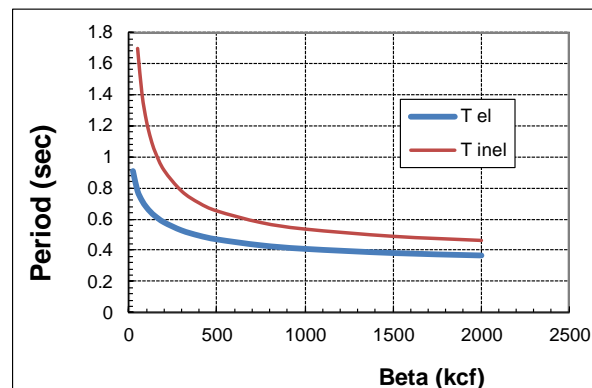
Figure 9-10. Period, before and after plug yield, as a function of soil stiffness

After the plug yields, it must undergo inelastic rotation when the load is increased. The inelastic rotation of the plug, between first yield of the plug and first yield of the pile below-grade, is given in Figure 9-11a as a function of soil stiffness. The required plug rotation is large at low soil stiffness, but rapidly diminishes in more competent soil, with $\beta_{soil} \geq 500$ kcf. As the cantilever bending tests showed, even the 0.01 radians (or 1%) of plug rotation predicted for $\beta_{soil} = 300$ kcf can easily be sustained, particularly if the above-grade column is jacketed. The implication is that below-grade pile yielding, rather than failure by insufficient rotational ductility capacity of the plug, will limit the seismic loading that can be resisted. Figure 9-11b shows the required inelastic plug rotation as a function of above-grade column height, using the reference values for other parameters. The rotation demands do not vary much and remain easily within the capacity of the plug. In all cases the below-grade pile length was taken to have its reference length of 20 ft. Except for very soft soils, increasing the below-grade pile length beyond 20 ft. (not shown here) made almost no difference to the outcome.
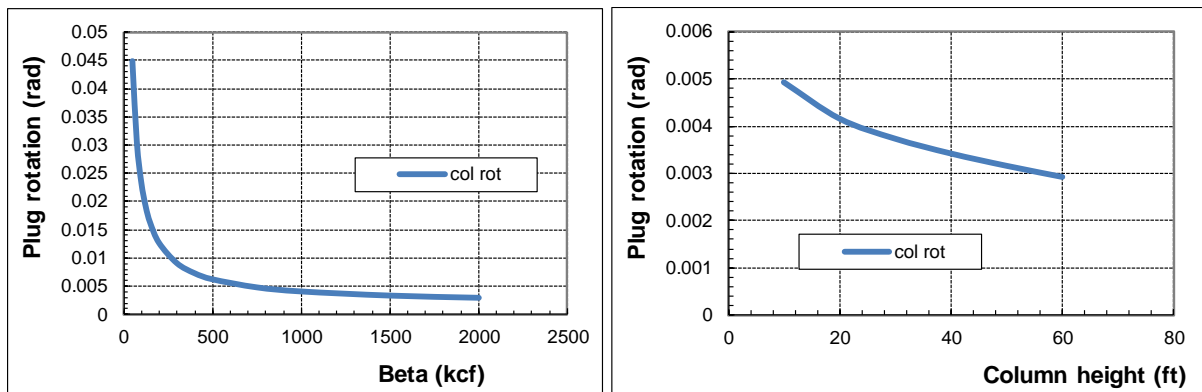
Figure 9-11. Inelastic rotation of the plug as a function of (a) soil stiffness and (b) column height.

9.1.4 *Comparison using OpenSees*

Tardieu, following publication of her thesis, modelled a single four-pile-column bent in OpenSees with linear elastic beam-column elements to represent the below-grade pile, above-grade column, and cap beam, representative of the same model shown in Figure 9-1. Each

165

element was six inches in length and the pile-columns were restrained from all displacements and rotations except for in the direction of loading at both the top and bottom.

Zero-length spring elements were used to model the soil and were connected to the pile along its depth at discrete points. These springs were assigned a uniaxial elastic material property in the lateral direction of loading. The spring elements were fixed on one end in all directions and attached to the pile nodes on the other end (see Figure 9-12).

An elasto-plastic rotational spring at the top of each pile-column was used to represent the expected non-linear behavior at the pile-column-cap beam connection. The spring was assumed to enter the plastic phase when the nominal yield moment of the filled section at the top of the above-grade columns was reached. The spring elastic stiffness was defined as 1000 times that of the pile-column (an arbitrarily high number). A linear spring represented the stiffness of the deck acting as a horizontal beam between the abutments, as appropriate.

The mass of the system was assumed to be shared equally among the pile-columns of the bent, and was comprised of the estimated mass of the superstructure elements, including the deck, girders and cap beam. The gravity load was applied using a load control integrator in ten steps and then held constant. The lateral loading was applied using a displacement-controlled pushover sequence at the cap beam level.

The Newton-Raphson method was used as the solution algorithm and convergence was tested using the Norm Displacement Increment Test command. A convergence loop was used for the nonlinear analyses in order to try other solution algorithms if the analysis failed before converging to the next displacement. The loop tries a Newton Raphson solution with an initial tangent and the Energy Increment test, a Broyden algorithm, and a Newton Raphson solution with a line search. If convergence is met within the set number of iterations, the analysis continues and returns to using a Newton Raphson algorithm, otherwise the analysis fails, and the pushover is completed.

166
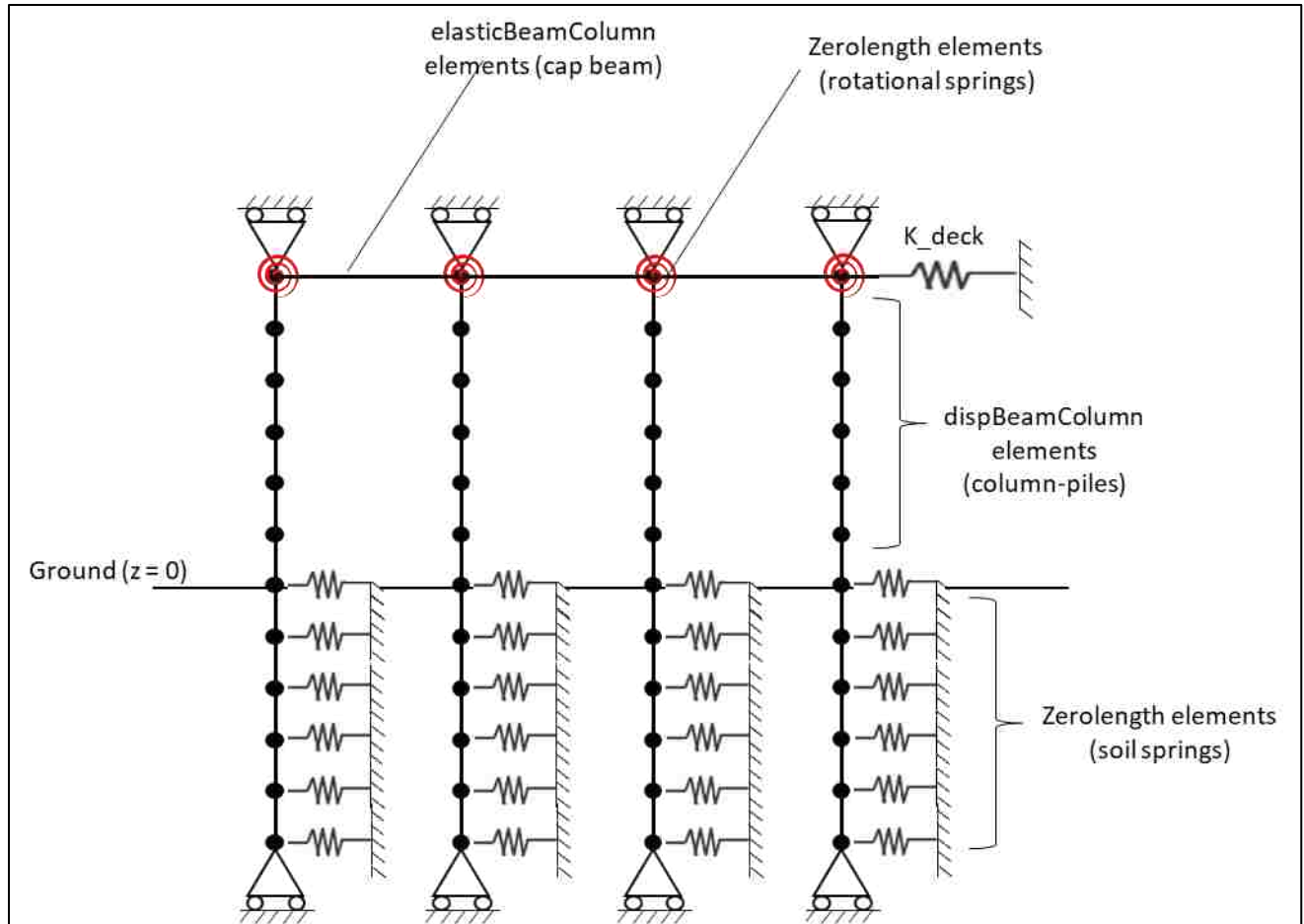
Figure 9-12. Illustration of OpenSees model

The forces, moment and displacements along the length of the pile-column were recorded. In particular, the lateral force and displacement at the top of the above-grade columns was determined for each iteration of the parameter study in order to use a response spectrum single-mode analysis for the earthquake loading to obtain the results of the parametric studies. The comparison of this model to the excel model using beam-on-elastic-foundation formulation for the parameters that had the most significant impact on F_{EQ}, namely soil stiffness and above-grade column height are shown in Figure 9-13. This earthquake scale factor represents the scale factor to cause flexural failure in the below-grade pile. The results are nearly identical. (Note the vertical scale in Figure 9-13b). This good agreement is taken as verification that the excel model was programmed correctly and working as expected, in which case its results can be accepted. It was used because of the time needed to learn OpenSees, and because it has an almost instantaneous run time, which is suitable for parametric studies.

167
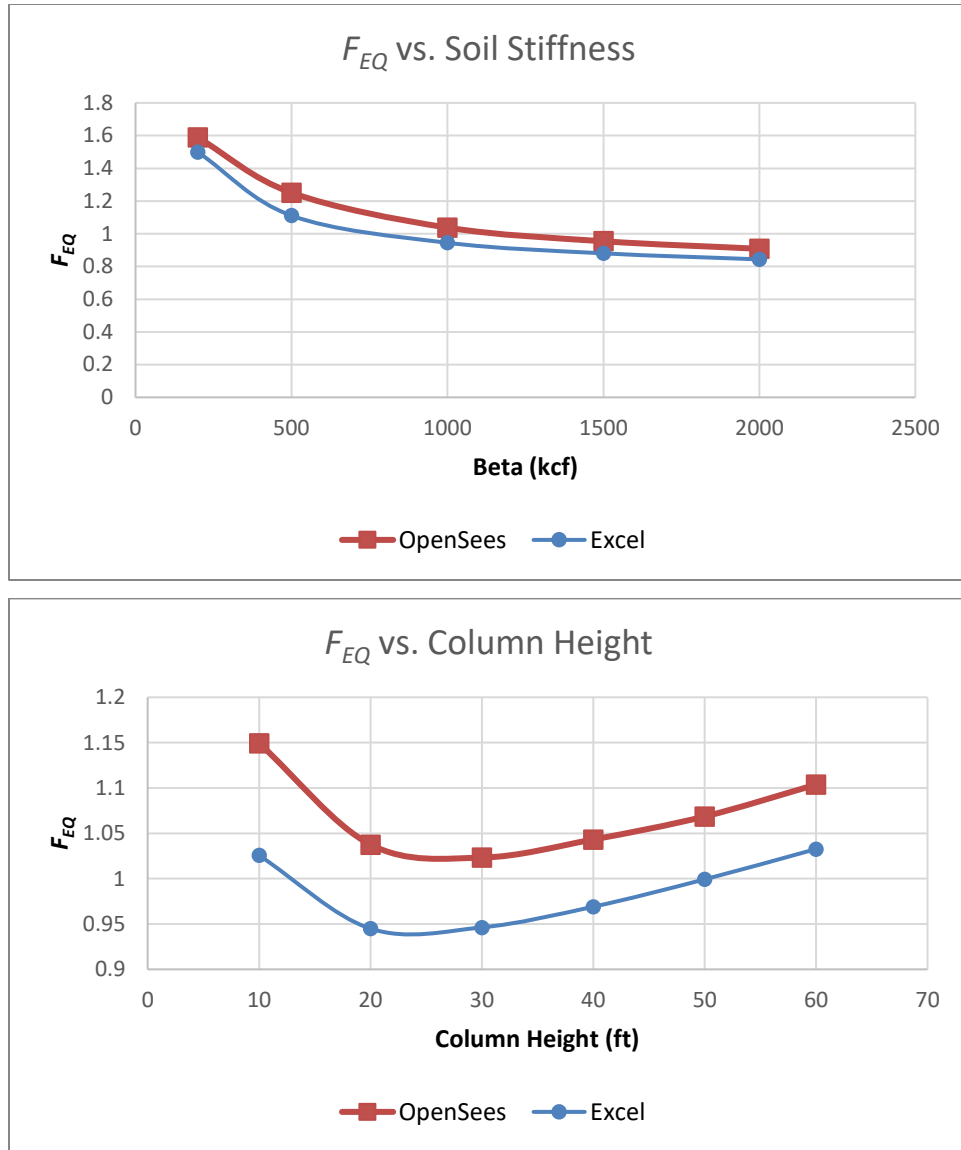
Figure 9-13. Earthquake Scale Factor vs. soil stiffness and above-grade column height

9.2 SYSTEM VULNERABILITIES

The various system vulnerabilities are reviewed here with the intent of providing guidance for prioritizing retrofit resources.

The primary vulnerability of the hollow pile-column system is

- Above-grade column cracking at about the end of the plug, followed almost immediately by strand bond failure, buckling, and fracture in succeeding half cycles.

Other, less probable, vulnerabilities include:

- Fracture of plug bars. No such fracture was observed in the tests, in which the filled section rotation reached 5%. The bar strain also exceeded 6%, after which the gages failed. As expected, the plug bars partially debonded during the test; this behavior relieves some of the strain concentration that would otherwise occur at the primary crack at the column-cap beam interface. Some slip also occurred at the interface between the plug and pile-column wall. It should be noted that, even if the plug bars were to fracture in tension, that event would not jeopardize the ability of the system to carry gravity load. The test evidence suggests that they will remain intact until at least 5% rotation (corresponding to more than 5% drift because of the additional elastic deformation of the column). After that level of drift, extensive damage to other parts of the bridge will have already taken place.

- Shear failure in the hollow section. This will occur only if the cantilever length (from peak moment to inflection point) is less than 2-2.5 pile-column diameters, depending on the reinforcement ratio (see Figure 9-14). The exact value also depends on other pile-column properties, such as level of prestressing, magnitude of axial load, and spiral steel content. The values plotted in Figure 9-14 were obtained using the reference dimensions found in Table 9-1 and Response2000. The lines titled "Vflex" represent the transverse load capacity if the specimen experiences a pure flexural failure, while the lines labeled with respective reinforcement ratios represent the transverse load capacity accounting for shear interaction. It is concluded that failure dominated by shear requires a combination of a very short above-grade column, a very deep below-grade pile embedment, and very stiff soil. Such pile-columns are either non-existent or in a very small minority.

169
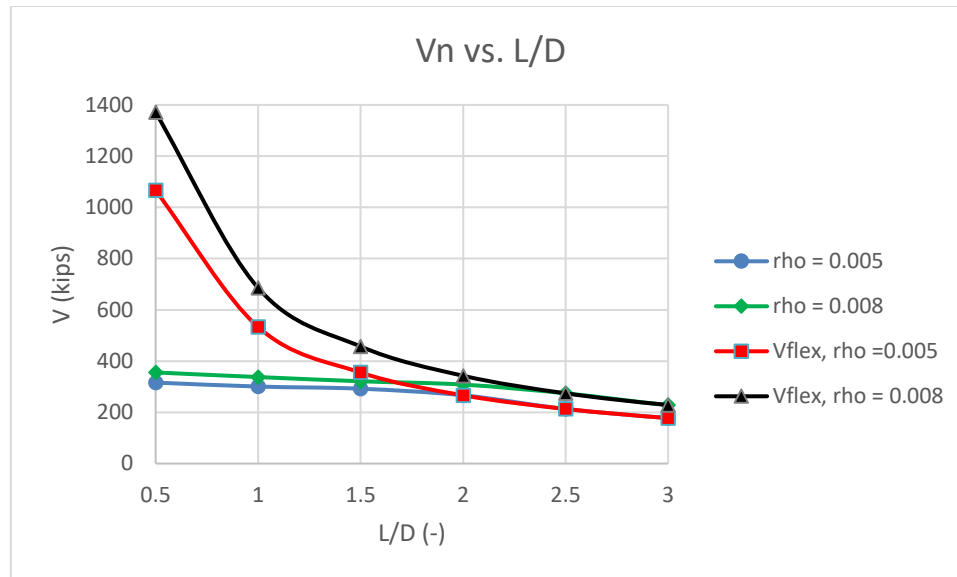
Figure 9-14. Transverse load capacity vs shear span ratio

- Flexural failure below-grade. The analyses showed that, for the reference conditions (20 ft. high above-grade column, 20 ft. long below-grade pile, β_{soil} = 1000 kcf) the pile below-grade will reach its flexural capacity at an Earthquake Scale Factor of approximately 1.0, i.e. under the design level earthquake. Note that this value was based on the 5% damped spectrum. In the field, the damping is expected to be higher, especially since the plug bars are yielding, in which case the Earthquake Scale Factor would be higher. However, the pure bending test showed that the hollow section has a flexural ductility ratio of approximately 3, so that, under that ground motion, it will undergo significant inelastic deformation before failing catastrophically. Even if the below-grade pile did lose its flexural strength, perhaps by fracture of the strands, the surrounding soil prevents relative lateral displacement of the two faces of the cracked concrete, so the below-grade pile is likely to retain its vertical load carrying capacity through direct bearing.

- Beam shear and joint shear in the cap beam. Many of the cap beams in the field have a depth approximately equal to or less than the pile-column diameter. They were typically reinforced for gravity shear alone, using two-legged rectangular ties with 90-degree closure bends at the corners. Furthermore, the beam-column joints typically contain little

170

or no joint shear reinforcement. These deficiencies leave the beams and joints potentially vulnerable to shear failure during an earthquake. The details are bridge-specific, and techniques for retrofitting them lay outside the scope of this study. However, they should be investigated on a case-by-case basis. Retrofit may be necessary.

This review, combined with the cantilever bending test results, shows that the most important, and most probable, failure mode is flexural failure associated with strand debonding near the end of the plug. The failure mode previously thought to be critical, namely implosive flexural failure of the hollow section, is prevented in these pile-columns by the fact that the plug acts as a fuse and capacity-protects the hollow section.

9.2.1 *Capacity Protection*

Capacity protection of the free height hollow column just beyond the end of the plug is ensured if the flexural capacity of the filled section (with the plug reinforcement only providing tension capacity) limits the maximum possible moment demand at the end of the plug to less than or equal to the capacity of the hollow section (with only the strands providing tension capacity). However, if the moment capacity of the filled section is greater than that of the hollow section, the moment demand in the hollow section (beyond the end of the plug) may or may not exceed the capacity. That outcome will depend on both the strength ratio of the filled and hollow sections, and the ratio of plug length to the distance down to the inflection point. Moment-curvature analyses of the field bridges, using the Raynor model for monotonic strain hardening and $f_y = 60$ ksi for the plug reinforcement, showed that all of the reference bridges except for Slide, possess this capacity protection. However, in the cantilever tests the strength of the plug reinforcement had to be set to approximately 82 ksi (using an elasto-plastic model to get the reinforcement stress at failure), as described in Section 8.3, to match the measured capacity. If the bar stresses in the field columns were to show similar increases, the level of capacity protection for the hollow columns would drop.

Figure 9-15 shows the effect of the plug reinforcement strength, using an elasto-plastic stress-strain relationship, on the capacity protection of the hollow section (represented by the DCR

171

described in the previous chapter). The elasto-plastic model was used to provide independence from the details of the strain hardening properties, for this particular investigation. The distance to the inflection point is taken as 14 ft. (or $0.7L_{col}$) and the plug length is taken as $1.0D_{col}$, the pile-column diameter for the respective bridge. The plot shows that the reference bridges have effective capacity protection for 20-foot tall above-grade columns (with all other reference parameters also in accordance with Table 9-1). If the above-grade column height is doubled, the capacity protection is jeopardized for the Slide Bridge (see Figure 9-16).
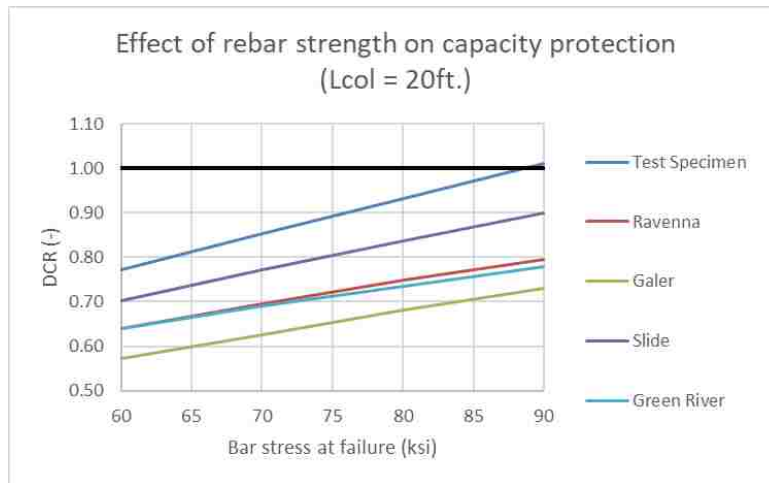

Figure 9-15. Effect of bar stress at failure on DCR at end of plug (Lcol = 20 ft.)
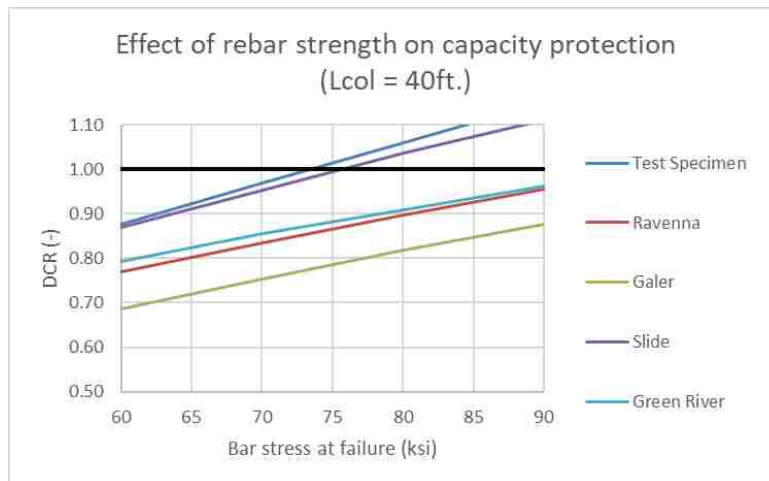
Figure 9-16. Effect of bar stress at failure on DCR at end of plug (Lcol = 40 ft.)

172

Table 8-3 provides the material properties for the strain hardening curve used in the monotonic moment-curvature analysis to match the test results. If the same strain hardening curve is applied to the reference bridges in the field the capacity protection may be in jeopardy; Table 9-2 shows the resulting DCR values for above-grade column heights of 20 ft. and 40ft. The conclusion is that the capacity protection of the tall columns in the field may be at risk if the plug reinforcement experiences an increase in strength due to cyclic strain hardening similar to what was seen in the cantilever tests. In addition, the increase in strength of the filled section increases the risk of debonding of the strands.

Table 9-2. Capacity protection of field bridges with Raynor strain hardening curve

Reference Bridge	$\dfrac{M_{n,filled}}{M_{n\_hollow}}$	DCR (L_{col} = 20 ft.)	DCR (L_{col} = 40 ft.)
Ravenna Overcrossing	1.04	0.75	0.90
Galer-Lakeview	0.96	0.69	0.82
LE Line Slide	1.23	0.96	1.09
Green River	1.08	0.85	0.96
Test Specimen	1.20	0.95	1.07

9.3   MITIGATION STRATEGIES

The following mitigation strategies are recommended. The discussion focuses on the problem of pile-column wall cracking, because without cracking the strand stress cannot increase and debonding will not occur.

9.3.1   *Pile-Column cracking and strand slip*

Possible approaches include:

- *Use the lateral strength and stiffness of the deck to resist most of the seismic loading.* This will provide the best protection for the pile-columns by keeping the displacements small enough to minimize the moments induced in the pile-columns. It is possible only if the deck is continuous, with no joints, and if the force can be transferred to the abutments through

173

reliable shear keys. However, the deck is likely to be much stiffer and stronger than the pile-column bents and offers a unique benefit in this situation. This approach is particularly plausible for continuous box girder bridges, such as the Green River Bridge, which lack the joints typical between prestressed girder spans of the era.

- *Add a CFRP jacket consisting of both vertical and hoop fibers.* The vertical fiber is intended to inhibit the splitting of the fiber jacket that was observed in the retrofit cantilever bending test. The sheets of vertical fiber should be stopped off progressively to prevent stress concentrations, with the longest extending down to the point where the net axial stress in the concrete (in the pile-column wall) is zero, and the shortest extending halfway from that point to the plug end.   It can be shown that the CFRP will not be stiff enough to materially affect the tension stress in the pile-column wall unless a very large number of layers are used, so the goal of this approach would be to restrain the width of the flexural crack once it has initiated. (Analysis shows that the thickness of CFRP jacket theoretically needed to provide the stiffness to *prevent* cracking is approximately 19 layers of Tyfo SCH-2X. This is both impractical and so thick that it is unlikely to behave in the manner predicted by classical theory). This retrofit method was not tested, so no information is available about the detailed requirements for its successful implementation. However, experience in other projects with applying CFRP sheets to flat surfaces suggests that providing sufficient bond of the sheets to the concrete may be the most difficult problem. The critical region lies near the end of the plug, where the strands are not fully developed. Since the CFRP will not be stiff enough to *prevent* cracking, it is logical to say it will not succeed in preventing the widening of the cracks without the aid of developed strands. The CFRP will start to debond on either side of the crack by forming a splitting plane, parallel to the fiber plane and in the concrete paste just below the interface. Once debonding has initiated, the splitting tends to propagate rapidly with little ductility. Wrapping the hoop-direction sheets over the longitudinal ones may help, but the benefits of that interaction are unknown.

- *Add a steel jacket, thick enough to stiffen the pile-column* in that region and so prevent the cracking, but as short as possible consistent with preventing the cracks from forming.   If, perchance, the pile-column cracks anyway, the steel jacket will be strong enough to inhibit crack opening. This retrofit option was not tested, so detailed proposals for implementation

174

can only be based on calculation. Proposed design procedures are developed in Section 9.4. However, it should be emphasized here that the jacket should stop just short of the cap beam in order to avoid increasing the flexural strength of the filled section there, hence jeopardizing the capacity protection that the filled section otherwise provides. A steel jacket will slightly increase the flexural stiffness of the body of the pile-column, in the region where it exists. However, the cantilever bending tests showed that the great majority of the drift capacity was furnished by inelastic rotation of the end of the plug; the rest of the specimen rotated essentially as a rigid body. Making that rigid body even more rigid by jacketing will not materially influence the total rotation capacity.

9.3.2 *Shear failure in the hollow pile-column*

Shear, or more precisely combined shear and bending, is a problem only in very short above-grade columns. In medium to long above-grade columns, the lateral strength is controlled by the formation of two flexural plastic hinges, one at the cap beam level (in the plug) and another near grade level. The accompanying shear demand is low enough that it has very little effect on the flexural strength. The flexural demand is highest at the top, and there it is controlled by the strength of the filled section. Near grade, the flexural demand is smaller, as a result of the flexibility of the soil. Shear failure in a medium to long above-grade column is therefore almost impossible. In a very short above-grade column, typified by a shear span ratio less than 3, the shear strength becomes more important. (The shear span ratio is the distance from the peak moment to the inflection point, divided by the pile-column diameter). It is believed that very few such pile-columns exist. If they do, the problem could be mitigated by the addition of a full-length jacket or perhaps by filling the void in the pile-column with concrete. Filling the pile-column might be difficult in practice, and would involve cutting some strands in order to accommodate a tremie tube. The consequences of cutting strands was not investigated here.

9.3.3 *Flexural failure in the below-grade hollow pile*

Retrofit of the below-grade pile for improved flexural performance is likely to be extremely difficult. Fortunately, the system analyses showed that a ground motion equal to approximately 1.0 times the design event would be needed to induce a moment of $M_{n,hollow}$ below-grade. Failure would be expected to be by flexural failure (strand yielding and concrete crushing). Failure by

175

strand debonding is unlikely because the peak moment occurs too far from the free end at the bottom of the below-grade pile. However, if the below-grade pile were spliced near the peak moment, the plug in the splice would behave like the plug at the cap beam level, and debonding would be possible. The below-grade piles at Green River might have been spliced, and the pile-columns at Galer might have been connected to a cast-in-place lower section. In both cases the solution chosen by the contractor is not clear. If retrofit were found to be necessary, for example because of an extreme combination of properties, the critical behavior is external spalling, for which the primary method of mitigation would be jacketing. This would require excavation. In an environmentally sensitive region, this could trigger regulatory restrictions.

9.3.4 *Cap beam joint shear failure*

The joint is likely to be one of the more difficult elements to retrofit, and the choice of method may dictate the method chosen for the cap beam as well, because they may be retrofitted as a unit. The retrofit should anyway be considered on a case by case basis, because, for example, the geometry of the elements is different for prestressed concrete bulb tee girders and for reinforced concrete box-girder bridges. One possibility would be to increase the size of the cross-beam cross-section by doweling, adding a supplementary cage, and casting more concrete around the existing cap beam. However, if this choice is implemented, it is important to avoid enveloping the above-grade column head in new concrete. Doing so would risk moving the point of fixity down the above-grade column, and hence subjecting the hollow region directly below the plug to a higher moment. That would jeopardize the hollow section there and be counter-productive.

9.3.5 *Abutments*

The shear keys at the abutments may need to be retrofitted if the deck is used as a horizontal beam to transmit lateral loads from the deck to the abutments. The lateral load capacity of the shear keys then plays a vital role in the load path. Standard methods of retrofit, or perhaps replacement, can be applied. The lateral shear strength of the girder webs should also be verified. Access for retrofitting is likely to be better at the abutments than at the internal piers, and no major implementation problems are foreseen for this type of retrofit.

9.4 RETROFIT OPTIONS

9.4.1 *Steel jacket*

The purpose of the steel jacket is to stiffen the above-grade column by acting compositely with the concrete wall of the pile-column, and to add to its moment of inertia. This will reduce the tension stress in the wall, and if the jacket is stiff enough, it will prevent cracking. Without cracking, the pile-column will not fail by debonding. The critical location is assumed to be near the end of the plug, as was the case in the tests, and is here taken to be at $z = 0.90 \, L_{plug}$, since the critical crack in the tests occurred at about $z = 35$ inches and L_{plug} was approximately 40 inches. The maximum applied moment that can occur at the critical location is governed by the flexural strength of the filled section adjacent to the cap beam. The design criterion is that, under that moment, the pile-column should not crack.

In the interests of simplicity, 100% of the pile-column moment, M_{col}, is assumed to be resisted by the wall at the critical location. That assumption is slightly conservative since the critical location lies within the disturbed region, so some of the demand is taken by the plug. The pile-column moment arises from seismic loading, after the jacket has been installed, so the stresses induced by it are shared between the pile-column wall and the steel jacket in accordance with their elastic stiffnesses (i.e. composite action). The peak bending stress, f_b, from the moment is given by:

$$f_b = \frac{E_c * M_{col} * \frac{D_{col}}{2}}{\sum EI} \tag{29}$$

To avoid cracking, the total stress must be less than the cracking stress, f_{cr}, multiplied by a suitable reduction factor, φ_{cr}. Thus:

$$f_b + f_{ax} + f_{0e} \leq \phi_{cr} f_{cr} \tag{30}$$

The value of φ_{cr} should be chosen to reflect the associated uncertainties. In reality, not only is the cracking strength uncertain, but so, too, are the axial load and effective prestressing level,

177

للاستشارات

both of which help to reduce the tension stress. The uncertainty in the cracking strength is expected to be greater than the uncertainty in the effective prestressing or axial load. It is suggested that a value of $\varphi_{cr} = 0.5$ be used to cover all of the uncertainties.
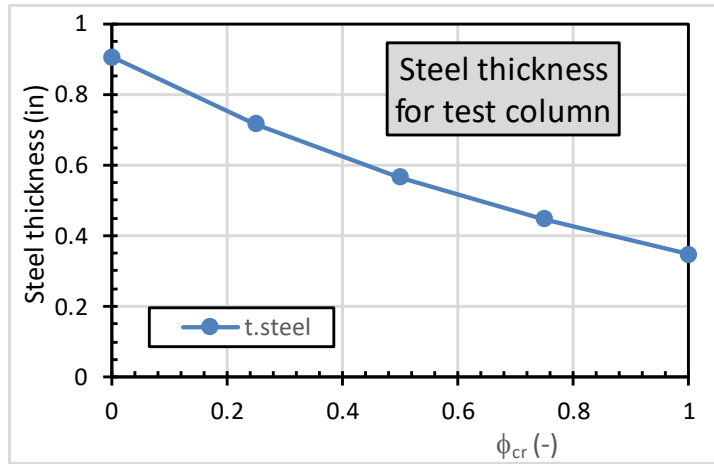
Figure 9-17. Effect of φ_{cr} on required jacket thickness (test specimen).

Figure 9-17 shows how φ_{cr} affects the required jacket thickness. A lower φ_{cr} value requires the total tension stress in the concrete to be lower, and thus the steel jacket to be thicker.
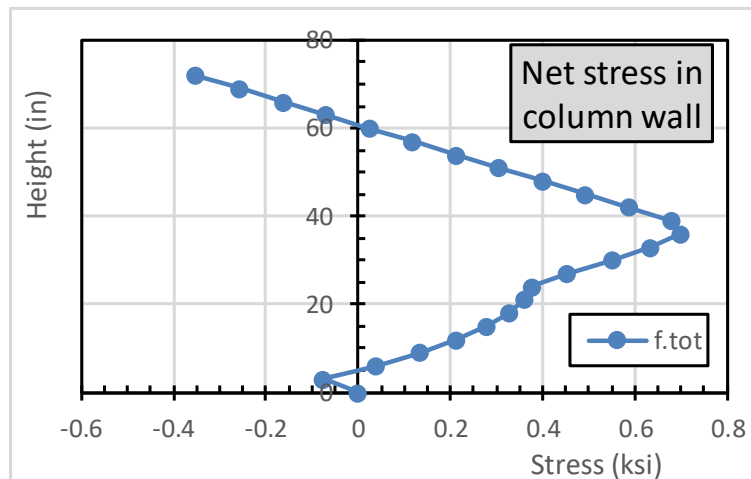

Figure 9-18. Vertical variation of total stress in pile-column wall. Test specimen, φ_{cr} $= 0.75$, $t_{jacket} = 0.44$-inches.

178

Figure 9-18 shows the variation of vertical stress in the pile-column wall for a jacket thickness of 0.44-inches, which is the thickness required if φ_{cr} were to be taken as 0.75. In all cases, the stress in the pile-column wall is maximal where the concentrated horizontal load is applied near the end of the plug and decreases above that. However, within the plug region ($z < 40$-inches here), the stress varies in a less clear pattern, especially for thinner jackets. This occurs because both the effective prestressing and the stress from the axial load vary in the plug region (see Section 8.3), but they depend respectively on the transfer length, L_t, and the variation shown in Figure 8-13.

The length of the jacket should also be chosen to ensure that debonding failure cannot occur. The simplest and most certain way to achieve that is to prevent cracking in the pile-column wall just beyond the end of the jacket. The stress there will consist of the prestressing, axial load and bending. The sudden change in stiffness caused by the jacket ending will likely cause a stress concentration, so it is advisable to ensure that the stress in the pile-column is less than the cracking stress. Ideally, the total stress in the pile-column should be zero or compressive. In a relatively short above-grade column, in which the moment gradient is high, reaching zero stress may require only a relatively short jacket. In a longer above-grade column, where the moment gradient is lower, the jacket length required to achieve zero stress in the concrete might be long enough to be expensive and cause practical difficulties. In that case, a second criterion is appropriate, namely that the jacket length be longer than the strand development length. Then, even if the pile-column cracks, debonding failure will not occur. The confinement provided by the jacket will, if anything, reduce the real development length (Scribner and Kobayashi, 1984), in which case the standard AASHTO l_d will be conservative.

9.4.2 *Other retrofit approaches*

Two other concepts were considered briefly, but were not analyzed in depth, nor were they tested. The first was a CFRP jacket, and the second was a concrete jacket.

179

For a CFRP jacket, the following considerations are important:

- The CFRP jacket used in the test contained only circumferential fibers and was ineffective in preventing the initiation of new transverse cracks or the widening of existing ones.

- A jacket with fibers oriented only in the hoop direction does have the potential to inhibit longitudinal splitting and prying action of the solid plug in a pile-column with inadequate spiral in the wall. The test pile-columns contained adequate spiral, so this longitudinal splitting and prying action were not observed.

- To inhibit transverse cracking, any jacket must have both strength and stiffness in the longitudinal direction. Theoretically these properties could be provided by a CFRP jacket with biaxial fibers; however, such a configuration was not tested. Furthermore, even theoretical predictions suggest that it would be unlikely to be effective. First, the longitudinal *strength* would probably be controlled by the bond between the fiber jacket the concrete, and that transfer usually results in failure of the cement paste approximately 1/8-inch below the surface of the concrete at a relatively low bond stress. Second, achieving sufficient longitudinal *stiffness* would require many layers of fiber - on the order of 20 layers, even if they were all 100% effective, which they would almost certainly not be.

- Without extensive further research, including testing, use of a CFRP jacket cannot be recommended for addressing the critical debonding mode of failure identified in this research.

For a concrete jacket, the following should be considered:

- The cross-sectional area must be great enough that the jacket satisfies the same flexural stiffness criteria as does the steel jacket. Thus, the concrete thickness should be about *n* times the thickness of the steel jacket, where *n* is the modular ratio.

- A form will be needed for casting (or pumping) the concrete. A good approach would be to use a steel tube as a form, and to then leave it in place. This is comparable to leaving the casing in place in a drilled shaft. For the equivalent of

180

a ¾-inch steel jacket, for example, 2.5-inch thick annular concrete region inside a $^3/_8$-inch thick steel casing would theoretically provide sufficient stiffness.

- UHPC would be a good choice for the filling material. Its high modulus value, combined with its good bond and tension capacity would help to maintain its integrity under load.
- The surface of the existing pile-column wall should be roughened prior to installing the retrofit.

Chapter 10. SUMMARY, CONCLUSIONS, AND RECOMMENDATIONS

10.1 SUMMARY

A research program was undertaken to investigate the seismic response of, and retrofit concepts for, bridges supported on hollow, prestressed concrete pile-columns. Previous studies have shown that hollow pile-columns are vulnerable to brittle flexural failure caused by internal implosion of the wall. Two locations in the pile-column are particularly susceptible to large moments which could trigger this mode of failure. These are (1) just below a solid reinforced concrete plug at the cap beam-column connection and (2) below-grade.

This work is the second phase of a two-phase research program. In this phase, three experiments were conducted:

- Hollow specimen under pure bending (a four-point bending test)
- Hollow specimen under combined shear and bending (a three-point bending test)
- Column-to-cap-beam connection retrofitted with a CFRP wrap (a cantilever bending test)

The behavior of the test specimens was modeled using moment-curvature analysis, Response2000, and maximum principal stress analysis in accordance with the criterion defined in ACI 318-19 Section 22.5.6.3.3. Good agreement was reached with the measured results.

Analyses of a complete bridge were conducted using a condensed model that had been verified against OpenSees for the purpose of determining the distribution of forces within the pile-column under different bridge geometries and soil properties. That distribution of forces was used to guide development of retrofit concepts.

The primary retrofit concept investigated was the use of the above-grade column-to-cap-beam connection as a ductile fuse that would provide capacity protection for the hollow regions of the above-grade column beyond the end of the plug region. The cantilever bending test, equipped

182

with a CFRP jacket, was intended to verify the performance of that concept. However, that test revealed an unexpected mode of failure, namely failure of the prestressing strands in the pile-column wall by debonding. Further analysis of the test data showed that this mode of failure, and not inwards spalling of the pile-column wall, which had previously been seen as the critical mode, would likely govern failure of most hollow pile-columns in the field.

Alternative retrofit concepts were therefore developed, but they could not be tested within the resources allocated to the project. The most promising concept developed analytically was to use a steel jacket around the plug region, in order to stiffen it sufficiently by composite action to reduce the tension stress in the pile-column wall and thereby prevent cracking and subsequent loss of anchorage of the strand.

10.2 CONCLUSIONS

10.2.1 *Experimental Results*

- The plug connection between the hollow pile-column and cap beam has the potential to undergo considerable inelastic deformation. If the flexural strength of the connection is low enough, it may be used to capacity protect the other hollow regions of the pile-column. However, the other failure mechanisms, such as loss of strand anchorage, must be suppressed.
- In the field bridges studied here, the flexural strengths, using nominal material strengths, of the plug (the "filled section") and the hollow pile-column, were similar. Then the effectiveness of any capacity protection depends on the reduction in moment over the length of the plug. Any strain hardening in the plug reinforcement, or a plug that is short relative to the above-grade column length, will reduce the effectiveness of the capacity protection.
- In pure bending, of an unconfined hollow pile-column, internal spalling does not <u>initiate</u> flexural failure. Rather, failure is initiated by external spalling, as in a solid column, at an extreme compressive strain of approximately 0.003 in/in. For the hollow pile-column geometry used for WA state bridges in the 1960s, typified by a diameter/wall thickness

183

ratio of approximately 11, the post-peak loss of strength will be much more sudden than in a solid column of the same size.

- A prestressed concrete section behaves quite differently from a non-prestressed reinforced concrete one. The load-displacement curve exhibits significant nonlinearity even while the materials remain elastic. If this behavior is used to define ductility, the ductility ratio was approximately 3 in the pure bending test.

- Good agreement was found between the result of the three-point combined shear and bending test and the two models used to characterize it. Either model (Response2000, based on the Modified Compression Field Theory, or the ACI maximum principal stress criterion) may be used to estimate the transverse load capacity of the pile-columns.

- When extrapolating the two models to field conditions, it was deduced that failure dominated by shear in a hollow section is likely to occur only in very short above-grade columns (i.e. with a shear span ratio less than approximately 3). Such configurations are believed to be rare in Western Washington.

- The critical mode of failure in the as-built column-to-cap-beam connections is expected to be cracking of the pile-column wall near the end of the plug, followed by bond failure of the strands. Once the strands slip, they will buckle on the next half cycle of displacement, and fracture on the following cycle when they re-straighten.

- The addition of the CFRP jacket (with only circumferential fibers) provided very little improvement in either strength or ductility. It also did not eliminate the critical failure mode (i.e. strand bond failure).

- The test specimens showed no evidence of being pried open by the plug at the end of the pile-column. This had originally been seen as a potential failure mode, but may have been suppressed by the tightly wound spiral at the ends of the specimens. If that spiral were not present in the field pile-columns, for example because the above-grade column head had been cut off after driving to refusal, a fiber jacket might still prove effective in inhibiting the pryout behavior.

- Utilizing the deck stiffness to resist lateral loads is a cost-effective and structurally efficient retrofit strategy.
- In order to prevent bond failure, cracking of the pile-column wall must be prevented. This may be achieved by using a stiffening agent, such as a steel jacket.

10.3   RECOMMENDATIONS

10.3.1 *Recommendations for field implementation*

The research program thus far has provided insight into the behavior of the hollow, prestressed concrete pile-columns; namely, a previously unexpected failure mode (debonding of the strands) was discovered. The following actions are recommended before a retrofit method is implemented on the field bridges:

- Each bridge should be reviewed individually to establish its response. For example, box girder superstructures, without joints over the interior piers, offer the possibility of resisting some of the seismic loading by horizontal beam action. That option will significantly reduce the load to be carried by the hollow pile-column bents. But it will require review, and possibly retrofit, of the shear resisting elements at the abutments.
- For bridges in which the seismic moments in the tops of the above-grade column are large enough to cause failure by strand debonding, the plug region of the hollow pile-columns should be encased in steel jackets. The jacket thickness and length should be selected so as to ensure that cracking will not initiate in the hollow section of the pile-column near the end of the plug. The criterion for this behavior is stiffness, and not strength, and the required jacket thickness is likely to be larger than that of a jacket for a comparable solid column. The jacket should start approximately 2-inches below the cap beam and should ideally extend down to the point where the calculated net tension stress in the pile-column wall is zero. For pretensioned pile-columns, it should also be longer than the strand development length. The calculated length will vary among pile-columns, but is expected to be approximately 1.5 times the plug length. Tentative

185

design procedures for the retrofit are presented, <u>but this retrofit approach should be tested, and its effectiveness verified, before implementing it in the field</u>.

- For bridges in which debonding failure will not prove critical, at least two choices are available:
  - o Encase the top of the above-grade column in a CFRP jacket made with uniaxial fibers, with the goal of preventing failure by prying action of the precast pile-column wall by the cast-in-place plug. The fibers in the jacket should be oriented in the hoop direction. This retrofit is likely to be beneficial for pile-columns in which the spiral reinforcement ratio at the end is relatively small.
  - o Encase the top of the above-grade column in a CFRP jacket made with biaxial fibers, with the goal of preventing any flexural crack from opening wide enough to cause strand debonding followed by buckling. The jacket would need both longitudinal and circumferential fibers. Bond of the fibers to the pile-column wall is likely to be the most prominent problem. <u>This retrofit method should be verified by testing</u>.

- For any bridge considered for retrofit, the shear capacity of the cap beam and the joint shear capacity should be reviewed. In those bridges for which drawings were available, the cap beam depth was less than the pile-column diameter and the transverse reinforcement consisted of two-legged rectangular hoops with 90-degree closure bends. These are likely to prove unsatisfactory.

10.3.2 *Recommendations for further research*

- Experimental test of a column-to-cap-beam connection retrofitted with a steel jacket, designed to suppress flexural cracking of the pile-column wall.
- Experimental test of a column-to-cap-beam connection retrofitted with a CFRP jacket with biaxial fibers, designed to suppress propagation and widening of flexural crack in the pile-column wall.
- Further investigation, using both experimental and computational methods, to determine the load transfer mechanism for moments between the plug and the pile-column wall.

- More advanced analytical modeling that allows for inelastic pile-column behavior as well as inelastic soil behavior to assess with more accuracy the susceptibility of the below-grade piles.

187

BIBLIOGRAPHY

AASHTO (2012). "AASHTO LRFD Bridge Design Specifications. 7th Edition." American Association of State Highway and Transportation Officials (AASHTO), Washington, DC.

ACI Committee 318 (2019). "Building Code Requirements for Structural Concrete and Commentary (ACI318R-19)". Farmington Hills, MI: American Concrete Institute.

ACI (1999). "Acceptance Criteria for Moment Frames Based on Structural Testing," ACI ITG/T1.1-99. Report by ACI Innovation Task Group 1 and Collaborators, ACI.

ACI ITG/T1.1-99

ASTM A370-15, 2015, "Standard Test Methods and Definition for Mechanical Testing of Steel Products," ASTM International, West Conshohocken, PA, 2015, DOI: 10.1520/ A0370-15, www.astm.org

ASTM A615-16, 2016, "Standard Specification for Deformed and Plain Carbon-Steel Bars for Concrete Reinforcement," ASTM International, West Conshohocken, PA, 2016, DOI: 10.1520/ A615-16, www.astm.org

ASTM C39/C39M-18, 2018, "Standard Test Method for Compressive Strength of Cylindrical Concrete Specimens," ASTM International, West Conshohocken, PA, 2018, DOI: 10.1520/C0039_C0039M-18, www.astm.org

Budek, A. M., Benzoni, G., & Priestley, M. N. (1997). Experimental investigation of ductility of in-ground hinges in solid and hollow prestressed piles. Report no. SSRP, 97, 17.

Budek, A.M., and Benzoni, G. (2009). Obtaining ductile performance from precast, prestressed concrete piles. PCI Journal, 54(3).

Caltrans (2013). Caltrans Seismic Design Criteria. Version 1.7. California Department of Transportation, Sacramento, CA.

CEB-FIP Model Code 1990. Model code for concrete structures. In: Comité Euro-international du Béton. Secretariat permanent. Case Postale 88, CH-1015 Lausanne, Switzerland; 1990

CEN (Comité Europeen de Normalization) (1998). Eurocode 8: Design of Structures for earthquake resistance – part 1: general rules, seismic actions and rules for buildings. PrEN 1998-1: 1998, CEN, Brussels

Collins, M., & Mitchell, Denis. (1991). Prestressed concrete structures (Prentice-Hall international series in civil engineering and engineering mechanics). Englewood Cliffs, N.J.: Prentice Hall.

EIGawady, M., Cofer, W. F., & Shafiei-Tehrany, R. (2009). Seismic assessment of WSDOT bridges with prestressed hollow core piles: part II (No. WA-RD 732.2). Washington (State). Dept. of Transportation. Office of Research and Library Services.

Freeman, S. A. (2004). Review of the development of the capacity spectrum method. ISET Journal of Earthquake Technology, 41(1), 1-13.

Greenwood, S. M. (2008). Analytical Performance Evaluation of Hollow Prestressed Piles and Pile-Cap Connections in the I-5 Ravenna Bridge (Master's Thesis, Washington State University).

Ikeda, S., Tsubaki, T., and Yamaguchi, T. (1982). Ductility Improvement of Prestressed Concrete Piles. Transactions of the Japan Concrete Institute, 113(2), 531-538.

Lignola, G., Prota, A., Manfredi, G., & Cosenza, E. (2008). Unified theory for confinement of RC solid and hollow circular columns. Composites Part B, 39(7-8), 1151-1160.

Maguara, D.D., Sozen, M.A. and Siess, C.P. (1964). "A study in Relaxation of Prestressing Reinforcement." *PCI Jo.*, 9(2), 13-57.

Mander, T., & Matamoros, A. (2019). Constitutive Modeling and Overstrength Factors for Reinforcing Steel. *ACI Structural Journal, 116*(3), 219-232.

Martí-Vargas, J., Serna, P., & Hale, W. (2013). Strand bond performance in prestressed concrete accounting for bond slip. Engineering Structures, 51(C), 236-244.

Meader, J., Janssen, D. and Eberhard, M.O. (2013) "Structural Design Parameters of Current WSDOT Concrete Mixes". WSDOT Report no. WA-RD 802.1, June, 125 p.

189

Menegotto, M., & Pinto, P. (1973). Method of Analysis for Cyclically Loaded Reinforced Concrete Plane Frames Including Changes in Geometry and Non-elastic Behavior of Elements Under Combined Normal Force and Bending. Proceedings. IABSE Sympoium on Resistance and Ultimate Deformability of Structures Acted on by Well-Defined Repeated Loads.

Mitchell, C., Mukai, David J., Dolan, Charles, & Garnich, Mark. (2008). A Review of Initial End Slip as Criteria of Acceptable Strand Bond Quality and the Relationship between Strand Diameter and Transfer Length for Prestressed Concrete Members, ProQuest Dissertations and Theses.

Pizzano, B. A. (1984). Behavior of prestressed concrete piles under seismic loading (Master's Thesis, University of Washington).

Popovics, S. (1973). A numerical approach to the complete stress-strain curve of concrete. Cement and Concrete Research, 3(5), 583-599.

Priestley, M. N., Seible, F., & Calvi, G. M. (1996). Seismic design and retrofit of bridges. John Wiley & Sons.

Ranzo, G., & Priestley, M. N. (2001). Seismic performance of circular hollow columns subjected to high shear. Structural Systems Research Project, University of California, San Diego.

Response 2000: http://www.ecf.utoronto.ca/~bentz/r2k.htm

Scribner, C.F and Kobayashi, K. (1984). "Prestressing Strand Bond Characteristics under Reversed Cyclic Loading." PCI Jo, Sept-Oct, 118-137.

Shafiei-Tehrany, R., ElGawady, M., & Coffer, W. (2011). Pushover Analysis of I-5 RAVENNA Bridge. Electronic Journal of Structural Engineering, 11(1), 2011.

Skogman, C. B., Tadros, M. K., and Grasmick, R., (1988). "Flexural Strength of Prestressed Concrete Members," PCI JOURNAL, V. 33, No.5, September-October, pp. 96-123.

Tardieu, T. (2018). Seismic Evaluation of Hollow Core Prestressed Concrete Bridge Pile-columns in Washington State (Master's Thesis, University of Washington).

Turmo, J., Ramos, G., & Aparicio, A. C. (2009). Shear truss analogy for concrete members of solid and hollow circular cross section. Engineering Structures, 31(2), 455-465.

Vecchio, F.J. and Collins, M.P. (1986) "The Modified Compression Field Theory for Reinforced Concrete Elements Subject to Shear." ACI Jo., Title 83-22, March-April, 291-231.

191

APPENDIX A: REFERENCE BRIDGE DETAILS

There are 22 bridges throughout Washington State that were founded on hollow-core prestressed concrete pile-columns. As part of this research program, the following four bridges were studied and their design details are given in this appendix. All drawing excerpts were provided by the Washington State Department of Transportation.

A.1 LOCATIONS

1. Ravenna Boulevard Overcrossing (Ravenna): 47°40'28.6"N, 122°19'15.1"W

2. East Galer St. to Lakeview Boulevard Viaduct (Galer): 47°38'04.0"N, 122°19'24.7"W

3. L^E Line Bridge over Slide, South 184th Street to South 144th Street (Slide): 47°27'0.60"N, 122°15'48.0"W

4. Green River Bridge (Green River): 47°27'45.4"N, 122°14'56.9"W

A.2 GENERAL DETAILS

Table A-1. Design details of reference bridges

	Ravenna	Galer	Slide	Green River
Overall				
Length (ft)	1372	1671	515	245
No. of spans	20	19	5	3
Superstructure type	Cap beam + girders	Cap beam + girders	Cap beam + girders	Box girder
Prestressing Type	Post-tensioned	-*	Pre-tensioned	Pre-tensioned
Average L_{col} (ft)	20.1	35.4	-*	27.5
Average L_{pile} (ft)	20.6	28.5	-*	22.2
Hollow Pile-column				
D_o (in)	48	48	54	54
D_i (in)	38	38	44	44
t_w (in)	5	5	5	5
A_{hollow} (in^2)	675.4	675.4	769.7	769.7
f'_c (psi)	6000	6000	7000	6500
Strand Reinforcement				
f_{pu} (ksi)	250	250	270	250

192

d_{str} (in)	0.6656	0.6656	0.5	0.5
No. of strands	12	14	44	28
A_{str} (in^2)	0.348	0.348	0.153	0.153
A_{ps} (in^2)	4.176	4.872	6.732	4.284
F_i (kip)	61.0	58.9	28.9	25.2
f_{ci} (psi)	1084	1221	1652	1244
Spiral Reinforcement (#2 Gage Spiral Hooping, ASTM 82)				
d_{sp} (in)	0.262	0.262	0.262	0.262
A_{sp} (in^2)	0.054	0.054	0.054	0.054
D_{core} (in)	43	43	49	49
s_{min} (in)	3.0	6.0	2.0	2.0
t_{sp} (in)	0.018	0.009	0.027	0.027
ρ_{hollow} (%)	0.36	0.18	0.54	0.54
ρ_{filled} (%)	0.167	0.084	0.22	0.22
s_{max} (in)	6.0	6.0	4.0	4.0
ρ_{hollow} (%)	0.18	0.18	0.27	0.27
ρ_{filled} (%)	0.084	0.084	0.11	0.11
t_{sp} (in)	0.009	0.009	0.0135	0.0135
Inner Plug				
f'_c (psi)	4000	4000	4000	4000
D_{plug} (in)	38	38	44	44
L_{plug} (ft) – typ.	4.167	4.25	4.33	5.00
A_{plug} (in^2)	1134	1134	1520.5	1520.5
Plug Reinforcement				
d_b (in)	1.0	1.0	1.375	1.375
No. of bars	16	16	18	12
c_{c_plug} (in)	2.0	2.0	2.0	2.0
Loads and Capacities				
P_{axial} per column (kip)	430	300	410	633
M_{n_hollow} (ft-kip)	2260	2305	3565	3700
$M_{n\_combined}$ (ft-kip)	1910	1750	3675	4205
M_{n_plug} (ft-kip)	1385	1260	2790	3235

* Not enough information found

A.3 RAVENNA BRIDGE OVERCROSSING

Hollow pile-column
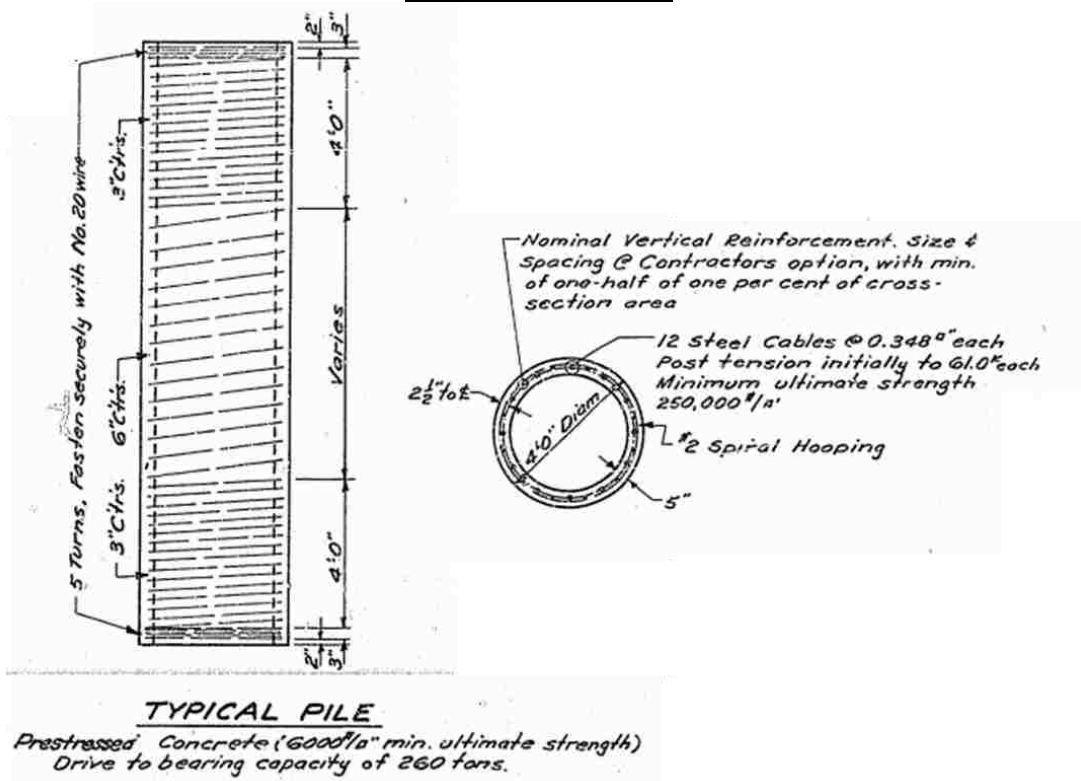
Figure A-1. Details of hollow prestressed concrete pile-column (Ravenna)

Inner plug
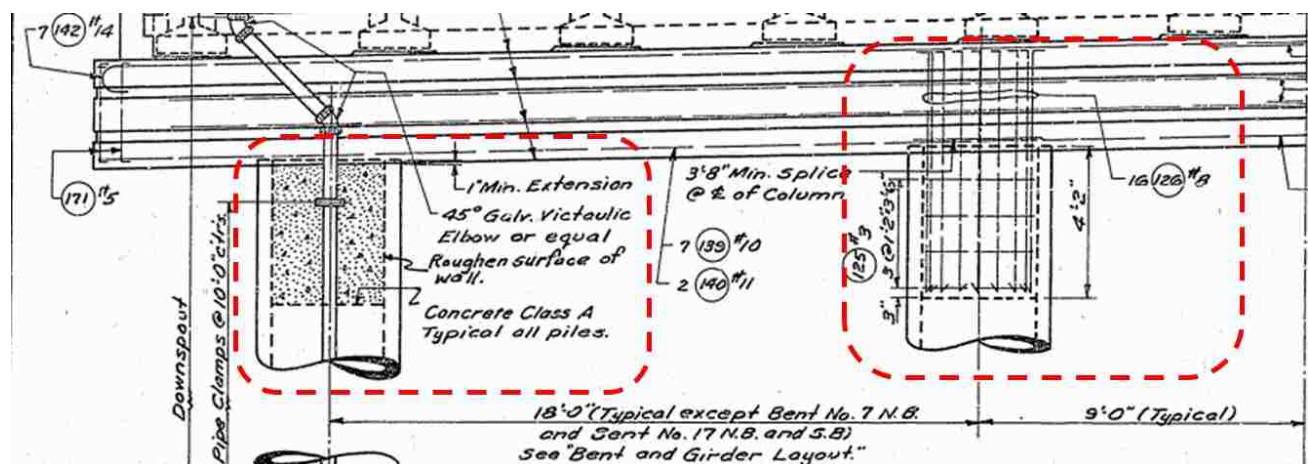

Figure A-2. Details of inner plug reinforcement (Ravenna)

Cap Beam
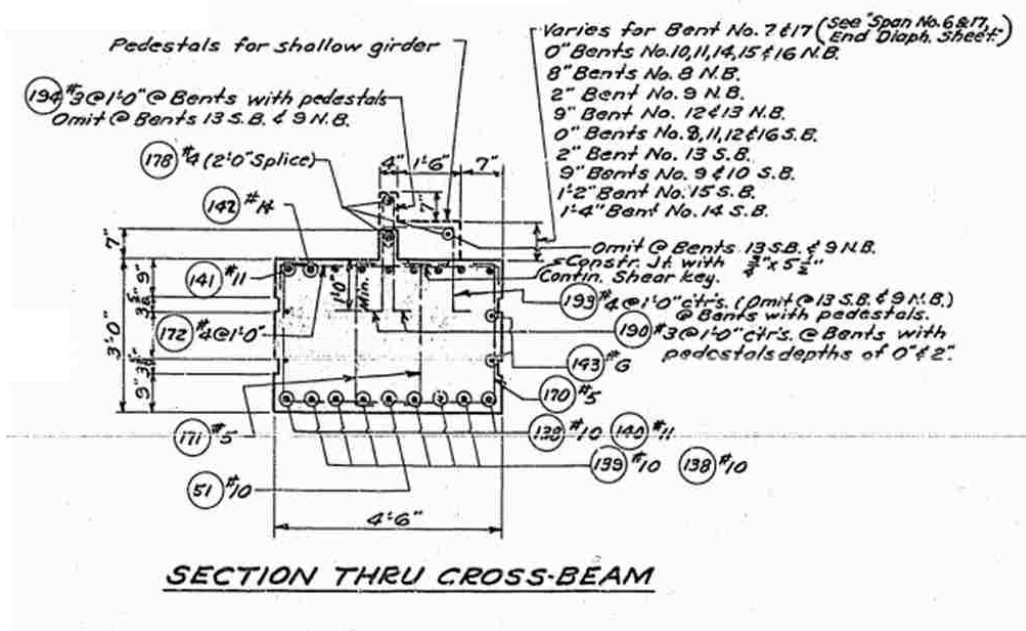
Figure A-3. Cap beam cross-section for typical bent (Ravenna)

Hollow Pile

Figure A-4. Details of hollow prestressed concrete pile-column (Galer-Lakeview)

Inner Plug

Figure A-5. Details of inner plug reinforcement (Galer-Lakeview)
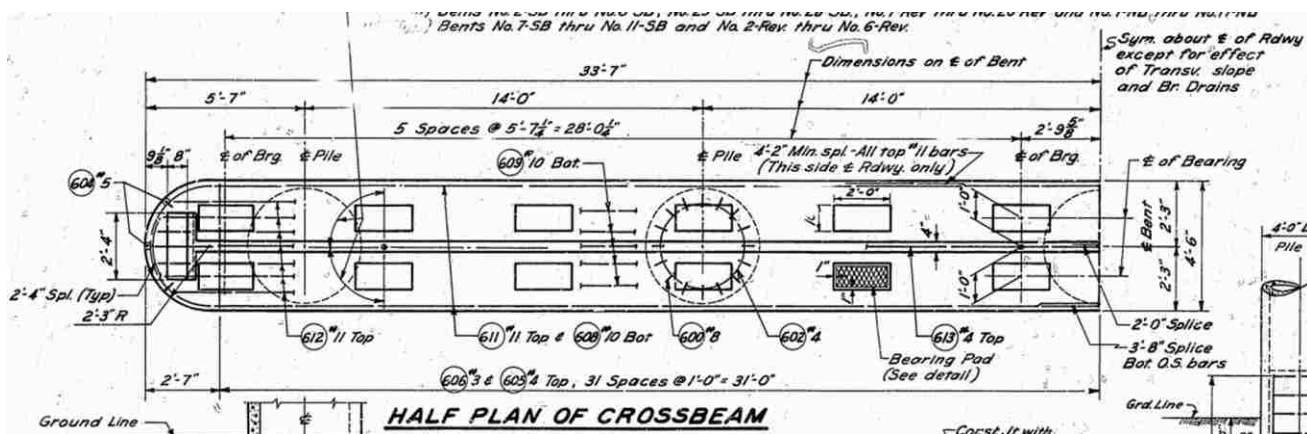
Cap Beam

Figure A-6. Plan view of cap beam for typical bent (Galer-Lakeview)
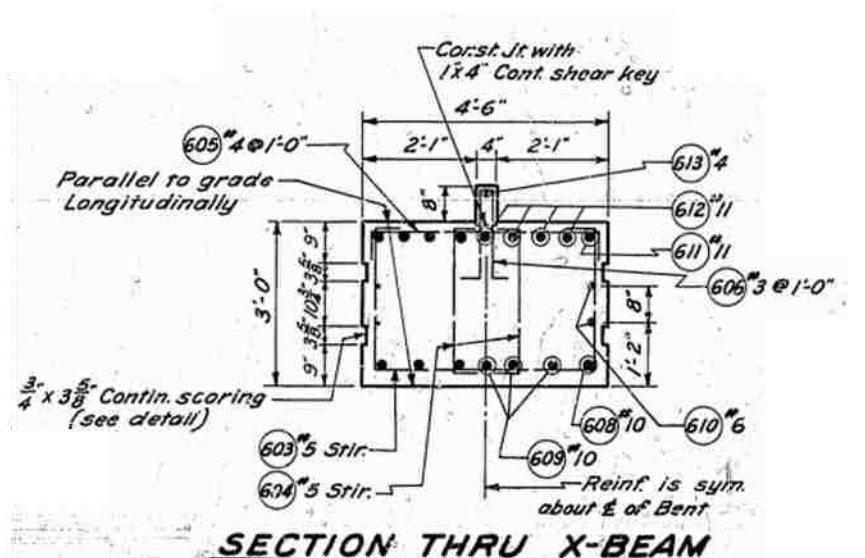
Figure A-7. Cap beam cross-section for typical bent (Galer-Lakeview)

197

Special Details
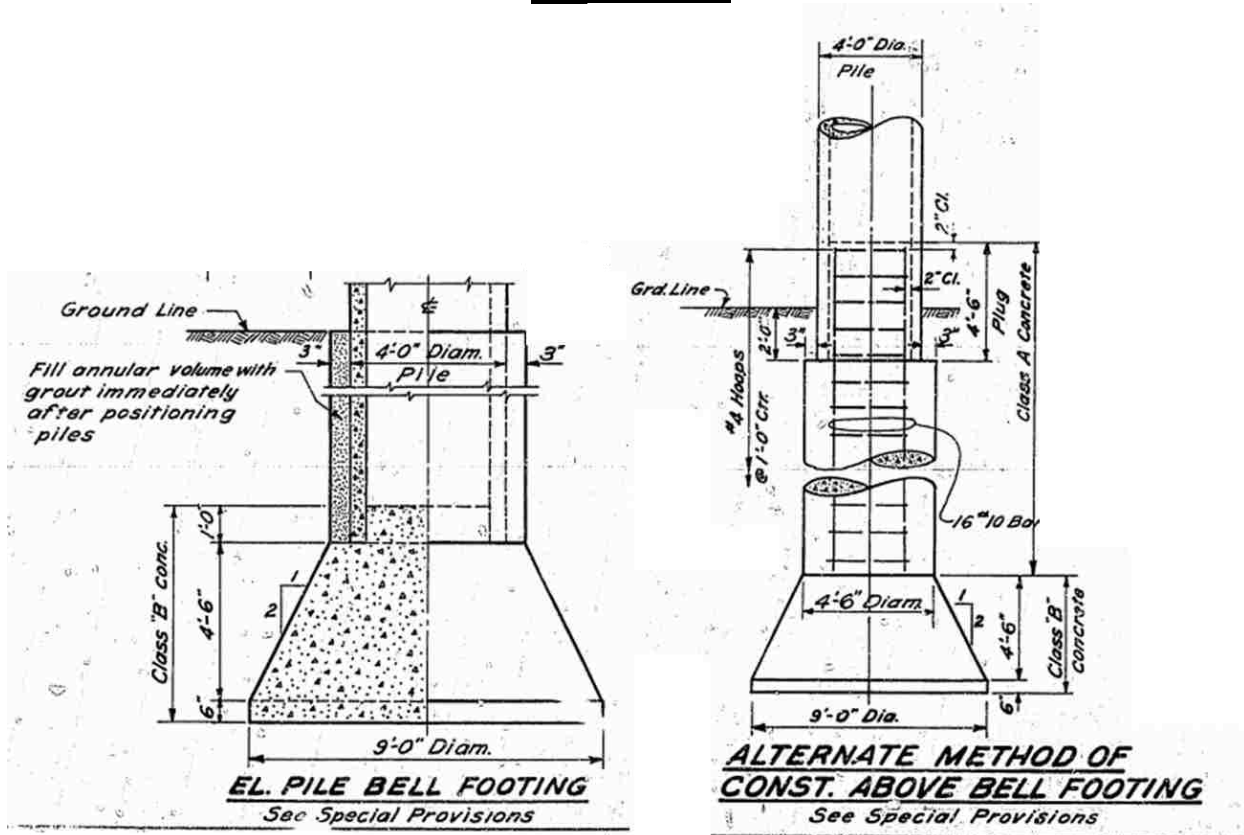
Figure A-8. Alternative below-grade and footing details (Galer-Lakeview)
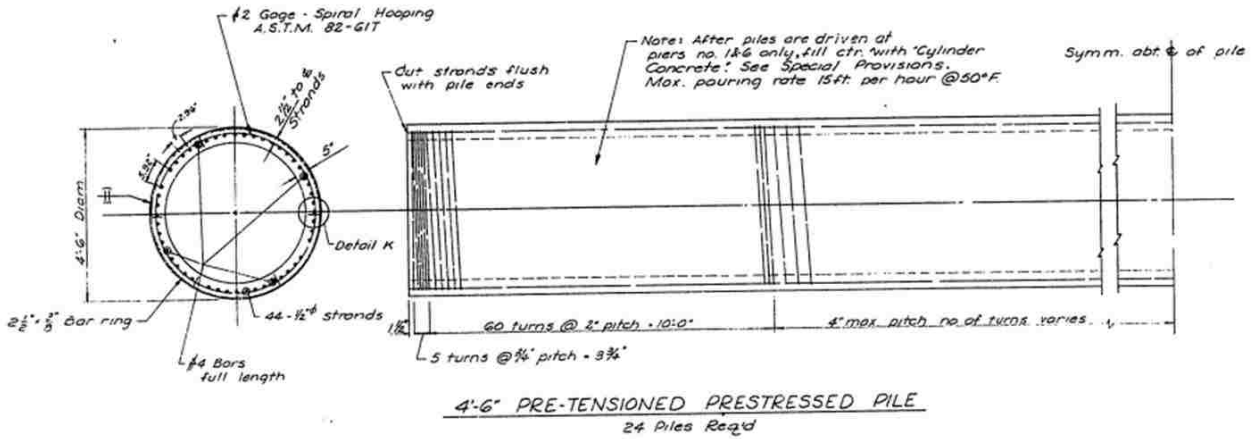
Hollow Pile

Figure A-9. Details of hollow prestressed concrete pile-column (Slide)

Inner Plug
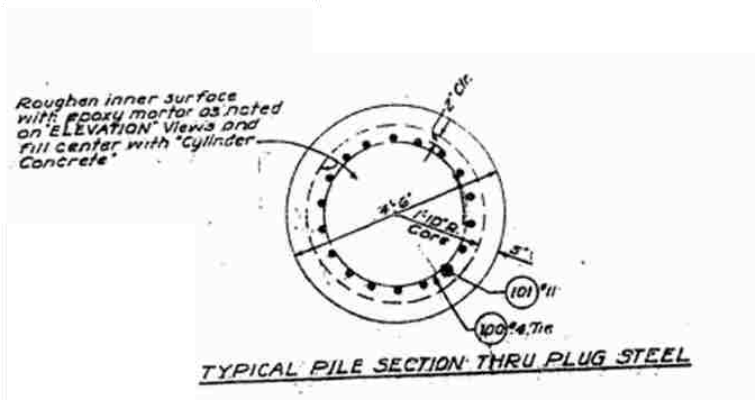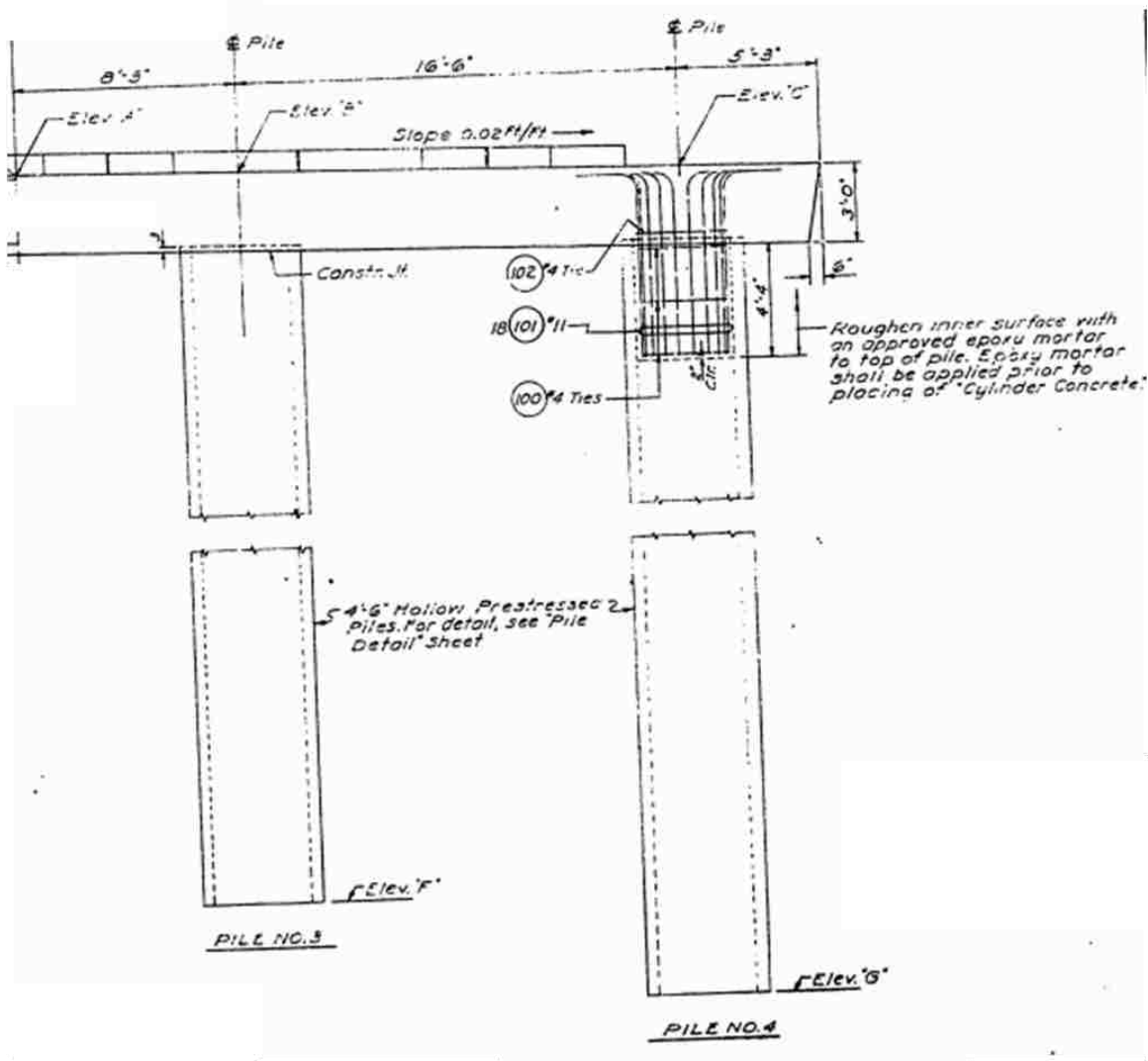
Figure A-10. Details of inner plug reinforcement (Slide)

200

www.manaraa.com
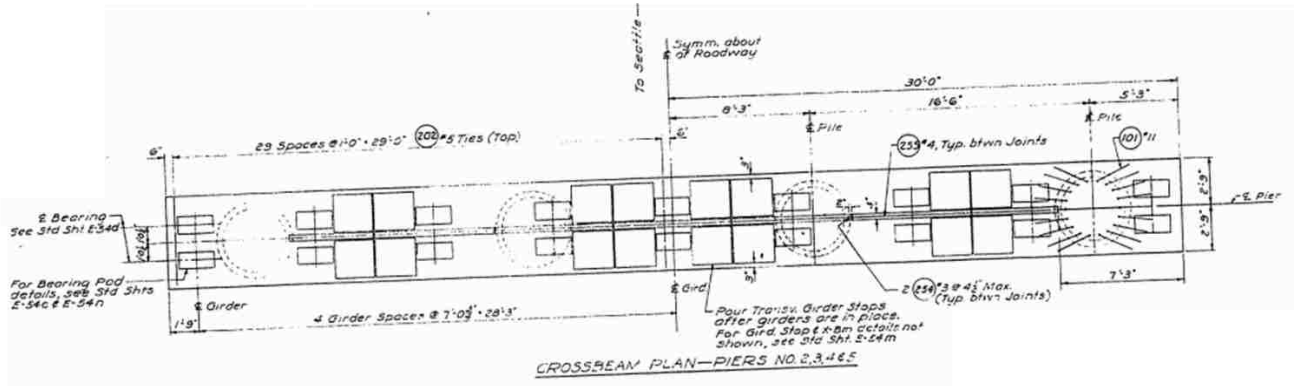
Cap Beam

Figure A-11. Plan view of typical cap beam (Slide)
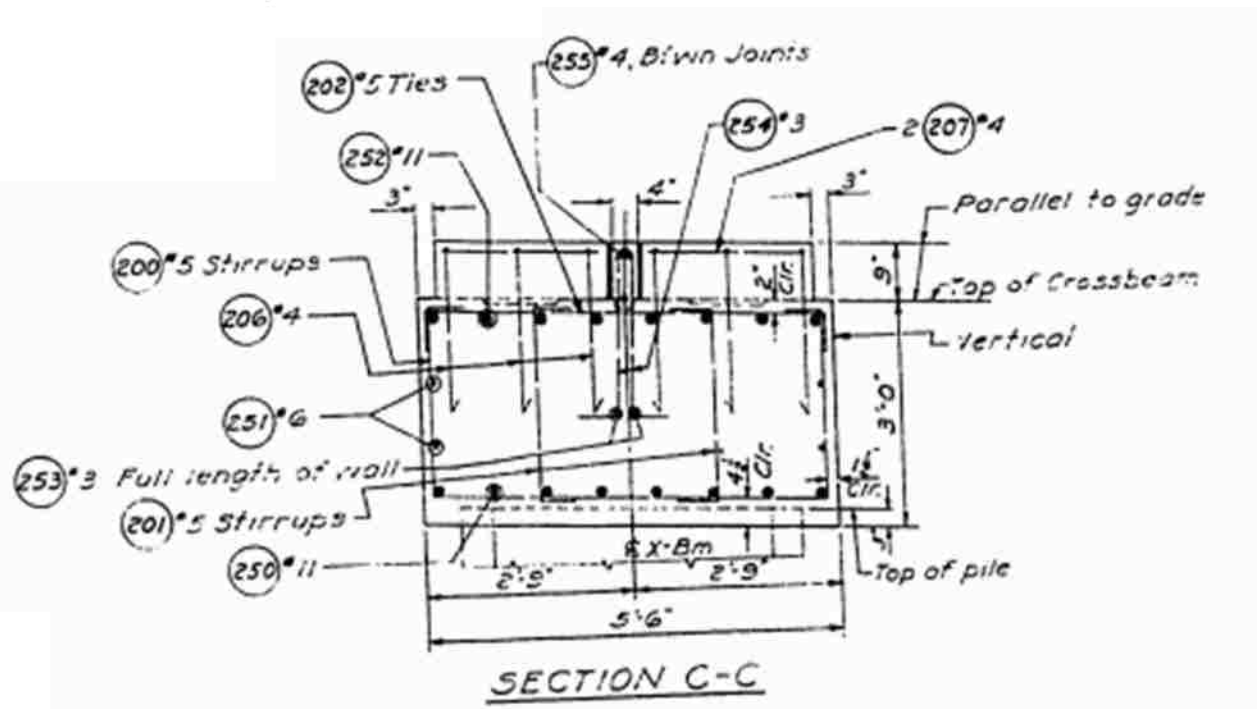
Figure A-12. Cap beam cross-section for typical bent (Slide)

Hollow Pile

Figure A-13. Details of hollow prestressed concrete pile-column (Green River)
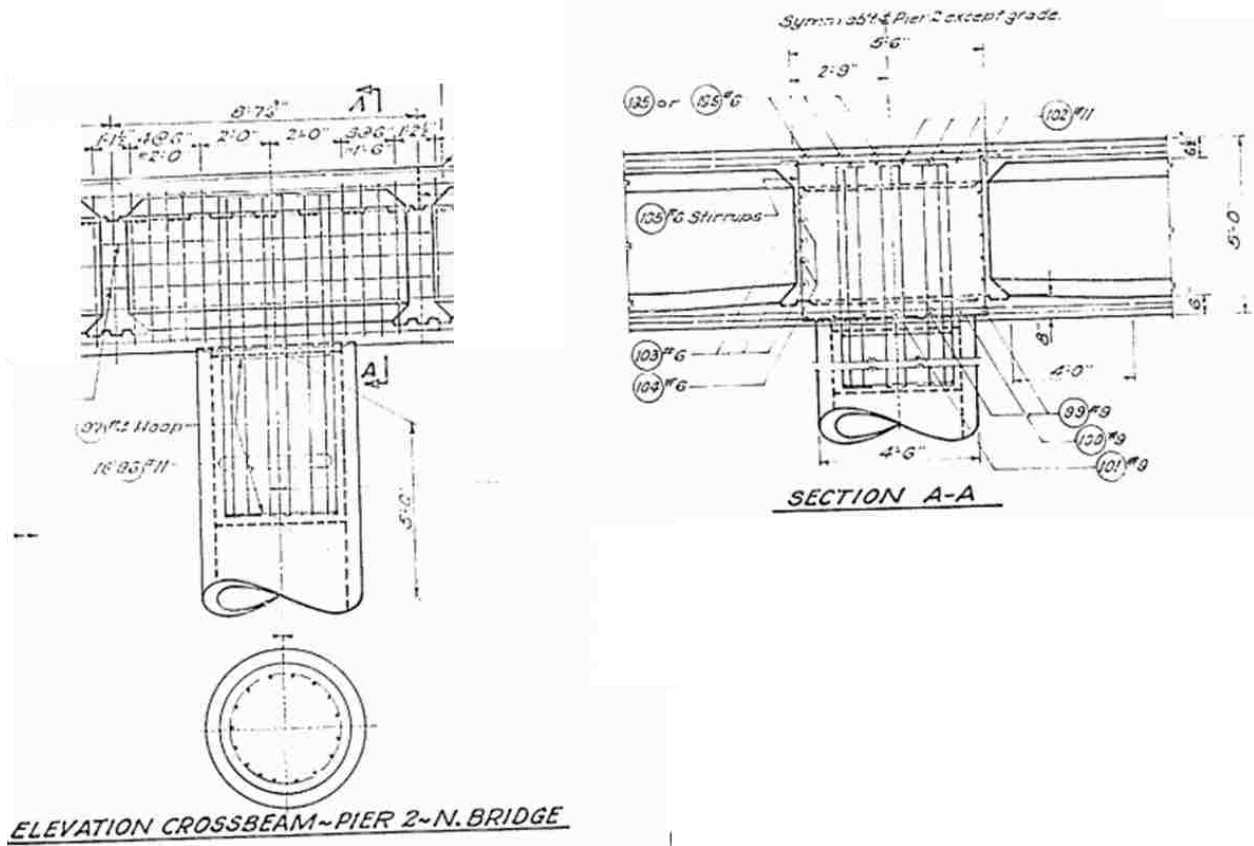
Inner Plug

Figure A-14. Details of inner plug reinforcement (Green River)
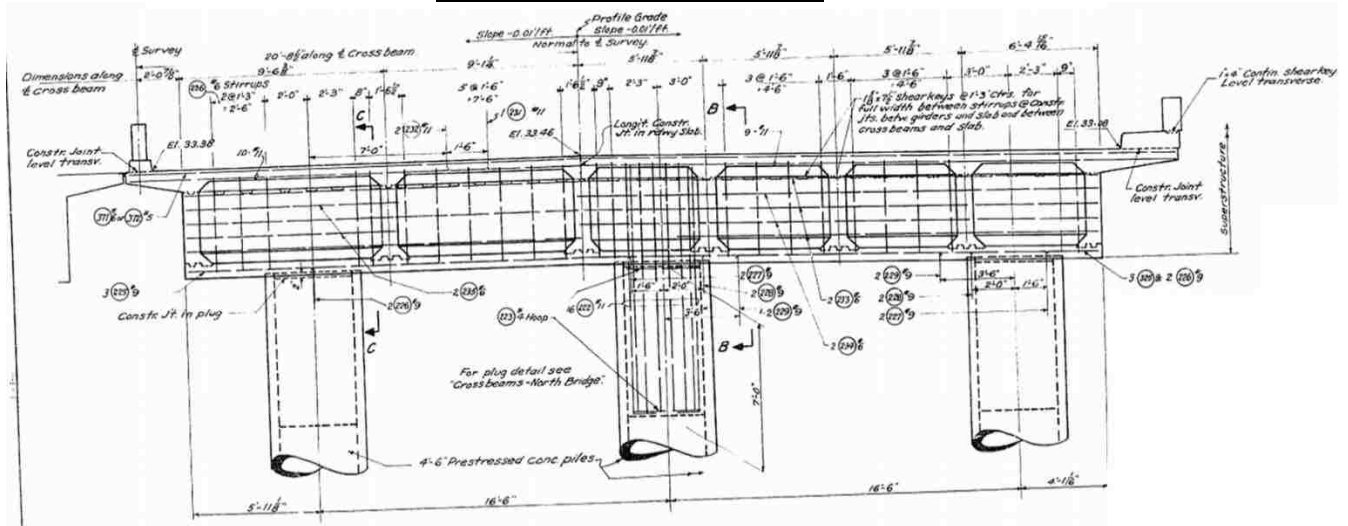
Special Details – Box Girder

Figure A-15. Elevation of typical box girder cross beam (Green River)

203
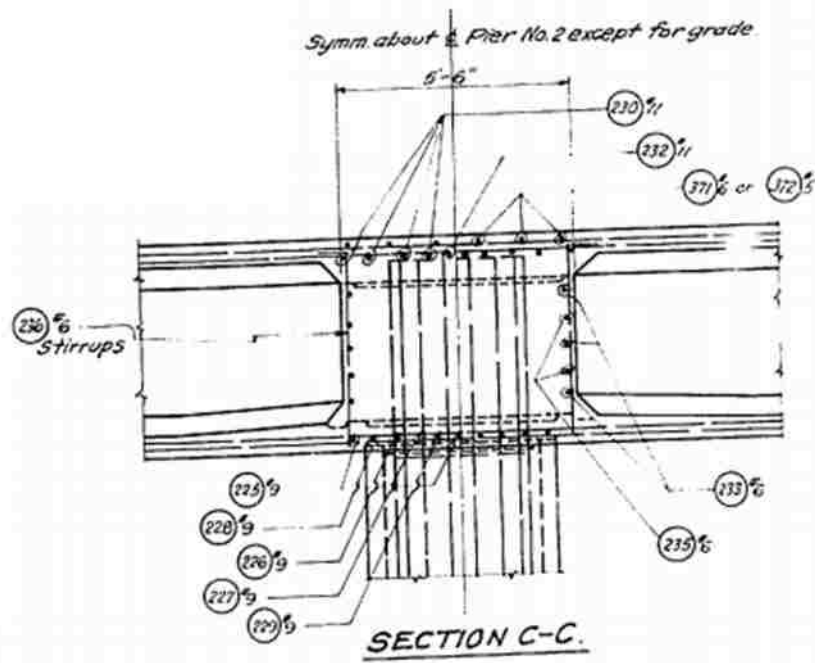
Figure A-16. Cross beam cross-section for typical bent (Green River)

APPENDIX B: VIRTUAL WORK FRICTION CALCULATIONS

The calculations conducted to determine the effective coefficient of friction of the spherical bearing assembly described in Chapter 7 are described here. There are two components of friction that are active in the system: one between the Baldwin loading plate and the top of the bearing, signified by μ_x; one between the top and bottom of the bearing, signified by μ_θ.

Figure B-1. Setup of virtual work calculations

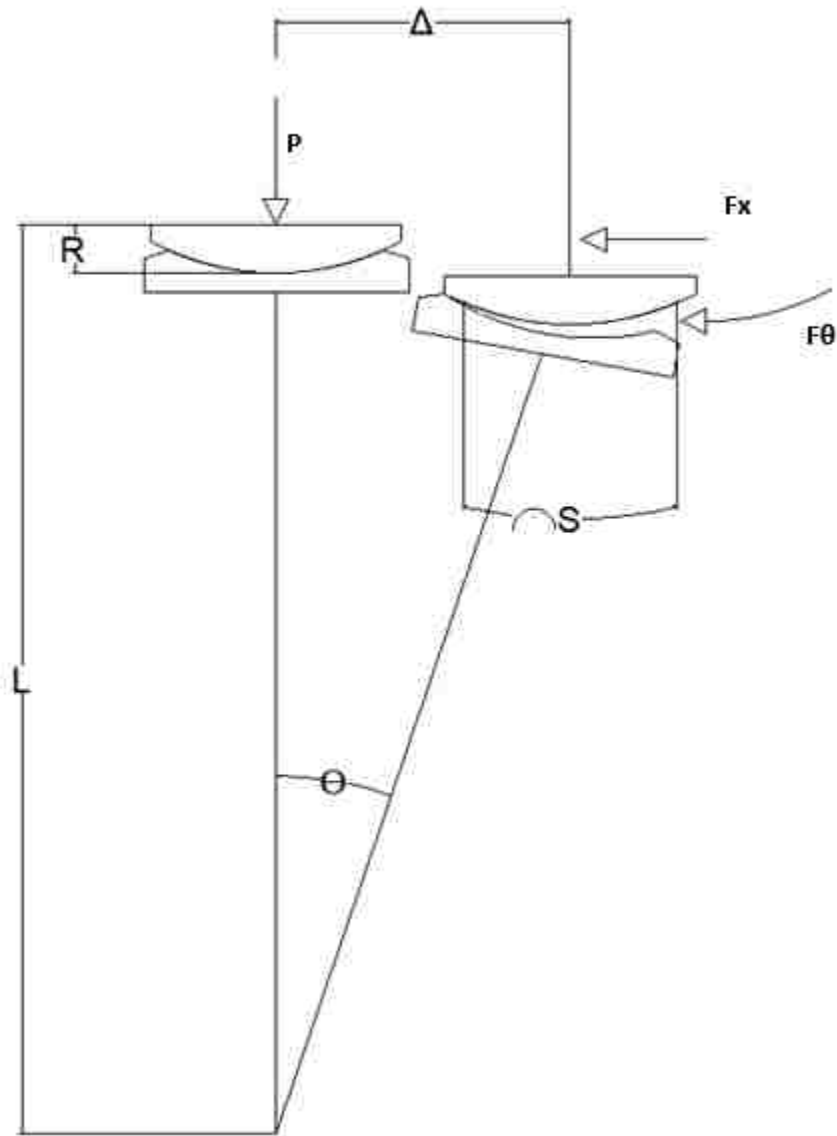The total work done by friction in the bearing on the system is shown in Equation B-1.

$$Work = F_x * \Delta + F_\theta * S \qquad \text{(B-1)}$$

The following quantities can be defined in terms of the specimen rotation:

$$\Delta = \theta * L \qquad \text{(B-2)}$$

$$S = R * \theta \qquad \text{(B-3)}$$

The friction forces induced in the bearing can be defined in terms of the axial load:

$$F_x = P * \mu_x \qquad \text{(B-4)}$$

$$F_\theta = P * \mu_\theta \qquad \text{(B-5)}$$

Plugging Equations B-2 through B-5 into Equation B-1 yields:

$$Work = P * \theta * L * \left(\mu_x + \mu_\theta * \left(\frac{R}{L}\right)\right) \qquad \text{(B-6)}$$

$$\mu_x = 0.05, \mu_\theta = 0.03$$

$$\mu_{eff} = \left(\mu_x + \mu_\theta * \left(\frac{R}{L}\right)\right) = 0.0541 \qquad \text{(B-7)}$$

APPENDIX C: THEORETICAL LINEAR ELASTIC STIFFNESS CALCULATION DETAILS

The theoretical linear elastic stiffness values for the pure bending ("Four-Point bending") and combined bending and shear ("Three-Point bending") tests were both higher than the tangent stiffness to the measured data. The implication of this is that the corresponding "elastic displacement (or rotation)" would be smaller, while the maximum displacement (or rotation) would be larger. Since the ductility is defined as the maximum displacement divided by the elastic displacement, the corresponding ductility factor would be higher. The theoretical stiffness values are presented below, and placed on the corresponding force-displacement plots.

Pure bending test

$$K = \frac{24EI}{a*(3L^2 - 4a^2)} = 6278 \; k/in \qquad \text{(C-1)}$$

Where:

- E = Young's Modulus
- I = Moment of Inertia
- a = distance from reaction to applied load
- L = distance between reactions

Figure C-1 shows the theoretical stiffness on the force-displacement curve for the pure bending test.
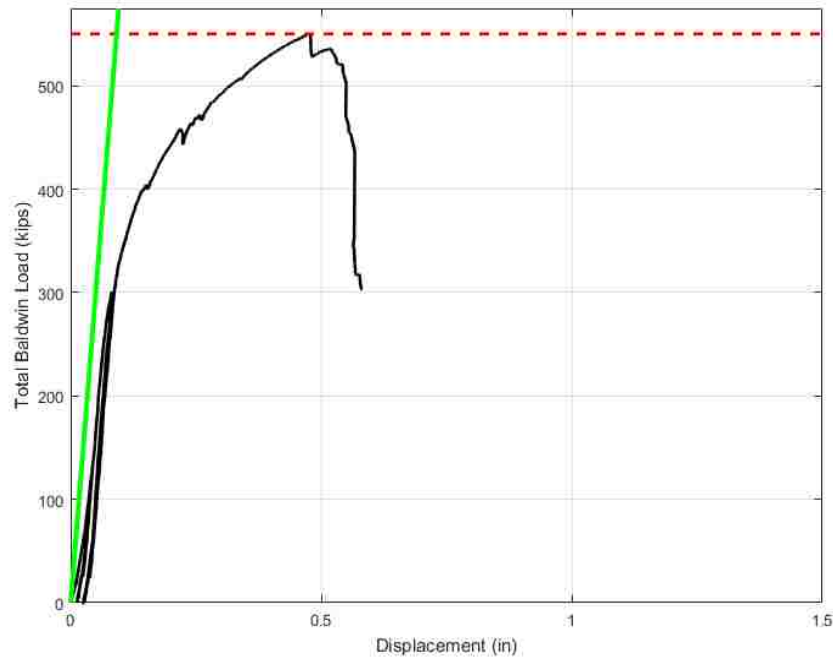
Figure C-1. Theoretical stiffness on pure bending force-displacement curve

Note that the theoretical stiffness is actually very nearly parallel to the measured stiffness, and that the main difference may be from the extra displacement captured by the string potentiometers when they start to get pushed by the specimen.

Combined bending and shear test

$$\Delta = \Delta_{fl} + \Delta_{sh} = \frac{PL^3}{48EI} + \frac{PL}{4GA_{sh}} = \frac{PL^3}{48EI}\left(1 + \frac{3(1+v)}{k}\left(\frac{D}{L}\right)^2\right) \quad \text{(C-2)}$$

Where:

- P = Applied load

- L = span

- E = Young's Modulus

- I = Moment of Inertia

- v = Poisson's ratio = 0.2 for concrete

208

- k = Ash/A = 0.5

- D = Diameter

Therfore:

$$K = \frac{48EI}{L^3(1+\frac{3(1+v)}{k}\left(\frac{D}{L}\right)^2)} = 10000 \; k/in \qquad \text{(C-3)}$$

Where:

- E = Young's Modulus

- I = Moment of Inertia

- l = distance between reactions

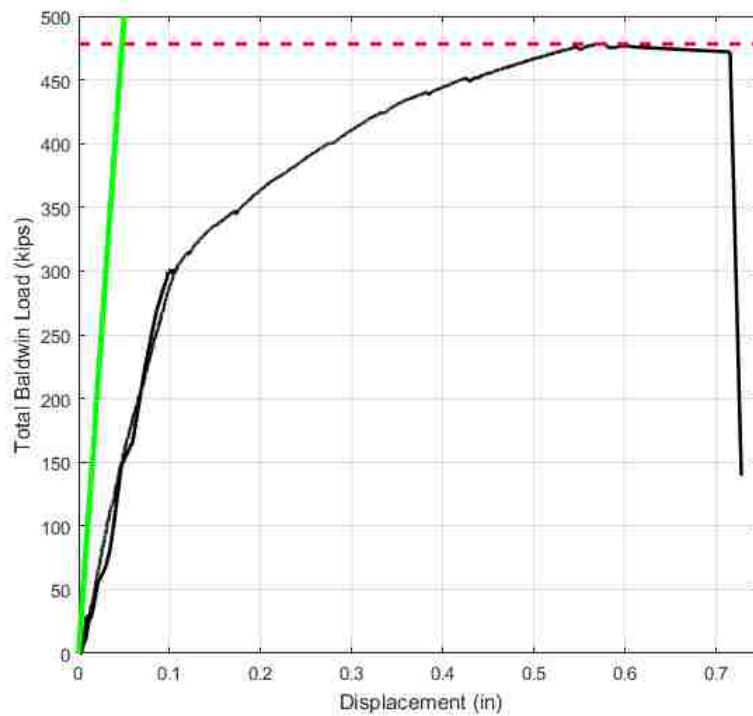Figure C-2 shows the theoretical stiffness on the force-displacement curve for the combined bending and shear test.

Figure C-2. Theoretical stiffness on combined shear and bending force-displacement curve

209

APPENDIX D: ANALYTICAL INVESTIGATION CALCULATION DETAILS

The numerical model in Chapter 9 used the formulation for a finite beam on an elastic foundation to represent the below-grade pile element embedded in soil of constant stiffness given by the modulus of subgrade reaction β_{soil}. The formulation is based on Hetenyi (1946).

The beam formulation has the following sign convention (Figure D-1).
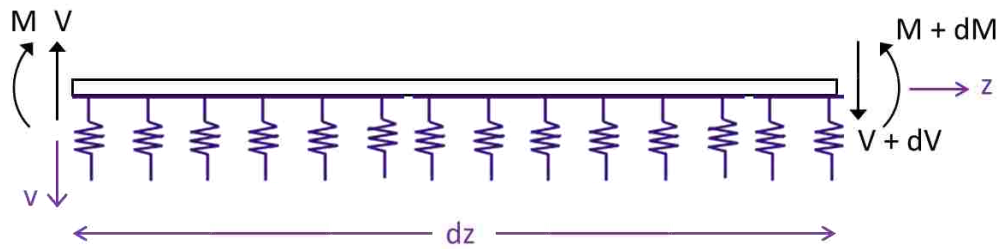
Figure D-1. Beam formulation

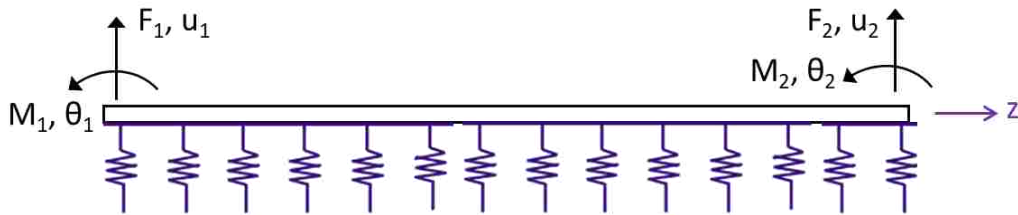The element formulation has the following sign convention (Figure D-2).

Figure D-2. Element formulation

The pile was modelled as a beam on elastic foundations, following the Winkler approach. It was modelled using a single element, but it was necessary to allow for the calculation of values, such as displacement and moment, at internal locations.

The equation of equilibrium is

$$EIv'''' + kv = 0 \qquad \text{(D-1)}$$

for which the solution is

$$v = e^{-\lambda z}[A \cos \lambda z + B \sin \lambda z] + e^{\lambda z}[C \cos \lambda z + D \sin \lambda z] \qquad \text{(D-2)}$$

given $\qquad\qquad \lambda = \sqrt[4]{\dfrac{\beta_{soil}}{4EI}}$

The constants *A, B, C, D* can be related to the end forces and moments by

$$\underline{R}\{A\} = \{f\} \qquad\qquad \text{(D-3)}$$

where

$\underline{R} =$

$$\begin{bmatrix} -2 & -2 & +2 & -2 \\ 0 & -2 & 0 & +2 \\ 2e^{-\lambda L}(\cos \lambda L - \sin \lambda L) & 2e^{-\lambda L}(\cos \lambda L + \sin \lambda L) & 2e^{\lambda L}(-\cos \lambda L - \sin \lambda L) & 2e^{\lambda L}(\cos \lambda L - \sin \lambda L) \\ 2e^{-\lambda L}\sin \lambda L & 2e^{-\lambda L}(-\cos \lambda L) & 2e^{\lambda L}(-\sin \lambda L) & 2e^{\lambda L}(2\cos \lambda L) \end{bmatrix}$$

$$\{A\} = \begin{Bmatrix} A \\ B \\ C \\ D \end{Bmatrix} \quad \text{and} \quad \{f\} = \begin{Bmatrix} F_1/_{EI\lambda^3} \\ M_1/_{EI\lambda^2} \\ F_2/_{EI\lambda^3} \\ M_2/_{EI\lambda^2} \end{Bmatrix}$$

It should be noted that the signs in the matrix must take account of the change from the beam sign convention in the equilibrium equation and the nodal sign convention used in the matrices. The vector of {A} values can also be related to the end displacement and slopes by:

$$\underline{Q}\{A\} = \{u\} \qquad\qquad \text{(D-4)}$$

where

211

$$\underline{Q} =$$

$$\begin{bmatrix} -1 & 0 & -1 & 0 \\ +1 & -1 & -1 & -1 \\ -e^{-\lambda L}(\cos \lambda L) & -e^{-\lambda L}(\sin \lambda L) & -e^{\lambda L}(\cos \lambda L) & -e^{\lambda L}(\sin \lambda L) \\ e^{-\lambda L}(\cos \lambda L + \sin \lambda L) & e^{-\lambda L}(-\cos \lambda L + \sin \lambda L) & e^{\lambda L}(-\cos \lambda L + \sin \lambda L) & e^{\lambda L}(-\cos \lambda L - \sin \lambda L) \end{bmatrix}$$

and $\quad \{u\} = \begin{Bmatrix} u_1 \\ \theta_1/\lambda \\ u_2 \\ \theta_2/\lambda \end{Bmatrix}$

The 4x4 stiffness matrix, $\underline{K}$ for the pile element can be obtained as:

$$\underline{K} = \underline{R} * \underline{Q}^{-1} \tag{D-5}$$

The 4x4 pile matrix can then be added to the 4x4 column matrix to form a 6x6 global stiffness matrix.

The global displacements are obtained from the global stiffness matrix and the applied loads, which in this structure occur at the two degrees of freedom at the top of the column.

Under elastic conditions, the loads are all zero except for the lateral load Q at the cap beam. Once the displacements are known, the constants A, B, C, D can be obtained from Eqn. D-3. The displacements and forces at any depth z can then be obtained using Eqns. D-3 and D-4 with z substituted for L.

If the pile is infinitely long, the two degrees of freedom at the bottom of the pile can be discarded, and the pile behavior is then represented by the 2x2 matrix:

$$\begin{Bmatrix} V \\ M \end{Bmatrix} = EI \begin{bmatrix} 4\lambda^3 & 2\lambda^2 \\ 2\lambda^2 & 2\lambda \end{bmatrix} \begin{Bmatrix} v \\ \theta \end{Bmatrix} \tag{D-6}$$

212

Use of this matrix, for values of L greater than about $10/\lambda$, helps to avoid overflow problems with the terms in $e^{\lambda L}$ in matrices R and Q.

Derivation of the 3-D span/depth ratio for deck stiffness.

The foregoing approximate criterion for deck stiffness may be developed as follows. Consider a three-span bridge of total length L_{deck}, with side span lengths αL_{deck}. The deck is continuous and contains no joints. The deck is subjected to a transverse seismic load that causes a sinusoidal distribution of transverse displacement. (This is exactly true if the deck is prismatic, the deck stiffness is much greater than the bent stiffness, and the load is sinusoidal. It is nearly true under a wide variety of circumstances). If the curvature at mid-span is ϕ_0, the deflected shape is:

$$v(z) = \phi_0 \left(\frac{L_{deck}}{\pi}\right)^2 \sin\left(\frac{\pi z}{L_{deck}}\right) \qquad \text{(D-7)}$$

The transverse displacement at the bents, where $z = \alpha L_{deck}$, is:

$$v(\alpha L_{deck}) = \phi_0 \left(\frac{L_{deck}}{\pi}\right)^2 \sin(\alpha\pi) \qquad \text{(D-8)}$$

If the displacement at the bent is limited to θL_{col}, where θ is a limiting drift ratio, such as 1%, then:

$$\theta L_{col} = \phi_0 \left(\frac{L_{deck}}{\pi}\right)^2 \sin(\alpha\pi) \qquad \text{(D-9)}$$

The magnitude of the curvature in the deck, ϕ_0, at first yield may be found by treating the deck as a rectangular beam of depth h with longitudinal reinforcement uniformly distributed within it. For a beam made from a single material with different tension and compression moduli, E_T and E_C, where $E_T = \beta^2 E_C$, it can be shown that the neutral axis depth, c, is kh, where:

$$k = \frac{\beta}{1+\beta} \qquad \text{(D-10)}$$

213

And the curvature, ϕ, is related to the extreme fiber tension strain by:

$$\phi = \frac{\varepsilon_T}{(1-k)h} \qquad \text{(D-11)}$$

Setting the mid-span curvature equal to the yield curvature, and the depth, h, of the beam to b_{deck}, and combining these equations, leads to:

$$\frac{L_{deck}^2}{b_{deck}L_{col}} = \frac{\theta}{\varepsilon_y}\frac{\pi^2}{(1+\beta)\sin(\alpha\pi)} \qquad \text{(D-12)}$$

For a beam containing reinforcement that is uniformly distributed throughout the cross-section, β may be found from:

$$\beta^2 = \frac{E_T}{E_C} = \frac{n\rho}{1+(n-1)\rho} \qquad \text{(D-13)}$$

If the effects of the reinforcement in the compression region are ignored, this simplifies to:

$$\beta^2 = \frac{E_T}{E_C} = n\rho \qquad \text{(D-14)}$$

The difference is small for $n\rho$ values $<< 1.0$, which are common in the field. In the cantilever column tests, the plug reached yield at about 1% drift, i.e. $\theta = 0.01$ radians. In a typical deck, the minimum reinforcement is approximately 0.3% top and bottom, so here $\rho \geq 0.006$. $\rho = 0.01$ is used here to account for the presence of the girders, and the steel that they contain. n is taken as 7.5, giving $\beta = \sqrt{n\rho} = 0.265$. Using a typical α value of 0.275 then gives:

$$\frac{L_{deck}^2}{b_{deck}L_{col}} = \frac{\theta}{\varepsilon_y}\frac{\pi^2}{(1+\beta)\sin(\alpha\pi)} = \frac{0.01}{0.002}\frac{\pi^2}{(1+0.265)\sin(0.275\pi)} = 51.3 \qquad \text{(D-15)}$$

This is rounded to 50 in the interests of simplicity. Decks with a ratio lower than 50 will be sufficiently stocky that the plug at the top of the column will not yield until after the deck has

214

yielded. This criterion provides a simple way of evaluating approximately the usefulness of the deck in protecting the columns.